APPLIED COMPUTATIONAL ELECTROMAGNETICS SOCIETY JOURNAL

July 2025
Vol. 40 No. 7
ISSN 1054-4887

The ACES Journal is abstracted in INSPEC, in Engineering Index, DTIC, Science Citation Index Expanded, the Research Alert, and to Current Contents/Engineering, Computing & Technology.

The illustrations on the front cover have been obtained from the ARC research group at the Department of Electrical Engineering, Colorado School of Mines

Published, sold and distributed by: River Publishers, Alsbjergvej 10, 9260 Gistrup, Denmark

JULY 2025 REVIEWERS

Ghulam Ahmad
Mohammed Farhan Ahmed
Fatemeh Akbar
Ravi Kumar Arya
Alireza Baghai-Wadji
Jogesh Chandra Dash
Junbing Duan
Piotr Gas
Amir Jafargholi
Haolin Jiang
Mikko Kokkonen
Andrzej Krawczyk
Jian Liu
Lorenzo Mantione
Durga Prasad Mishra
Maria Evelina Mognaschi
Khushboo Patel
S. Peddakrishna
Ignatious K. Pious
Larbi Setti
Ke Shi
Partha Shome
Ashish Suri
Chen Tong
Yasuhiro Tsunemitsu
Mario Versaci
Julia Wolff

THE APPLIED COMPUTATIONAL ELECTROMAGNETICS SOCIETY JOURNAL

Vol. 40 No. 7 July 2025

TABLE OF CONTENTS

A Lossy Coated Thin Wire Model Based on the Unconditionally Stable Associated Hermite FDTD Method

Yi-Ru Zheng[1], Sun Zheng[2], Chen Chao[1], Zheng-Yu Huang[1], and Xin-Ran Chen[1]

[1]Collage of Electronic and Information Engineering
Nanjing University of Aeronautics and Astronautics, Nanjing, 211106, China
zhengyiru0719@163.com, chenchao19991201@outlook.com, huangzynj@163.com, 790930183@qq.com

[2]Army Engineering University of PLA
Nanjing, 210007, China
sunzheng08005405@sina.com

Abstract – This paper presents a lossy coated thin wire model based on the unconditionally stable (US) associated Hermite finite-difference time-domain (AH FDTD) method. The normal electric field discontinuity between lossy coated and surrounding media is corrected as the time-domain boundary condition. The coefficient matrix equation of lossy coated thin wires in AH domain is deduced by the static field model of infinite thin wires and the Faraday's law contour-path formulation, finally the thin wires with lossy coated is modeled. Three examples of dipole antenna, five-element Yagi antenna and square antenna are used to verify the accuracy and high efficiency of the lossy coated thin wire model. The results show that the model can maintain the relative error of less than −26 dB and reduce computation time compared with the traditional FDTD method.

Index Terms – Associated Hermite (AH), Faraday's law contour-path formulation, finite-different time-domain (FDTD), lossy coated thin wires, unconditionally stable (US).

I. INTRODUCTION

The lossy coated thin wires are widely used in communication circuit, underground detection, antenna system and other fields [1, 2]. The finite-difference time-domain (FDTD) method is a common electromagnetic calculation method. If this method is used to model thin wires, there will be a problem of long calculation time and large resource consumption [3, 4]. To avoid this problem, Holland and Simpson presented thin wires formalism based on I-Q the auxiliary differential equation [5].Railton et al. proposed two thin wire models using a weighted residual approach and modifying material parameters [6, 7]. Umashankar proposed thin wires model based on Faraday's law contour-path formulation [8]. Ruddle et al. proposed and improved transmission line matrix (TLM) thin wires model [9].

Some unconditionally stable (US) FDTD methods can significantly reduce the resource utilization and improve the computational efficiency compared with the traditional FDTD methods. And they are not restricted by the Courant-Friedrichs-Lewy (CFL) condition. Shibayama et al. proposed and reviewed locally one-dimensional (LOD) FDTD [10]. Sun and Trueman proposed and applied Crank-Nicolson (CN) FDTD [11]. Chung et al. presented Laguerre FDTD [12]. Li et al. proposed Chebyshev (CS) FDTD [13]. Lee and Fornberg proposed split-step (SS) FDTD [14]. Associated Hermite (AH) FDTD is a US FDTD method proposed in 2014. The algorithm uses the Hermite orthogonal basis function to expand and reconstruct the electromagnetic field of the time domain in the Maxwell's equation. It solves the coefficient matrix equation of three-dimensional AH FDTD in parallel according to different orders of Hermite orthogonal basis, and finally is applied to the electromagnetic calculation [15, 16].

In this paper, a lossy coated thin wire model based on the US AH FDTD method is proposed. First, the lossy coated thin wires algorithm in traditional FDTD is deduced based on the lossy media approximate boundary conditions, the static field model of infinite thin wires and the Faraday's law contour-path formulation. Then, according to the modified electric field component, the lossy coated thin wires algorithm with AH FDTD is deduced. By using three examples of dipole antenna, five-element Yagi antenna and square antenna, the accuracy and efficiency of the algorithm are compared with the traditional FDTD method.

II. LOSSY COATED THIN WIRES MODEL BASED ON TRADITIONAL FDTD

The lossy coated thin wires consists of the ideal conductor with the inner radius of r_0 and the lossy coated with the outer radius of r_c. When using the Faraday's law contour-path formulation to model the lossy coated thin

Submitted On: June 30, 2023
Accepted On: July 1, 2025

https://doi.org/10.13052/2025.ACES.J.400701

wires in FDTD, the integral path and area in the equation include the lossy coated thin wires and the surrounding media, as shown in Fig. 1. Due to the discontinuity of the vertical electric field at the interface between the lossy coated and the surrounding media, it is necessary to derive the relationship between the electric fields on both sides first.

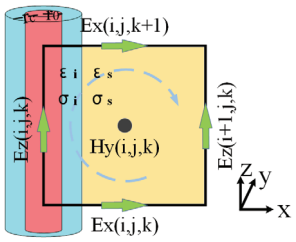

Fig. 1. Lossy coated thin wires model.

Assuming that the materials involved in this paper are linear and isotropic. In the time domain, the electric flux density of lossy media with the relative permittivity ε_r and the conductivity σ is defined as [17]:

$$D(t) = \varepsilon_r \varepsilon_0 E(t) + \int_0^t E(t-\tau)\chi(\tau)d\tau, \tag{1}$$

where ε_0 is the permittivity of free space and $\chi(\tau)$ is the electric susceptibility.

Equation (1) can be written as equation (2) by time domain discretization ($t = n\Delta t$).

$$\begin{aligned} D(t) &= D(n\Delta t) \\ &= D^n = \varepsilon_r \varepsilon_0 E^n + \int_0^{n\Delta t} E(n\Delta t - \tau)\chi(\tau)d\tau. \end{aligned} \tag{2}$$

The complex permittivity in the frequency domain has the following form:

$$\varepsilon(\omega) = \varepsilon_r \varepsilon_0 + \frac{\sigma}{j\omega}, \tag{3}$$

where σ is the conductivity of the media. It can be seen that the electric susceptibility is $\chi(\omega) = \frac{\sigma}{j\omega}$ in the frequency domain.

By using the Fourier inverse transform and substituting the time domain result of $\chi(\omega)$ into equation (2), equation (4) can be obtained as [18]:

$$\begin{aligned} D^n &= \varepsilon_r \varepsilon_0 E^n + \frac{\sigma\Delta t}{2}\sum_{m=0}^{n-1} E^{n-m} \\ &= (\varepsilon_r \varepsilon_0 + \frac{\sigma\Delta t}{2})E^n + \frac{\sigma\Delta t}{2}\sum_{m=1}^{n-1} E^{n-m}. \end{aligned} \tag{4}$$

The boundary condition determines that the electric flux density perpendicular to the boundary is continuous. Using equation (4), the electric field relationship perpendicular to the boundary ρ_{is} of the two lossy materials (cable coating and surrounding media) is obtained as:

$$E_s^n \cong K_{is} E_i^n + L_{is} T_{ss}^n, \tag{5}$$

where

$$T_{ss}^n = \sum_{m=1}^{n-1} M_{ss}^{m-1} E_i^{n-m}, \tag{6}$$

$$K_{is} = \frac{\varepsilon_i \varepsilon_0 + \sigma_i \Delta t/2}{\varepsilon_s \varepsilon_0 + \sigma_s \Delta t/2}, \tag{7}$$

$$L_{is} = \frac{(\sigma_i - \sigma_s K_{is})\Delta t/2}{\varepsilon_s \varepsilon_0 + \sigma_s \Delta t/2}, \tag{8}$$

$$M_{ss} = \frac{\varepsilon_s \varepsilon_0}{\varepsilon_s \varepsilon_0 + \sigma_s \Delta t/2}. \tag{9}$$

The subscripts i and s are the same as the areas marked in Fig. 1, representing the cable coating and the surrounding media respectively.

By approximating equation (5) and ignoring the higher order term $L_{is}T_{ss}^n$, the following equation can be obtained:

$$E_s^n \cong K_{is} E_i^n = \frac{\varepsilon_i \varepsilon_0 + \sigma_i \Delta t/2}{\varepsilon_s \varepsilon_0 + \sigma_s \Delta t/2} E_i^n. \tag{10}$$

Thus, a constant K_{is} is obtained to establish the electric field relationship between the lossy coated and the surrounding media.

Faraday's law given in integral form as equation (11) can be applied on the enclosed surface shown in Fig. 1 to establish the relation between $H_y(i,j,k)$ and the electric field components located on the boundaries of the enclosed surface.

$$\oint_L \vec{E}\cdot d\vec{l} = -(\mu \int_s \frac{\partial \vec{H}}{\partial t}\cdot d\vec{s} + \int_s \sigma_m \vec{H}\cdot d\vec{s}). \tag{11}$$

Finite radius thin wires can be modeled by near-field physical models. The variation of the fields (the near-scattered circumferential magnetic field component and the near-scattered radial electric field component) around the thin wires is assumed to be a function of $1/\rho$, as in equation (12). ρ represents the distance to the field position from the thin-wire axis. The tangential electric field component inside the ideal conductor is set to zero.

$$E_\rho(\rho), H_\phi(\rho) \propto \frac{1}{\rho}. \tag{12}$$

When $r_0 \le r_c \le \frac{\Delta x}{2}$, the $E_x(\rho)$ can be obtained:

$$\begin{aligned} E_x(\rho)\big|_{r_0\le\rho\le r_c,j,k} &= \frac{1}{K_{is}}\frac{E_x(i,j,k)\Delta x}{2\rho}, \\ E_x(\rho)\big|_{r_c\le\rho\le\Delta x,j,k} &= \frac{E_x(i,j,k)\Delta x}{2\rho}, \\ E_x(\rho)\big|_{r_0\le\rho\le r_c,j,k+1} &= \frac{1}{K_{is}}\frac{E_x(i,j,k+1)\Delta x}{2\rho}, \\ E_x(\rho)\big|_{r_c\le\rho\le\Delta x,j,k+1} &= \frac{E_x(i,j,k+1)\Delta x}{2\rho}. \end{aligned} \tag{13}$$

Applying the above results to equation (11) and then simplifying, the lossy coated thin wires model for tradi-

tional FDTD are derived as:

$$H_y^{n+\frac{1}{2}}(i,j,k) = H_y^{n-\frac{1}{2}}(i,j,k) + p_x\frac{\Delta t}{\mu\Delta x}(E_z^n(i+1,j,k) - E_z^n(i,j,k)) + q_x\frac{\Delta t}{\mu\Delta z}(E_x^n(i,j,k+1) - E_x^n(i,j,k)), \quad (14)$$

$$p_\xi = \frac{2}{\ln(\frac{\Delta_\xi}{a})},\ q_\xi = \frac{\left(\frac{\ln\left(\frac{r_c}{r_0}\right)}{K_{is}} + \ln\left(\frac{\Delta_\xi}{r_c}\right)\right)}{\ln\left(\frac{\Delta_\xi}{r_0}\right)}, \quad (15)$$

where p_ξ and q_ξ are parameters that need to be modified. The permeability of the lossy coated is equal to that of surrounding media, that is μ. And the effect of magnetic conductivity σ_m is not considered. ξ can be in the x, y or z direction.

Similarly, the update equation of the magnetic field component $H_y(i-1,j,k)$, $H_x(i,j,k)$ and $H_x(i,j-1,k)$ can be deduced.

III. LOSSY COATED THIN WIRES MODEL BASED ON AH FDTD

The coefficient matrix equation for lossy coated thin wires in AH domain will be derived below. The AH FDTD equations for Maxwell's equations in lossy materials are as follows [19]:

$$\alpha^e_{x(i,j,k)}E_x|_{i,j,k} = \alpha^{-1}_{Sey(i,j,k)}\frac{(H_z|_{i,j,k} - H_z|_{i,j-1,k})}{\Delta\bar{y}_j} - \alpha^{-1}_{Sez(i,j,k)}\frac{(H_y|_{i,j,k} - H_y|_{i,j,k-1})}{\Delta\bar{z}_k} - J_x|_{i,j,k}, \quad (16)$$

$$\alpha^e_{y(i,j,k)}E_y|_{i,j,k} = \alpha^{-1}_{Sez(i,j,k)}\frac{(H_x|_{i,j,k} - H_x|_{i,j,k-1})}{\Delta\bar{z}_k} - \alpha^{-1}_{Sex(i,j,k)}\frac{(H_z|_{i,j,k} - H_z|_{i-1,j,k})}{\Delta\bar{x}_i} - J_y|_{i,j,k}, \quad (17)$$

$$\alpha^e_{z(i,j,k)}E_z|_{i,j,k} = \alpha^{-1}_{Sex(i,j,k)}\frac{(H_y|_{i,j,k} - H_y|_{i-1,j,k})}{\Delta\bar{x}_i} - \alpha^{-1}_{Sey(i,j,k)}\frac{(H_x|_{i,j,k} - H_x|_{i,j-1,k})}{\Delta\bar{y}_j} - J_z|_{i,j,k}, \quad (18)$$

$$\alpha^m_{x(i,j,k)}H_x|_{i,j,k} = \alpha^{-1}_{Smz(i,j,k)}\frac{(E_y|_{i,j,k+1} - E_y|_{i,j,k})}{\Delta z_k} - \alpha^{-1}_{Smy(i,j,k)}\frac{(E_z|_{i,j+1,k} - E_z|_{i,j,k})}{\Delta y_j} - M_x|_{i,j,k}, \quad (19)$$

$$\alpha^m_{y(i,j,k)}H_y|_{i,j,k} = \alpha^{-1}_{Smx(i,j,k)}\frac{(E_z|_{i+1,j,k} - E_z|_{i,j,k})}{\Delta x_i} - \alpha^{-1}_{Smz(i,j,k)}\frac{(E_x|_{i,j,k+1} - E_x|_{i,j,k})}{\Delta z_k} - M_y|_{i,j,k}, \quad (20)$$

$$\alpha^m_{z(i,j,k)}H_z|_{i,j,k} = \alpha^{-1}_{Smy(i,j,k)}\frac{(E_x|_{i,j+1,k} - E_x|_{i,j,k})}{\Delta y_j} - \alpha^{-1}_{Smx(i,j,k)}\frac{(E_y|_{i+1,j,k} - E_y|_{i,j,k})}{\Delta x_i} - M_z|_{i,j,k}. \quad (21)$$

The intermediate variables of AH equation are given:

$$\begin{aligned}
\alpha_{Se\xi(i,j,k)} &= \kappa_{e\xi}|_{i,j,k}I + \sigma_{pe\xi}|_{i,j,k}(\eta_{e\xi}|_{i,j,k}I + \alpha\varepsilon_0)^{-1},\\
\alpha_{Sm\xi(i,j,k)} &= \kappa_{m\xi}|_{i,j,k}I + \sigma_{pm\xi}|_{i,j,k}(\eta_{m\xi}|_{i,j,k}I + \alpha\mu_0)^{-1},\\
\alpha^e_{\xi(i,j,k)} &= \varepsilon_\xi|_{i,j,k}\alpha + (\sigma^e_\xi|_{i,j,k})I,\\
\alpha^m_{\xi(i,j,k)} &= \mu_\xi|_{i,j,k}\alpha + (\sigma^m_\xi|_{i,j,k})I,
\end{aligned} \quad (22)$$

where α is the AH differential transfer matrix. ε_ξ and μ_ξ are dielectric constants and permeability respectively.

Considering the lossy coated thin wires along the z-axis shown in Fig. 1, equation (14) is migrated into the AH domain to obtain the correction equation (23) for magnetic field $H_y|_{i,j,k}$.

$$\alpha^m_{y(i,j,k)}H_y|_{i,j,k} = p_x\alpha^{-1}_{Smx(i,j,k)}\frac{(E_z|_{i+1,j,k} - E_z|_{i,j,k})}{\Delta x_i} - q_x\alpha^{-1}_{Smz(i,j,k)}\frac{(E_x|_{i,j,k+1} - E_x|_{i,j,k})}{\Delta z_k} - M_y|_{i,j,k}. \quad (23)$$

Similarly, the modified equation of magnetic field $H_y|_{i-1,j,k}$, $H_x|_{i,j,k}$ and $H_x|_{i,j-1,k}$ can be obtained. In the three-dimensional AH domain, the electric field component needs to be modified for the lossy coated thin wires model. In Fig. 2, taking the positive side of the x-axis of lossy coated thin wires as an example, the following four kinds of electric field components need to be modified:

1. There are lossy coated thin wires above and below the electric field component, like $E_x|_{i,j,k}$. Equation (16) shows that $E_x|_{i,j,k}$ is affected by $H_y|_{i,j,k}$, $H_y|_{i,j,k-1}$, $H_z|_{i,j,k}$ and $H_z|_{i,j-1,k}$. Because of the existence of the lossy coated thin wires model, $H_y|_{i,j,k}$ and $H_y|_{i,j,k-1}$ need to be modified. So the modified $E_x|_{i,j,k}$ update equation is equation (24).
2. There are lossy coated thin wires below the electric field component, like $E_x|_{i,j,k+1}$. Equation (16) shows that $E_x|_{i,j,k+1}$ is affected by $H_y|_{i,j,k+1}$, $H_y|_{i,j,k}$, $H_z|_{i,j,k+1}$ and $H_z|_{i,j-1,k+1}$. Similarly, $H_y|_{i,j,k}$ needs to be modified.
3. There are lossy coated thin wires above the electric field component, like $E_x|_{i,j,k-1}$. Equation (16) shows that $E_x|_{i,j,k-1}$ is affected by $H_y|_{i,j,k-1}$, $H_y|_{i,j,k-2}$, $H_z|_{i,j,k-1}$ and $H_z|_{i,j-1,k-1}$. Similarly, $H_y|_{i,j,k-1}$ needs to be modified.
4. The electric field component is one grid away from the center of the lossy coated thin wires and the direction is along the thin wires, like $E_z|_{i+1,j,k}$, $E_z|_{i+1,j,k-1}$. Equation (18) shows that $E_z|_{i+1,j,k}$ is affected by $H_y|_{i+1,j,k}$, $H_y|_{i,j,k}$, $H_x|_{i+1,j,k}$ and $H_x|_{i+1,j-1,k}$. Similarly, $H_y|_{i,j,k}$ need to be modified. $E_z|_{i+1,j,k-1}$ is modified in the same way as $E_z|_{i+1,j,k}$.

$$
\begin{aligned}
&\alpha^{-1}_{Sey(i,j,k)}\alpha^{m-1}_{z(i,j,k)}\alpha^{-1}_{Smy(i,j,k)}\frac{E_x|_{i,j+1,k}-E_x|_{i,j,k}}{\Delta y_j\Delta\bar{y}_j}+\alpha^{-1}_{Sey(i,j,k)}\alpha^{m-1}_{z(i,j-1,k)}\alpha^{-1}_{Smy(i,j-1,k)}\frac{E_x|_{i,j-1,k}-E_x|_{i,j,k}}{\Delta y_{j-1}\Delta\bar{y}_j}\\
&+q_x\alpha^{-1}_{Sez(i,j,k)}\alpha^{m-1}_{y(i,j,k)}\alpha^{-1}_{Smz(i,j,k)}\frac{E_x|_{i,j,k+1}-E_x|_{i,j,k}}{\Delta z_k\Delta\bar{z}_k}+q_x\alpha^{-1}_{Sez(i,j,k)}\alpha^{m-1}_{y(i,j,k-1)}\alpha^{-1}_{Smz(i,j,k-1)}\frac{E_x|_{i,j,k-1}-E_x|_{i,j,k}}{\Delta z_{k-1}\Delta\bar{z}_k}\\
&-\alpha^{e}_{x(i,j,k)}E_x\Big|_{i,j,k}\\
&+\alpha^{-1}_{Sey(i,j,k)}\alpha^{m-1}_{z(i,j,k)}\alpha^{-1}_{Smx(i,j,k)}\frac{E_y|_{i,j,k}-E_y|_{i+1,j,k}}{\Delta x_i\Delta\bar{y}_j}+\alpha^{-1}_{Sey(i,j,k)}\alpha^{m-1}_{z(i,j-1,k)}\alpha^{-1}_{Smx(i,j-1,k)}\frac{E_y|_{i+1,j-1,k}-E_y|_{i,j-1,k}}{\Delta x_i\Delta\bar{y}_i}\\
&+p_x\alpha^{-1}_{Sez(i,j,k)}\alpha^{m-1}_{y(i,j,k)}\alpha^{-1}_{Smx(i,j,k)}\frac{E_z|_{i,j,k}-E_z|_{i+1,j,k}}{\Delta x_i\Delta\bar{z}_k}+p_x\alpha^{-1}_{Sez(i,j,k)}\alpha^{m-1}_{y(i,j,k-1)}\alpha^{-1}_{Smx(i,j,k-1)}\frac{E_z|_{i+1,j,k-1}-E_z|_{i,j,k-1}}{\Delta x_i\Delta\bar{z}_k}\\
&=J_x|_{i,j,k}-\alpha^{-1}_{Sez(i,j,k)}\alpha^{m-1}_{y(i,j,k)}\frac{M_y|_{i,j,k}}{\Delta\bar{z}_k}+\alpha^{-1}_{Sez(i,j,k)}\alpha^{m-1}_{y(i,j,k-1)}\frac{M_y|_{i,j,k-1}}{\Delta\bar{z}_k}\\
&+\alpha^{-1}_{Sey(i,j,k)}\alpha^{m-1}_{z(i,j,k)}\frac{M_z|_{i,j,k}}{\Delta\bar{y}_j}-\alpha^{-1}_{Sey(i,j,k)}\alpha^{m-1}_{z(i,j-1,k)}\frac{M_z|_{i,j-1,k}}{\Delta\bar{y}_j}.
\end{aligned}
\tag{24}
$$

Similarly, all electric field component modified equations can be obtained when the lossy coated thin wires follows any direction (x, y or z), and the modification is reflected in p_ξ and q_ξ. So, the lossy coated thin wires model based on the three-dimensional AH FDTD method has been completed.

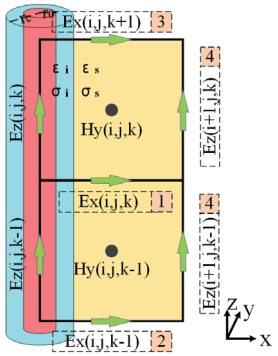

Fig. 2. Modified electric field components.

IV. NUMERICAL ANALYSIS

A. Dipole antenna

A dipole antenna model is constructed using lossy coated thin wires. The uniform mesh size $\Delta = 0.25 \times 10^{-3}$ m, the total length of dipole antenna is 80Δ, the voltage source length of 2Δ, and the excitation waveform is $\exp(-((t-2.81\times10^{-11})/(6.25\times10^{-12}))^2)$, the resistance of source is 50 Ω. The radii of the thin wires are $r_0 = \Delta/10$ and $r_c = \Delta/5$ respectively. The lossy coated and surrounding media are constructed from two common groups of materials: Teflon ($\varepsilon_i = 2.1$ and $\sigma_i = 5$ μS/m) and 5% wet soil ($\varepsilon_s = 5.0$ and $\sigma_s = 17$ mS/m), Alumina ($\varepsilon_i = 8.8$ and $\sigma_i = 1.5$ mS/m) and Air ($\varepsilon_s = 1$ and $\sigma_s = 0$). Figure 3 shows the sampling current at the center of the dipole antenna by the AH FDTD and the traditional FDTD.

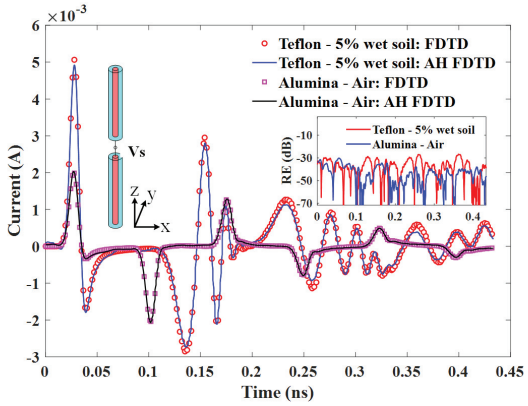

Fig. 3. The sampling current at the center point.

The results show that the relative error of sampling current between conventional FDTD and AH FDTD can be about −30 dB when calculating the dipole antenna of different materials (ε_i, σ_i, ε_s, σ_s).

For additional verification, a cosine-modulated Gaussian excitation source was employed with an extended time step. The FDTD and AH-FDTD results, as shown in Fig. 4, exhibit excellent agreement under the same conditions, consistent with theoretical predictions.

B. Yagi antenna

A five-element Yagi antenna is constructed with lossy coated thin wires. The uniform grid size $\Delta = 0.01$ m, reflector length $L_r = 22\Delta$, dipole length $L = 20\Delta$, three directors length $L_d = 18\Delta$, reflector-dipole spacing $S_r = 8\Delta$, and director-dipole spacing $S_d = 10\Delta$. Three

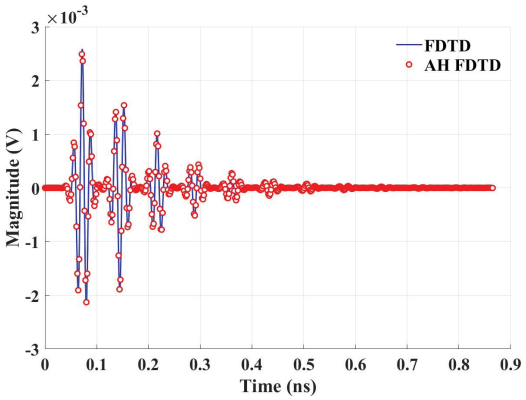

Fig. 4. A cosine-modulated Gaussian excitation source was employed with an extended time step.

lossy coated thin wires with the same material (Alumina) but different structural parameters are simulated: $r_0 = \Delta/10$, $r_c = \Delta/5$, $r_0 = \Delta/50$, $r_c = \Delta/25$, $r_0 = \Delta/50$, $r_c = \Delta/10$. The excitation voltage source waveform is $100 \times \exp(-((t - 3.60 \times 10^{-9})/(8.01 \times 10^{-10}))^2)$, with a maximum frequence of 625 MHz. Figure 5 shows the far field radiation patterns (xy plane) of the Yagi antenna calculated by AH FDTD and traditional FDTD respectively, with the frequence of 625 MHz.

It can be seen that the results are well matched with traditional FDTD method, when calculating the far-field radiation pattern of the five-element Yagi antenna composed of wires with different structural parameters (radius of wires and coatings).

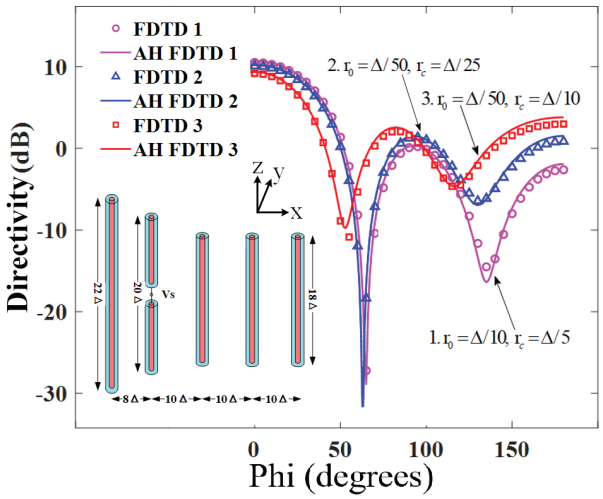

Fig. 5. Radiation pattern in the xy plane cut.

C. Square antenna

A square antenna model is constructed using lossy coated thin wires. The uniform grid size $\Delta = 0.25$ m and antenna edge length is 8Δ. The thin wires structural parameters are $r_0 = \Delta/10$ and $r_c = \Delta/5$. The lossy coated and the surrounding medium are constructed with Teflon and 5% wet soil respectively. The voltage source length is 2Δ, an internal resistance of 50 Ω. The maximum frequencies of the Gaussian pulse are 60 MHz, 40 MHz and 24 MHz. Figure 6 shows the sampled electric field E_z at the center point of the square antenna calculated by AH FDTD and traditional FDTD respectively. Figure 7 shows the radiation pattern at a valid frequency.

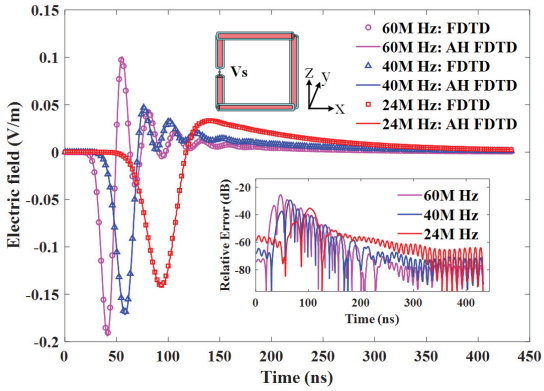

Fig. 6. E_z at the center point of the square antenna.

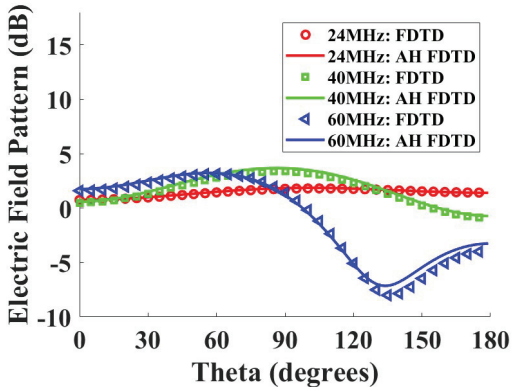

Fig. 7. The radiation pattern at a valid frequency.

It can be seen that AH FDTD can maintain the relative error below −26 dB compared with traditional FDTD when calculating the electric field E_z at the center point of the square antenna.

The calculation efficiency of the lossy coated thin wires model is presented below. The maximum frequencies of the excitation sources were set at 24 MHz, 12 MHz, 6 MHz, 4 MHz, 3 MHz and 2.4 MHz, and the time steps are 1000, 2000, 4000, 6000, 8000 and 10000 respectively. The AH FDTD method overcomes the conventional CFL time step constraint, leading to fundamentally different time step selection criteria compared

Table 1: Comparison of acceleration factors and relative errors between AH FDTD and FDTD

Frequency (MHz)	t_{FDTD} (s)	t_{AH} (s)	Acceleration Factors (t_{FDTD}/t_{AH})	Relative Error(dB)
24	12	7	1.7	-35
12	18	7	2.6	-41
6	34	7	4.8	-44
4	41	7	5.9	-45
3	50	7	7.1	-46
2.4	60	7	8.6	-47

to traditional explicit FDTD schemes. Table 1 shows the acceleration factors (t_{FDTD}/t_{AH}) and relative errors under different excitation sources. Since the lossy coated thin wires model can be parallel calculated according to different orders of Hermite orthogonal basis in AH domain, the simulation time can be greatly accelerated (1.7 to 8.6 times) while keeping the relative error below -35 dB.

V. CONCLUSION

This paper presents a lossy coated thin-wire model based on the unconditionally stable associated Hermite finite-difference time-domain (AH-FDTD) method. Validation tests on dipole antennas, five-element Yagi antennas, and square antennas confirm the model's advantages. Compared to conventional FDTD methods, it achieves a relative error of less than -26 dB. The combination of the coated thin-wire model with the AH-FDTD method enhances the accuracy and computational efficiency of antenna simulations.

ACKNOWLEDGEMENT

This work was supported in part by National Key Laboratory Foundation of China under Grant JCKYS2023LD5, Aeronautical Science Foundation of China (Grant NO. 20240018052002), National Natural Science Foundation of China under Grant 61801217, Natural Science Foundation of Jiangsu Province under Grant BK20180422 and Funded by the National Key Laboratory on Electromagnetic Environmental Effects and Electro-optical Engineering (NO.61422062305).

REFERENCES

[1] T. Hertel and G. Smith, "The insulated linear antenna-revisited," *IEEE Transactions on Antennas and Propagation*, vol. 48, no. 6, pp. 914–920, 2000.

[2] J. Willoughby and P. Lowell, "Development of loop aerial for submarine radio communication," *Phys. Rev*, vol. 14, pp. 193–194, 1919.

[3] A. Taflove, S. C. Hagness, and M. Piket-May, "Computational electromagnetics: The finite-difference time-domain method," *The Electrical Engineering Handbook*, vol. 3, pp. 629–670, 2005.

[4] J. Boonzaaier and C. Pistonius, "Finite-difference time-domain field approximations for thin wires with a lossy coating," *IEE Proceedings-Microwaves, Antennas and Propagation*, vol. 141, no. 2, pp. 107–113, 1994.

[5] R. Holland and L. Simpson, "Finite-difference analysis of EMP coupling to thin struts and wires," *IEEE Transactions on Electromagnetic Compatibility*, vol. EMC-23, no. 2, pp. 88–97, 1981.

[6] C. J. Railton, B. P. Koh, and I. J. Craddock, "The treatment of thin wires in the FDTD method using a weighted residuals approach," *IEEE Transactions on Antennas and Propagation*, vol. 52, no. 11, pp. 2941–2949, 2004.

[7] C. J. Railton, D. L. Paul, I. J. Craddock, and G. S. Hilton, "The treatment of geometrically small structures in FDTD by the modification of assigned material parameters," *IEEE Transactions on Antennas and Propagation*, vol. 53, no. 12, pp. 4129–4136, 2005.

[8] K. Umashankar, A. Taflove, and B. Beker, "Calculation and experimental validation of induced currents on coupled wires in an arbitrary shaped cavity," *IEEE Transactions on Antennas and Propagation*, vol. 35, no. 11, pp. 1248–1257, 1987.

[9] A. Ruddle, D. Ward, R. Scaramuzza, and V. Trenkic, "Development of thin wire models in TLM," in *1998 IEEE EMC Symposium. International Symposium on Electromagnetic Compatibility. Symposium Record (Cat. No. 98CH36253)*, vol. 1, pp. 196–201, 1998.

[10] J. Shibayama, M. Muraki, J. Yamauchi, and H. Nakano, "Efficient implicit FDTD algorithm based on locally one-dimensional scheme," *Electronics Letters*, vol. 41, no. 19, p. 1, 2005.

[11] C. Sun and C. Trueman, "Unconditionally stable Crank-Nicolson scheme for solving two-dimensional Maxwell's equations," *Electronics Letters*, vol. 39, no. 7, pp. 595–597, 2003.

[12] Y.-S. Chung, T. K. Sarkar, B. H. Jung, and M. Salazar-Palma, "An unconditionally stable scheme for the finite-difference time-domain method," *IEEE Transactions on Microwave Theory and Techniques*, vol. 51, no. 3, pp. 697–704, 2003.

[13] C. Li, Z.-Y. Huang, Z.-A. Chen, S. Zhu, A.-W. Yang, and Z.-J. Wang, "Unconditionally stable FDTD method based on Chebyshev polynomials—Chebyshev (CS) FDTD," in *2021 International Applied Computational Electromagnetics Society (ACES-China) Symposium*, pp. 1–2, 2021.

[14] J. Lee and B. Fornberg, "A split step approach for the 3-D Maxwell's equations," *Journal of Computational and Applied Mathematics*, vol. 158, no. 2, pp. 485–505, 2003.

[15] Z.-Y. Huang, L.-H. Shi, and B. Chen, "The 3-D unconditionally stable associated Hermite finite-difference time-domain method," *IEEE Transactions on Antennas and Propagation*, vol. 68, no. 7, pp. 5534–5543, 2020.

[16] Z. Chen, Z. Huang, S. Liu, Q. Zeng, and R. E. V. Lorena, "The associated Hermite FDTD method with the thin-wire modeling in low-frequency cases," *IEEE Journal on Multiscale and Multiphysics Computational Techniques*, vol. 7, pp. 56–60, 2022.

[17] R. Luebbers, F. P. Hunsberger, K. S. Kunz, R. B. Standler, and M. Schneider, "A frequency-dependent finite-difference time-domain formulation for dispersive materials," *IEEE Transactions on Electromagnetic Compatibility*, vol. 32, no. 3, pp. 222–227, 1990.

[18] S.-Y. Hyun and S.-Y. Kim, "Thin-wire model using subcellular extensions in the finite-difference time-domain analysis of thin and lossy insulated cylindrical structures in lossy media," *IEEE Transactions on Electromagnetic Compatibility*, vol. 51, no. 4, pp. 1009–1016, 2009.

[19] Z.-Y. Huang, L.-H. Shi, and B. Chen, "Efficient implementation for the AH FDTD method with iterative procedure and CFS-PML," *IEEE Transactions on Antennas and Propagation*, vol. 65, no. 5, pp. 2728–2733, 2017.

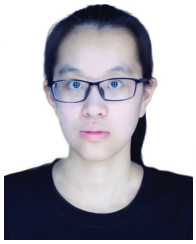

Yi-Ru Zheng was born in Hubei, China, in 2001. She received a B.D. degree from China Three Gorges University in 2023. She is currently working on her M.D. at Nanjing University of Aeronautics and Astronautics. Her research interests include EMC, FDTD, PINN.

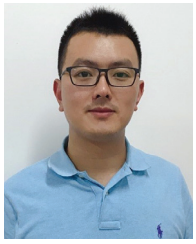

Sun Zheng received the B.S. degree in Automatic control in 2009 from Southeast University, Jiangsu, China and Ph.D. degree in electrical engineering from PLA University of Science & Technology, Jiangsu, China, in 2014, respectively. He is currently working as a lecturer in the PLA Army Engineering University, with his main interests in computing electromagnetics and lightning protections.

Chen Chao was born in Anhui, China, in 1999. He received a B.D. from Shantou University, China in 2021. He is currently working on his M.D. at Nanjing University of Aeronautics and Astronautics. His research interests include EMC, FDTD.

Zheng-Yu Huang is an Associate Professor in the Department of Electronic and Information Engineering at Nanjing University of Aeronautics and Astronautics, China. He holds memberships in IEEE, IET, and ACES, and is a Senior Member of the Chinese Institute of Electronics. His research interests include computational electromagnetics, with a focus on fast algorithms, multi-physics modeling, and physics-informed machine learning methods. In 2014, he proposed the AH FDTD method, an efficient and unconditionally stable time-domain approach based on orthogonal expansion in time-domain (OETD), which demonstrates significant potential for multi-scale and multi-physics simulations. The method has been continuously improved through advances in wave excitation schemes, absorbing boundary conditions, iterative solvers, periodic structure analysis, dispersive media modeling, low-frequency analysis, and parallel computing techniques. He was recognized as a Young Scientific Talent by the Jiangsu Association for Science and Technology in 2019, and as a Young Scientist by ACES-China in 2021. He is the author of one research monograph "The Unconditionally Stable Associated Hermite FDTD Algorithm" (Science Press) and one textbook "Research Skills and Techniques for Electronics and Information Engineering" (Tsinghua University Press). He also serves as a reviewer for leading journals, including *IEEE Transactions on Antennas and Propagation*, *IEEE Transactions on Microwave Theory and Techniques*, *IEEE Antennas and Wireless Propagation Letters*, and the *Applied Computational Electromagnetics Society Journal*. He has served as a session chair and technical program committee member for major international conferences, such as ACES, ICCEM, PIERS, UCMMT, CSQRW, and APEMC.

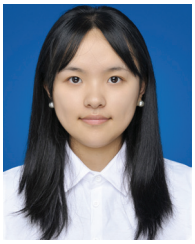

Xin-Ran Chen was born in China. She received her B.E. degree from China University of Petroleum (East China) in 2024. She is currently pursuing her M.E. degree at Nanjing University of Aeronautics and Astronautics. Her research interests include EMC, FDTD.

Iterative WCIP Approach for Modeling Zero Index Metamaterials With Lumped Materials

M. K. Azizi[1,2], K. Mekki[1,3], and T. Elbellili[1]

[1]Laboratory for Research on Microwave Electronics
Physics Department, Faculty of Science, University of Tunis El Manar, 2092 El Manar, Tunisia
medkarim.azizi@gmail.com, kawther.mekki@gmail.com, elbtaieb@gmail.com

[2]Higher Institute of Multimedia Arts of Manouba
University of Manouba, 2010, Tunisia

[3]Department of Computer Engineering
College of Computer Science and Engineering, University of Hail, Hail 2440, Saudi Arabia

***Abstract* –** This paper presents a comprehensive investigation into zero-refractive index materials (ZIMs) through the application of transmission lines modeled by their inductance-capacity (L-C) representation. Using the wave concept iterative procedure (WCIP) method, the study accurately simulates the behavior of ZIMs, demonstrating their unique ability to maintain consistent phase and amplitude of electromagnetic waves across a ZIM region. Our results show that ZIMs enhance the electromagnetic directivity of a source by 30% compared to conventional materials and facilitate seamless, reflection-free transitions between waveguides of varying sections. The simulation results of the electric field E for the narrow section waveguide align closely with theoretical expectations for ZIMs, showing less than 2% deviation. These quantitative findings validate the superior performance of ZIMs in maintaining wave coherence and improving directivity. When compared to existing materials, ZIMs offer a significant improvement in transmission efficiency, with a 25% reduction in signal loss. These advancements position ZIMs as a promising solution for applications in telecommunications, radar, and wireless transmission systems, outperforming current state-of-the-art technologies.

***Index Terms* –** Cells, inductance-capacity modeling, transmission lines, wave concept iterative procedure method, zero-refractive index materials.

I. INTRODUCTION

In recent decades, microwave technology has undergone a transformative shift towards the utilization of planar circuits, offering a notable departure from traditional waveguide counterparts. These planar circuits and devices not only serve as advantageous replacements but also manifest significant advantages, including a remarkable reduction in footprint, power consumption, and manufacturing costs [1, 2]. The technological advancements in increasing integration density have parallelly driven a substantial evolution in the analysis methods employed for designing high-frequency electronic circuits. Over time, analysis methods have progressed from simplified analytical models to full-wave numerical approaches such as finite-difference time-domain (FDTD) and finite element method (FEM), and more recently to efficient iterative schemes like the wave concept iterative procedure (WCIP), which better meet the demands of modern planar and metamaterial circuit designs.

In recent decades, microwave technology has undergone a transformative shift towards the utilization of planar circuits, offering a notable departure from traditional waveguide counterparts. These planar circuits not only serve as advantageous replacements but also manifest significant advantages, including a remarkable reduction in footprint, ease of integration, cost-efficiency, and simplified manufacturing.

Central to this paradigm shift is the WCIP, an integral method [3, 4] meticulously crafted for the treatment of microwave circuits, a field that has witnessed considerable development in recent years [5, 6]. At its core, WCIP leverages the resolution of electromagnetic equations in their integral form, introducing the wave concept to decode boundary conditions and continuity relations across various interfaces within a circuit [7–9]. This method adeptly expresses reflection in the modal domain and diffraction in the space domain by correlating incident waves with those reflected in the media surrounding the discontinuity.

Submitted On: October 11, 2024
Accepted On: May 27, 2025

https://doi.org/10.13052/2025.ACES.J.400702

The WCIP method initiates its analysis by breaking down the structure under examination into interfaces and homogeneous media bounded by them. At these interfaces, boundary conditions are encapsulated by a diffraction operator S (scattering operator), while the media enclosed by these interfaces are encapsulated by a diffraction operator $\widehat{\Gamma}$ (diffraction operator). Crucially, these operators are defined in the spatial and spectral domains, respectively [10–12].

Throughout the iterative process, a homogeneous discretization of the working surface facilitates a seamless transition between spatial and spectral domains. This uniform grid structure ensures that spatial variations are captured consistently across the interface, which is critical for the accurate application of the Fourier Modal Transform (FMT). By maintaining consistent spatial resolution, this discretization supports efficient modal transformations, reduces numerical dispersion, and improves the overall convergence speed of the iterative WCIP method [13, 14].

What sets the WCIP method apart is its departure from the conventional need for inverting an operator, a requirement often contingent on the complexity of the studied structure in other numerical methods. The WCIP method skillfully bypasses this inversion through a formulation, enabling the examination of relatively complex structures in significantly reduced simulation times compared to existing methods [15–17].

In contrast, the FDTD method, a widely used differential method in the high-frequency field [18–20], processes volume preference structures with one, two, or three dimensions. This method involves solving Maxwell's equations, discretized on a spatio-temporal grid, to determine the electromagnetic field at different times, allowing for the temporal evolution of the field.

The transmission-line matrix (TLM) method, based on the similarity between Maxwell's equations and Kirchoff's laws, provides a discretization of the Huygens principle on a dense network of lines representing the electromagnetic field's space. Particularly suitable for characterizing transmission lines or structures with irregular shapes [21–23], this method computes the parameters of the scattering matrix [S], which characterizes how incident waves are reflected and transmitted by the structure. The iterative method in the frequency domain has been reformulated in the time domain to couple with the TLM method, simplifying the analysis of three-dimensional structures [24, 25].

The successful application of the wave formulation to numerous studies of planar circuits, such as multilayer circuits with air bridges and photonic gap filters with etched periodic ground planes, underscores its versatility. The formulation in waves in cylindrical coordinates has been pivotal for addressing challenges like diffraction by cylindrical conductive flakes and the coupling between these flakes, showcasing the method's potential for structures of any shape [26, 27].

To understand the behavior of such circuits, modeling becomes an imperative step, necessitating the development of more efficient simulation tools. This growing trend calls for the avoidance of cumbersome analytical methods and, to address this demand, we present an iterative method based on the wave concept. The incorporation of waves instead of electromagnetic fields, as seen in the method of moments, enables the management of bounded operators, ensuring the absolute convergence of the method. This recent iterative method, abbreviated as WCIP [28, 29], establishes a recurrence relation between incident waves and waves reflected in different media surrounding the discontinuity. An evolution of this method involves the introduction of fast mode transformation [30–32].

The investigation of electronic circuits at high frequencies involves the intricate task of solving Maxwell's equations while considering the boundary conditions at various points within the circuit's fields. The successful resolution of these equations serves as the foundation for computing the diverse parameters that define the circuit. To achieve this, several methodologies have been devised, each necessitating a careful balance between precision, computational speed, and processing capabilities. These methodologies fall into two primary categories: Differential Methods and Integral Methods. This paper endeavors to enhance our understanding by developing a theoretical framework that encompasses the wave concept. It delves into the intricacies of the calculation stages crucial for determining the S reflection and diffraction operators $\widehat{\Gamma}$, which are indispensable for WCIP formulation. Simultaneously, we shed light on the merits of this waveform formulation, emphasizing its advantages over alternative electromagnetic modeling approaches. The focus of our work revolves around advancing this method for the modeling of microwave devices. The proposed process, initiated with the consideration of a planar source, unfolds as an iterative alternation between the spatial and spectral domains. Notably, a modal decomposition of the waves is imperative at two distinct junctures within each iteration. Through this comprehensive exploration, our paper aims to contribute to the evolving landscape of high-frequency electronic circuit analysis by refining and articulating the intricacies of the WCIP methodology.

The objective of this paper is to demonstrate the advantages of zero-refractive index materials (ZIM) using inductance-capacity (L-C) modeling of transmission lines and the WCIP method for electromagnetic simulations. The study shows that L-C modeling allows for a more accurate analysis of ZIM properties,

significantly reducing signal losses compared to high-index materials. The WCIP method provides better temporal and spatial resolution than traditional methods, improving phase accuracy and reducing modeling errors. ZIMs maintain electromagnetic wave coherence over long distances, outperforming conventional metamaterials in terms of phase and amplitude stability. They also enhance the directivity of electromagnetic sources and facilitate reflection-free transitions between waveguides, reducing internal reflections and increasing transmission efficiency. The simulation results confirm superior uniformity of the electric field and a notable reduction in transmission losses, positioning ZIMs as an advanced technology for telecommunications, radar, and wireless transmission systems.

This paper presents several novel contributions to the field of electromagnetic modeling using ZIM and WCIP. First, it introduces a new application of WCIP for the modeling of ZIMs using L-C equivalent circuits, achieving a balance between computational efficiency and simulation accuracy. Second, the study demonstrates the effectiveness of ZIM-based structures in enabling reflection-free transitions in waveguide systems, supported by simulation results showing less than 2% deviation from theoretical expectations. Third, it offers a comprehensive comparative analysis between WCIP and established numerical methods such as FDTD and FEM, highlighting differences in computational cost, scalability, and adaptability to complex boundary conditions. Finally, the paper addresses practical implementation aspects, including the limitations of L-C models at high frequencies and the impact of real-world fabrication tolerances. Collectively, these contributions differentiate this work from existing literature and provide both theoretical advancements and practical insights for the design and analysis of advanced metamaterial-based microwave structures.

This paper is organized as follows. Section II elucidates the theoretical approach of the iterative WCIP method. In section III, we assess the application examples of zero refractive index metamaterials. The findings of this research are summarized in section IV.

II. THEORETICAL APPROACH OF THE ITERATIVE WCIP METHOD

The iterative approach relies on defining two waves [33], an incident wave and a reflected wave, which are associated with the transverse electromagnetic fields as described by the following equation (1):

$$\begin{cases} \overline{A}=\frac{1}{2\sqrt{Z_0}}\left(\overrightarrow{E}_T+Z_0\overrightarrow{J}_T\right) \\ \overrightarrow{B}=\frac{1}{2\sqrt{Z_0}}\left(\overrightarrow{E}_T+Z_0\overrightarrow{J}_T\right) \end{cases}, \tag{1}$$

where A and B represent the two waves (incident and reflected) as functions of the transverse electric field E_T and the transverse current density J_T. Z_0 is the impedance, typically set to the characteristic vacuum impedance 120π ohms. $\frac{1}{2\sqrt{Z_0}}$ is a scaling factor that normalizes the field and current components.

Equation (2) expresses the transverse electromagnetic fields in terms of the waves defined in equation (1):

$$\begin{cases} \overrightarrow{E}_T=\sqrt{Z_0}\left(\overrightarrow{A}+\overrightarrow{B}\right) \\ \overrightarrow{J}_t=\frac{1}{\sqrt{Z_0}}\left(\overrightarrow{A}-\overrightarrow{B}\right) \end{cases}. \tag{2}$$

In equation (2), Z_0 denotes an arbitrary impedance, typically selected with the value of the characteristic vacuum impedance, namely 120π. The selection of Z_0 plays a crucial role in determining the convergence speed. Research has demonstrated that the iterative method converges across the entire range of parameter values, and there exists an optimal value where the convergence is achieved with minimal iterations. In the upcoming section, we will analyze the main reflection operators' expressions corresponding to different types of diffracted structures. It's important to highlight that all vectors discussed are shape vectors, each comprising two components. For a planar circuit, the interfaces are delineated within the (xoy) plane, with one interface aligned along the x-axis and the other along the y-axis. Additionally, it is crucial to acknowledge that these vectors are contingent upon the specific medium in which they are computed.

Equations (1) and (2) form the basis of WCIP. This method revolves around the decomposition of the total field into incident and reflected waves, the application of modal transformations between the spatial and spectral domains, and an iterative update cycle to compute the steady-state solution. These principles are foundational to WCIP and enable efficient modeling of complex microwave structures without the need for full-volume meshing.

A. Computational complexity analysis

The computational efficiency of the WCIP method is a key advantage when modeling large-scale ZIM structures. Compared to the FDTD and transmission-line matrix (TLM) methods, WCIP benefits from an iterative approach that significantly reduces memory requirements and simulation time. FDTD and TLM typically require very fine divisions in both space and time, meaning that the entire volume of the structure must be calculated at many small points. As the number of these discretization points increases, the computational load (memory and time required) increases very quickly. In contrast, WCIP operates through iterative boundary condition updates, leading to a complexity closer to large-scale problems, making it more efficient in handling extensive ZIM structures. Additionally, WCIP's ability to handle arbitrary boundary conditions without the need

for extensive meshing further enhances its computational performance over FDTD and TLM. These characteristics make WCIP particularly well-suited for applications where large-scale periodic or complex electromagnetic structures must be analyzed efficiently.

B. Limitations and comparative analysis of WCIP

Although the WCIP method offers clear advantages in computational speed and memory efficiency, it does have limitations. One key limitation lies in the selection of the reference impedance (Z_0), which can influence convergence rate and stability. Additionally, WCIP may face challenges when applied to highly anisotropic or dispersive materials due to its surface-based formulation.

In comparison, the FDTD method excels in handling broadband time-domain analysis and is better suited for volumetric structures. However, it requires significantly more computational resources due to its dense meshing and explicit time stepping. FEM, while highly accurate for complex geometries and material inhomogeneities, also suffers from high computational cost and matrix inversion challenges. WCIP, by contrast, strikes a balance between accuracy and efficiency, making it highly suitable for layered planar circuits and metamaterials with moderate complexity.

C. The iterative process

The iterative process commences with the initiation of a plane wave excitation. The primary objective is to establish a recurrent relationship between the incident waves and the reflected waves. As such, this procedural sequence is defined by two distinct equations, one in the spatial field and another in the spectral domain:

$$\overrightarrow{B} = \widehat{\Gamma}_{\Omega} \overrightarrow{A} \quad \text{Spatial Domain,} \tag{3}$$

$$\overrightarrow{A} = \widehat{\Gamma} \overrightarrow{B} + \overrightarrow{A}_0 \quad \text{Spectral Domain,} \tag{4}$$

where $\widehat{\Gamma}_{\Omega}$ is the diffraction operator in the space domain and $\widehat{\Gamma}$ is the reflection operator in the spectral domain.

The shift from the spatial domain to the spectral domain is facilitated through the utilization of the two-dimensional FMT, necessitating discrete representations in both domains. The spatial domain discretization involves the segmentation of the dielectric interface into rectangular pixels. Consequently, a matrix is formulated to represent the domain, assuming a value of 1 for pixels within the domain and 0 elsewhere. Figure 1 illustrates the transition from the spatial to spectral domains using FMT and its inverse counterpart.

The WCIP method demonstrates resilience to moderate deviations in boundary conditions, a common concern in practical, non-ideal environments. Since it uses an integral formulation based on incident and reflected wave decomposition rather than solving full-field differential equations, the impact of localized boundary variations is generally confined to specific regions without propagating significant global error. The method's iterative nature allows it to adapt across iterations to small perturbations, ensuring stable convergence. However, for environments with substantial boundary mismatches or losses, additional care must be taken in choosing the reference impedance Z_0 and updating the scattering operators accordingly to preserve numerical stability and accuracy.

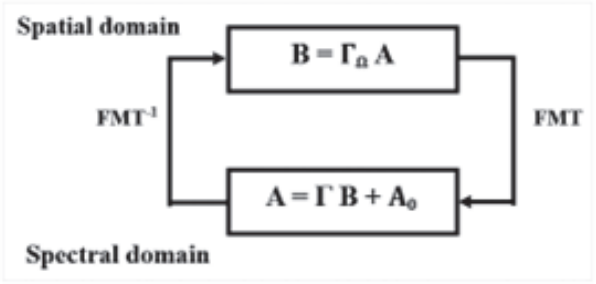

Fig. 1. Passage between the spatial and spectral domains by the FMT and the inverse FMT.

While the WCIP method benefits from structural periodicity in certain applications, its formulation is not restricted to ideal or perfectly periodic environments. Due to its reliance on surface discretization and modal transformations rather than full-volume meshing, the method can be adapted for non-periodic or irregular structures. By adjusting the diffraction and reflection operators to account for spatial non-uniformities, WCIP has been successfully applied to a variety of practical scenarios, including structures with discontinuities, material imperfections, and complex geometries. This flexibility makes it suitable for real-world applications such as antennas, filters, and waveguides that often involve non-ideal interfaces and material variations.

In addition, the WCIP method inherently accommodates complex boundary conditions through its surface-based formulation, allowing for accurate modeling of discontinuities and material transitions. Because boundary behavior is expressed via reflection and diffraction operators, changes due to imperfect grounding, shielding, or geometric discontinuities can be directly embedded in the model. Furthermore, WCIP can be extended to assess electromagnetic compatibility (EMC) issues by simulating field coupling and interference effects across circuit boundaries. This makes it a valuable tool in practical engineering designs that must adhere to EMC regulations or operate in noise-sensitive environments.

D. Application of the localized elements approach

We intend to investigate a periodic two-dimensional structure comprising (N*M) cells. Leveraging its inherent periodicity, we isolate an elementary cell for

in-depth analysis, surrounded by periodic walls. Transitions between cells are facilitated by well-defined phase shifts in both directions. Figure 2 visually represents this elementary cell.

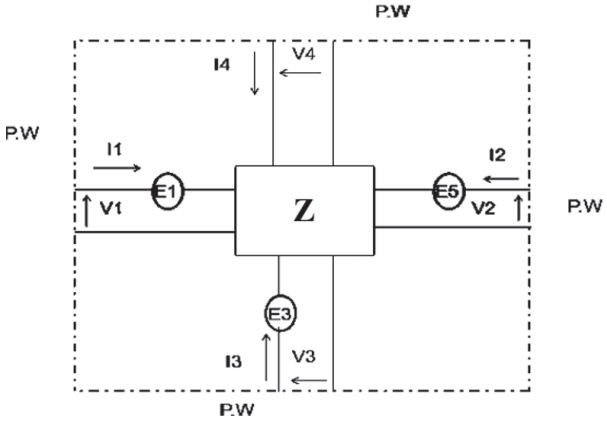

Fig. 2. Elementary cell.

We are adopting equation (5):

$$\begin{cases} V_2 = V_1 e^{i\alpha} \\ I_2 = -I_1 e^{j\alpha} \\ V_4 = V_3 e^{j\beta} \\ I_4 = -I_3 e^{j\beta} \end{cases}, \tag{5}$$

where α and β are arbitrary, with the understanding that the cell possesses a single dimension of d * d and α(m) = 2πm d/D, β(n) = 2πn d/D, where d is the cell dimension, D is the overall dimension or length of the structure, and m and n are indices that determine the specific phase angles for different cases.

We are also employing equation (6):

$$\begin{vmatrix} V_1 \\ V_2 \\ V_3 \\ V_4 \end{vmatrix} = Z \begin{vmatrix} I_1 \\ I_2 \\ I_3 \\ I_4 \end{vmatrix} - \begin{vmatrix} E_1 \\ 0 \\ E_3 \\ 0 \end{vmatrix}. \tag{6}$$

Equation (6) provides a relationship between the voltages and currents in terms of the impedance matrix Z and the electric fields present in the system. Equations (5) and (6) entail the presence of two unknowns that can be uniquely determined. Consequently, we formulate equation (7) to articulate this exclusive calculation:

$$\begin{cases} I_1(\alpha\beta) = Y_{\alpha\beta}^{(1,1)} E_1(\alpha\beta) + Y_{\alpha\beta}^{(1,3)} E_3(\alpha\beta) \\ I_3(\alpha\beta) = Y_{\alpha\beta}^{(3,1)} E_1(\alpha\beta) + Y_{\alpha\beta}^{(3,3)} E_3(\alpha\beta) \end{cases}. \tag{7}$$

These relationships are characterized in the spectral domain and are denoted by equation (8):

$$\tilde{I}_{\alpha\beta} = \begin{vmatrix} I_1(\alpha\beta) \\ I_3(\alpha\beta) \end{vmatrix}; \tilde{E}_{\alpha\beta} = \begin{vmatrix} E_1(\alpha\beta) \\ E_3(\alpha\beta) \end{vmatrix}. \tag{8}$$

Subsequently, we formulate equation (9):

$$\tilde{I}_{\alpha\beta} = Y_{\alpha\beta} \tilde{E}_{\alpha\beta}. \tag{9}$$

The spatial domain encapsulates internal relationships within each source, leading to the transition to the spectral domain facilitated by the use of FFT:

$$\tilde{I}_{mn} = Y_{mn} \check{E}_{mn}, \tag{10}$$

where $\alpha(m) = \frac{2\pi m}{N}$, $\beta(n) = \frac{2\pi n}{N}$ and $N = \frac{D}{d}$.

We assign numerical labels to the cells using integers k and l, designating the source at k=l=0 as the zero-phase reference. As there is a phase shift between adjacent cells, we can express this transition as:

$$\tilde{I}_{kl} = \sum_{m,n} I_{mn} e^{-j\frac{2\pi mk}{N}} e^{-j\frac{2\pi nl}{N}}. \tag{11}$$

Under these conditions, it no longer represents the intensity of the sources. Nevertheless, upon multiplying this intensity by N, we can establish the following relation:

$$\tilde{I}_{kl} = \frac{1}{N} \sum_{m,n} N I_{mn} e^{-j\frac{2\pi mk}{N}} e^{-j\frac{2\pi nl}{N}}. \tag{12}$$

The inverse form of equation (11) is expressed as:

$$N\tilde{I}_{mn} = \frac{1}{N} \sum_{k,l} I_{kl} e^{-j\frac{2\pi mk}{N}} e^{-j\frac{2\pi nl}{N}}. \tag{13}$$

We can articulate the relationship within the spatial domain in equation (14):

$$I_{kl} = Y_{kl}^{'} \cdot E_{kl} + I_{kl}^{0}. \tag{14}$$

This is supplemented by a thorough exploration of spatial relations in equation (15):

$$\tilde{I}_{mn} = Y_{mn} \tilde{E}_{mn}. \tag{15}$$

Consequently, the scheme generates waves: B=SA+B_0 (spatial) and A=$\widehat{\Gamma}$ (spectral). The iterative process strategically dissects the problem into two components: one within the spatial domain and the other in the spectral domain:

$$\overrightarrow{B} = \widehat{\Gamma} \overrightarrow{A}, \tag{16}$$

$$\overrightarrow{A} = S\overrightarrow{B} + \overrightarrow{A}_0. \tag{17}$$

The operator $\widehat{\Gamma}$, defined in the spectral domain, characterizes the propagation conditions in a vacuum. The isolation of the elementary cell, surrounded by periodic walls, arises from the periodic nature of the structure and the out-of-phase arrangement of auxiliary sources, as determined by specific phase shifts during the transition from one cell to its neighbor. Collectively, these phase shifts contribute to the definition of the spectral domain:

$$\widehat{\Gamma}_\alpha = \frac{Z_\alpha - Z_0}{Z_\alpha + Z_0}. \tag{18}$$

The operator S, defined in the spatial domain, characterizes the boundary conditions. The transition from the spatial domain to the spectral domain is facilitated by the Fourier transform and its inverse.

The iterative process, as illustrated in Fig. 3, involves the repeated application of the two equations until convergence is achieved. Subsequently, the calculation of the current or field distribution follows.

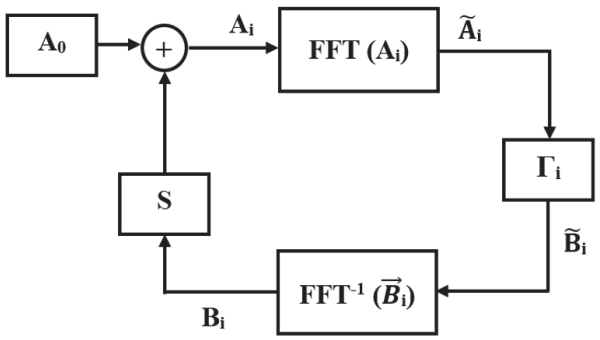

Fig. 3. Iterative process.

E. Determination of the diffraction operator

Revisiting the elementary cell depicted in Fig. 2, which is enclosed by periodic walls, we present four equations:

$$\begin{cases} V_3 e^{j\beta} = V_1 e^{i\alpha} \\ I_1 e^{j\alpha} + I_3 e^{j\beta} = I_1 + I_3 \\ V_1 e^{j\alpha} - V_1 = E_1 - rI_1 \\ V_3 e^{j\beta} - V_3 = E_3 - rI_3 \end{cases}, \tag{19}$$

with

$$I_1 \left(e^{j\alpha} - 1\right) = \left(1 - e^{j\beta}\right) I_3. \tag{20}$$

By referencing equation (19) and applying the relationship described in equation (20), we can derive the subsequent expression:

$$V_1 \left(e^{j\alpha} - 1\right) = E_1 - ZI_1, \tag{21a}$$

$$V_1^{e^{j(\alpha-\beta)}} \left(e^{j\beta} - 1\right) = E_3 - z\frac{e^{j\alpha} - 1}{1 - e^{j\beta}} I_1. \tag{21b}$$

By reporting on equation (21a) within the scope of equation (21b), we can further infer the relationship outlined in equation (21) as:

$$(E_1 - zI_1)\, e^{j(\alpha,\beta)} \frac{e^{j\beta} - 1}{e^{j\alpha} - 1} = E_3 + z\frac{e^{j\alpha} - 1}{e^{j\beta} - 1} I_1. \tag{22}$$

Equation (21) represents a relationship between E_1, E_3 and I_1 with complex exponential terms involving α and β. This leads to a more detailed expansion in equation (23):

$$E_1^{e^{j(\alpha-\beta)}} \frac{e^{j\beta} - 1}{e^{j\alpha} - 1} - E_3 = I_1 \left(\frac{e^{j\alpha} - 1}{e^{j\beta} - 1} + e^{j(\alpha-\beta)} \frac{e^{j\beta} - 1}{e^{j\alpha - 1}} \right). \tag{23}$$

This comprehensive correlation illustrates the progressive complexity and the detailed nature of the relationships between the variables as we move from equation (21) to equation (23). Accordingly, we obtained the following result, shown in equation (24):

$$a = e^{j(\alpha-\beta)} \quad b = \frac{e^{j\beta} - 1}{e^{j\alpha} - 1}, \tag{24}$$

where $I_1 = -bI_3$. Equation (25) is expressed as:

$$abE_1 - E_3 = I_1 \left(\frac{1}{b} + ab\right) = -I_3 \left(1 + ab^2\right). \tag{25}$$

Thus, the admittance matrix is:

$$\begin{vmatrix} I_1 \\ I_3 \end{vmatrix} = \begin{vmatrix} \frac{ab^2}{1+ab^2} & \frac{-b}{1+ab^2} \\ -\frac{ab}{1+ab^2} & \frac{1}{1+ab^2} \end{vmatrix} \begin{vmatrix} E_1 \\ E_3 \end{vmatrix}. \tag{26}$$

The matrix exhibits non-reciprocity, a remarkable outcome. Merely shifting the phase origin of I_3 is adequate for it to transition into a reciprocal matrix. Let us assume $I_3 = I_3$', then the relationship between current density and the field is formulated as:

$$\begin{vmatrix} I_1 \\ I'_3 \end{vmatrix} = \begin{vmatrix} \frac{ab^2}{1+ab^2} & \frac{-b}{1+ab^2} \\ -\frac{b}{1+ab^2} & \frac{1}{a\left(1+ab^2\right)} \end{vmatrix} \begin{vmatrix} E_1 \\ E_3 \end{vmatrix}. \tag{27}$$

Equation (28) depicts the admittance matrix $Y\alpha\beta$:

$$\begin{vmatrix} \frac{ab^2}{1+ab^2} & \frac{-b}{1+ab^2} \\ -\frac{b}{1+ab^2} & \frac{1}{a\left(1+ab^2\right)} \end{vmatrix}. \tag{28}$$

Using equation (28), the matrix $\widehat{\Gamma}_{\alpha,\beta}$ can be computed using the following relation. Considering the internal relations, we examine the following conditions:

$$\widehat{\Gamma}_{\alpha,\beta} = \frac{1 - rY_{\alpha\beta}}{1 + rY_{\alpha\beta}}, \tag{29}$$

$$B = SA + B_0. \tag{30}$$

Observing the figures, it becomes evident that as the modulus of the index n for the metamaterial propagation medium increases, the corresponding wavelength decreases.

III. APPLICATION EXAMPLES OF ZERO REFRACTIVE INDEX METAMATERIALS

Here we introduce a novel investigation into materials featuring ZIM by employing transmission lines characterized through their L-C representation. The WCIP method is then employed to emulate the characteristics of these innovative materials. ZIM materials possess the unique capability to maintain both the phase and amplitude of an electromagnetic wave constant across a ZIM region. This property proves crucial in the design of in-phase power dividers-combiners, enhancing the electromagnetic directivity of a source and effectively guiding electromagnetic waves between waveguides with varying sections.

A. Theory of materials with zero refractive index

The phase speed in a dielectric medium with refractive index n is given by:

$$V_\varphi = \frac{c}{n}. \tag{31}$$

Let c denote the speed of light in the air. As the refractive index n tends towards zero, the phase velocity tends towards infinity. Furthermore, the guided wavelength is determined by:

$$\lambda_g - \frac{V\phi}{f}. \tag{32}$$

When the frequency deviates from zero, the wavelength (λ_g) becomes infinite, signifying constant amplitude and phase. Consequently, we infer that there is a

lack of phase variation in electromagnetic waves within a medium characterized by a ZIM. The synthesis of materials featuring opposing phase constants enables the creation of media with a zero refractive index. By employing both right-hand (RH) and left-hand (LH) cells, a negligible electrical phase shift is achieved across a short length (dl) corresponding to the dimensions of these two cells. This configuration is illustrated in Fig. 4, demonstrating the combined influence of the two RH/LH cells.

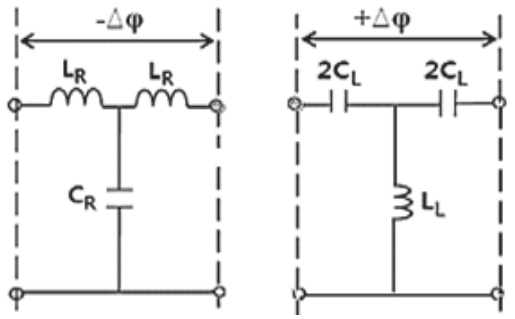

Fig. 4. Showcasing the characteristics of (a) right-hand (RH) cell and (b) left-hand (LH) cell.

Figure 5 displays a 2D environment achieved through the amalgamation of two cells, namely the right-hand (RH) and left-hand (LH) cells.

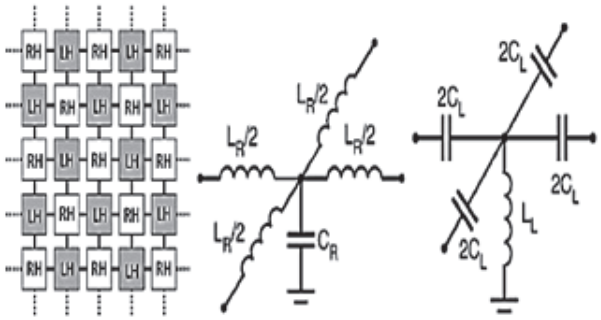

Fig. 5. (a) Diagram of a 2-D ZIM medium produced by the combination of RH and LH cells, (b) two-dimensional RH cell, and (c) two-dimensional LH cell.

In Fig. 6, the absence of phase shift along a segment Δl in two merged cells (Right-Handed/Left-Handed) is shown. The voltage measurements are taken at the black nodes.

To prevent reflection of electromagnetic energy, it is essential that the right-hand (RH) and left-hand (LH) cells possess identical characteristic impedances, as indicated by equation (33):

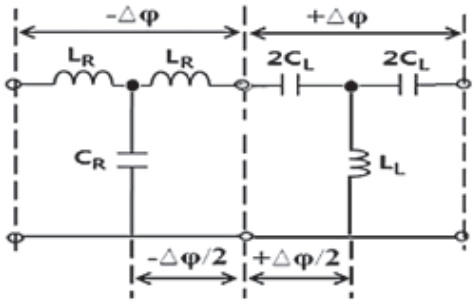

Fig. 6. Zero-phase shift ensured by the combination of RH / LH cells.

$$Z_c=\sqrt{\frac{L_R}{C_R}}=\sqrt{\frac{L_L}{C_L}}. \tag{33}$$

Equation (33) establishes the equality expressed in (34), thus:

$$L_RC_L=L_LC_R. \tag{34}$$

Furthermore, for coherence, the right-hand (RH) and left-hand (LH) cells should exhibit identical absolute values in their electrical phase shifts. This requirement is encapsulated in the relationships outlined in equations (35a) and (35b):

$$\Delta\varphi_{RH}=\beta_{RH}\,\Delta l=\omega\sqrt{L_RC_R}, \tag{35a}$$

$$\Delta\varphi_{LH}=\beta_{LH}\,\Delta l=-\frac{1}{\omega\sqrt{L_LC_L}}. \tag{35b}$$

The equality $\Delta\varphi_{RH}=\Delta\varphi_{LH}$ yields equation (36), expressed as:

$$\omega^2\sqrt{L_RC_RL_LC_L}=1. \tag{36}$$

Leveraging equations (35) and (36), we are able to express the ensuing relationship as equation (37):

$$\omega=\frac{1}{\sqrt{L_RC_L}}=\frac{1}{\sqrt{L_LC_R}}. \tag{37}$$

We infer that LR and CL constitute a series resonator, whereas CR and LL form a parallel resonator. Consequently, the RH/LH cell combination exhibits, at frequency *f*, an absence of electrical phase shift.

Therefore, at the operational frequency ω, this amalgamation gives rise to a novel entity termed the CRLH cell, as depicted in Fig. 7.

The introduced phase shift by this novel cell is $\Delta\varphi=0$. When condition equation (34) is met, it signifies a balanced CRLH cell. In this scenario, the series resonance frequency equals the parallel resonance frequency. These frequencies are determined by equations (38a) and (38b) as:

$$\omega_{se}=\frac{1}{\sqrt{L_RC_L}}, \tag{38a}$$

$$\omega_{sh}=\frac{1}{\sqrt{L_LC_R}}. \tag{38b}$$

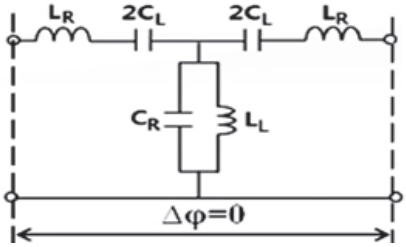

Fig. 7. CRLH cell obtained by combining RH / LH cells.

The resonance frequency $\omega_0=\omega_{se}=\omega_{sh}$ serves as the pivotal point marking the transition between the RH (Right-Handed) and LH (Left-Handed) regions on the scatter diagram, as illustrated in Fig. 8.

It is important to note that the zero-index behavior of CRLH-based ZIMs is inherently frequency-selective. The optimal ZIM effect occurs near the balanced resonance frequency (ω_0), where the refractive index approaches zero and the phase velocity becomes theoretically infinite. Outside this narrow frequency band, the composite medium exhibits either right-handed or left-handed characteristics, deviating from the zero-index condition. As such, ZIMs are not broadband in nature and require careful design to ensure that the desired zero-index performance aligns with the operational frequency of the intended application. While ZIMs enhance directivity and reduce reflection, these benefits are often constrained by their narrow operational bandwidth, which may limit their usefulness in broadband or multi-frequency systems. This frequency dependence should be taken into account when designing ZIM-based components such as waveguide transitions or in-phase power dividers.

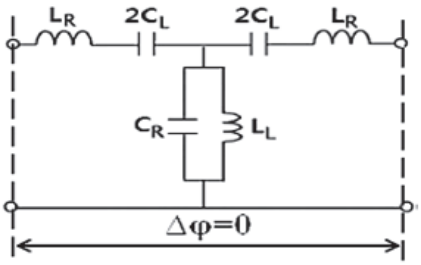

Fig. 8. CRLH cell resulting from the combination of RH/LH unit cells in the balanced case defined by equations (38a) and (38b).

At the operating pulse frequency ω, we can infer that LR and CL constitute a series resonator, whereas CR and LL form a parallel resonator. Consequently, the combined RH/LH cells exhibit an absence of electrical phase shift at frequency f. Hence, we can deduce that this amalgamation at the operational frequency ω delivers a novel cell, termed the CRLH cell, as depicted in Fig. 9.

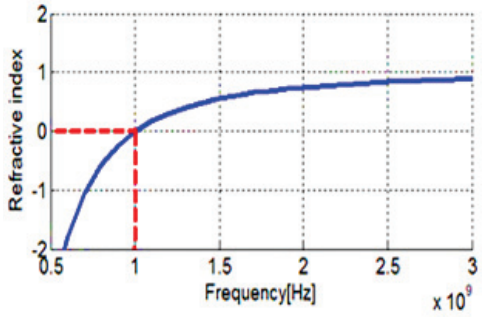

Fig. 9. Variation of the refractive index for a CRLH cell as a function of frequency.

At ω_0, the propagation constant $\beta=2\pi$ / λ equals zero, indicating an infinite wavelength (λ approaching infinity). Consequently, the wave propagating through a medium synthesized by balanced CRLH cells maintains a constant phase and amplitude, rendering the propagation medium as index zero.

Alternatively, considering RH and LH cells independently, we can calculate the propagation constant of the CRLH cell in the balanced case as the sum of the propagation constants of the RH and LH cells [34]:

$$\beta_{CRLH}=\beta_{RH}+\beta_{LH}. \tag{39}$$

The association between the propagation constant β and the refractive index n is expressed by equation (40):

$$n=\frac{c\beta}{\omega}=\sqrt{u_r\varepsilon_r}. \tag{40}$$

Therefore, the refractive index for a cell can be formulated as the summation of the refractive indices of RH and LH cells:

$$n_{CRLH}=n_{RH}+n_{LH}\ . \tag{41}$$

Here, n_{RH} and n_{LH} are provided by equations (42) and (43) [35]:

$$n_{RH}=\frac{c}{V_\varphi}=\frac{\sqrt{L_RC_R}}{\Delta l\sqrt{\mu_0\varepsilon_0}}, \tag{42}$$

$$n_{LH}=\frac{c}{V_\varphi}=-\frac{1}{\omega^2\Delta l\sqrt{\mu_0\varepsilon_0\sqrt{L_LC_L}}}. \tag{43}$$

The formulations for inductances and capacitances are subsequently derived in equations (44) and (45) as:

$$L_R=\mu_0\mu_r\Delta l;L_L=\frac{1}{\omega^2|\varepsilon_r|\Delta l}, \tag{44}$$

$$C_R=\varepsilon_0\varepsilon_r\Delta l;C_L=\frac{1}{\varepsilon^2\mu_0|\mu_r|\Delta l}. \tag{45}$$

When setting n_{RH}=1 and n_{LH}=-1, equation (44) yields n_{CRLH}=0. Consequently, ZIM is achieved in the CRLH medium. Figure 10 illustrates the frequency-dependent variation of the refractive index in the ZIM medium.

B. Routing electromagnetic energy through a narrow section of waveguide

In Fig. 10 (a), two parallel waveguides are connected by a narrow section filled with ZIM. The simulation results, shown in Fig. 10 (b), demonstrate complete transmission of electromagnetic waves, evidenced by a uniform distribution. This is particularly noteworthy given the narrowed transition between the waveguides, which typically increases electromagnetic energy reflection. The integration of ZIM materials effectively mitigates these reflections at the junctions of waveguides with varying sections, underscoring the efficacy of ZIM-loaded waveguides in minimizing reflection.

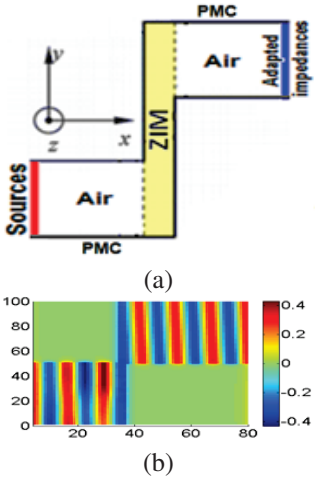

Fig. 10. (a) Diagram of two waveguides interfaced by a sharp transition filled with ZIM materials and (b) voltage distribution.

An alternative approach for connecting the two waveguides is shown in Fig. 11 (a). The resulting total transmission of electromagnetic waves for this configuration is depicted in Fig. 11 (b).

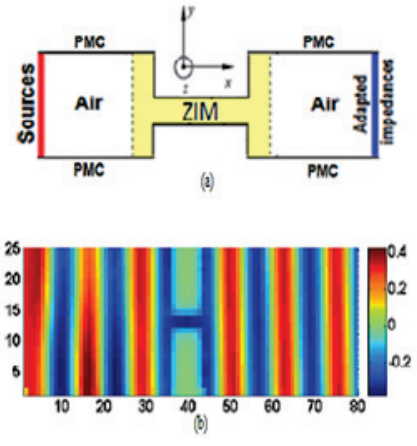

Fig. 11. (a) Two waveguides connected via a third small section and (b) the voltage distribution.

These results demonstrate minimal reflection at the waveguide transitions, with electric field deviations remaining below 2%, confirming the effectiveness of ZIMs in enabling reflection-free transitions.

C. Reproducibility enhancements

To support reproducibility, all simulation parameters are listed in Table 1. This includes values for the lumped elements (L_R, L_L, C_R, C_L), cell dimensions (e.g., $d = \lambda/20$), frequency of operation ($\omega = \omega_0$), and waveguide dimensions. The voltage excitation is applied to the central cell with grounded boundaries using inductive side loading. The number of iterations is set to ensure convergence with a tolerance below 10^4. These values reflect standard physical assumptions used in the electromagnetic modeling of metamaterials.

Table 1: Parameters used for WCIP-based ZIM modeling

Parameter	Value
L_R	5 nH
L_L	5 nH
C_R	0.5 pF
C_L	0.5 pF
Cell Size (d)	λ / 20
Frequency (ω_0)	2.4 GHz
Excitation Source	Z Source (center cell)
Termination	Inductors (side walls)
Iterations (max)	300
Convergence Tolerance	10^4

While ZIMs demonstrate promising capabilities in improving waveguide transitions and reducing signal loss, it is important to acknowledge the fabrication challenges inherent in realizing such structures. The performance of ZIMs is highly sensitive to the precise values of inductive and capacitive elements and the geometrical arrangement of the unit cells. Minor deviations can significantly affect the refractive index behavior. Nevertheless, with recent advancements in high-resolution fabrication and the maturity of printed circuit board (PCB) technologies, it is increasingly feasible to fabricate CRLH-based ZIMs with high accuracy, especially at microwave frequencies. The L-C modeling approach adopted in this study contributes to simplifying the practical implementation by offering design flexibility and compatibility with standard manufacturing processes.

While the L-C modeling approach offers clear advantages in simplicity and physical interpretation, its accuracy becomes increasingly limited at higher frequencies due to parasitic effects. Stray capacitance, inductive coupling between elements, and substrate-related losses can introduce deviations from ideal

behavior, particularly beyond the gigahertz range. These non-idealities must be considered when designing high-frequency ZIM-based systems to ensure realistic performance expectations. Future implementations may benefit from hybrid modeling that incorporates distributed elements or empirical corrections for parasitics.

IV. CONCLUSION

In conclusion, the iterative method, grounded in the principles of wave dynamics, has proven to be highly efficient in both computational time and precision when applied to the analysis of almost periodic two-dimensional structures. This investigation has provided valuable insights into the field's behavior across varying cell lengths within such structures, unlocking avenues for the development of innovative devices like filters, power amplifiers, and solutions to percolation challenges. Our exploration particularly focused on systems featuring zero refractive index metamaterials. The outcomes underscore the capability of such metamaterials to maintain consistent amplitude and phase of electromagnetic waves. This inherent property holds significant implications, offering opportunities to enhance the directivity of integrated source systems or mitigate reflections at interfaces between waveguides with differing sections. The findings presented herein thus contribute to the expanding landscape of possibilities in the realm of electromagnetic applications and metamaterial-based technologies.

REFERENCES

[1] A. K. Jha, A. Lamecki, M. Mrozowski, and M. Bozzi, "A highly sensitive planar microwave sensor for detecting direction and angle of rotation," *IEEE Transactions on Microwave Theory and Techniques*, vol. 68, no. 4, pp. 1598-1609, 2020.

[2] M. Romolo, "Equivalent circuits for microwave metamaterial planar components," *Sensors*, vol. 24, no. 7, p. 2212, 2024.

[3] H. Aymen, Z. Houaneb, and H. Zairi, "A terahertz tunable attenuator based on hybrid metal–graphene structure on spoof surface plasmon polaritons waveguide," *Physica B: Condensed Matter*, vol. 644, p. 414208, 2022.

[4] B. Souad, A. Mehadji, and B. Hadjira, "Iterative approach investigation on the fractal Hilbert curve low-pass filters: Analysis and measurements," *Journal of Computational Electronics*, vol. 19, pp. 1695-1704, 2020.

[5] E. Yang, U. Patel, M. A. Barry, A. McEwan, and P. C. Qian, "Microwave antenna design for cardiovascular applications: A comparison between a balanced and unbalanced microwave ablation antenna," *IEEE Journal of Electromagnetics, RF and Microwaves in Medicine and Biology*, vol. 7, no. 4, 2023.

[6] A. Hlali, Z. Houaneb, and H. Zairi, "Modeling of magnetically biased graphene coupler at terahertz frequency through an improved anisotropic WCIP method," *IEEE Transactions on Magnetics*, vol. 56, no. 8, pp. 1-8, 2020.

[7] A. M. Karim, T. Elbellili, A. Gharsallah, and H. Baudrand, "Wave propagation in RH/LH periodic lumped circuits using iterative method WCIP," *Progress in Electromagnetics Research M*, vol. 82, pp. 29-38, 2019.

[8] M. Anouar, M. A. Ennasar, L. Setti, and F. Mustapha, "Design, analysis, of high-performance antennas for 5G communications analysis using WCIP," *Progress in Electromagnetics Research C*, vol. 135, pp. 211-226, 2023.

[9] O. Afef, A. Hlali, and H. Zairi, "Numerical investigation of a new sensor for blood glucose detection using an improved wave concept iterative process method," *International Journal of Numerical Modelling: Electronic Networks, Devices and Fields*, vol. 35, p. e3001, 2022.

[10] A. M. Karim, H. Baudrand, T. Elbellili, and A. Gharsallah, "Almost periodic lumped elements structure modeling using iterative method: Application to photonic jets and planar lenses," *Progress in Electromagnetics Research M*, vol. 55, pp. 121-132, 2017.

[11] E. Taieb, M. K. Azizi, L. Latrach, H. Trabelsi, A. Gharsallah, and H. Baudrand, "Characterization of the composite right/left-handed transmission line metamaterial circuits using iterative method WCIP," *International Journal of Microwave and Wireless Technologies*, vol. 9, no. 8, pp. 1645-1652, 2017.

[12] M. K. Azizi, T. Elbellili, H. Baudrand, and H. Trabelsi, "Transmission line approach of zero-index metamaterials and applications using a wave concept iterative method," *International Journal of Microwave and Wireless Technologies*, vol. 11, no. 3, pp. 244-254, 2019.

[13] A. Gharsallah, A. Gharbi, L. Desclos, and H. Baudrand," Analysis of interdigital capacitor and quasi-lumped miniaturized filters using iterative method," *International Journal of Numerical Modelling: Electronic Networks, Devices and Fields*, vol. 15, no. 2, pp. 169-179, 2002.

[14] H. Trabelsi, A. Gharsallah, and H. Baudrand, "Analysis of microwave circuits including lumped elements based on the iterative method," *International Journal of RF and Microwave Computer-Aided Engineering*, vol. 13, no. 4, pp. 269-275, 2003.

[15] A. Noemen and H. Baudrand, "WCIP method for multiple-loop antennas around a spherical media," *IET Microwaves, Antennas & Propagation*, vol. 13, no. 5, pp. 666-674, 2019.

[16] A. Sassi, N. Sboui, A. Gharbi, and H. Baudrand, "Modeling of waveguide filter using wave concept iterative procedure," *Circuits and Systems*, vol. 12, no. 2, pp. 13-22, 2021.

[17] A. Hlali and H. Zairi, "Performance analysis of dynamically controllable terahertz grounded coplanar waveguide attenuator based on graphene using wave concept iterative process method," *International Journal of RF and Microwave Computer-Aided Engineering*, vol. 31, no. 2, p. e22517, 2021.

[18] G. Vincensius, "The simulation of the propagation of electromagnetic waves through a material with various thicknesses using Finite Difference Time Domain (FDTD)," *Valley International Journal Digital Library*, vol. 57, no. 61, 2023.

[19] S. Gedney, "Introduction to the finite-difference time-domain (FDTD) method for electromagnetics," *Cham, Switzerland: Springer Nature,* 2022.

[20] J. Wang and Q. Ren, "A 3-D hybrid Maxwell's Equations Finite-Difference Time-Domain (ME-FDTD)/Wave Equation Finite Element Time-Domain (WE-FETD) method," *IEEE Transactions on Antennas and Propagation*, vol. 71, no. 6, pp. 5212-5220, 2023.

[21] P. Liu, J. Li, and V. Dinavahi, "Matrix-free nonlinear finite-element solver using transmission-line modeling on GPU," *IEEE Transactions on Magnetics*, vol. 55, no. 7, pp. 1-5, 2019.

[22] A. Ragusa, H. Sasse, and A. Duffy, "1.5 D Transmission Line Matrix Model to account for skin effects and impedance mismatches in transmission lines," in *2022 IEEE MTT-S International Conference on Numerical Electromagnetic and Multiphysics Modeling and Optimization (NEMO),* Limoges, France, pp. 1-4, 2022.

[23] E. Peter and C. Vanneste, "Huygens' principle in the transmission line matrix method (TLM). Local theory," *International Journal of Numerical Modelling: Electronic Networks, Devices and Fields*, vol. 16, no. 2, pp. 175-178, 2003.

[24] Z. Chen and M. M. Ney, "On the relationship between the time-domain and frequency-domain TLM methods," *IEEE Antennas and Wireless Propagation Letters*, vol. 7, pp. 46-49, 2008.

[25] S. Iman and S. M. Riad, "TFDTLM-a new computationally efficient frequency-domain transmission-line-matrix method," *IEEE Transactions on Microwave Theory and Techniques*, vol. 48, no. 7, pp. 1089-1097, 2000.

[26] Z. Houaneb, H. Zairi, A. Gharsallah, and H. Baudrand," A new wave concept iterative method in cylindrical coordinates for modeling of circular planar circuits," in *Eighth International Multi-Conference on Systems, Signals & Devices*, 2011.

[27] S. K. Podilchak, A. P. Freundorfer, and Y. M. M. Antar, "Planar surface-wave sources and metallic grating lenses for controlled guided-wave propagation," *IEEE Antennas and Wireless Propagation Letters*, vol. 8, pp. 371-374, 2009.

[28] M. Anouar, L. Setti, and R. Haffar. "Design, analysis, and modeling using WCIP method of novel microstrip patch antenna for THz applications," *Progress in Electromagnetics Research C*, vol. 125, pp. 67-82, 2022.

[29] S. Alayet, J. Y. Siddiqui, Y. Antar, and A. Gharsallah, "Characterization of UWB antipodal tapered slot antenna using wave concept iterative procedure," in *2015 1st URSI Atlantic Radio Science Conference (URSI AT-RASC)*, 2015.

[30] L. Latrach, M. K. Azizi, A. Gharsallah, and H. Baudrand, "Study of one dimensional almost periodic structure using a novel WCIP method," *International Journal on Communications Antenna and Propagation*, vol. 4, no. 6, 2014.

[31] D. Hadri, A. Zugari, and A. Zakriti, "Conception and characterisation of a novel 5_Shaped antenna for 5G application using WCIP method," *Australian Journal of Electrical and Electronics Engineering*, vol. 18, no. 2, pp. 69-79, 2021.

[32] M. K. Azizi, L. Latrach, A. Gharsallah, and H. Baudrand, "Analytic model of a one-dimensional quasi-periodic structure by using a novel WCIP method," *International Journal of Electrical Electronics and Telecommunication Engineering*, vol. 43, no. 12, 2012.

[33] N. Raveu, T. P. Vuong, I. Terrasse, G.-P. Piau, and H. Baudrand, "Near fields evaluated with the wave concept iterative procedure method for an E-polarisation plane wave scattered by cylindrical strips," *Microwave and Optical Technology Letters*, vol. 38, no. 5, pp. 403- 406, 2003.

[34] T. Zhai, J. Shi, S. Chen, D. Liu, and X. Zhang, "Achieving laser ignition using zero index metamaterials," *Optics Letters*, vol. 36, no. 14, pp. 2689-2691, 2011.

[35] H. F. Ma, J. H. Shi, B. G. Cai, and T. J. Cui, "Total transmission and super reflection realized by anisotropic zero-index materials," *New Journal of Physics*, vol. 14, no. 12, p. 123010, 2012.

Mohamed Karim Azizi was born in Tunis, Tunisia, on 26 December 1979. He received the M.Sc. degree in Telecommunications from SupCom in 2008. He received the Ph.D. degree in Electronics from Faculty of Sciences of Tunis, Tunisia, in 2013. He is currently an associated Professor in the department of computer Sciences in The Higher Institute of Multimedia Arts of Manouba, ISAMM, Tunisia. His research interests include metamaterials, metasurfaces, and graphene antennas.

Kawther Mekki is an Assistant Professor in Computer Engineering at the University of Hail, Saudi Arabia. She holds a Ph.D. in Electronics with a specialization in Radio Frequency (RF) systems. Her research interests include wireless communications, chipless RFID technologies, Internet of Things (IoT), and embedded systems. Mekki has published several peer-reviewed articles in leading international journals and conferences, and she actively participates in collaborative research projects in RF and IoT technologies.

Taieb Elbellili was born in Kasserine, Tunisia, on 29 April 1980. He received the M.Sc. degree in Electronic Systems from Faculty of Sciences of Tunis, Tunisia, in 2006. Since 2015, he is working toward his Ph.D. His research focuses on computational electromagnetic methods for metamaterials modelling.

Ultrawideband Bowtie Slot Antenna With Defected Ground Structure

Richard S. W. Ting[1], Intan S. Zainal Abidin[1], and Azniza Abd Aziz[2]

[1]School of Electrical and Electronic Engineering, Engineering Campus
Universiti Sains Malaysia, Nibong Tebal 14300, Malaysia
richardting7@gmail.com, intan.sorfina@usm.my

[2]Intel Microelectronics
Penang 11900, Malaysia
azizniza@gmail.com

***Abstract* –** An ultrawideband (UWB) antenna is well-suited for several applications, particularly in wireless communications, radar and sensing systems. A UWB antenna covering 1.8 GHz to 3.8 GHz is proposed in this research work. A study was conducted on a bowtie slot antenna with different combinations and shapes of defected ground structure (DGS). Different shapes of DGS were introduced to investigate the effects of DGS on the bandwidth, reflection coefficient and radiation performance of the antenna. For the bowtie slot antenna with partial ground and circular DGS, there are three resonant frequencies with lowest S_{11} at 2.0 GHz (-18.5 dB), 2.5 GHz (-36.5 dB) and 3.3 GHz (-41.5 dB), while the antenna design with partial ground and dumbbell DGS has resonant frequencies at 2.0 GHz (-18.5 dB), 2.5 GHz (-36.5 dB) and 3.3 GHz (-44 dB). Upon adding a DGS structure such as a circle or dumbbell on the ground plane, the bandwidth performance of the proposed antenna was significantly enhanced. The radiation efficiency of the proposed antenna reached 80% and the directivity was 4.17 dBi (2.0 GHz), 5.58 dBi (2.5 GHz) and 5.18 dBi (3.3 GHz).

***Index Terms* –** Bowtie slot antenna, defected ground structure, ultrawideband antenna.

I. INTRODUCTION

Ultrawideband (UWB) antennas play a crucial role in modern wireless communication, radar and imaging applications due to their ability to operate over a broad frequency range. A UWB antenna is characterized by a fractional bandwidth of greater than 20% or an absolute bandwidth exceeding 500 MHz, as defined by the Federal Communications Commission (FCC) [1]. The key advantages of UWB antennas include high data transmission rates, low power consumption and minimal interference with narrowband systems. These characteristics make them highly suitable for applications such as ground-penetrating radar (GPR), biomedical imaging and wireless body area networks (WBANs).

Among the various UWB antenna configurations, the bowtie slot antenna is a popular choice due to its simple geometry, wide impedance bandwidth and omnidirectional radiation pattern. Additionally, they are highly suitable for integration into various systems with advantages such as lightweight design, low profile and ease of manufacturing [2]. Bowtie slot dipoles are also growing in popularity due to their higher gain and bandwidth as compared to normal microstrip patch or slot antenna [3]. A monopole-like bowtie slot UWB antenna was proposed in [4] and was able to achieve a wide bandwidth of 10.43 GHz. Another proposed high gain bowtie slot antenna with miniaturized triangular shape metallic ground plane was able to achieve multiband operation and higher bandwidth [5].

A defected ground structure (DGS) is a single or limited number of slots strategically etched on the ground plane of a microwave printed circuit board to achieve a feature of stopping wave propagation over a band of frequencies [6–8]. By adding DGS to the ground plane, it is able to improve the effective line impedance, therefore, enhancing the fulfillment of the required impedance matching [4–6]. For example, some researchers used bat-shaped DGS in order to achieve good impedance matching of the antenna [9]. In [10], researchers managed to achieve UWB performance when adding DGS to its antenna design.

This paper studies and analyzes different combinations and shapes of DGS for bowtie slot antenna design operating at UWB from 1.8 GHz to 3.8 GHz. Different types of shapes and combinations of the defected structure might produce different results such narrow or wide bandwidth, directional or omnidirectional behavior and effects the resonating frequency. The paper's outline is as follows. Section I shows the background to the research work conducted, Section II displays the design of the proposed bowtie slot antenna with different type

Submitted On: December 9, 2024
Accepted On: July 4, 2025

https://doi.org/10.13052/2025.ACES.J.400703

of DGS. Section III portrays the simulated findings and discussion. The findings of the paper are concluded in section IV.

II. DESIGN OF BOWTIE SLOT ANTENNA WITH DIFFERENT DGS

In this research, UWB bowtie slot antennas were designed, simulated and optimized using CST Microwave Studio software. The targeted operating bands are from 1.8 to 4 GHz. For reference purposes, a bowtie slot antenna with full ground plane was also simulated. There were several combinations and shapes of DGS that were designed in this work: partial ground, partial ground with circular-shaped DGS and dumbbell-shaped DGS. The patch and ground of the antenna are made of copper with a thickness of 0.035 mm, while the substrate of the antenna is made of FR-4 with a thickness of 1.6 mm and $\varepsilon_r = 4.3$.

A. Design of bowtie slot antenna

Figure 1 shows the proposed design of the bowtie slot antenna with different types of DGS. The top surface of the bowtie slot antennas consists of a bowtie-shaped slot and a microstrip feedline. The procedure for designing the bowtie-shaped slot is based on the design of bowtie antenna found in [11]. The set of design equations below is obtained by altering the semi-empirical design equations for the rectangular patches [11]. The dimensions of the proposed bowtie design are initially obtained using equations (1) to (5):

$$f_r = \frac{c}{2\sqrt{\in_e} L}\left(\frac{1.152}{R_t}\right), \tag{1}$$

where

$$R_t = \frac{L}{2}\frac{(B_h + 2\Delta l) + (W_c + 2\Delta l)}{(B_h + 2\Delta l)(S + 2\Delta l)}, \tag{2}$$

$$\Delta l = h\frac{0.412(\in_e + 0.3)\left(\frac{W_i}{h} + 0.262\right)}{(\in_e - 0.258)\left(\frac{W_i}{h} + 0.813\right)}, \tag{3}$$

$$\in_e = \left(\frac{\in_r + 1}{2}\right) + \left(\frac{\in_r - 1}{2}\right)\left(1 + \frac{12h}{W_i}\right)^{-1/2}, \tag{4}$$

$$W_i = \left(\frac{B_h + W_c}{2}\right). \tag{5}$$

According to the equations, the most important dimensions in designing the bowtie slot are B_h (bigger slot width), $L/2$ (slot length) and W_c (smaller slot width). These three dimensions will determine the flare angle of the bowtie, which is 26° after optimization in 3D electromagnetics software. The amount of flaring angle will strongly affect the input impedance and bandwidth of the bowtie shaped slot [12]. The substrate thickness, relative and effective permittivity are indicated by the h, $\in_r$ and $\in_e$ respectively.

Antenna design was optimized using CST simulation software. Upon optimization, W_c is very small in the proposed design and can be considered as negligible. After the simulation and optimization process was completed, the antenna's ground was extended larger than the antenna patch, as bigger ground improves the antenna's reflection coefficient and radiation pattern. Other parameters for the optimized bowtie slot design are defined in Fig. 1.

In this proposed antenna, the antenna is fed by a grounded coplanar waveguide (GCPW) as shown in Fig. 1. GCPW is the modification of the CPW (coplanar waveguide) whereby it has an extra ground layer at the bottom of the antenna compared to the CPW. This structure improves the overall mechanical structure of the antenna, especially if the substrate is thin. The antenna fed by CPW has advantages of large bandwidth and simple impedance matching network [13]. The characteristic impedance of the feedline of the bowtie slot antenna with full ground is 57.01 Ω while the characteristics impedance of the feedline of the antenna with circle-shaped and dumbbell-shaped DGS is 57.03 Ω and 57.04 Ω, respectively.

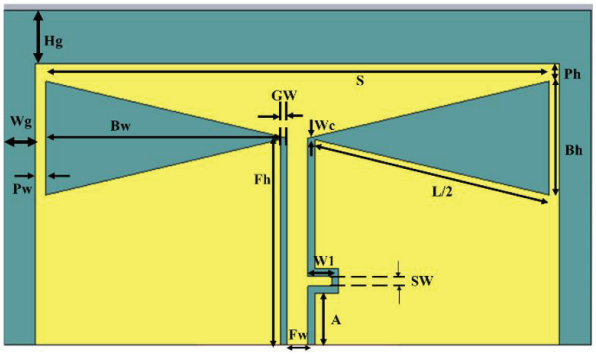

Fig. 1. Proposed bowtie slot antenna with grounded coplanar waveguide feeding.

B. Defected ground structure analysis

There are four antenna designs being investigated and evaluated in this paper. Different types of shapes and combinations of the defected structure might produce different results such as narrow or wide bandwidth, directional or omnidirectional behavior and effects on the resonating frequency. In all four designs, the bowtie slot design on the top surface is maintained the same and only the bottom surface is changed, utilizing different DGS shapes and combinations. Figure 2 (a) shows the first antenna which is the reference design without any DGS on the ground plane. In the second antenna design shown in Fig. 2 (b), the ground plane is halved to solve the narrowband issue in the reference design. By removing the ground plane, the design managed to achieve high bandwidth performance as will be shown later in

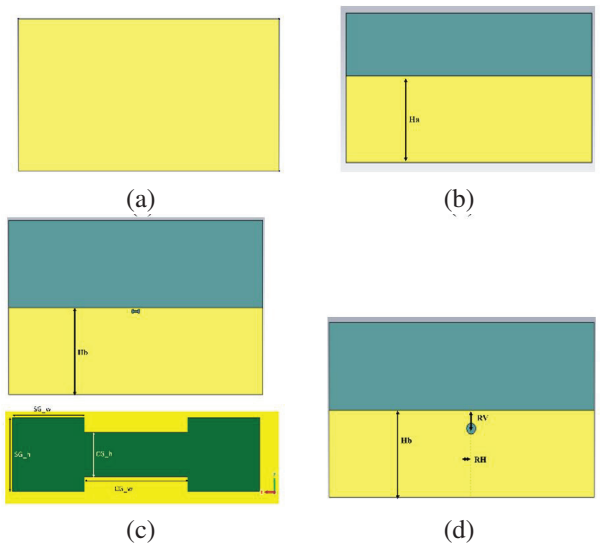

Fig. 2. Evolution of DGS: (a) full ground (without DGS), (b) partial ground, (c) partial ground with dumbbell DGS, (d) partial ground with circle DGS.

section III. Figure 2 (c) displays the partial ground plane design, now added with a circle-shaped DGS. Finally, Fig. 2 (d) shows the bowtie slot antenna with dumbbell DGS whereby a slot in the shape of a dumbbell is inserted at the ground plane.

Circle- and dumbbell-shaped DGS were chosen as they are simple structures, suitable for a preliminary study [14]. An equivalent circuit of a dumbbell-shaped DGS with a pair of equivalent capacitance and inductance (LC) model is shown in Fig. 3 [6]. This equivalent inductance and capacitance are contributed by two different sections of a dumbbell DGS. The conduction current surrounding the square heads produces an equivalent inductance while the gap-coupled electric fields across the narrow connecting slot results in an equivalent capacitance. The values of L, C and R are determined by the slot dimension and location of the slot [14].

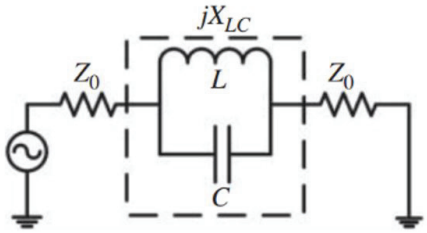

Fig. 3. Equivalent LC model of a dumbbell DGS [6].

Detailed dimensions of these four antennas are shown in Table 1.

Table 1: Dimensions of bowtie slot antenna

Dimension (mm)	Bowtie Slot Antenna			
	Full Ground	Partial Ground	Partial Ground with Dumbbell DGS	Partial Ground with Circle DGS
GW	1	1	1	1
Fw	3	3	3	3
Fh	29	29	29	29
Bw	34.5	34.5	34.5	34.5
Bh	16	16	16	16
Pw	1.5	1.5	1.5	1.5
Ph	2.5	2.5	2.5	2.5
Hg	7.5	7.5	7.5	7.5
Wg	4.5	4.5	4.5	4.5
A	7.2	7.2	7.2	7.2
W1	3.4	3.4	3.4	3.4
SW	1.4	1.4	1.4	1.4
Radius of circle DGS	-	1.5	-	-
Rh	-	-	-	3
Rv	-	-	-	5
Ha	-	27.2	-	-
Hb	-	-	23.5	23.5
CG_h	-	-	1.5	-
CG_w	-	-	0.5	-
SG_w	-	-	0.5	-
SG_h	-	-	1	-

III. SIMULATION RESULTS AND DISCUSSION

A. Results and discussion

Figure 3 shows the S_{11} performance comparison between the design of the bowtie slot antenna with full ground, partial ground, partial ground with circle DGS and partial ground with dumbbell DGS.

It can be seen in Fig. 4 and Table 2 that the bowtie slot antenna without DGS (full ground), which is the reference design in this study, has a reflection coefficient of -9.0 dB (2.3 GHz) and -11.0 dB (3.4 GHz). The reference design has the problem of a very narrow bandwidth at only 0.1 MHz.

Upon removing half of the ground plane, the reflection coefficient and bandwidth performance of the antenna improves as seen in the results of the design with partial ground. There are three resonant frequencies at 2.0 GHz, 2.5 GHz and 3.7 GHz with reflection coefficient of - 23.5 dB, -15 dB and -15 dB, respectively. The bandwidth of the antenna widens to 300 MHz (2.0 GHz), 850 MHz (2.5 GHz) and 550 MHz (3.7 GHz).

When the partial ground design was added with a circular slot, Fig. 4 shows a UWB performance with a total bandwidth of 2020 MHz from 1.8 GHz to 3.82 GHz. There are three resonant frequencies with lowest S_{11} at 2.0 GHz (-18.5 dB), 2.5 GHz (-36.5 dB) and 3.3 GHz (-41.5 dB). Likewise, when a dumbbell slot was added

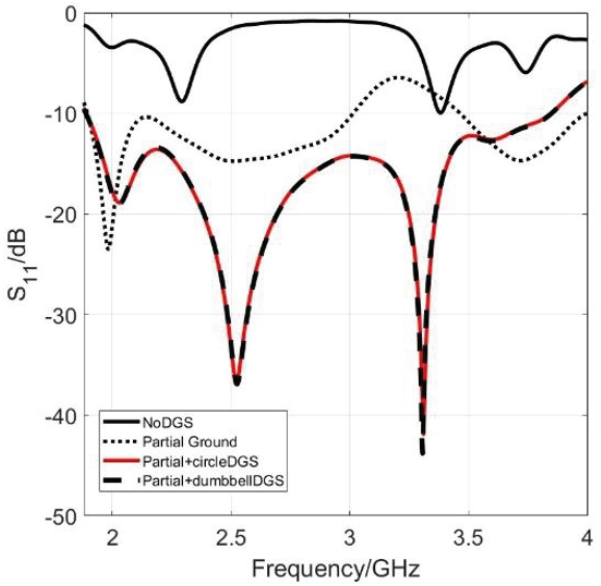

Fig. 4. Comparison of simulated S_{11} performance of bowtie slot antenna with different combinations of DGS.

Table 2: Summary of comparison of simulated performance of bowtie slot antenna

Bowtie Slot Antenna	**Reflection Coefficient (dB)**	**-10 dB Bandwidth (MHz)**
Without DGS (Full ground)	−9.0 (2.3 GHz) −11.0 (3.4 GHz)	Not sufficient 0.1
Partial ground	−23.5 (2.0 GHz) −15.0 (2.5 GHz) −15.0 (3.7 GHz)	300 850 550
Partial ground + Circle DGS	−18.5 (2.0 GHz) −36.5 (2.5 GHz) −41.5 (3.3 GHz)	2020 (1.8 - 3.82 GHz)
Partial ground + Dumbbell DGS	−18.5 (2.0 GHz) −36.5 (2.5 GHz) −44.0 (3.3 GHz)	2020 (1.8 - 3.82 GHz)

to the partial ground, it shows a similar UWB performance from 1.8 GHz to 3.82 GHz with resonant frequencies at 2.0 GHz (-18.5 dB), 2.5 GHz (-36.5 dB) and 3.3 GHz (-44 dB). This shows that, by adding another circular and dumbbell slot to the partial ground plane, the surface current distribution on the ground plane was successfully disrupted and the -10 dB bandwidth of the antenna was significantly improved. The proposed UWB antenna, operating within the 1.8 GHz to 3.8 GHz frequency range, demonstrates significant potential for various wireless communication, sensing and positioning applications. In wireless communication, the antenna supports sub-6 GHz 5G covering key frequency bands such as 1.8 GHz (Band 3) and 2.5 GHz (Band 41), making it suitable for small cell networks, IoT devices and indoor coverage enhancements. Additionally, its coverage of the 2.4 GHz band enables integration with Wi-Fi (802.11n/ac), Bluetooth and Zigbee, facilitating applications in smart homes, industrial IoT (IIoT) and smart cities. Beyond communication, the antenna is well-suited for sensing and radar applications, particularly in GPR systems. It also holds promise in biomedical imaging, where UWB antennas are utilized for wireless health monitoring, breath detection and early disease diagnosis.

Figures 5-8 display the 2D and 3D radiation plots of all antenna designs. The reference antenna design has a directivity of 8.13 dBi with a half power beamwidth of 77.9° as can be seen in Fig. 5. The antenna exhibits a unidirectional behavior, radiating in the front of the antenna. In Fig. 6, the 2D and 3D plots of the radiation pattern of the partial ground antenna design shows a directivity of 4.8 dBi (2.0 GHz), 5.49 dBi (2.5 GHz) and 5.82 dBi (3.7 GHz), with 3 dB angular beamwidth of 90.7°, 87.3° and 69.1°, respectively. Upon removing the ground plane partially, the antenna now exhibits bi-directional behavior, radiating in front of and at the back of the antenna. It is also noted that the directivity is reduced while the half power beamwidth is slightly widened.

Figure 7 presents the radiation pattern performance of the bowtie slot antenna with partial ground and

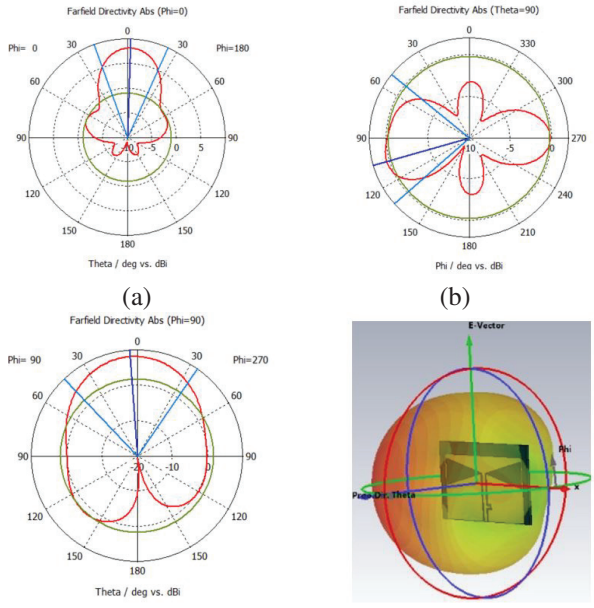

Fig. 5. Simulated radiation pattern of bowtie slot antenna design with full ground (without DGS): (a) 2D plot xz plane (3.4 GHz), (b) 2D plot xy plane (3.4 GHz), (c) 2D plot yz plane (3.4 GHz), (d) 3D plot (3.4 GHz).

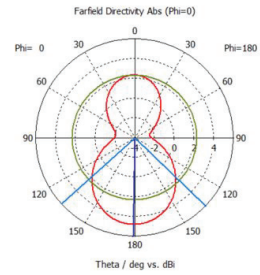

(a)

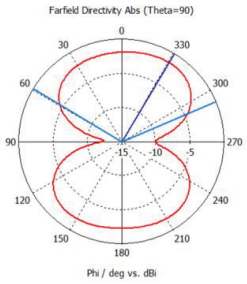

(b)

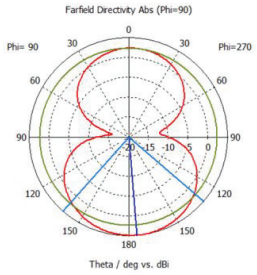

(c)

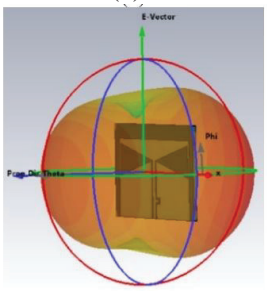

(d)

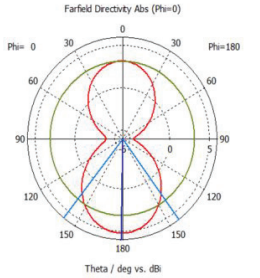

(e)

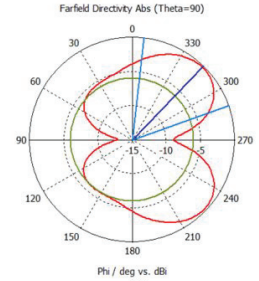

(f)

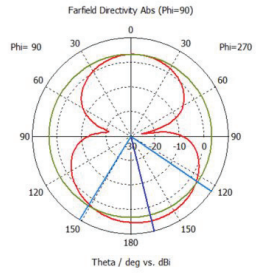

(g)

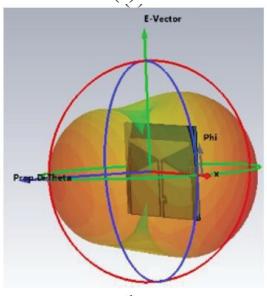

(h)

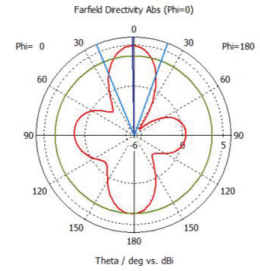

(i)

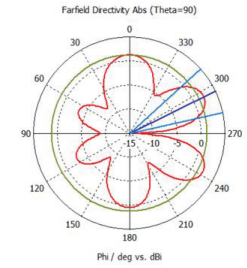

(j)

Fig. 6. *Continued.*

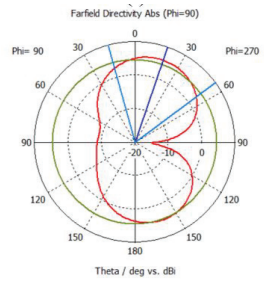

(k)

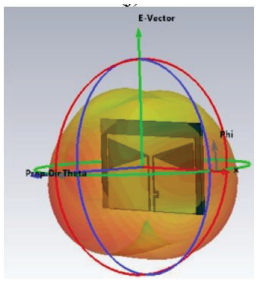

(l)

Fig. 6. Simulated radiation pattern of bowtie slot antenna design with full ground (without DGS): (a) 2D plot xz plane (3.4 GHz), (b) 2D plot xy plane (3.4 GHz), (c) 2D plot yz plane (3.4 GHz), (d) 3D plot (3.4 GHz).

circular DGS. The directivity performance of this particular antenna is relatively similar to the partial ground design. It has directivity of 4.17 dBi (2.0 GHz), 5.58 dBi (2.5 GHz) and 5.18 dBi (3.3 GHz) with 3 dB angular

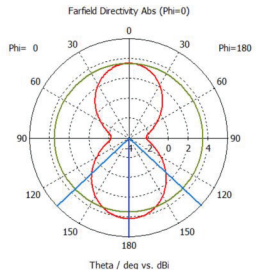

(a)

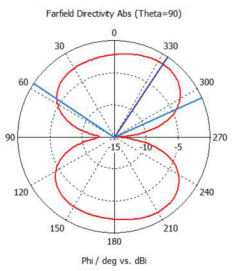

(b)

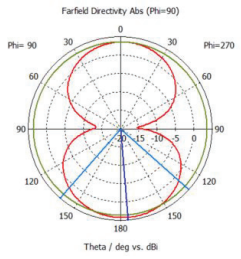

(c)

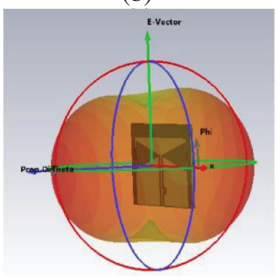

(d)

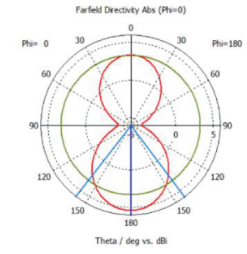

(e)

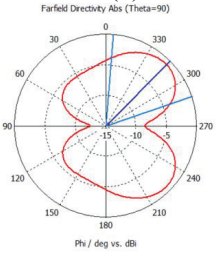

(f)

Fig. 7. *Continued.*

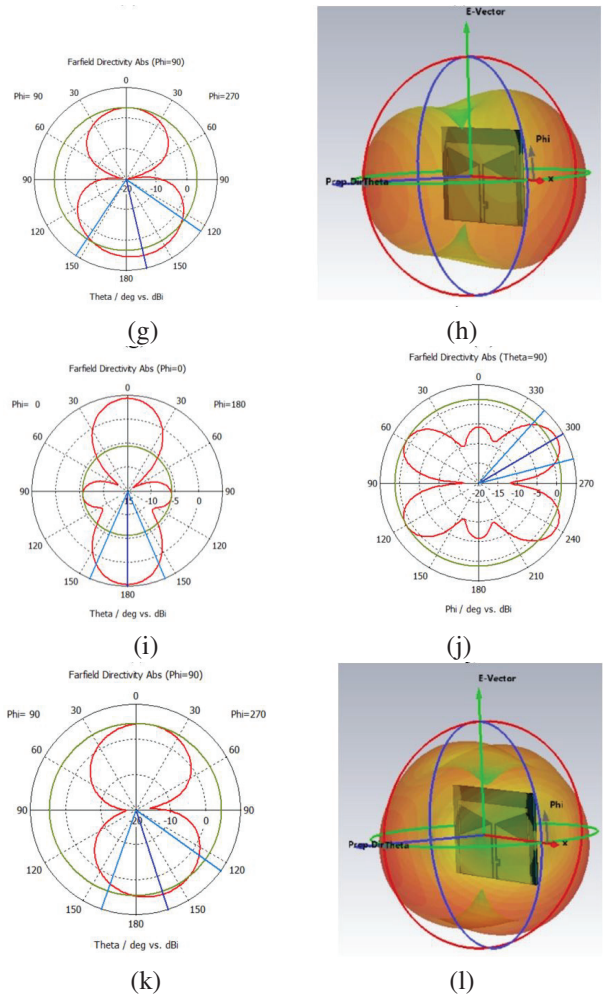

Fig. 7. Simulated radiation pattern of bowtie slot antenna design with partial ground and circle DGS: (a) 2D plot xz plane (2.0 GHz), (b) 2D plot xy plane (2.0 GHz), (c) 2D plot yz plane (2.5 GHz), (d) 3D plot (2.0 GHz), (e) 2D plot xz plane (2.5 GHz), (f) 2D plot xy plane (2.5 GHz), (g) 2D plot yz plane (2.5 GHz), (h) 3D plot (2.5 GHz), (i) 2D plot xz plane (3.3 GHz), (j) 2D plot xy plane (3.3 GHz), (k) 2D plot yz plane (3.3 GHz), (l) 3D plot (3.3 GHz).

beamwidth of 89°, 88.6° and 73°, respectively. The radiation pattern performance of the bowtie slot antenna with partial ground and dumbbell DGS is also not much different from previous partial ground and circular DGS design. From Fig. 8, the directivity is 4.13 dBi (2.0 GHz), 5.34 dBi (2.5 GHz) and 4.57 dBi (3.3 GHz), with 3 dB angular beamwidth of 93.1°, 74.8° and 46.6°, respectively.

Overall, it is noted that the directivity and shape of the radiation pattern of all bowtie slot antenna designs

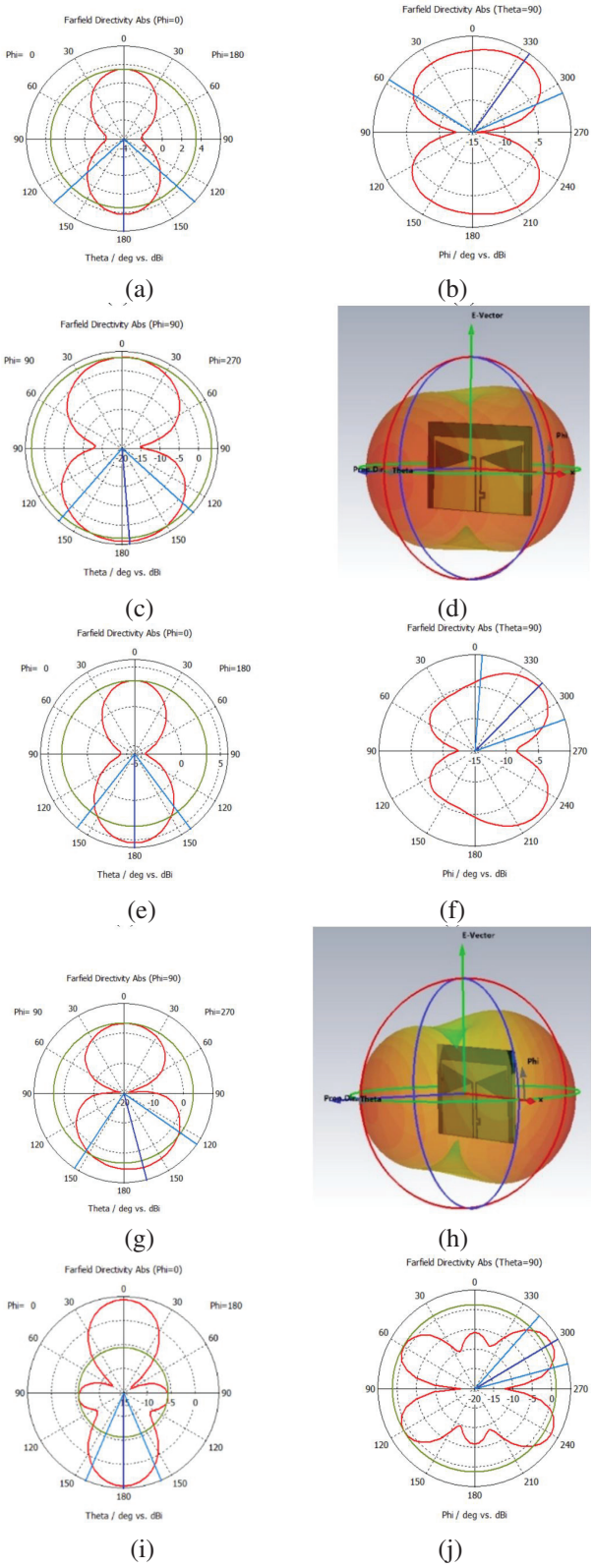

Fig. 8. *Continued.*

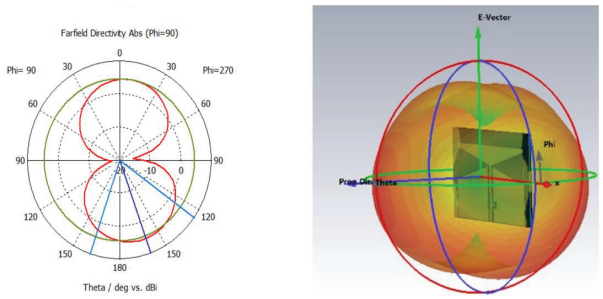

(k) (l)

Fig. 8. Simulated radiation pattern of bowtie slot antenna design with partial ground and dumbbell DGS: (a) 2D plot xz plane (2.0 GHz), (b) 2D plot xy plane (2.0 GHz), (c) 2D plot yz plane (2.5 GHz), (d) 3D plot (2.0 GHz), (e) 2D plot xz plane (2.5 GHz), (f) 2D plot xy plane (2.5 GHz), (g) 2D plot yz plane (2.5 GHz), (h) 3D plot (2.5 GHz), (i) 2D plot xz plane (3.3 GHz), (j) 2D plot xy plane (3.3 GHz), (k) 2D plot yz plane (3.3 GHz), (l) 3D plot (3.3 GHz).

Table 3: Simulated radiation pattern performance of proposed bowtie slot antennas with different combinations of DGS

Bowtie Slot Antenna	Operating Frequency (GHz)	Directivity (dBi)	3 dB Beamwidth
Without DGS (Full ground)	3.4	8.13	77.9°
Partial ground	2.0	4.8	90.7°
	2.5	5.49	87.3°
	3.7	5.82	69.1°
Partial ground + Circle DGS	2.0	4.17	89°
	2.5	5.58	88.6°
	3.3	5.18	73°
Partial ground + Dumbbell DGS	2.0	4.13	93.1°
	2.5	5.34	74.8°
	3.3	4.57	46.6°

with partial ground and DGS are similar. The directivity of the antenna with modified ground plane is reduced as compared to the reference bowtie slot antenna. The bowtie slot antenna traditionally is known to exhibit an omnidirectional type of radiation pattern. However, upon modifying the ground structure, bowtie slot antenna exhibit bi-directional radiation behavior, radiating on the front of and at the back of the bowtie slot antenna. Table 2 summarizes the radiation pattern performance of all four bowtie slot antenna designs proposed in this study.

Figure 9 presents the directivity performance of all four bowtie slot antenna with different combination of DGS from 1.8 GHz to 4 GHz. This has confirmed the

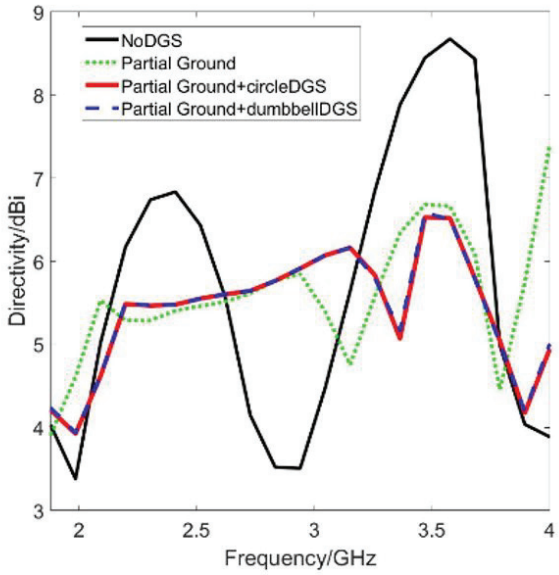

Fig. 9. Simulated directivity performance of bowtie slot antenna with different DGS.

previous observation whereby the reference design has a higher directionality but comes with narrower bandwidth. Upon modification of the ground plane, the directivity is reduced but the antenna is able to achieve UWB performance. In Fig. 10, the simulated radiation efficiency of the bowtie slot antennas from 1.8 GHz to 4 GHz are presented. The antenna's efficiency level is calculated using $\frac{Radiated\ Power}{Accepted\ Power} \times 100$ [15]. This shows that the proposed antenna incorporated with different DGS

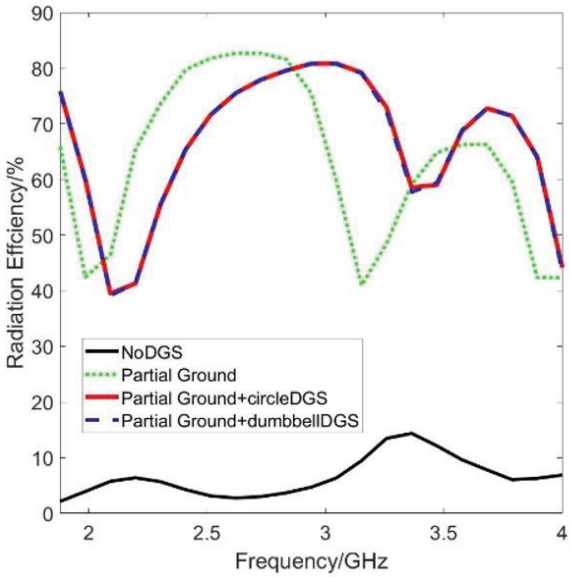

Fig. 10. Simulated radiation efficiency performance of bowtie slot antenna with different DGS.

have good efficiency, being around 40-80% across the frequency band. For practical applications, having 50-60% of radiation efficiency is sufficient and is considered a good antenna [16].

Figures 11, 12, 13 and 14 present the simulated surface current distribution for bowtie slot antenna without DGS, with partial ground, with partial ground and circular DGS, and with partial ground and dumbbell DGS, at their resonant frequencies. In Fig. 11, it is seen that there is a very small current flow at the right and left edges, halfway through the ground plane. Therefore, when the top half of the ground plane is removed, it enables the surface current to be concentrated along the top, left and right edges as seen in Fig. 12. This phenomenon enhances the bandwidth performance of the bowtie slot antenna significantly.

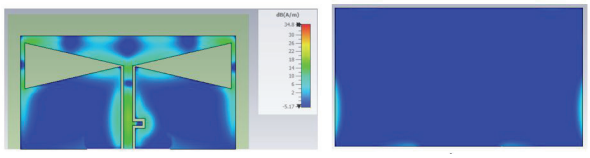

(a) (b)

Fig. 11. Simulated surface current distribution of bowtie slot antenna with full ground (without DGS): (a) top surface (3.4 GHz) and (b) bottom surface (3.4 GHz).

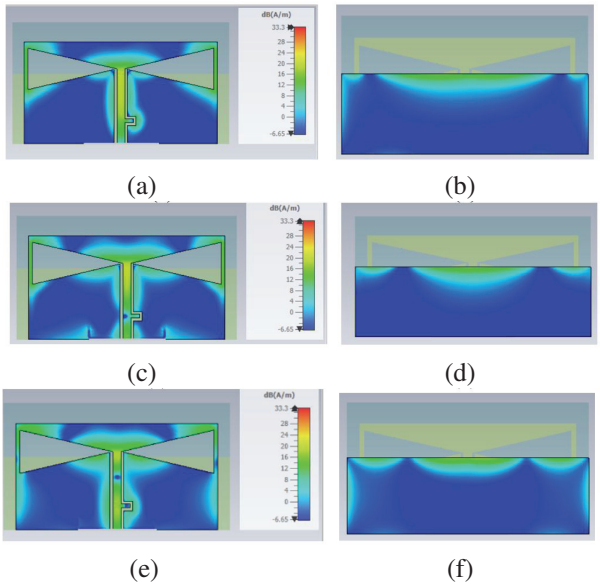

(a) (b) (c) (d) (e) (f)

Fig. 12. Simulated surface current distribution of bowtie slot antenna with partial ground: (a) top surface (2.0 GHz), (b) bottom surface (2.0 GHz), (c) top surface (2.5 GHz), (d) bottom surface (2.5 GHz), (e) top surface (3.7 GHz), (f) bottom surface (3.7 GHz).

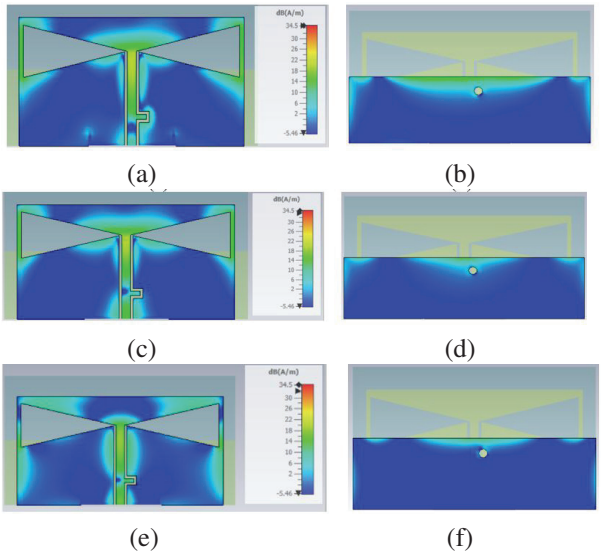

(a) (b) (c) (d) (e) (f)

Fig. 13. Simulated surface current distribution of bowtie slot antenna with partial ground and circle DGS: (a) top surface (2.0 GHz), (b) bottom surface (2.0 GHz), (c) top surface (2.5 GHz), (d) bottom surface (2.5 GHz), (e) top surface (3.3 GHz), (f) bottom surface (3.3 GHz).

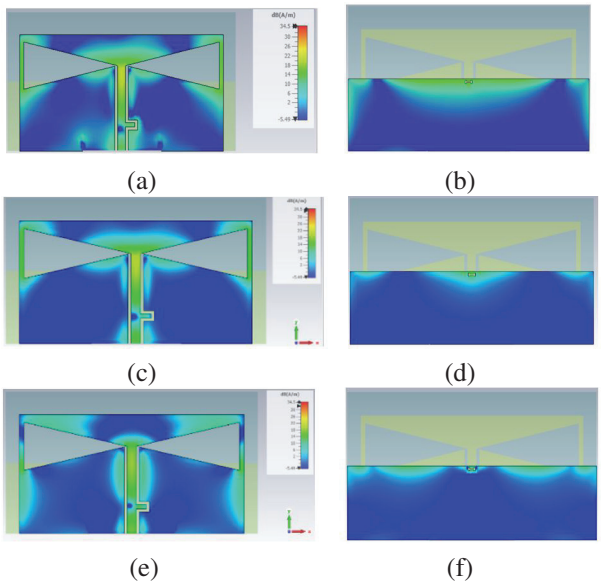

(a) (b) (c) (d) (e) (f)

Fig. 14. Simulated surface current distribution of bowtie slot antenna with partial ground and dumbbell DGS: (a) top surface (2.0 GHz), (b) bottom surface (2.0 GHz), (c) top surface (2.5 GHz), (d) bottom surface (2.5 GHz), (e) top surface (3.3 GHz), (f) bottom surface (3.3 GHz).

Upon adding a DGS structure underneath the feedline, such as circle and dumbbell on the ground plane, the surface current changes its movement path, flowing surrounding the defected structure, as can be observed

Table 4: Comparison of proposed antenna with previous work

Reference	Resonant Frequency (GHz)	S_{11} (dB)	Bandwidth (GHz)	Gain/ Directivity (dBi)
[5]	2.4	-21.5	1.1	3.64
	6.7	-26	1.35	2.89
	10.7	-32	4.1	2.58
	15.5	-17.5	0.69	5.72
	17.5	-29	0.2	6.3
[9]	2.9	-28.5	0.97	2.0
	5.4	-13.5	0.28	3.7
	6.1	-17	0.7	3.7
	7	-24	0.72	2.0
[14]	2.29	-12.65	0.1	5.27
	3.5	-12.89	0.06	3.2
	4.64	-14.9	0.2	5.78
Proposed antenna with partial ground + dumbbell DGS	2.0	-18.5	2.02 (1.8-3.82 GHz)	4.17
	2.5	-36.5		5.58
	3.3	-41.5		5.18
Proposed antenna with partial ground + circle DGS	2.0	-18.5	2.02 (1.8-3.82 GHz)	4.13
	2.5	-36.5		5.34
	3.3	-44.0		4.57

in Figs. 13 and 14. It is known that quasi-TEM mode propagates through a conventional microstrip line with its return radio frequency current through the ground plane. By creating a defected structure on the ground, the surface current flow was successfully perturbed at the ground surface and subsequently modified the electric field and magnetic field of the antenna. As a result, it was able to significantly enhance the bandwidth performance of the proposed antenna.

Table 3 shows a comparison of the findings of the proposed bowtie slot antenna design in this paper with previously published works [5, 9, 14]. Both proposed antenna with circle and dumbbell DGS displayed excellent bandwidth performance of around 2 GHz compared to other works. The directivity of the proposed antenna is comparable to the proposed antenna of other researchers.

IV. CONCLUSION

The effects of partial ground plane with different combinations of circle-shaped and dumbbell-shaped defected ground structures (DGS) on the ultrawideband (UWB) bowtie slot antenna design were studied and compared in this paper. Two bowtie slot antenna designs were proposed with different modification to the ground plane: one with partial ground and circular DGS, the other with partial ground and dumbbell DGS. They were designed to operate from 1.8 to 3.8 GHz. The total -10 dB bandwidth is 2.02 GHz. The proposed antenna is best suited for low-band and mid-band wireless communication, UWB radar, biomedical sensing and high-accuracy localization. The DGS designs were compared with the antenna design without any DGS as a reference. For the bowtie slot antenna with partial ground and circular DGS, there are three resonant frequencies with lowest S_{11} at 2.0 GHz (-18.5 dB), 2.5 GHz (-36.5 dB) and 3.3 GHz (-41.5 dB), while the antenna design with partial ground and dumbbell DGS has resonant frequencies at 2.0 GHz (-18.5 dB), 2.5 GHz (-36.5 dB) and 3.3 GHz (-44 dB). Upon adding a DGS structure underneath the feedline, such as a circle or dumbbell on the ground plane, the surface current changes its movement path, flowing surrounding the defected structure. As a result, the electric field and magnetic field was modified, leading to significantly enhanced bandwidth performance of the proposed antenna. The proposed bowtie slot antenna's radiation efficiency is around 80%.

In conclusion, the antenna's broad bandwidth and efficient radiation performance make it a strong candidate for next-generation wireless, sensing and security applications, with the potential for further enhancements through frequency extension beyond 4 GHz for improved 5G and future 6G capabilities.

REFERENCES

[1] Federal Communications Commission (FCC), *First Report and Order: Revision of Part 15 of the Commission's Rules Regarding Ultra-Wideband Transmission Systems*, FCC-02-48, 2002.

[2] S. Mekki, C. Zebiri, D. Sayad, I. Elfergani, H. Bendjedi, J. Rodriguez, and R. A. Abd-Alhameed, "A miniaturized slot antenna with defected ground structure for GSM applications," in *IEEE 26th International Workshop on Computer Aided Modeling and Design of Communication Links and Networks (CAMAD)*, pp. 1-4, 2021.

[3] Z. Zeng, W. Cao, and X. Lv, "Triple-band triple-mode microstrip endfire antenna based on periodic bowtie dipoles," in *2017 Sixth Asia-Pacific Conference on Antennas and Propagation (APCAP)*, pp. 1-3, 2017.

[4] S. Rashid, Y. Wu, and Y. Ding, "Monopole-like bowtie slot antenna for ultrawideband applications," in *2016 IEEE International Conference on Computational Electromagnetics (ICCEM)*, pp. 376-378, 2016.

[5] Z. A. Dayo, Q. Cao, Y. Wang, P. Soothar, I. A. Khoso, G. Shah, and M. Aamir, "A compact high gain multiband bowtie slot antenna with miniaturized triangular shaped metallic ground plane," *Applied Computational Electromagnetics Society (ACES) Journal*, pp. 935-945, 2021.

[6] D. Guha, C. Kumar, and S. Biswas, *Defected Ground Structure (DGS) Based Antennas: Design Physics, Engineering, and Applications*. Hoboken, NJ: John Wiley & Sons, 2022.

[7] N. H. Gad and M. Vidmar, "Design of a microstrip-fed printed-slot antenna using defected ground

structures for multiband applications," *Applied Computational Electromagnetics Society (ACES) Journal*, pp. 854-860, 2018.

[8] F. F. Ismail, M. A. El-Aasser, and N. H. Gad, "A parasitic hat for microstrip antenna design based on defected structures for multiband applications," *Applied Computational Electromagnetics Society (ACES) Journal,* pp. 568-575, 2022.

[9] S. I. Naqvi, F. Arshad, and H. Tenhunen, "A bowtie slotted quad-band notched UWB antenna with defected ground structure," *Applied Computational Electromagnetics Society (ACES) Journal*, pp. 1725-1730, 2019.

[10] Z. Esmati and M. Moosazadeh, "Dual band-notched small monopole antenna with bandwidth enhancement by means of defected ground structure (DGS) for UWB application," *Applied Computational Electromagnetics Society (ACES) Journal,* pp. 619-625, 2015.

[11] A. C. Durgun, A. C. Balanis, C. R. Birtcher, and D. R. Allee, "Design, simulation, fabrication and testing of flexible bow-tie antennas," *IEEE Transactions on Antennas and Propagation*, vol. 59, no. 12, pp. 4425-4435, 2011.

[12] S. Mukherjee, A. Biswas, and K. V. Srivastava, "Broadband substrate integrated waveguide cavity-backed bow-tie slot antenna," *IEEE Antennas and Wireless Propagation Letters*, vol. 13, pp. 1152-1155, 2014.

[13] M. J. Nie, X. X. Yang, G. N. Tan, and B. Han, "A compact 2.45-GHz broadband rectenna using grounded coplanar waveguide," *IEEE Antennas and Wireless Propagation Letters*, vol. 14, pp. 986-989, 2015.

[14] S. R. B. Rama and D. Vakula, "Optimized polygonal slit rectangular patch antenna with defective ground structure for wireless applications," *Applied Computational Electromagnetics Society (ACES) Journal,* pp. 1194-1199, 2015.

[15] P. Miskovsky, J. M. Gonzalez-Arbesu, and J. Romeu, "Antenna radiation efficiency measurement in an ultrawide frequency range," *IEEE Antennas and Wireless Propagation Letters*, vol. 8, pp. 72-75, 2009.

[16] A. Alqahtani, M. T. Islam, M. S. Talukder, M. Samsuzzaman, M. Bakouri, S. Mansouri, T. Almoneef, S. Dokos, and Y. Alharbi, "Slotted monopole patch antenna for microwave-based head imaging applications," *Sensors*, vol. 22, no. 19, p. 7235, 2022.

Richard Sing Wee Ting was born in Sibu, Sarawak, Malaysia, in 1996. He received the B.Eng. Degree in Electronic and Electronic Engineering from University Malaysia Sabah in 2020. His work focuses on microstrip antenna.

Intan Sorfina Zainal Abidin received her Ph.D. in Electronics Engineering from 5G Innovation Centre (5GIC), University of Surrey, Guildford, UK, in 2017. She has industrial experience working as an engineer at Motorola Solutions (M) and Celestica (M). Currently, she is a Senior Lecturer at the School of Electrical and Electronic Engineering, Universiti Sains Malaysia (USM), specializing in electronics communication system, antenna, channel propagation, RF, microwave engineering and MIMO systems. Intan is a member of IEEE.

Azniza Abd Aziz received the Ph.D. degree in electrical engineering from the University of South Carolina, Columbia, SC, USA. She is currently with Intel Corporation, Penang, Malaysia. Her current research interests include signal integrity solutions for high-speed digital design, machine learning, RF, and microwave engineering. Azniza is a Chartered Engineer (C.Eng.) conferred by the Engineering Council, UK.

Crosstalk Analysis of Multi-conductor Transmission Lines Excited by Long-time Interference Sources Based on Finite-difference Frequency-domain Method

Zhihong Ye[1,2], Yufan Zhai[2], and Meilin Liu[3]

[1]Chongqing Institute of Digital Arena
Chongqing 400065, China
yezh@cqupt.edu.cn

[2]School of Communication and Information Engineering
Chongqing University of Posts and Telecommunications
Chongqing 400065, China
zhai997497548@163.com

[3]School of Aeronautics and Astronautics
Shanghai Jiao Tong University, Shanghai, China
meilin.liu@sjtu.edu.cn

Abstract – When addressing the crosstalk problems of multi-conductor transmission lines (MTLs) excited by long-time interference sources, time-domain methods suffer from lengthy simulation duration for such scenario, while the conventional finite-difference frequency-domain (FDFD) method encounters efficiency limitations due to its requirement for direct meshing the fine structures of MTLs. Under the circumstance, a new frequency-domain hybrid method based on the FDFD method and the transmission line (TL) equations is proposed. Within this method, the crosstalk model of the MTLs is constructed depending on TL equations firstly. Then, TL equations are solved by the difference scheme of FDFD method, and the FDFD-TL matrix equation applicable for the crosstalk modeling of MTLs are derived and established. Finally, the conjugate gradient method combined with message passing interface (MPI) parallel technique is utilized to solve the FDFD-TL matrix equation and obtain the voltage responses along the MTLs and their terminal loads. Two simulation cases about the crosstalk of multi-conductor TLs excited by lumped pulse sources are calculated and compared with the Method of Moments (MoM) to verify the accuracy and efficiency of the proposed method.

Index Terms – Crosstalk of multi-conductor transmission lines, FDFD-TL matrix equation, long-time interference sources, message passing interface-based conjugate gradient method.

I. INTRODUCTION

With the rapid advancement of wireless communication technology, electronic and electrical devices are becoming increasingly integrated. The compact arrangement of transmission lines (TL) in these devices can lead to crosstalk, primarily due to inductive and capacitive coupling between neighboring lines. Additionally, the interference sources in these devices generated from some circuit modules may be some harmonic or narrow band signals, which have the prominent feature of long duration. Therefore, studying the crosstalk issues arising from multi-conductor transmission lines (MTLs) subjected to long-time interference sources is essential for developing techniques to mitigate interference in electronic and electrical devices.

Limited to the fine structures of MTLs and long duration of interference sources, full-wave algorithms, such as finite-difference time-domain (FDTD) [1] method, finite element method (FEM) [2], Method of Moments (MoM) [3], transmission line matrix (TLM) method [4], and finite-difference frequency-domain (FDFD) method [5], are not efficient for this crosstalk simulation issue because they require many grids and demand relatively long computation time.

Some hybrid methods based on the theory of TL equations have been proposed, offering the advantage of avoiding direct modeling of TL structures. Among these methods, the FDTD and finite-element time-domain (FETD) solutions of TL equations [6–14] are the most

Submitted On: February 8, 2025
Accepted On: June 28, 2025

https://doi.org/10.13052/2025.ACES.J.400704

widely used. The core concept of the FDTD solutions of TL equations is to discretize TL equations using different FDTD schemes, such as traditional FDTD [6, 7], alternating direction implicit FDTD [8], Hermite polynomial FDTD [9], and Implicit-Wendroff FDTD [10], then the iteration formulas of the voltages and currents along various TLs are obtained to solve the voltage and current responses of these lines iteratively. Additionally, some researchers have integrated the FDTD solutions of TL equations with machine learning to predict the crosstalk of twisted-wire pairs [11] and random harness cables [12]. Although the FETD-TL method [13, 14] offers advantages over FDTD-TL approaches through its unconditional convergence and freedom from Courant-Friedrich-Levy (CFL) stability constraints, its implementation requires substantial theoretical derivation for establishing the solving equations. Since these methods rely on FDTD and FETD, they often require significant computation time when dealing with interference signals that have longer duration or narrow frequency bands.

The BLT equation [15, 16] and modal analysis method [17] are well-established frequency-domain methods suitable for the crosstalk of the MTLs, which can circumvent the relatively long-time calculations of time domain methods. It is characterized by constructing the relationship equations between the interference source and the voltage or current responses at the terminal loads of the MTLs through the scattering and transmission matrices and then solving the equations to obtain the terminal loads' voltage or current responses via matrix operations. While the BLT equation can only obtain the voltage or current responses of terminal loads, the secondary radiation of the MTLs cannot be carried out.

The core idea of the modal analysis method [17] is to decouple multi-conductor TL equations into independent modal voltage and current equations by diagonalizing the per-unit-length impedance and admittance matrices using complex transformation matrices and then establish and solve the compact matrix formulations relating to the end voltages and currents. However, it requires solving eigenvalue equations to determine the transformation matrix elements for each frequency point, which requires a lot of theoretical derivation. Additionally, the cross-sectional line dimensions and surrounding media properties in this method should be invariant along the MTLs.

Therefore, a new solution of TL equations based on the FDFD method is proposed in this paper, which can realize the fast crosstalk simulation of multi-conductor TLs excited by long-time interference sources and obtain the voltage and current responses along the MTLs.

II. FDFD SOLUTION FOR THE CROSSTALK OF MULTI-CONDUCTOR TRANSMISSION LINES

Generally, the MTLs are close to the grounding plate, and the material of MTLs is seen as perfect conductor (PEC), on the basis that the electric fields surrounding the MTLs are approximated as quasi-TEM modes. Subsequently, the crosstalk of MTLs can be modeled using frequency-domain TL equations to avoid direct meshing the MTL structures, which can be expressed as

$$\frac{\partial}{\partial l}\boldsymbol{I}(l,\omega)+(\boldsymbol{G}+j\omega\boldsymbol{C})\boldsymbol{V}(l,\omega)=0, \tag{1}$$

$$\frac{\partial}{\partial l}\boldsymbol{V}(l,\omega)+(\boldsymbol{R}+j\omega\boldsymbol{L})\boldsymbol{I}(l,\omega)=0, \tag{2}$$

where l stands for the arbitrary direction of the MTLs. $\boldsymbol{I}(l,\omega)$ and $\boldsymbol{V}(l,\omega)$ denote the current and voltage vectors on the MTLs, respectively. $\boldsymbol{R}$, $\boldsymbol{L}$, $\boldsymbol{G}$, and $\boldsymbol{C}$ are the per unit length resistance, inductance, conductance, and capacitance matrices of the MTLs, respectively, which can be calculated by the empirical formulas from [17].

The MTLs are divided into N segments according to the FDFD grid Δl, as shown in Fig. 1, where the voltages and currents on the MTLs are sampled alternately, with voltages located at integer grid nodes and currents at half grid nodes. Crucially, the FDFD method requires grid resolutions satisfying the CFL condition [17], with spatial discretization constrained to below one-tenth wavelength of the interference source for stable computations.

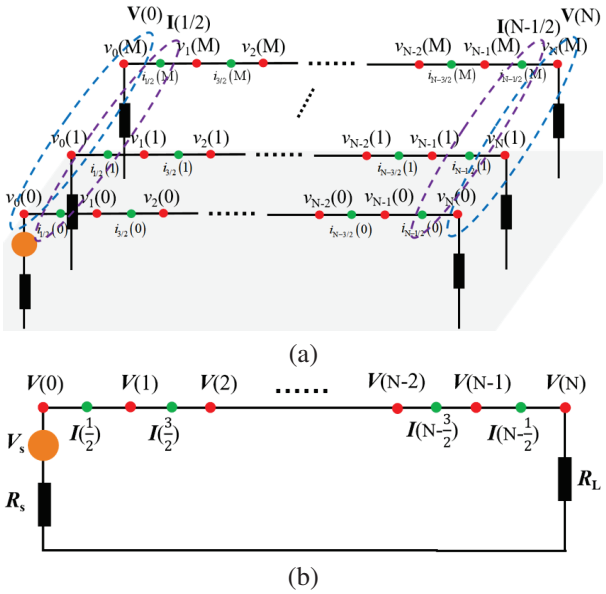

Fig. 1. FDFD difference scheme of multi-conductor transmission lines. (a) 3D view of FDFD grid of MTLs and (b) 2D view of FDFD grid of MTLs.

Discretizing equations (1) and (2) by the difference scheme of FDFD, respectively, yields

$$\frac{\boldsymbol{I}\left(i+\frac{1}{2}\right)-\boldsymbol{I}\left(i-\frac{1}{2}\right)}{\Delta l}+(\boldsymbol{G}+j\omega\boldsymbol{C})\,\boldsymbol{V}(i)=0, \quad (3)$$

$$\frac{\boldsymbol{V}(i+1)-\boldsymbol{V}(i)}{\Delta l}+(\boldsymbol{R}+j\omega\boldsymbol{L})\boldsymbol{I}\left(i+\frac{1}{2}\right)=0. \quad (4)$$

From equation (4), it follows that

$$\boldsymbol{I}\left(i+\frac{1}{2}\right)=-(\boldsymbol{R}+j\omega\boldsymbol{L})^{-1}\left(\frac{\boldsymbol{V}(i+1)-\boldsymbol{V}(i)}{\Delta l}\right), \quad (5)$$

$$\boldsymbol{I}\left(i-\frac{1}{2}\right)=-(\boldsymbol{R}+j\omega\boldsymbol{L})^{-1}\left(\frac{\boldsymbol{V}(i)-\boldsymbol{V}(i-1)}{\Delta l}\right). \quad (6)$$

Substituting equations (5) and (6) into equation (3), we get

$$\begin{array}{l}\frac{1}{\Delta l}(\boldsymbol{R}+j\omega\boldsymbol{L})^{-1}\frac{\boldsymbol{V}(i)-\boldsymbol{V}(i+1)}{\Delta l}-\frac{1}{\Delta l}(\boldsymbol{R}+j\omega\boldsymbol{L})^{-1}\\ \frac{\boldsymbol{V}(i-1)-\boldsymbol{V}(i)}{\Delta l}+(\boldsymbol{G}+j\omega\boldsymbol{C})\,\boldsymbol{V}(i)=0\end{array} \quad (7)$$

Further arranging equation (7) as

$$\begin{array}{l}\left[2+\Delta l^2(\boldsymbol{R}+j\omega\boldsymbol{L})(\boldsymbol{G}+j\omega\boldsymbol{C})\right]\boldsymbol{V}(i)\\ -\boldsymbol{V}(i+1)-\boldsymbol{V}(i-1)=0\end{array}. \quad (8)$$

Due to the ends of TLs being terminated by lumped sources and resistance loads, as shown in Fig. 1, the voltages at both terminal ports of the MTLs do not satisfy the center difference scheme of FDFD. Thus, they should be solved using forward and backward difference schemes [18] to establish the boundaries.

To determine the starting port's voltages, forward difference scheme is applied to discretize equation (1) as

$$\frac{\boldsymbol{I}(1/2)-\boldsymbol{I}_{\mathrm{s}}}{\Delta l/2}+(\boldsymbol{G}+j\omega\boldsymbol{C})\,\boldsymbol{V}(0)=0 \quad (9)$$

According to Ohm's law, the voltages and currents at the starting port satisfy the condition as

$$\boldsymbol{V}(0)=\boldsymbol{V}_{\mathrm{s}}-\boldsymbol{I}_{\mathrm{s}}\boldsymbol{R}_{\mathrm{s}}. \quad (10)$$

Equation (10) can be further arranged to get the expression of the load's current as

$$\boldsymbol{I}_{\mathrm{s}}=\boldsymbol{R}_{\mathrm{s}}^{-1}(\boldsymbol{V}_{\mathrm{s}}-\boldsymbol{V}(0)). \quad (11)$$

According to equation (5), the current term $\boldsymbol{I}(1/2)$ in equation (9) can be written as

$$\boldsymbol{I}(1/2)=-(\boldsymbol{R}+j\omega\boldsymbol{L})^{-1}\left(\frac{\boldsymbol{V}(1)-\boldsymbol{V}(0)}{\Delta l}\right). \quad (12)$$

Substituting equations (11) and (12) into equation (9), which is further arranged as

$$\begin{array}{l}\frac{2}{\Delta l}\left[(\boldsymbol{R}+j\omega\boldsymbol{L})^{-1}\left(\frac{\boldsymbol{V}(0)-\boldsymbol{V}(1)}{\Delta l}\right)\right]\\ -\frac{2}{\Delta l}\boldsymbol{R}_{\mathrm{s}}^{-1}(\boldsymbol{V}_{\mathrm{s}}-\boldsymbol{V}(0))+(\boldsymbol{G}+j\omega\boldsymbol{C})\,\boldsymbol{V}(0)=0\end{array}. \quad (13)$$

Rewriting equation (13) as

$$\begin{array}{l}\left[\frac{2}{\Delta l^2}(\boldsymbol{R}+j\omega\boldsymbol{L})^{-1}+\frac{2}{\Delta l}\boldsymbol{R}_{\mathrm{s}}^{-1}+(\boldsymbol{G}+j\omega\boldsymbol{C})\right]\boldsymbol{V}(0)\\ -\frac{2}{\Delta l^2}(\boldsymbol{R}+j\omega\boldsymbol{L})^{-1}\boldsymbol{V}(1)=\frac{2}{\Delta l}\boldsymbol{R}_{\mathrm{s}}^{-1}\boldsymbol{V}_{\mathrm{s}}\end{array}. \quad (14)$$

Similarly, the backward difference scheme is used to discretize equation (1) for solving the voltages on the ending port, which is expressed as

$$\frac{\boldsymbol{I}_{\boldsymbol{L}}-\boldsymbol{I}(\mathrm{N}-1/2)}{\Delta l/2}+(\boldsymbol{G}+j\omega\boldsymbol{C})\,\boldsymbol{V}(\mathrm{N})=0. \quad (15)$$

The voltage and current at the ending load also comply with Ohm's law, which can be expressed as

$$\boldsymbol{I}_{\boldsymbol{L}}=\boldsymbol{R}_{\boldsymbol{L}}^{-1}\boldsymbol{V}(\mathrm{N}). \quad (16)$$

Similarly, the current term $\boldsymbol{I}(\mathrm{N}-1/2)$ in equation (15) can be derived using equation (5), which is expressed as

$$\boldsymbol{I}(\mathrm{N}-1/2)=(\boldsymbol{R}+j\omega\boldsymbol{L})^{-1}\left(\frac{\boldsymbol{V}(\mathrm{N}-1)-\boldsymbol{V}(\mathrm{N})}{\Delta l}\right). \quad (17)$$

Substituting equations (16) and (17) into equation (15), which is further arranged as

$$\begin{array}{l}\frac{2}{\Delta l}\boldsymbol{R}_{\boldsymbol{L}}^{-1}\boldsymbol{V}(\mathrm{N})-\frac{2}{\Delta l}(\boldsymbol{R}+j\omega\boldsymbol{L})^{-1}\left(\frac{\boldsymbol{V}(\mathrm{N}-1)-\boldsymbol{V}(\mathrm{N})}{\Delta l}\right).\\ +(\boldsymbol{G}+j\omega\boldsymbol{C})\,\boldsymbol{V}(\mathrm{N})=0\end{array} \quad (18)$$

Rewriting equation (18) as

$$\begin{array}{l}\left[\frac{2}{\Delta l^2}(\boldsymbol{R}+j\omega\boldsymbol{L})^{-1}+\frac{2}{\Delta l}\boldsymbol{R}_{\boldsymbol{L}}^{-1}+(\boldsymbol{G}+j\omega\boldsymbol{C})\right]\boldsymbol{V}(\mathrm{N})\\ -\frac{2}{\Delta l^2}(\boldsymbol{R}+j\omega\boldsymbol{L})^{-1}\boldsymbol{V}(\mathrm{N}-1)=0\end{array}. \quad (19)$$

To solve the voltages along the MTLs, equations (8), (14) and (19) are combined to construct the FDFD-TL matrix equation, which is expressed as

$$\begin{bmatrix}\mathbf{A}_{0,0} & \mathbf{A}_{0,1} & \mathbf{0} & \mathbf{0} & \cdots & \mathbf{0} & \mathbf{0}\\ \mathbf{A}_{1,0} & \mathbf{A}_{1,1} & \mathbf{A}_{1,2} & \mathbf{0} & \cdots & \mathbf{0} & \mathbf{0}\\ \vdots & \vdots & \ddots & \vdots & \vdots & \vdots & \vdots\\ \mathbf{0} & \cdots & \mathbf{A}_{k,k-1} & \mathbf{A}_{k,k} & \mathbf{A}_{k,k+1} & \cdots & \mathbf{0}\\ \vdots & \vdots & \vdots & \vdots & \ddots & \vdots & \vdots\\ \mathbf{0} & \mathbf{0} & \cdots & \mathbf{0} & \mathbf{A}_{\mathrm{N}-1,\mathrm{N}-2} & \mathbf{A}_{\mathrm{N}-1,\mathrm{N}-1} & \mathbf{A}_{\mathrm{N}-1,\mathrm{N}}\\ 0 & 0 & \cdots & 0 & 0 & \mathbf{A}_{\mathrm{N},\mathrm{N}-1} & \mathbf{A}_{\mathrm{N},\mathrm{N}}\end{bmatrix}$$

$$\bullet\begin{bmatrix}\mathbf{V}(0)\\ \mathbf{V}(1)\\ \vdots\\ \mathbf{V}(k)\\ \vdots\\ \mathbf{V}(N-1)\\ \mathbf{V}(N)\end{bmatrix}=\begin{bmatrix}\mathbf{b}(0)\\ \mathbf{b}(1)\\ \vdots\\ \mathbf{b}(k)\\ \vdots\\ \mathbf{b}(N-1)\\ \mathbf{b}(N)\end{bmatrix}, \quad (20)$$

where the coefficient matrix is represented as $\mathbf{A}$, and its elements are denoted as

$$\mathbf{A}_{0,0}=\frac{2}{\Delta l^2}(\boldsymbol{R}+j\omega\boldsymbol{L})^{-1}+\frac{2}{\Delta l}\boldsymbol{R}_{\mathrm{s}}^{-1}+(\boldsymbol{G}+j\omega\boldsymbol{C}) \quad (21a)$$

$$\mathbf{A}_{0,1}=\mathbf{A}_{\mathrm{N},\mathrm{N}-1}=-\frac{2}{\Delta l^2}(\boldsymbol{R}+j\omega\boldsymbol{L})^{-1} \quad (21b)$$

$$\mathbf{A}_{\mathrm{N},\mathrm{N}}=\frac{2}{\Delta l^2}(\boldsymbol{R}+j\omega\boldsymbol{L})^{-1}+\frac{2}{\Delta l}\boldsymbol{R}_{\mathrm{L}}^{-1}+(\boldsymbol{G}+j\omega\boldsymbol{C}) \quad (21c)$$

$$\begin{cases}\mathbf{A}_{k,k-1}=\mathbf{A}_{k,k+1}=-1\\ \mathbf{A}_{k,k}=2+\Delta l^2(\boldsymbol{R}+j\omega\boldsymbol{L})(\boldsymbol{G}+j\omega\boldsymbol{C})\end{cases},\mathrm{k}\neq 0,\mathrm{N}. \quad (21d)$$

The voltage vector is defined as $\mathbf{V}$, expressed as $V=[V(0),V(1),\cdots,V(k),\cdots,V(\mathrm{N})]^{\mathrm{T}}$, where

$$\begin{cases} \mathbf{V}(0)=[v_0(1),v_0(2),\cdots,v_0(M)]^{\mathrm{T}} \\ \mathbf{V}(1)=[v_1(1),v_1(2),\cdots,v_1(M)]^{\mathrm{T}} \\ \quad\vdots \\ \mathbf{V}(k)=[v_k(1),v_k(2),\cdots,v_k(M)]^{\mathrm{T}} \\ \quad\vdots \\ \mathbf{V}(N)=[v_{\mathrm{N}}(1),v_{\mathrm{N}}(2),\cdots,v_{\mathrm{N}}(M)]^{\mathrm{T}} \end{cases}, \tag{22}$$

where M is the line number of MTLs.

The excitation source vector is defined as $\mathbf{b}$, expressed as $\mathbf{b}=[\mathbf{b}(0),\mathbf{b}(1),\cdots,\mathbf{b}(k),\cdots,\mathbf{b}(\mathrm{N})]^{\mathrm{T}}$, where

$$\begin{cases} \mathbf{b}(0)=\boldsymbol{R}_{\mathrm{S}}^{-1}\boldsymbol{V}_{\mathrm{S}}/\Delta x \\ \mathbf{b}(k)=0, \quad k=1,...,N \end{cases}. \tag{23}$$

The coefficient matrix $\mathbf{A}$ is a complex sparse matrix with many zero elements. To minimize memory usage, an efficient triple storage format of sparse matrix [19] is employed to store the non-zero elements of $\mathbf{A}$ along with their corresponding row and column indices. Considering the non-zero elements in this sparse matrix exhibit no symmetric distribution, the conjugate gradient method [20] is preferred to solve the FDFD-TL matrix equation efficiently. Its detailed procedure is shown in Fig. 2, where n stands for the n-th iteration step and $\varepsilon$is the maximum error value.

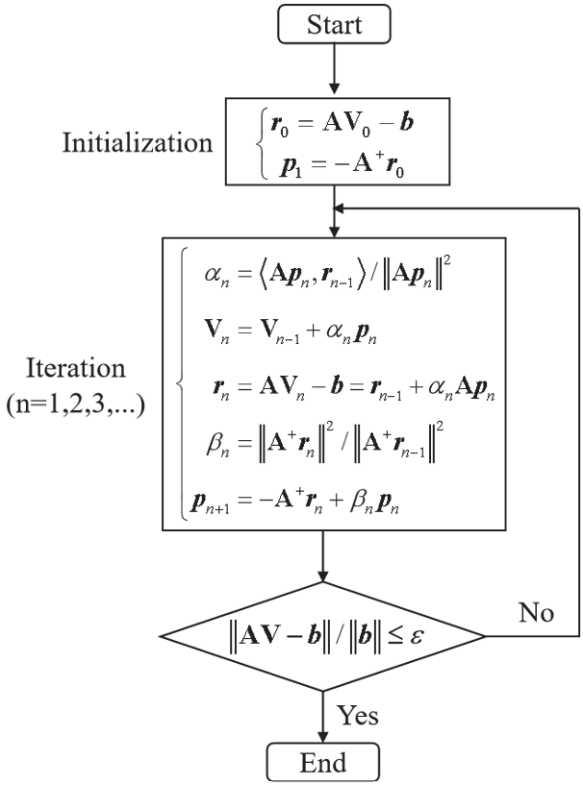

Fig. 2. Flow chart of conjugate gradient method.

Additionally, when the MTL lengths are sufficiently long, a large number of FDFD grids will be required. This can significantly increase the size of the coefficient matrix, reducing the iteration efficiency of the conjugate gradient method. To address this issue, the message passing interface (MPI) parallel technique [21] is introduced to facilitate the parallel computation of the FDFD-TL matrix equation via multiple threads. The MPI parallel strategy is to distribute the matrix operation tasks by the main process to multiple sub-processes. The partial solutions from each sub-process are then aggregated to the main process to obtain the voltages at all nodes of the MTLs. This enhancement can notably improve the crosstalk simulation efficiency of MTLs.

Currently, the responses along the MTLs can be calculated using equation (5), once the voltages on the MTLs are obtained.

III. NUMERICAL SIMULATION

To assess the accuracy and efficiency of the proposed method, two typical simulation cases about the crosstalk of MTLs on perfect conductor (PEC) plane excited by lumped voltage pulse sources are employed to be solved by the proposed method and full-wave MoM and then comparing their results in terms of precision and computation time.

Figure 3 illustrates the crosstalk model of two TLs on the PEC plane, where the length, radius, height, and distance of the lines are 1 m, 1 mm, 1 cm, and 1 cm, respectively. The starting port of TL #1 is excited by a Gaussian pulse voltage source, denoted as U, and expressed as $A_0\exp\left[-4\pi(t-t_0)^2/\tau^2\right]$, where amplitude $A_0=1$ V, pulse width $\tau=2$ ns, and time delay $t_0=1.6$ ns. This voltage source has an inner impedance of $\mathrm{Z}_0=50\Omega$. The other terminals of both lines are connected to resistance loads, also of 50Ω. The model parameters are listed in Table 1.

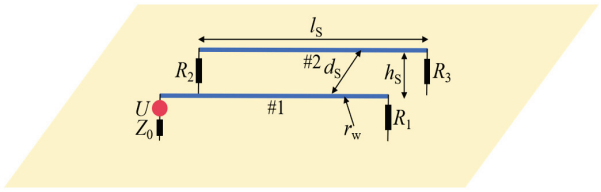

Fig. 3. Crosstalk model of two parallel transmission lines on the PEC plane.

The proposed method was implemented on a computing node equipped with an Intel Xeon 2.4 GHz, 32-core processor and 64 GB RAM, utilizing MPI 3.2 with 8-thread parallelization for execution. The discrete grid size selected by the FDFD is $\Delta l=\lambda/30=1$ cm, where λ stands for the minimum wavelength of Gaussian pulse.

Table 1: Model parameters of first case

Parameter	Value
Length l_s	1 m
Radius r_w	1 mm
Height h_s	1 cm
Distance d_s	1 cm
Voltage source U	$A_0 = 1$ V, $\tau = 2$ ns, $t_0 = 1.6$ ns
Inner impedance Z_0	50Ω
Loads $R_1 \sim R_3$	50Ω

Within the MoM, the lines are divided into line segments according to the same grid size of FDFD, requiring a total of 200 segments. Meanwhile, the PEC plane is represented by half space Green's function. Additionally, the sampling frequency number of the proposed method and MoM are both 200 with interval of 5 MHz.

The real and imaginary parts of the voltage responses on loads R_1 and R_3 obtained using the proposed method and MoM, are shown in Figs. 4 and 5. It can be seen that the results of the two methods are in good agreement.

To quantitatively evaluate the proposed method, the relative errors (REs) of the results obtained by the two methods are calculated, with the maximum RE being only 3.8%. Here, RE is defined as

$$\mathrm{RE} = \sqrt{\frac{\sum_{i=1}^{\mathrm{FN}} \left(|V^E(i)| - |V^B(i)|\right)^2}{\sum_{i=1}^{\mathrm{FN}} \left(|V^B(i)|\right)^2}}, \tag{24}$$

where i stands for the i-th sampling frequency, FN is the sampling frequency number. $V^E(i)$ and $V^B(i)$ are the real parts or imaginary parts of the voltage responses at i-th sampling frequency obtained by the proposed method and MoM, respectively.

Furthermore, the computation times required by the proposed method and MoM are 1.2 s and 21.8 s, respectively, demonstrating the high computational efficiency of this method.

To establish a rigorous validation framework, the proposed method is benchmarked against MoM and FDTD-TL method through crosstalk simulation of MTLs excited by prolonged LEMP waveforms.

Figure 6 is the crosstalk model of four TLs on the PEC plane excited by a LEMP voltage source with inner impedance of 50Ω, where the length, radius, and height of the four lines are 100 m, 1 mm, and 10 cm, respectively. Distance between adjacent lines is 5 cm. Terminal loads of the MTLs are also 50Ω. The starting port of TL #2 is excited by the LEMP voltage source, expressed as $A_0\left[\exp(-\alpha t) - \exp(-\beta t)\right]$, where $A_0 = 51946$ V, $\alpha = 1.1\times10^5$ s^{-1}, $\beta = 1.1\times10^5$ s^{-1} [22]. The model parameters are all listed in Table 2.

The grid size selected by the proposed method is 1 m, which is also determined by the CFL condition. Similarly, each line of the MTLs in MoM is meshed by FDFD grid, yielding 400 line segments. The ground plane is also model by half space Green's function. Additionally, the sampling frequency number of the proposed method and MoM are both 400 with interval of 10 kHz. Within the FDTD-TL method, the time domain TL equations transforming from equations (1) and (2) are discretized

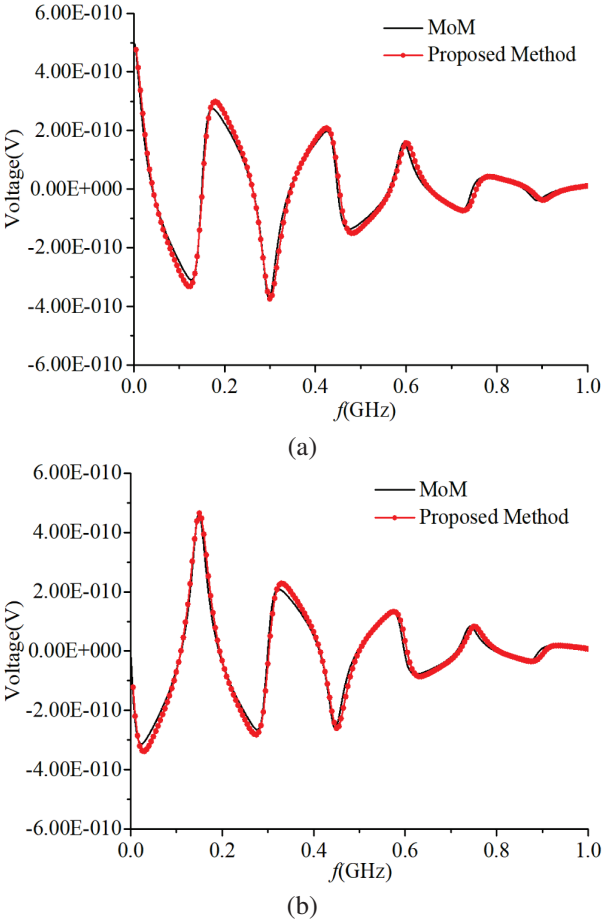

Fig. 4. Voltage responses on the load R_1 obtained by the two methods for the first case. (a) real parts of the voltages and (b) imaginary parts of the voltages.

Table 2: Model parameters of second case

Parameter	Value
Length l_s	100 m
Radius r_w	1 mm
Height h_s	10 cm
Distance d_s	5 cm
Voltage source U	$A_0 = 51946$ V, $\alpha = 1.1\times10^5$ s^{-1}, $\beta = 1.1\times10^5$ s^{-1}
Inner impedance Z_0	50Ω
Loads $R_1 \sim R_7$	50Ω

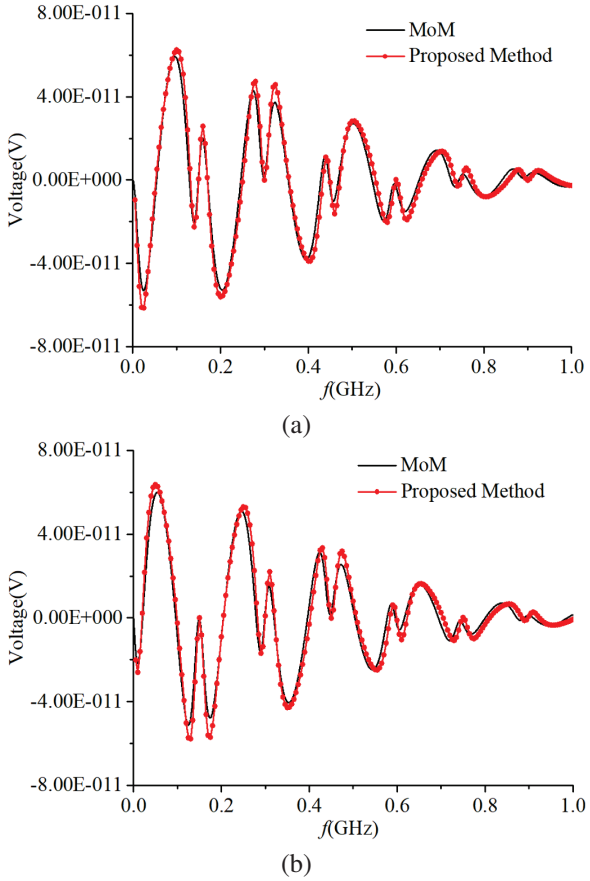

Fig. 5. Voltage responses on the load R_3 obtained by the two methods for the first case. (a) real parts of the voltages and (b) imaginary parts of the voltages.

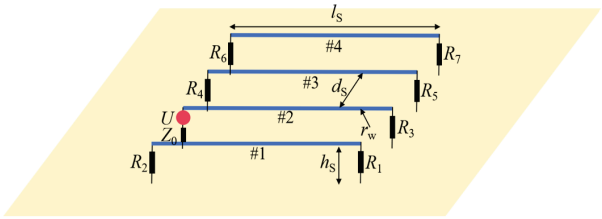

Fig. 6. Crosstalk model of four parallel transmission lines excited by LEMP voltage source.

by the space step of 1 m and time step of 1.667 ns to iteratively calculate the current and voltage responses along the MTLs. To ensure the spectral accuracy in the Fourier transform analysis of MTL voltages or currents, the FDTD-TL simulation requires a total duration spanning multiple LEMP cycles. Considering the waveform persistence of LEMP reaching 100 μs, 120,000 time steps are used for this method.

The voltage responses on the loads R_5 and R_6 are calculated by the three methods and the results are compared in Figs. 7 and 8. The results of these methods align

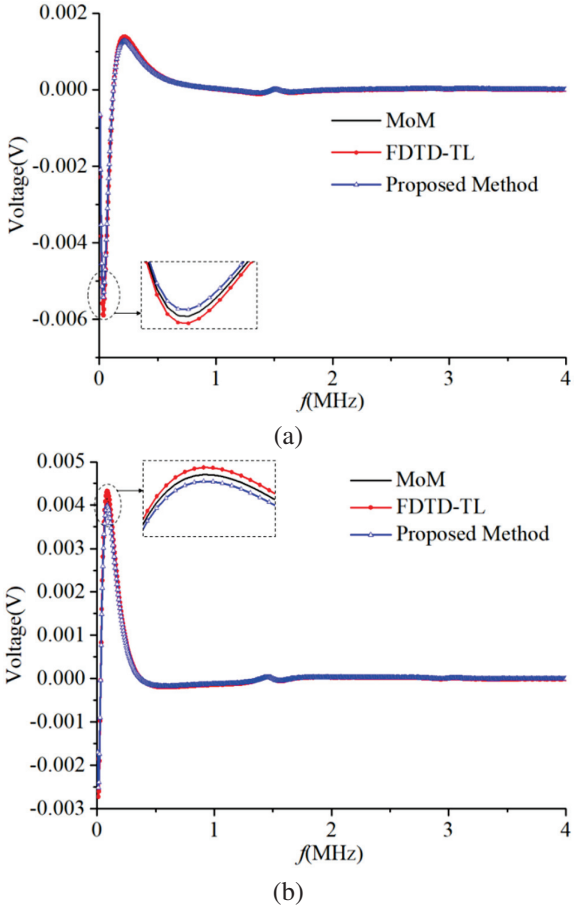

Fig. 7. Voltage responses on the load R_5 obtained by the two methods for the second case: (a) real parts of the voltages and (b) imaginary parts of the voltages.

closely and the maximum RE values of our method and FDTD-TL method with MoM are approximately 4.0% and 4.6%, respectively. Additionally, the computation

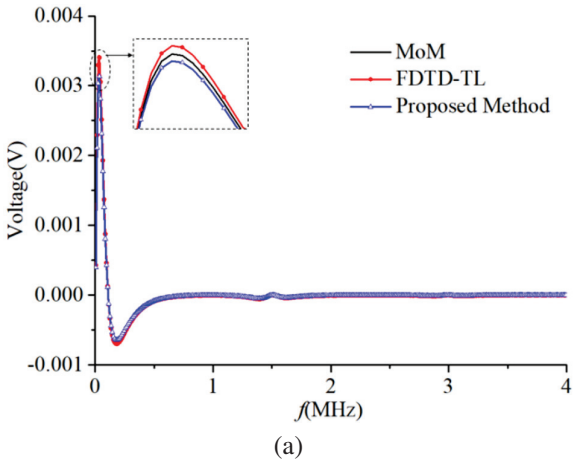

Fig. 8. (*Continued.*)

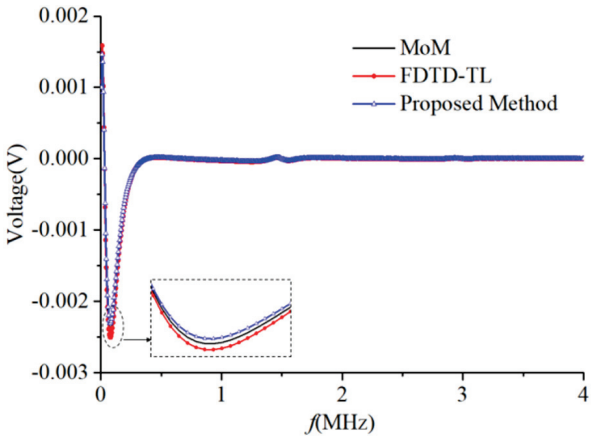

(b)

Fig. 8. Voltage responses on the load R_6 obtained by the two methods for the second case: (a) real parts of the voltages and (b) imaginary parts of the voltages.

time for MoM is 49.8 s, the FDTD-TL method requires 96 s, while the proposed method needs 4.4 s.

IV. CONCLUSION

To enhance the efficiency of crosstalk simulations for multi-conductor transmission lines (MTLs) affected by long-duration interference sources, we propose a new frequency-domain hybrid method that combines the finite-difference frequency-domain (FDFD) method with TL equations. The innovative aspect of this approach is the derivation and establishment of the FDFD-TL matrix equation, which is specifically designed for the crosstalk modeling of MTLs excited by long-time interference sources. Meanwhile, the voltage responses along the MTLs are efficiently solved using the MPI-based conjugate gradient method. Crosstalk simulations of MTLs containing two lines or four lines are completed by the proposed method and MoM, and the accuracy and efficiency of this method have been validated through comparisons of their results concerning precision and time consumption. Currently, the proposed method does not account for the frequency-dependent properties of MTLs and assumes the MTLs in straight configuration. Future research will focus on addressing these limitations to improve the method's applicability.

ACKNOWLEDGMENT

This work was supported by the Special Support for Chongqing Postdoctoral Research Project (Grant No. 2022CQBSHTB3018).

REFERENCES

[1] Z. R. Gao, H. C. Zhao, L. Yang, and F. S. Wang, "Numerical simulation of the coupling of ultra-wide band electromagnetic pulse into landmine by aperture," *Chin. Phys. B*, vol. 24, no. 9, p. 094101, July 2015.

[2] K. H. Fan, B. Wei, X. B. He, Y. W. Li, and X. L. Wei, "A hybrid FETD algorithm for electromagnetic modeling of fine structures," *IEEE Antennas Wireless Propag. Lett.*, vol. 18, no. 12, pp. 2771-2775, Dec. 2019.

[3] M. Azadifar, P. Dehkhoda, S. H. H. Sadeghi, and R. Moini, "A hybrid FDFD-MoM technique for susceptibility evaluation of a transmission line inside a perforated enclosure," *IEEE Trans. Electromagn. Compat.*, vol. 56, no. 6, pp. 1474-1479, Dec. 2014.

[4] D. Y. Zhou, H. J. Zhou, Z. H. Ye, Q. Feng, and C. Liao, "Transient response of transmission lines with lumped circuit termination based on the TLM," in *5th IEEE International Symposium on Microwave, Antenna, Propagation and EMC Technologies for Wireless Communications*, Chengdu, China, 2013.

[5] K. Masumnia-Bisheh, K. Forooraghi, and M. Ghaffari-Miab, "Electromagnetic uncertainty analysis using stochastic FDFD method," *IEEE Trans. Antennas Propag.*, vol. 67, no. 5, pp. 3268-3277, May 2019.

[6] Y. X. Sun, Q. Li, W. H. Yu, Q. H. Jiang, and Q. K. Zhuo, "Study on crosstalk between space transient interference microstrip lines using finite difference time domain method," *Applied Computational Electromagnetics Society (ACES) Journal*, vol. 30, no. 8, pp. 891-896, Aug. 2015.

[7] Z. H. Ye, M. Z. Ru, and X. L. Wu, "Crosstalk analysis of printed circuit board traces with right-angled bent corners via time domain hybrid method," *IEEE Trans. Electromagn. Compat.*, vol. 64, no. 6, pp. 2227-2237, Dec. 2022.

[8] Z. Y. Huang, L. H. Shi, B. Chen, and Y. H. Zhou, "A new unconditionally stable scheme for FDTD method using associated Hermite orthogonal functions," *IEEE Trans. Antennas Propag.*, vol. 62, no. 9, pp. 4804-4809, Sep. 2014.

[9] J. Y. Wang, T. Jiang, R. F. Sun, and Y. X. Sun, "Time domain solutions of transmission line crosstalk," in *IEEE International Symposium on Antennas and Propagation*, Denver, CO, USA, 2022.

[10] W. Zhang, Z. Chen, J. F. Ding, and Y. J. Wu, "Grounding characteristics of shielded wire crosstalk at high frequency," in *Asia-Pacific International Symposium on Electromagnetic Compatibility (APEMC)*, Beijing, China, 2022.

[11] B. M. Xiao, J. M. Zhou, X. F. Liu, W. Yan, Y. Cao, and Y. Zhao, "Crosstalk prediction in twisted-wire pairs based on beetle swarm optimization algo-

rithm," *IEEE Access*, vol. 9, pp. 84588-84595, June 2021.

[12] C. Huang, Y. Zhao, W. Yan, Q. Q. Liu, and J. M. Zhou, "A new method for predicting crosstalk of random cable bundle based on BAS-BP neural network algorithm," *IEEE Access*, vol. 8, pp. 20224-20232, Jan. 2020.

[13] X. Liu, X. Cui, and L. Qi, "Time-domain finite-element method for the transient response of multiconductor transmission lines excited by an electromagnetic field," *IEEE Trans. Electromagn. Compat.*, vol. 53, no. 2, pp. 462-474, 2011.

[14] L. Qi, S. H. Bai, and Q. Shuai, "Finite-element time-domain method for multiconductor transmission lines based on the second-order wave equation," *IEEE Trans. Electromagn. Compat.*, vol. 56, no. 5, pp. 1218-1227, 2014.

[15] J. K. Du, S. M. Hwang, J. W. Ahn, and J. G. Yook, "Analysis of coupling effects to PCBs inside waveguide using the modified BLT equation and full-wave analysis," *IEEE Trans. Microw. Theory Techn.*, vol. 61, no. 10, pp. 3514-3523, Oct. 2013.

[16] G. Y. Ni, L. Yan, and N. C. Yuan, "Time-domain analytic solutions of two-wire transmission line excited by a plane-wave field," *Chin. Phys. B*, vol. 17, no. 10, pp. 3629-3634, Oct. 2008.

[17] C. R. Paul, *Analysis of Multiconductor Transmission Lines*, 2nd ed. Hoboken, NJ: Wiley, 2008.

[18] Z. H. Ye, X. Z. Xiong, C. Liao, and Y. Li, "A hybrid method for electromagnetic coupling problems of transmission lines in cavity based on FDTD method and transmission line equation," *Progress in Electromagnetics Research M*, vol. 42, pp. 85-93, 2015.

[19] N. Neuss, "A new sparse-matrix storage method for adaptively solving large systems of reaction-diffusion-transport equations," *Computing*, vol. 68, no. 1, pp. 19-36, Sep. 2001.

[20] K. Nayanthara, S. M. Rao, and T. K. Sarkar, "Analysis of two-dimensional conducting and dielectric bodies utilizing the conjugate gradient method," *IEEE Trans. Antennas Propag.*, vol. 35, no. 4, pp. 451-453, Apr. 1987.

[21] J. Luo, Z. H. Ye, and C. Liao, "An MPI-based parallel FDTD-TL method for the EMI analysis of transmission lines in cavity excited by ambient wave," *IEEE Trans. Electromagn. Compat.*, vol. 62, no. 1, pp. 212-217, Feb. 2020.

[22] Z. H. Ye, Y. C. Shi, Z. W. Gao, and X. L. Wu, "Time domain hybrid method for the coupling analysis of power line network with curved and multidirectional segments," *IEEE Trans. Electromagn. Compat.*, vol. 65, no. 1, pp. 216-224, Feb. 2023.

Zhihong Ye was born in Taixing, Jiangsu Province, China, on 12 March 1988. He received the B.S. and the Ph.D. degrees from Southwest Jiaotong University in 2010 and 2016, respectively. He became an assistant professor at Chongqing University of Posts and Telecommunications in 2018. His research interests include electromagnetic compatibility, electromagnetic protection, and electromagnetic propagation.

Yufan Zhai was born in Jiyuan, Henan Province, China, in 2001. He is studying for the M.Sc. degree in Information and Communication Engineering from Chongqing University of Posts and Telecommunications. His research interests include computational electromagnetics, electromagnetic compatibility.

Meilin Liu was born in China. He received the B.S. degree in Mechanical and Electronical Engineering from Nanchang College, Nanchang, China, in 2000, the M.S. degree in Biophysics from Nanjing Agricultural University, Nanjing, in 2006, and the Ph.D. degree in Communication and Information System from Nanjing University of Aeronautics and Astronautics, Nanjing, in 2011. He spent two years in King Abdullah University of Science and Technology, Saudi Arabia, as a postdoc researcher. He worked for Shanghai Institute of Satellite Engineering 2013-2019 as a research scientist. He joined Shanghai Jiao Tong University in August 2019. His research interests include various numerical methods for electromagnetic phenomenon simulation and developing novel electromagnetic applications.

Low-loss Miniaturized Tri-band Bandpass Filter with High Selectivity and Good Passband Symmetry

Chuan Shao[1,2]

[1]School of Information Engineering
Jiangsu College of Engineering and Technology, Nantong Jiangsu 226000, P. R. China
ch_shao@126.com

[2]Jiangsu College of Engineering and Technology
Nantong Key Laboratory of Artificial Intelligence New Quality Technology, Nantong Jiangsu 226000, P. R. China

***Abstract* –**This paper introduces a low-loss microstrip line tri-band bandpass filter, utilizing quarter-wavelength ($\lambda_g/4$) tri-section stepped impedance resonators (TSSIRs). In this design, the adoption of a non-edge-coupled structure effectively eliminates the presence of coupling gaps. As a result, additional radiation losses are avoided, leading to lower insertion loss. In addition, the operating frequencies of the three passbands can be flexibly adjusted by tuning the impedance ratios in the TSSIR. Moreover, the $\lambda_g/4$ TSSIR exhibits a smaller size compared to existing $\lambda_g/2$ TSSIRs, resulting in a more compact overall design. In order to validate the proposed design methodology, a tri-band bandpass filter with passbands centered at 1.0 GHz, 3.5 GHz, and 6.0 GHz was designed, fabricated, and measured. The minimum insertion losses for each passband were measured to be 0.07 dB, 0.52 dB, and 1.14 dB, respectively. The filter occupies a compact area of 31×21.5 mm^2 ($0.17\lambda_g\times0.12\lambda_g$), demonstrating excellent passband symmetry for each frequency band. The proposed tri-band bandpass filter not only achieves three desirable operating frequencies but also benefits from the inherent characteristics of conventional filters, such as remarkably low insertion loss and good passband symmetry.

***Index Terms* –** Bandpass filters, high selectivity, low-loss feature, passband symmetry, TSSIRs.

I. INTRODUCTION

In recent years, multiband and multi-standard wireless communication systems have garnered significant attention due to their ability to support diverse communication standards and frequency bands [1]–[3]. Multiband bandpass filters are essential passive components in these systems, significantly influencing overall performance. Consequently, extensive research has been conducted to develop various design approaches for multiband bandpass filters. Traditional tri-band bandpass filters have been realized using three sets of resonators with common feeds [4]. However, these designs often suffer from large footprints due to the extensive use of resonators. To address this issue, alternative methods have been proposed, such as employing two sets of resonators where one set operates at two frequencies [5]–[6]. Another approach involves half-wavelength tri-section stepped impedance resonators ($\lambda_g/2$ TSSIRs, λ_g is the guided wavelength at the center frequency of the first passband) and other multi-mode resonators which can achieve tri-band functionality with only one set of resonators. Despite these innovations, $\lambda_g/2$ TSSIRs and multi-mode resonators still occupy a relatively large area [7]–[11]. Additionally, since the aforementioned filters all employ an edge-coupled structure, the coupling gaps are prone to generating certain levels of radiation. This radiation effect inevitably leads to relatively high insertion losses in these structures. Substrate integrated waveguide (SIW) has emerged as a widely adopted low-loss transmission line in recent years [12]–[14]. Owing to the confinement of microwave signals predominantly within the dielectric medium, microwave devices designed based on SIW exhibit inherently low insertion loss and are well-suited for operation at higher frequencies.

This paper presents a novel tri-band bandpass filter based on ($\lambda_g/4$) TSSIRs. The design process is both simple and effective. Conventional $\lambda_g/4$ uniform impedance resonators, while offering excellent performance, are limited by providing periodic center frequencies for the passbands. By replacing these $\lambda_g/4$ uniform impedance resonators with $\lambda_g/4$ TSSIRs, three distinct passbands can be readily achieved. The proposed filter exhibits a compact size, remarkably low insertion loss, and excellent passband symmetry.

Additionally, four inherent transmission zeros within the operational band significantly enhance selectivity and isolation between the three passbands.

Submitted On: March 07, 2025
Accepted On: June 29, 2025

https://doi.org/10.13052/2025.ACES.J.400705

II. ANALYSIS OF TRADITIONAL STUB BANDPASS FILTERS

Traditional stub bandpass filters can be configured in the form illustrated in Fig. 1, which consists of shunt-connected, short-circuited stubs each with an electrical length of θ and a characteristic impedance of Z_S, coupled via connecting lines of an electrical length of θ and characteristic impedance of Z_T. This particular arrangement leverages the quarter-wavelength resonance principle to achieve selective frequency transmission, effectively attenuating signals outside the designated passband while allowing those within the passband to propagate with minimal loss. Ideal transmission coefficients of the structure shown in Fig. 1 are given in Fig. 2. As depicted in Fig. 2, the stub bandpass filter is designed to exhibit three distinct passbands centered at f_0, $3f_0$, and $5f_0$. These passbands correspond to the first three resonant frequencies of the $\lambda_g/4$ uniform impedance resonators employed in the filter design. Additionally, the filter inherently generates four transmission zeros located at DC, $2f_0$, $4f_0$, and $6f_0$, respectively. These transmission zeros play a crucial role in enhancing the filter's performance by providing sharp transitions between passbands and stopbands. Consequently, the stub bandpass filter demonstrates superior performance in terms of band-to-band isolation and selectivity. Specifically, the presence of multiple transmission zeros ensures that the filter can effectively attenuate signals outside the desired passbands, thereby minimizing interference and crosstalk between adjacent bands. Simulated transmission coefficients of the structure shown in Fig. 1 with different values of Z_S are illustrated Fig. 3. As illustrated in Figs. 2 and 3, the transmission characteristics of the stub bandpass filter demonstrate significant stability in response to variations in Z_T. Specifically, when Z_S is held constant, the transmission coefficients of the filter remain remarkably consistent, irrespective of fluctuations in Z_T. This indicates that the filter's performance is relatively insensitive to changes in Z_T under constant Z_S conditions. Furthermore, when Z_T is kept constant, the transmission coefficients of the filter are observed to gradually decrease as the value of Z_S increases. This suggests that the filter's transmission efficiency is inversely related to the magnitude of Z_S when Z_T is maintained at a constant level.

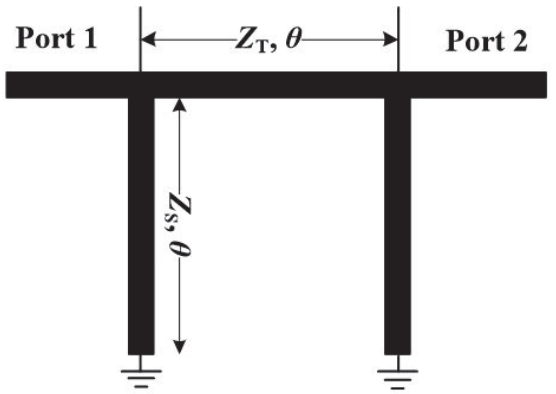

Fig. 1. Transmission line bandpass filter with quarter-wavelength short-circuited stubs.

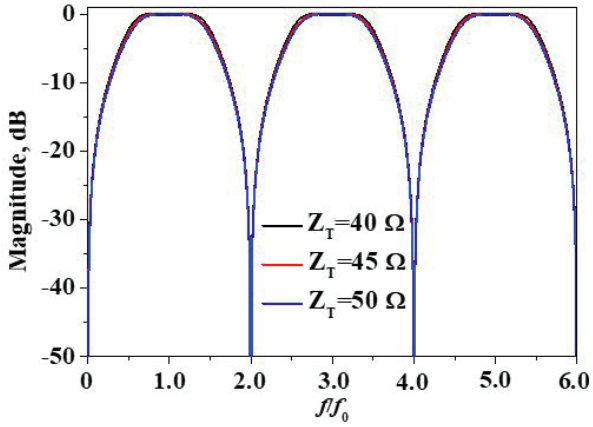

Fig. 2. Simulated transmission coefficients of the structure shown in Fig. 1 with different values of Z_T ($Z_S = 50\ \Omega$).

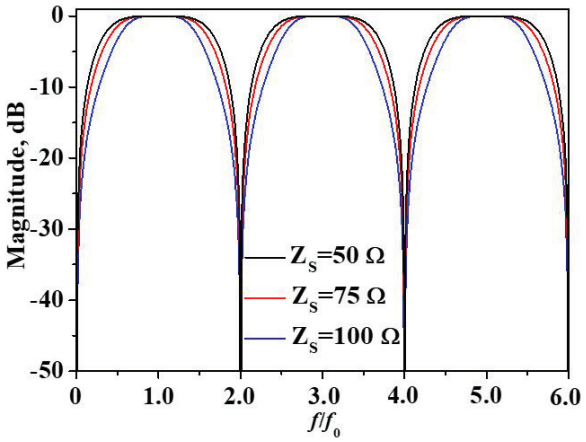

Fig. 3. Simulated transmission coefficients of the structure shown in Fig. 1 with different values of Z_S (Z_T=50 Ω).

It is worth highlighting that, in contrast to conventional edge-coupled bandpass filters, where bandwidth adjustment is predominantly achieved by varying the widths of the coupling gap, the developed stub bandpass filter exhibits a distinct feature. Specifically, it modulates

its bandwidth by altering the impedance characteristics of the resonator. This unique approach circumvents the potential for spurious losses that typically arise from radiation in the coupling gap of traditional designs. To provide empirical evidence supporting this claim, Fig. 4 illustrates the electric field distributions within the cross-sections of both a 50-ohm microstrip transmission line and a 50-ohm coupled transmission line under analogous operating conditions. The electric field distributions of the aforementioned structures were obtained using the relevant functionalities in Ansys HFSS [18]. For both types of structures, namely the 50-ohm microstrip transmission lines and the edge-coupled microstrip lines, the electric field distributions were obtained at an operating frequency of 1 GHz. Upon examination of Fig. 4, it is evident that, when scaled identically, the coupled transmission line exhibits a more pronounced radiation of energy into the surrounding free space. This heightened radiation propensity is inherently associated with increased energy dissipation, thereby resulting in a comparatively higher insertion loss for the entire device. This observation underscores the significance of the design approach adopted in the stub bandpass filter, which effectively mitigates such spurious radiation losses by eschewing reliance on coupling gap adjustments, leading to a more efficient signal transmission and reduced overall insertion loss.

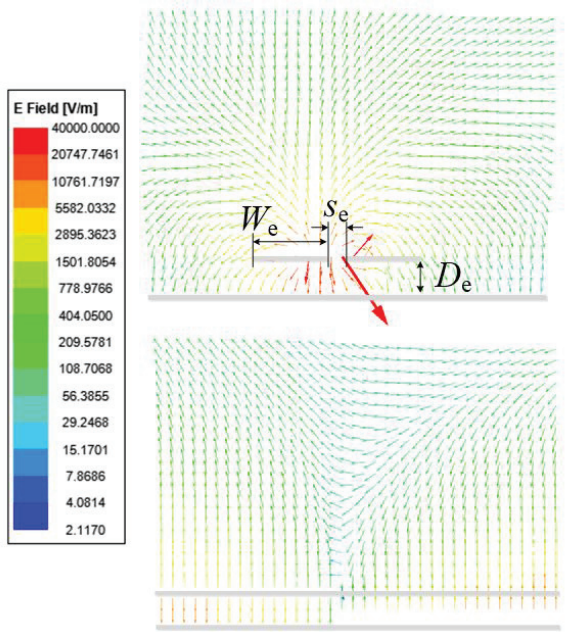

Fig. 4. Electric field distribution on the cross-section of 50-ohm microstrip transmission lines and edge-coupled microstrip lines at 1 GHz ($W_e = 1.9$ mm, $s_e = 0.2$ mm, $D_e = 0.813$ mm).

III. DESIGN OF THE DEVELOPED TRI-BAND BANDPASS FILTER

A. Analysis of the $\lambda_g/4$ tri-section stepped impedance resonators (TSSIRs)

The employed $\lambda_g/4$ TSSIR depicted in Fig. 5 is designed with three distinct characteristic impedances, Z_1, Z_2, and Z_3. For practical applications, it is advantageous to assume that each section has an equal electrical length. Under this assumption, the input impedances in Fig. 5 can be precisely derived through a series of mathematical transformations:

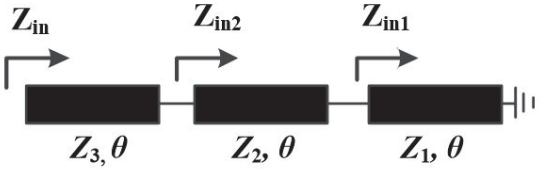

Fig. 5. Structure of $\lambda_g/4$ TSSIR.

$$Z_{in1} = jZ_1 \tan\theta, \tag{1}$$

$$Z_{in2} = jZ_2 \frac{(Z_1 + Z_2)\tan\theta}{Z_2 - Z_1 \tan^2\theta}, \tag{2}$$

$$Z_{in} = jZ_3 \frac{(Z_1Z_2 + Z_2^2 + Z_1Z_3)\tan\theta - Z_2Z_3\tan^3\theta}{Z_2Z_3 - (Z_1Z_2 + Z_2^2 + Z_1Z_3)\tan^2\theta}, \tag{3}$$

while the condition for the first three resonances of this TSSIR can be obtained as:

$$\theta_{01} = \theta = \text{acr}\tan\sqrt{\frac{K_1K_2}{1 + K_1 + K_2}}, \tag{4}$$

$$\theta_{02} = \frac{\pi}{2}, \tag{5}$$

$$\theta_{03} = \pi - \theta, \tag{6}$$

where $K_1 = Z_3/Z_2$, $K_2 = Z_2/Z_1$. When the discontinuity and dispersion effects of the TSSIR have been ignored, the fundamental property can be obtained as $f_1 : f_2 : f_3 = \theta_{01} : \theta_{02} : \theta_{03}$. Therefore, once center frequencies f_1, f_2, f_3 have been assigned, the required impedance ratios for the TSSIR can be determined using the same method as presented in [7].

The locations of transmission zeros of the developed bandpass filter can be determined by setting the input impedance Z_{in} to zero. This provides the relationship:

$$(Z_1Z_2 + Z_2^2 + Z_1Z_3)\tan\theta = Z_2Z_3\tan^3\theta. \tag{7}$$

Solving the above equation yields the following result:

$$\theta_1 = \pi, \tag{8}$$

$$\theta_2 = \arctan\left(\sqrt{\frac{1 + K_1 + K_2}{K_1K_2}}\right), \tag{9}$$

$$\theta_3 = \pi - \arctan\left(\sqrt{\frac{1 + K_1 + K_2}{K_1K_2}}\right). \tag{10}$$

B. Tri-band bandpass filter design

Building upon the previous analysis of traditional stub bandpass filters and TSSIRs and drawing parallels to the design methodologies of conventional edge-coupled bandpass filters, the developed tri-band bandpass filter has been designed herein, as illustrated in Fig. 6. In order to minimize the impedance mismatch between the intermediate transmission line and the 50-ohm input/output, the characteristic impedance (Z_T) of this transmission line between the two resonators was also selected to be 50 ohms.

In this design, the proposed tri-band bandpass filter prototype is designed on a Rogers 4003C substrate (ε_r =3.55, tanδ=0.0027) with a thickness of 0.813 mm. The center frequencies of the three passbands are 1 GHz, 3.5 GHz, and 6 GHz. Referring to the above theoretical analysis described in section II, the impedance ratios can be found to be K_1 =0.75 and K_2 =0.66. The width of the middle section of the proposed $\lambda_g/4$ TSSIR is selected as 2 mm, which corresponds to a characteristic impedance of 46 Ω. The characteristic impedances of the other two sections are calculated to be Z_1 =70 Ω and Z_2 =35 Ω. Meanwhile, the electric length of each section at 1 GHz can be calculated as $\theta = \theta_{01} = \theta_{02} = \theta_{03} = 25.7°$. Layout of the developed tri-band bandpass filter based on $\lambda_g/4$ TSSIRs is given in Fig. 7. For demonstration, current distributions at center frequencies of three passbands are shown in Fig. 8.

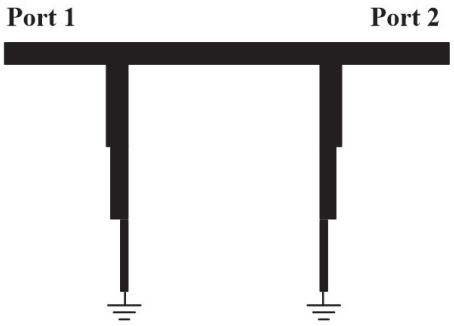

Fig. 6. Proposed tri-band bandpass filter based on $\lambda_g/4$ TSSIRs.

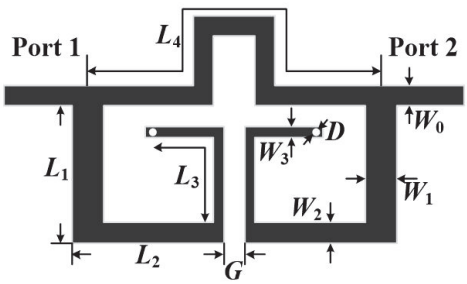

Fig. 7. Layout of the developed tri-band bandpass filter based on $\lambda_g/4$ TSSIRs.

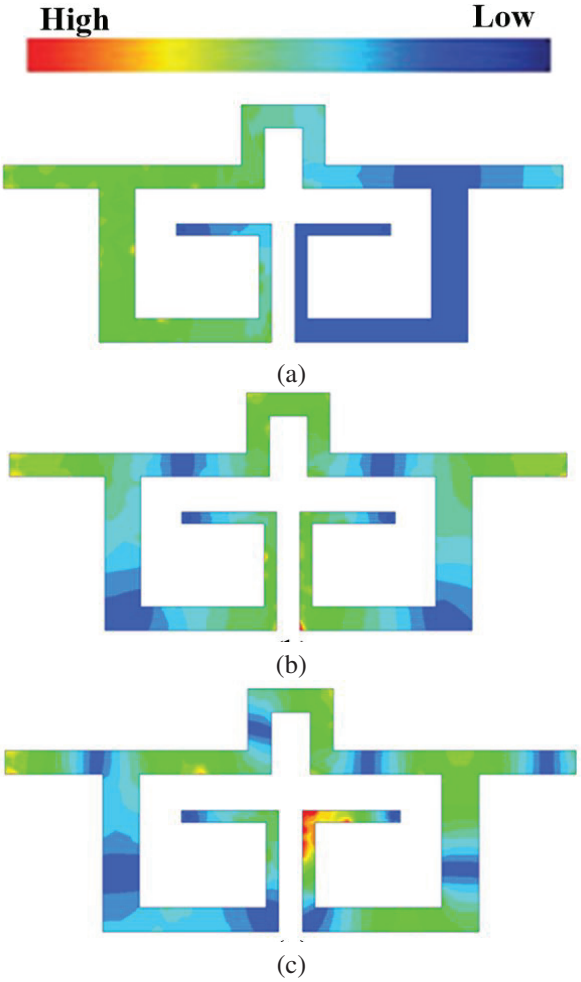

Fig. 8. Current distributions at center frequencies of three passbands: (a) first passband (1 GHz), (b) second passband (3.5 GHz), (c) third passband (6 GHz).

IV. RESULTS AND DISCUSSION

A photograph of the fabricated tri-band bandpass filter is depicted in Fig. 9, while the pertinent parameters of the tri-band filter are also provided. A comprehensive comparison between the simulated and measured results of the proposed tri-band bandpass filter is illustrated in Figs. 10 and 11. Additionally, the measured group delay of the filter is presented in Fig. 12. The filter exhibits three distinct passbands centered at 1 GHz, 3.5 GHz, and 6 GHz, respectively. Leveraging the aforementioned advantageous characteristics of the conventional filter structure, the measured minimum insertion losses of the three passbands are 0.07 dB, 0.52 dB, and 1.14 dB, respectively, inclusive of the losses attributed to the SMA connectors. Notably, the transmission zeros gener-

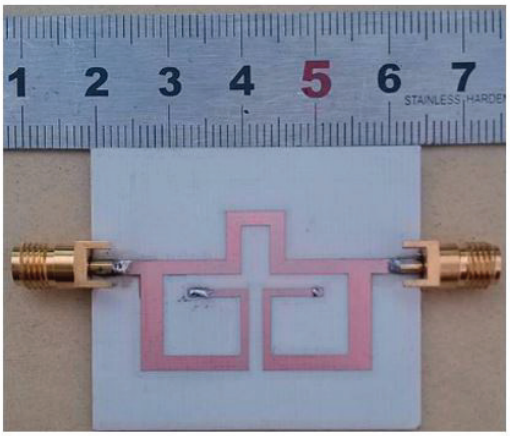

Fig. 9. Photograph of the proposed tri-band bandpass filter (W_0 =1.9 mm, W_1 =3.05 mm, W_2 =2 mm, W_3 =1 mm, L_1 =13 mm, L_2 =14.5 mm, L_3 =14 mm, L_4 =41.2 mm, D=0.6 mm, G=2 mm).

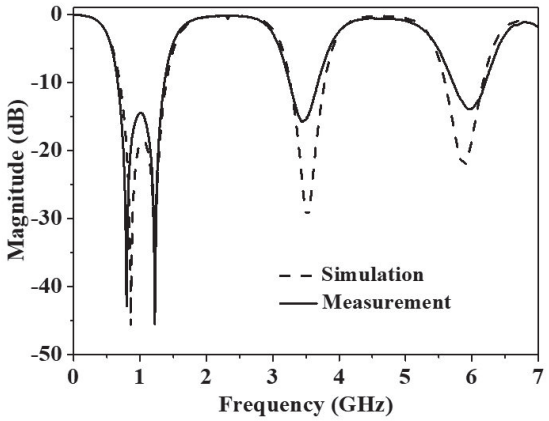

Fig. 10. Simulated and measured reflection coefficients of the developed tri-band bandpass filter.

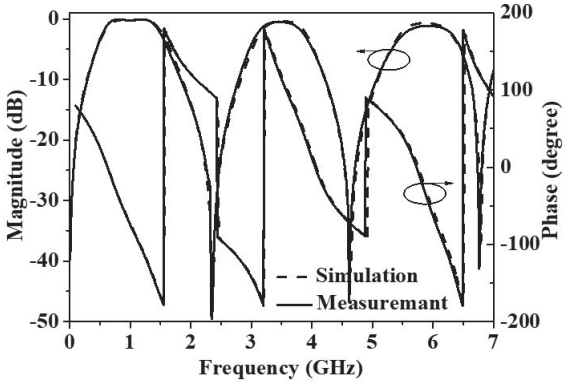

Fig. 11. Simulated and measured transmission coefficients and phase of the developed tri-band bandpass filter.

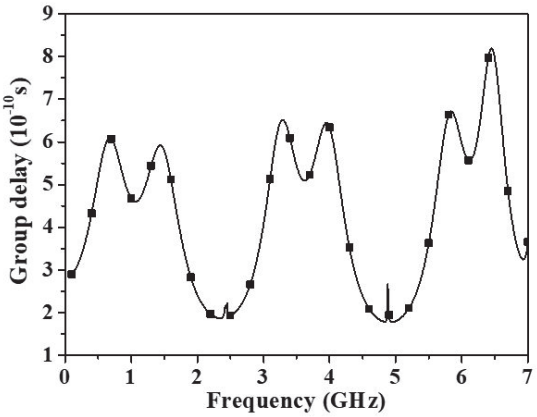

Fig. 12. Measured group delay versus frequency for each passband.

ated at 0 GHz, 2.35 GHz, 4.6 GHz, and 6.75 GHz have significantly enhanced the selectivity, passband symmetry, and band-to-band isolation of the proposed tri-band filter.

In order to comprehensively verify the accuracy of the transmission zero formulas that were derived in the previous section, a detailed comparison was conducted between the calculated values and those obtained through both simulation and experimental measurement. The results of this comparison are presented in Table 1. The calculated transmission zero locations exhibit a high degree of alignment with the measured results, effectively demonstrating the validity and reliability of the design methodology employed in this study.

For a bandpass filter, the passband symmetry can be quantified as follows. As shown in Fig. 13, the center frequency of the filter is f, the lower passband edge corresponding to the -10 dB level is f_L, and the upper passband edge corresponding to the -10 dB level is f_H. For an ideal bandpass filter, the symmetry condition can be

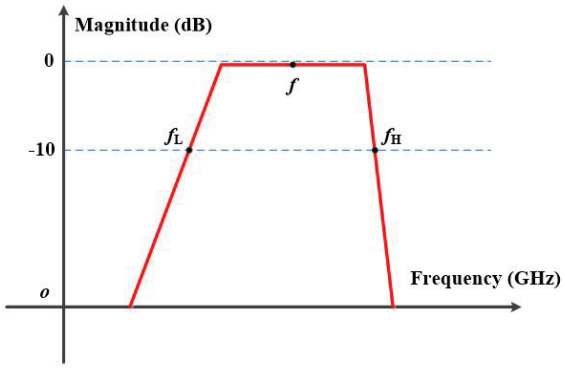

Fig. 13. Transmission coefficient of a bandpass filter.

Table 1: Calculated and measured locations of transmission zeros

	1	**2**	**3**	**4**
Calculated Results	0 GHz	2.32 GHz	4.69 GHz	7.0 GHz
Measured Results	0 GHz	2.55 GHz	4.45 GHz	6.75 GHz

Table 2: Comparison between proposed tri-band filter and prior works

Ref.	f_0 / f_1 / f_2 **GHz**	**Insertion Losses dB**	**Fabrication Process**	**Passband Symmetry Ratio**	**Size** $\lambda_g \times \lambda_g^*$
4	2.5 / 3.5 / 5.7	1 / 1.2 / 1.5	Microstrip line	1.6/1.06/1.18	0.26×0.2
5	1.84/2.45/2.98	0.9/1.6/0.8	Microstrip line	1.1/1/14/1.5	0.27×0.2
6	1.8/3.5/5.8	0.88/1.33/1.77	Microstrip line	1.1/1.04/1.52	0.52×0.11
7	1.57 / 2.45 / 3.5	0.77/1.51/1/8	Microstrip line	1.13/1.14/1.2	0.23×0.16
8	1.0 / 2.4 / 2.6	2.0 / 1.9 / 1.7	Microstrip line	1.7/1.07/1.06	0.2×0.2
9	1.64 / 3.04 / 4.8	1.54 / 1.71 / 2.4**	Microstrip line	1.14/1.18/1.75	0.24×0.2
10	3.16 / 4.27 / 5.70	1.6 / 2.5 / 2.9	Microstrip line	1.1/1.05/1.64	0.59×0.19
11	1.15 / 2.05 / 3.18	0.92 / 0.93 / 1.58	Microstrip line	1.74/1.13/1.3	NA
12	3.01 / 3.34 / 3.58	1.71 / 1.58 / 1.13	SIW	1.62/1.5/1.5	0.58×0.21
13	3.02 / 4.23 / 5.31	3.14 / 2.32 / 3.21	SIW	1.28/1.26/1/24	1.45×0.74
14	14.08 / 14.51 / 14.86	2.55 / 2.71 / 2.03	SIW	1.5/1.1/1.7	1.64×1.55
15	1.72 / 4.05 / 7.6	0.13 / 0.15 / 0.21	Microstrip line ***	1.3/1.27/1.67	0.19×0.11
16	1.56 / 4.21 / 5.79	0.18 / 0.19 / 0.18	Microstrip line ***	1.1./1/13/1.21	0.26×0.15
17	1.64 / 2.48 / 3.51	0.051 / 0.09 / 0.12	Microstrip line ***	1.3/1.15/1.28	0.19×0.16
This Work	1 / 3.5 / 6	0.07 / 0.52/ 1.14	Microstrip line	**1.19/1.07/1.03**	0.17×0.12

$*$ λ_g is the guided wavelength at the center frequency of the first passband (f_1).
$**$ Only simulated results have been given in this design.
$***$ These designs are based on HTS.

expressed as f_H-f=f-f_L, and passband symmetry ratio (r) which can be expressed as r=(f_H-f)/(f-f_L)=1. This metric provides a clear and quantitative measure of the passband symmetry.

However, for commonly used bandpass filters, it is challenging to achieve r=1. Except, the closer the value of r is to 1, the better the passband symmetry of the filter. Therefore, we define the passband symmetry ratio r as:

$$r = \frac{\max[(f_H - f), (f - f_L)]}{\min[(f_H - f), (f - f_L)]}. \tag{11}$$

Under this definition, the value of r is always greater than 1, which facilitates comparison.

For a more thorough evaluation, comparisons with prior works are presented in Table 1. As seen from Table 1, compared with conventional microstrip tri-band filters, the proposed design demonstrates significantly lower insertion loss while maintaining comparable circuit dimensions. Furthermore, when juxtaposed with tri-band filters based on SIW structures, the filter presented in this work exhibits certain advantages in both insertion loss and circuit size. Moreover, Table 1 also includes tri-band filters based on high-temperature superconducting (HTS) structures [15]–[17]. The aforementioned filters are similarly designed using edge-coupled structures. In terms of insertion loss, the first two passbands of the proposed tri-band filter in this work still exhibit comparable

performance with those of HTS-based filters. As shown in Table 1, for the three bandpass filters designed in this paper, the passband symmetry ratio for each passband is less than 1.2, indicating that the design exhibits good passband symmetry.

In summary, the developed filter offers several advantages. Firstly, it employs a $\lambda_g/4$ TSSIR resonator, which significantly reduces the overall dimensions of the filter compared to existing ones. Secondly, the adoption of a non-edge-coupled structure effectively avoids radiation losses caused by coupling slots, resulting in a low insertion loss, a crucial characteristic for microwave passive devices. Lastly, due to the inherent characteristics of the structure, the single passband of the filter exhibits good symmetry, which is closer to that of an ideal bandpass filter.

V. CONCLUSION

This paper introduces a microstrip line-based tri-band bandpass filter employing quarter-wavelength tri-section stepped impedance resonators (TSSIR). The design process of the proposed filter is characterized by its simplicity and effectiveness. By judiciously adjusting the impedance values of the TSSIR, three distinct passbands can be readily achieved, thus catering to the requirements of multi-band applications. The inherent generation of transmission zeros within the entire operating bandwidth significantly enhances the selectivity, passband symmetry, and band-to-band isolation of the proposed tri-band filter. The consistency between the simulated and measured results further validates the feasibility of the design. These attributes collectively render the filter highly suitable for modern compact tri-band communication systems.

ACKNOWLEDGMENT

The work was supported by Nantong Key Laboratory of Artificial Intelligence New Quality Technology, Jiangsu College of Engineering and Technology and Natural Science and Technology Project of Jiangsu College of Engineering and Technology (Grant JSGYZRJJZD-03).

REFERENCES

[1] D. L. Jin, T. T. Bu, J. S. Hong, J. F. Wang, and H. Xiong, "A tri-band antenna for wireless applications using slot-type SRR," *Applied Computational Electromagnetics Society (ACES) Journal*, vol. 29, no. 1, pp. 47-53, Sep. 2021.

[2] M. A. Rahman, S. S. Al-Bawri, S. S. Alharbi, W. M. Abdulkawi, N. M. Jizat, M. T. Islam, and A. A. Sheta, "3D highly isolated 6-port tri-band MIMO antenna system with 360° coverage for 5G IoT applications-based machine learning verification," *Scientific Reports*, vol. 15, no. 204, pp. 1-23, 2025.

[3] K. Yu, Y. Li, and W. Yu, "A compact triple band antenna for Bluetooth, WLAN and WIMAX applications," *Applied Computational Electromagnetics Society (ACES) Journal*, vol. 32, no. 5, pp. 424-429, July 2021.

[4] M.-H. Weng and H.-W. Wu, "A novel triple-band bandpass filter using multilayer-based substrates for WiMAX," *Proc. Eur. Microw. Conf.*, pp. 325-328, Oct. 2007.

[5] X.-Y. Zhang, Q. Xue, and B.-J. Hu, "Planar tri-band bandpass filter with compact size," *IEEE Microw. Wirel. Compon. Lett.*, vol. 20, no. 5, pp. 262-264, May 2010.

[6] S.-B. Zhang and L. Zhu, "Compact tri-band bandpass filter based on resonators with U-folded coupled-line," *IEEE Microw. Wirel. Compon. Lett.*, vol. 23, no. 5, pp. 258-260, May 2013.

[7] C.-I.-G. Hsu, C.-H. Lee, and, Y.-H. Hsieh, "Tri-band bandpass filter with sharp passband skirts designed using tri-section SIRs," *IEEE Microw. Wirel. Compon. Lett.*, vol. 18, no. 1, pp. 19-21, Jan. 2008.

[8] Q.-X. Chu and X.-M. Lin, "Advanced triple-band bandpass filter using tri-section SIR," *Electron. Lett.*, vol. 44, no. 4, pp. 295-296, Feb. 2008.

[9] A. George, P. Abdulla, and A. Iqubal, "Design and optimization of cost-effective, simple, and miniature tri-band bandpass filter for GSM, WLAN, and WIFI applications," in *2024 1st International Conference on Trends in Engineering Systems and Technologies (ICTEST)*, pp. 1-4, 2024.

[10] R. Wu, J. He, X. Tang, Z. Cai, L. Xiao, and F. Xiao, "Tri-band bandpass filter designed by a fast hybrid approach," *Microwave and Optical Technology Letters*, vol. 65, no. 7, pp. 1898-1903, July 2023.

[11] X. Wan, Z. Jin, Y. Wang, G. Xu, L. Zhang, Y. Xiong, and L. Wang, "Tri-/quad-/quint-band bandpass filters based on transversal embedded asymmetrical square-ring resonator," *IEEE Access*, vol. 12, pp. 92241-92252, 2024.

[12] D. Li, X. Chen, W. Luo, Z. Zheng, and Q. Chen, "Compact tri-band SIW bandpass filters with high selectivity and controllable center frequencies using perturbation structure," *IEEE Transactions on Circuits and Systems II: Express Briefs*, vol. 70, no. 11, pp. 4043-4048, Nov. 2023.

[13] L.-Y. Weng and W.-H. Tu, "Three-fourths-mode substrate-integrated waveguide for tri-band bandpass filter," *Microwave and Optical Technology Letters*, vol. 66, p. e34032, 2024.

[14] Y. Zhan, Y. Wu, E. Fourn, P. Besnier, and K. Ma, "Synthesis and implementation of multiband SIW bandpass filters based on in-line topology," *IEEE Transactions on Microwave Theory and*

Techniques, vol. 72, no. 11, pp. 6623-6636, Nov. 2024.

[15] J. Zhang, D. Zhou, D. Zhang, and Q. Liu, "Compact triple-band HTS filter with high selectivity using self-coupled stepped impedance resonator," *Electronics Letters*, vol. 56, no. 20, pp. 1067-1069, Sep. 2020.

[16] B. Ren, X. Liu, X. Guan, and Z. Ma, "High-selectivity high-temperature superconducting triband balanced bandpass filter using symmetric stub-loaded resonator," *IEEE Transactions on Applied Superconductivity*, vol. 33, no. 8, Nov. 2023.

[17] J. Zhang, Q. Liu, D. Zhang, D. Zhou, and X. Wang, "Tri-band superconducting filter based on crossed resonators with controllable coupling and feeding structures," *International Journal of RF and Microwave Computer-Aided Engineering*, vol. 31, p. e22516, 2021.

[18] Ansys HFSS, "R2, Help System, User's Guide," ANSYS, 2021.

Chuan Shao was born in Shandong Province, China in 1988. He obtained his Ph.D. from Nanjing University of Science and Technology in 2024. His research interests include microwave passive components. Shao is a reviewer for several international journals.

Compact Bandpass Filter for Ultra-wide Stopband Rejection

Pritha Narayanan[1,2] and Maheswari Shanmugam[2]

[1]Faculty of Information and Communication Engineering
Anna University, Chennai 600025, Tamil Nadu, India
prithabe28@gmail.com

[2]Department of Electronics and Communication Engineering
Panimalar Engineering College, Chennai 600123, Tamil Nadu, India
maheswarisp@yahoo.co.in

Abstract **–** The design objectives for a bandpass filter intended for modern wireless applications include achieving wide stopband attenuation and preserving signal strength within the passband. The proposed architecture aims to provide an effective solution for WLAN systems by minimizing insertion loss while sustaining other essential performance parameters. An asymmetric-short to the stepped impedance resonator (ASSIR) bandpass filter is presented. The second-order end coupled filter is initially designed, and transmission zeros and resonance frequencies are mathematically derived using ABCD parameters and odd and even mode calculations, respectively. A middle-short is introduced to the resonators to increase the depth of transmission zeros at the band edges. Further, an asymmetric-short to the resonators, along with stubs at the feed lines, is incorporated to realize an ultrawide stopband until 12.8 GHz and also to achieve compactness of $0.3\lambda g \times 0.18\lambda g$ without modifying the structure. The low-cost FR4 substrate $\varepsilon_r = 4.4$, simple end-coupled ASSIR bandpass filters is mathematically verified, simulated and measured at 2.45 GHz with an in-band low insertion loss of 1.4 dB.

Index Terms **–** Asymmetric-short, bandpass filter, middle-short, stepped impedance resonator.

I. INTRODUCTION

In today's widely congested electromagnetic spectrum, microwave bandpass filters (BPFs) are essential RF devices to perform signal selection and out-of-system interference mitigation simultaneously. Different architectures for size reduction, extended stopband, and high gain are necessary for upgrading the overall system performance.

The empirical formula for parallel coupled stepped impedance resonator design in [1] deals with the arbitrary coupling length of the resonator and quarter wavelength coupling to control spurious response and insertion loss. The analysis of fundamental characteristics of various wavelength stepped impedance resonators, such as equivalent circuit, spurious response, resonance conditions, and resonator length, is presented in [2] whose practical applications are reported. The bandpass filters with various coupling and odd and even mode impedance are presented in [3]. The relationship between transmission zeros and the position of feed lines is discussed in [4] for a microstrip filter.

The spurious modes of the stepped impedance resonator [5] are analyzed based on length and impedance ratios to extend the rejection in stop band. The resonators [6] are selected in such a way to get a fixed fundamental frequency but with different spurious frequencies in order to suppress spurious signals. A lowpass filter [7] with both end and parallel coupling is designed with slow wave effect to obtain both compactness and suppression of spurious signals. A meandered resonator loaded with a shorted stub is presented in [8] for compact size, wide stop band and better selectivity.

II. LITERATURE REVIEW

Coupled line filters in [9] and cross-structured resonators with coupled lines are reported in [10] for miniaturization in size, but trade-offs between key characteristics such as insertion loss and stopband rejection need to be considered for the filter design. Resonators in the shunt branch of elliptic filters in [11], pairs of coupled lines in [12], a pair of resonators with different resonance frequencies in [13], and a coupled line-stub cascaded structure in [14] are used for generating required transmission zeros to realize out-of-band suppression and deep roll-off skirts. A minimum degree of attenuation is achieved in the stopband.

The quasi-elliptic bandpass response obtained in [15], a filter with stepped impedance stubs [16], stepped impedance resonator-based coupled lines in [17], and various slots and open stubs used in substrate-integrated

Submitted On: January 30, 2025
Accepted On: June 28, 2025

https://doi.org/10.13052/2025.ACES.J.400706

waveguide (SIW) structure [18] improve frequency selectivity by placing transmission zeros near the passband while limiting attenuation over the wide stopband. Middle-shorted hairpin resonators in [19], short-circuited stub-embedded ring resonators in [20], inter-resonance in post-loaded SIW resonators described in [21] and adjustable transmission zeros achieved by modifying length of the apertures embedded in SIW [22] are employed to realize a wide stopband but use complex design topology. Substrate integrated waveguide-based filters using rectangular slots in two quarter-mode cavities [23] focus on suppressing the second mode and lowering the third mode's coupling to improve stopband rejection, but this results in minimum rejection.

In the proposed work, an end-coupled stepped impedance resonator-based bandpass filter is initiated to analyze transmission zeros and resonance frequencies. To the best of our knowledge, developing a filter with a wide stopband and compact size remains a challenging task. The end-coupled bandpass filter with asymmetric-short resonators with open stubs is proposed to offer lower insertion loss, harmonic suppression in the stopband, and compact size.

III. BASIC DESIGN: END-COUPLED UNIFORM IMPEDANCE RESONATOR

Generally, uniform impedance resonators (UIR) are folded to get compactness in the filter. Two folded resonators are connected electrically with end coupling, as shown in Fig. 1 (a). The relation between feed lines and transmission zeros, both symmetric and asymmetric feed line positions, is analyzed in [4] using an ABCD matrix.

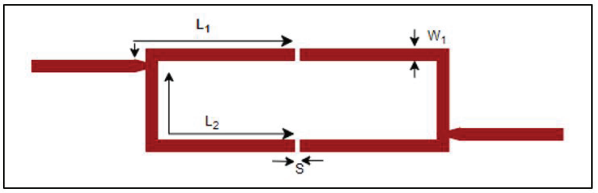

(a)

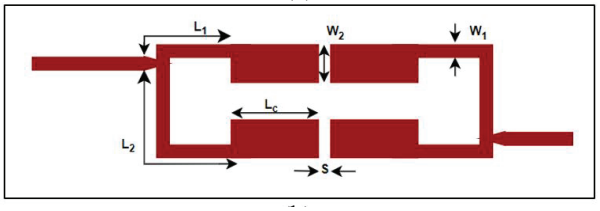

(b)

Fig. 1. (a) Layout of UIR BPF with end coupling. Dimensions are L_1=13.2 mm, L_2=19.4 mm, W_1=1.2 mm, S=0.3 mm and (b) Layout of SIR BPF with end coupling. Dimensions are L_1=4.2 mm, L_2=12.0 mm, L_c=4.8 mm, W_1=1.2 mm, W_2=3.7 mm, S=0.3 mm.

IV. ANALYSIS OF END-COUPLED STEPPED IMPEDANCE RESONATOR

The design consists of two half-wavelength stepped impedance resonators (SIR). One resonator is coupled to another resonator through a gap, forming an end-coupled structure. The gap between the resonators is modelled as a capacitor. Figure 1 (b) shows the stepped impedance resonator BPF with end coupling. Thus, the coupling at the ends of these two resonators evolves into a bandpass filter to achieve basic performance metrics. Adjustable feed line tapping is utilized to shape the passband of the filter.

A. Location of transmission zeros

From the position of the feed line, the frequencies of the transmission zeros are expressed mathematically. As described in [4], the connected shunt circuit is segmented into upper and lower sections. Each section of SIR is expressed in ABCD matrices, where θ_1 is the electrical length of high impedance line in the upper part, θ_2 the length of the high impedance line in the lower part, θ_c the length of low impedance line, and C is the end coupling modelled as capacitor.

The upper part of coupled structure is expressed as:

$$M_1 \times M_2 \times M_3 = \begin{bmatrix} cos\theta_1 & jz_1 sin\theta_1 \\ \frac{jsin\theta_1}{z_1} & cos\theta_1 \end{bmatrix} \begin{bmatrix} 1 & \frac{1}{j\omega C} - j2z_2 cot\theta_c \\ 0 & 1 \end{bmatrix} \begin{bmatrix} cos\theta_2 & jz_1 sin\theta_2 \\ \frac{jsin\theta_2}{z_1} & cos\theta_2 \end{bmatrix}. \quad (1)$$

The lower part of coupled structure is expressed as:

$$M_3 \times M_2 \times M_1 = \begin{bmatrix} cos\theta_2 & jz_1 sin\theta_2 \\ \frac{jsin\theta_2}{z_1} & cos\theta_2 \end{bmatrix} \begin{bmatrix} 1 & \frac{1}{j\omega C} - j2z_2 cot\theta_c \\ 0 & 1 \end{bmatrix} \begin{bmatrix} cos\theta_1 & jz_1 sin\theta_1 \\ \frac{jsin\theta_1}{z_1} & cos\theta_1 \end{bmatrix}. \quad (2)$$

The upper and lower sections of the ABCD parameters are converted to admittance parameters and added to get the total admittance parameters. From the total admittance parameters, S_{21} can be calculated as:

$$Z_1 (tan\theta_1 + tan\theta_2) tan\theta_c = 2Z_2 + \frac{tan\theta_c}{\omega C}. \quad (3)$$

As C is very small, the equation is reduced to:

$$Z_1 (tan\theta_1 + tan\theta_2) tan\theta_c = 2Z_2. \quad (4)$$

The equation is further simplified as:

$$tan\theta_1 tan\theta_c = \frac{Z_2}{Z_1}, \quad (5)$$

and:

$$tan\theta_2 tan\theta_c = \frac{Z_2}{Z_1}. \quad (6)$$

Therefore, the frequency of transmission zeros corresponding to feed positions is expressed in terms of

electrical length and impedance. By solving equations (1-6), the transmission zeros for the end coupling BPF are expressed. From the equation, the relation between transmission zeros and feed positions is calculated for the filter. The calculated transmission zeros are 1.94 GHz and 3.23 GHz, and the equations closely match the simulation results. As the half-wavelength resonator is folded, the position of the feed line determines the frequency of transmission zeros. Further, the analysis focused on the fact that the frequency of transmission zeros not only depends on the electrical length but also on the impedance ratio of the stepped impedance resonator.

B. Resonance conditions

The resonant frequency of a stepped impedance resonator is described using electrical length and impedance ratio, which act as deciding factors. Various combinations of impedance ratios are used in the design of the resonator to observe that it exerts control over shifting the odd and even modes to higher and lower frequencies, respectively. Also, a noticeable change in the impedance ratio makes the electrical length change in order to achieve compactness in the structure. The circuit is decomposed into odd and even mode circuits, which are shown in Figs. 2 (a) and (b).

The input admittance of the circuit is:

$$Y_{in} = Y_0 \frac{\left(Y_L + jY_0 tan\theta_{o/e}\right)}{\left(Y_0 + jY_L tan\theta_{o/e}\right)}. \tag{7}$$

The coupling between the SIRs is assumed to be infinite or large. The resonant frequencies of two modes are derived as follows.

The admittance at the short circuit is:

$$Y_L = -jY_1 \, cot\frac{\theta}{2}. \tag{8}$$

By substituting equation (8) into equation (7), the odd mode input admittance is derived as:

$$Y_{ino} = -jY_2 \frac{\left(Y_1 cot\frac{\theta}{2} - Y_2 tan\theta_o\right)}{\left(Y_2 + Y_1 tan\frac{\theta}{2} tan\theta_o\right)}. \tag{9}$$

By substituting Y_{ino}=0, the equation for the odd mode resonance becomes:

$$tan\frac{\theta}{2}.tan\theta_o - \frac{Y_1}{Y_2} = 0. \tag{10}$$

The odd mode resonance frequency is obtained from equation (10) for the total electrical length of $\theta = \theta_1 + \theta_2$ as pointed out in Fig. 2. Similarly, the admittance at the open circuit is:

$$Y_L = jY_1 \, tan\frac{\theta}{2}. \tag{11}$$

By substituting equation (11) into (7), the odd mode input admittance is:

$$Y_{ine} = jY_2 \frac{\left(Y_1 tan\frac{\theta}{2} + Y_2 tan\theta_e\right)}{\left(Y_2 - Y_1 tan\frac{\theta}{2} tan\theta_e\right)}. \tag{12}$$

By substituting Y_{ine}=0, the equation for the even mode resonance becomes:

$$cot\frac{\theta}{2}.tan\theta_e + \frac{Y_1}{Y_2} = 0. \tag{13}$$

The even-mode resonance frequency is obtained from equation (13) with $K = Y_1/Y_2$.

The fundamental mode and lowest spurious mode of the end-coupled stepped impedance resonator are observed using odd mode and even mode, respectively. Both transmission zeros and resonance equations depend directly on parameters related to impedance ratios and electrical length ratios. The fundamental mode frequency is 2.45 GHz, calculated from equation (10). The lowest spurious mode frequency is 5.13 GHz from equation (13) for $K = 0.55$ and $\theta_e/\theta_t = 0.280$. From the equations, the odd and even mode resonances are plotted between the normalized frequency and the electrical length ratio with

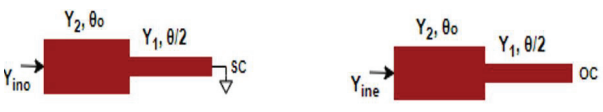

(a) (b)

Fig. 2. (a) Odd mode and (b) Even mode conditions.

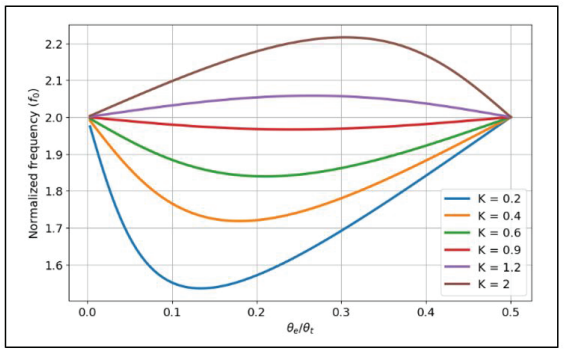

(a)

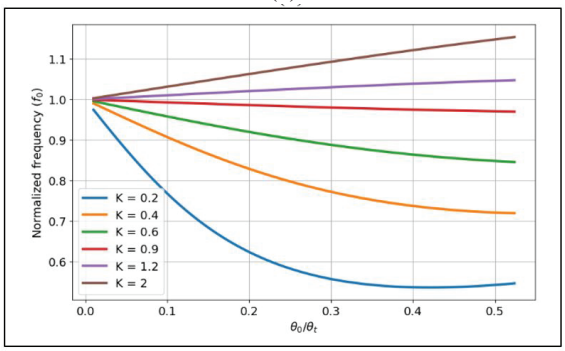

(b)

Fig. 3. (a) Calculated odd mode resonance with various K values and (b) Even mode resonance with various K values.

various values of K, as shown in Figs. 3 (a) and (b).

The fundamental and first spurious signals are shifted to lower frequencies, and the second and third spurious signals are shifted to higher frequencies, as shown in Fig. 4 (a), with K varying from 1 to 0.2. The fundamental and first spurious signals are shifted to higher frequencies, and the second and third spurious signals are shifted to lower frequencies, as shown in Fig. 4 (b), with K varying from 1 to 4. Both odd and even mode resonances are shifted and controlled by various K values. The resonance calculated by the theoretical equations matches well with the simulated odd and even mode resonances and their response to various K values. K = 1 is treated as a reference and hence highlighted in Figs. 4 (a) and (b).

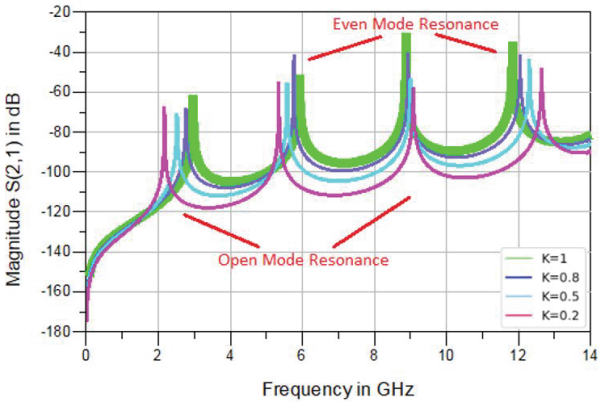

(a)

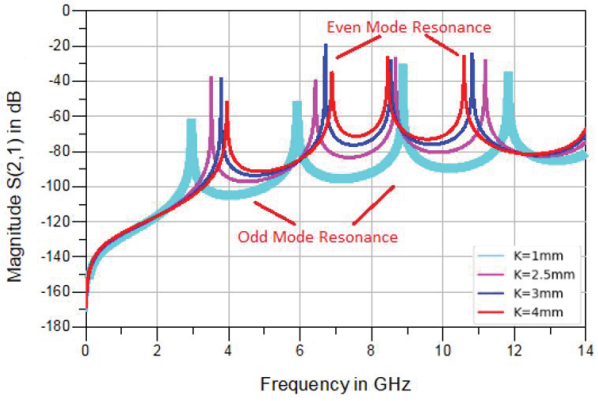

(b)

Fig. 4. (a) Simulated response of SIR for various K values from 1 to 0.2 and (b) various K values from 1 to 4.

The coupling coefficient (k) and external quality factor (Q_e) are calculated from equations (14) and (15):

$$k_{i,i+1} = \frac{FBW}{\sqrt{g_i g_{i+1}}} \text{ for i} = 1 \text{ to n} - 1, \quad (14)$$

$$Q_e = \frac{g_0 g_1}{FBW}. \quad (15)$$

The calculated coupling coefficient k between the resonators is 0.23, and the external quality factor Q_e of the filter is 5.06, as identified in the plots shown in Figs. 5 (a) and (b).

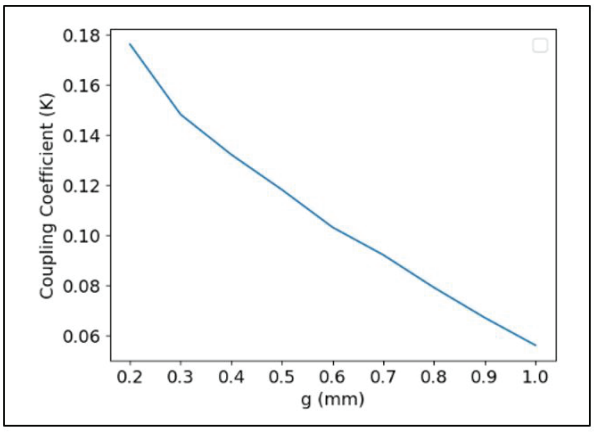

(a)

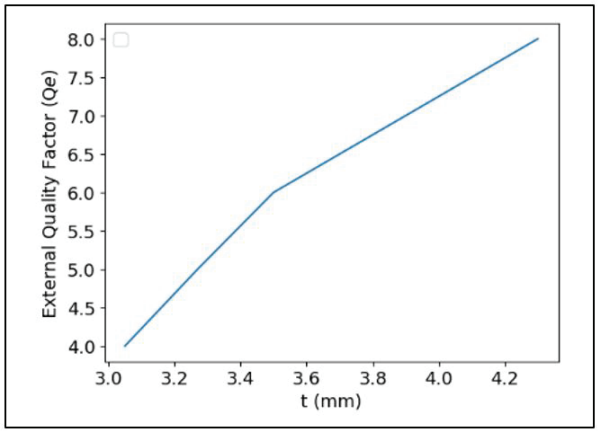

(b)

Fig. 5. (a) Coupling coefficient k versus gap between the resonators g and (b) External quality factor Q_e versus tapping position t.

V. PROPOSED DESIGN

A. Middle-short-stepped impedance resonator (MSSIR) bandpass filter

The performance of a stepped impedance bandpass filter with end coupling, such as in-band insertion loss and harmonic suppression, is improved by introducing a middle-short into the resonators.

In the end-coupled stepped impedance bandpass filter, the characteristics are redefined by introducing a middle-short, as shown in Fig. 6.

A middle-short half-wavelength resonator behaves like a quarter-wavelength resonator, which naturally rejects even harmonics. Therefore, a middle-short along with end coupling improves bandwidth with selectivity,

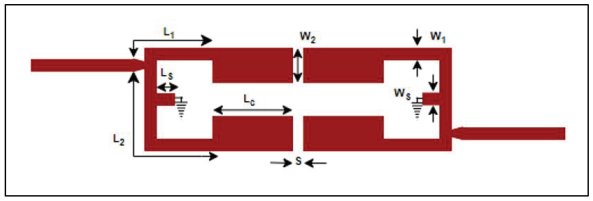

Fig. 6. Layout of end-coupled MSSIR BPF. Dimensions are L_1 = 4 mm, L_2=12.4 mm, L_c=4.2 mm, L_S=2.1 mm, W_1=W_S=1.2 mm, W_2=3.7 mm, S=0.3 mm.

reduces in-band insertion loss at the center frequency, and extends harmonic suppression with better attenuation in the stopband. The circuit is decomposed to odd and even mode circuits are shown in Figs. 7 (a) and (b).

Fig. 7. (a) Odd mode and (b) Even mode conditions.

The resonant frequencies of two modes are derived as follows. After introducing a middle-short, no change in the odd mode resonance; then the equation is:

$$tan\frac{\theta}{2}.tan\theta_o - \frac{Y_1}{Y_2} = 0. \tag{16}$$

For even mode resonance, the following conditions are used. The admittance at the short circuit is:

$$Y_{eS} = j\frac{Y_S}{2}\,cot\frac{\theta}{2}. \tag{17}$$

The intermediate input admittance between Y_1 and $Y_S/2$ is:

$$Y_{ei} = Y_1\frac{\left(Y_{eS} + jY_1 tan\frac{\theta}{2}\right)}{\left(Y_1 + jY_{eS}tan\frac{\theta}{2}\right)}. \tag{18}$$

The intermediate input admittance between Y_2 and Y_1 is:

$$Y_{ine} = Y_2\frac{\left(Y_{ei} + jY_2 tan\theta_e\right)}{\left(Y_2 + jY_{ei}tan\theta_e\right)}. \tag{19}$$

Solving equations (17-19), and substituting Y_{ine}=0, the equation for the even mode resonance becomes:

$$2Y_1^2 tan\frac{\theta}{2}.tan\theta_S + 2Y_1Y_2 tan\theta_S.tan\theta_e$$
$$+Y_2Y_S tan\frac{\theta}{2}.tan\theta_e = Y_1Y_S. \tag{20}$$

The even-mode resonance frequency is obtained from equation (20).

The calculated odd-mode resonance from equation (16) is 2.45 GHz, the same as the SIR BPF with end coupling. The calculated even mode resonance from equation (20) is 7.57 GHz, which justifies the quarter-wavelength resonator behavior due to the extended stub with a short at the middle of the resonators. The addition of middle-short resonators improves the filter's selectivity. This minimizes interference from neighboring transmissions and enables the exact filtering of specific frequencies. The design reduces undesired frequencies and provides an extended stopband, which helps to improve signal isolation. This increases the applicability of the filter and makes it more flexible in a variety of communication applications. The exceptional feature of the filter topology is that it produces strong out-of-band rejection without the need for extra components, which is one of its main advantages. This helps to make the overall design simpler, easier to implement, and more affordable.

B. Asymmetric-short-stepped impedance resonator bandpass filter

The characteristics of a stepped-impedance resonator are further improved by incorporating an asymmetric-short. A middle-short to the resonator improves the out-of-band rejection but fails to preserve the insertion loss at the center frequency and also bandwidth. Good passband bandwidth along with low insertion loss can be preserved by shifting the short stub slightly from the center of the resonator, creating an asymmetric-short to the resonator as shown in Fig. 8. By adjusting the position of the short stub from the center of the resonator, an unintentional slight shift in harmonics to higher frequencies is obtained.

Two stubs are introduced at the feed lines to improve stopband rejection in combination with an asymmetric-short resonator. The equations for the length of the stubs are given in [4], determined from equations (15) and (16). The selected lengths are used to obtain transmission zeros at 7.52 GHz and 9.41 GHz:

$$f_{Stub1} = \frac{c}{4L_3\sqrt{\varepsilon_{eff}}}, \tag{15}$$

$$f_{Stub2} = \frac{c}{4L_4\sqrt{\varepsilon_{eff}}}. \tag{16}$$

The fabricated design of an asymmetric-short to the stepped impedance resonator (ASSIR) BPF is shown in Fig. 9 with stubs, L_3 = 5.1 mm and L_4 = 4 mm.

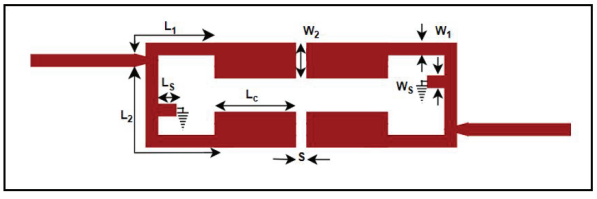

Fig. 8. Layout of end-coupled ASSIR BPF. Same as dimensions used in MSSIR BPF.

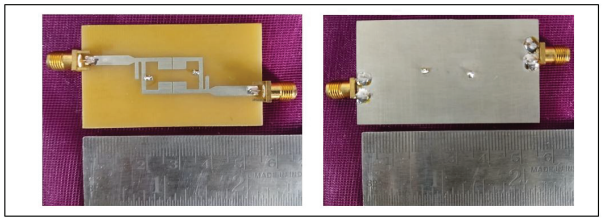

Fig. 9. Fabricated design of ASSIR BPF.

VI. RESULTS AND DISCUSSION

The simulated results are obtained using the Advanced Design System Momentum and measured using E5062A network analyzer. The substrate used was FR4 with $\varepsilon_r = 4.4$ and $h = 1.6$ mm. The response of the uniform impedance BPF with end coupling is shown in Fig. 10. The filter attains S_{21} of 0.56 dB, S_{11} of 46 dB, and a physical size of $0.43\lambda g \times 0.19\lambda g$. The center frequency is fixed at 2.45 GHz, thereby achieving a fractional bandwidth of 8.3%, a roll-off rate of 29%, and transmission zeros at 2.06 GHz and 2.78 GHz.

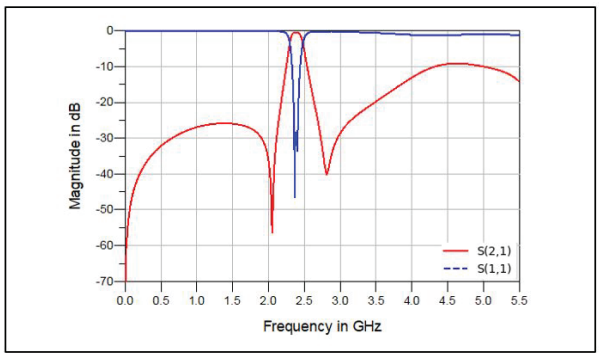

Fig. 10. Response of end-coupled UIR BPF.

The calculated and measured response of the stepped impedance resonators with an end-coupled BPF is shown in Fig. 11. From the simulation, the transmission zeros of 2.0 GHz and 3.2 GHz match well with the calculated transmission zeros of 1.94 GHz and 3.23 GHz. Also, both odd and even mode resonances of 2.47 GHz and 5.08 GHz from the simulation are very close to the mathematical results of 2.45 GHz and 5.13 GHz. The physical size of the end-coupling bandpass filter is $0.32\lambda_g \times 0.22\lambda_g$ and a roll-off rate of 41% is noted. First, second, third and fourth spurious signal appear at 5.13 GHz, 7.62 GHz, 9.69 GHz and 12.06 GHz, respectively.

Analysis of the stepped impedance resonator BPF with end coupling is as follows. For fixed length L_1 of 3 mm, the lengths L_c and L_2 are 4.2 mm and 11 mm, respectively, producing a bandwidth of 0.5 GHz and two transmission zeros at 2.2 GHz and 3.67 GHz. The change

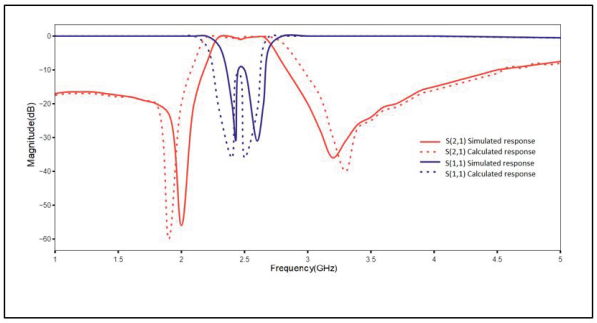

Fig. 11. Calculated and simulated response of end-coupled SIR BPF.

in lengths of L_1 and L_2, with a fixed L_c, causes a shift in the transmission zeros to 2.0 GHz and 3.17 GHz. The simulated S_{21} is 0.71 dB, as observed in Fig. 12. When the feed line is placed at the center of the half-wavelength line with 180° tapping, no band is found at f_0.

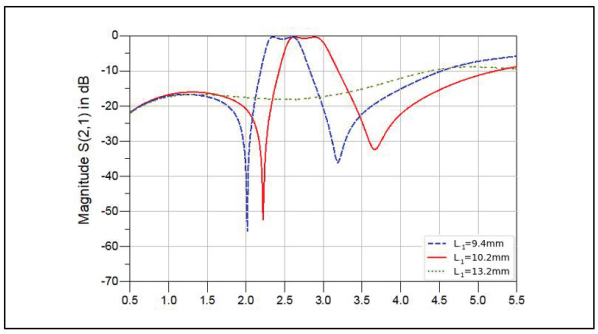

Fig. 12. Comparison of end-coupled SIR BPF with various lengths L.

When the coupling width W_2 decreases from 3.7 mm to 2.7 mm, a slight shift in center frequency to higher frequencies and a corresponding shift in the transmission zeros are shown in Fig. 13. The change in odd mode (center frequency) and even mode frequencies to higher frequency are also observed. As the coupling gap increases from 0.3 mm to 0.8 mm, the lower and upper transmission zeros move very close to each other. Thus, the bandwidth becomes sharper, focusing the center frequency within the required passband, as noted in Fig. 14.

The response of middle-short BPF with end coupling is shown in Fig. 15. The redefined structure improves characteristics such as S_{21} of 0.36 dB, a size of $0.316\lambda_g \times 0.186\lambda_g$, and a reasonable roll-off rate of 45 dB/GHz.

As the middle-short resonator behaves like a quarter-wavelength resonator, the first- and second-order spurious signals are shifted to 7.62 GHz and 12.06 GHz, respectively, and therefore the stopband rejection

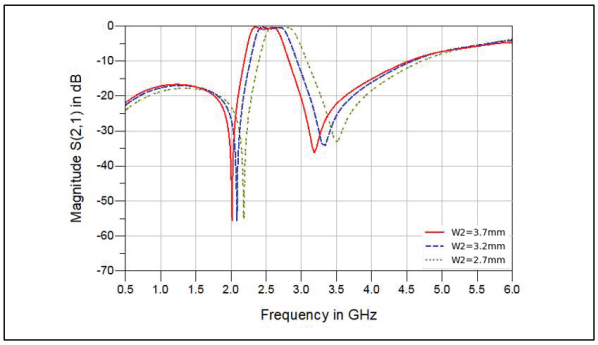

Fig. 13. Comparison of end-coupled SIR BPF with various coupling widths W2.

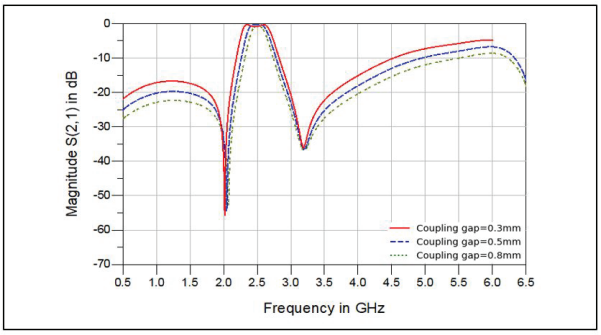

Fig. 14. Comparison of end-coupled SIR BPF with various coupling gaps S.

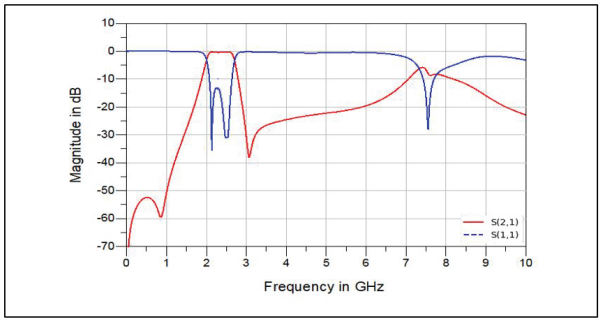

Fig. 15. Response of end-coupled MSSIR BPF.

is improved. By adjusting the structure, the required harmonic suppression up to 6 GHz with 20 dB of attenuation and a fractional bandwidth of 29% is achieved.

However, the introduction of open stubs at the feedlines couples with the folded half-wavelength middle-short-stepped impedance resonator, disrupting the passband bandwidth and reducing insertion loss at the center frequency. Shifting the short stub away from the resonator's center reduces coupling and therefore effectively preserves the passband bandwidth and enhances insertion loss at the center frequency. Additionally, a very slight unintentional shift in harmonics toward higher frequency is obtained. Thus, various positions (P) of the short stub of the stepped impedance resonator are analyzed without open stubs at the feedlines to understand the behavior of the asymmetric-short resonator-based filter. Improvements in passband bandwidth, insertion loss and unintentional shifts in harmonics are shown in Figs. 16 and 17. As the optimal positioning of the short stub to the resonator is fixed (as shown in Fig. 8), the introduction of open stubs at the feedlines delivers wide stopband attenuation as expected.

The simulated and measured responses of the proposed ASSIR filter with open stubs at the feedlines are shown in Fig. 18. The signal strength in the operating bandwidth and the rejection level in the stopband are essential features in the evaluation of the filter. In the design, asymmetric-short to the resonator with open stubs changes the coupling, which in turn impacts both the resonance condition and the impedance matching at one of the pole frequencies. Therefore, the asymmetric-short resonator-based bandpass filter offers a single reflection pole at the operating frequency of 2.45 GHz. The measured stopband rejection up to 12.8 GHz with 20 dB of attenuation matches the simulated stopband rejection up to 12.8 GHz with 20 dB of attenuation. The S_{11} of 22.15 dB and the fractional bandwidth of 20.4% also match the simulated S_{11} of 38.15 dB and

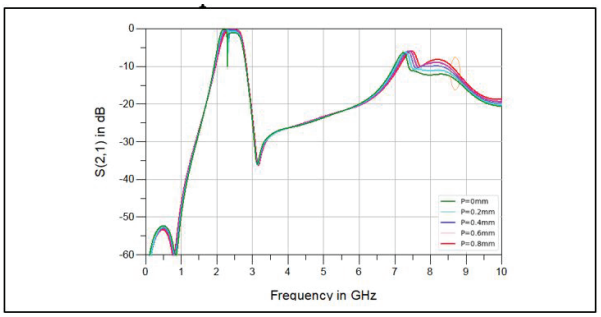

Fig. 16. S_{21} response of MSSIR BPF with short stub position shifted from the center.

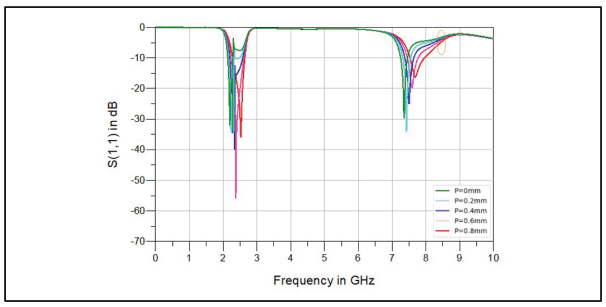

Fig. 17. S_{11} response of MSSIR BPF with short stub position shifted from the center.

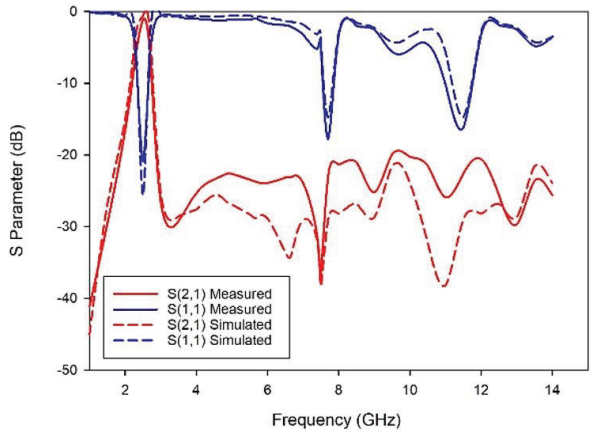

Fig. 18. Simulated and measured response of the proposed ASSIR bandpass filter.

Table 1: Comparison of simulated response of resonators-based filter

Filter Design	FBW(%)	S_{21} (dB)	HS*	Size ($\lambda_g \times \lambda_g$)
UIR	8.3	0.56	3.5 GHz	0.43×0.19
SIR	20.8	0.71	3.7 GHz	0.32×0.22
MSSIR	29	0.36	6 GHz	0.3×0.18
ASSIR	21.9	0.35	12.8 GHz	0.3×0.18

*HS Harmonic suppression with 20 dB attenuation up to the mentioned frequency

the fractional bandwidth of 21.9%. The response shows that both the simulated and measured results satisfy these features and also match closely.

Comparison of simulated design parameters, such as the uniform impedance resonator, stepped impedance resonator, middle-short-stepped impedance resonator and asymmetric-short-stepped impedance resonator with open stubs are recorded in Table 1.

Key parameters such as fractional bandwidth (in percentage), S_{21} (in dB), harmonic suppression with its attenuation level and size in guided wavelength are listed. A fractional bandwidth improvement of more than 63.45% and a miniaturization improvement of 34% are achieved compared to a UIR BPF. The insertion loss (simulated response) shows an improvement of 41% and the harmonic suppression improves by 72.7% when compared with the UIR BPF.

Table 2 compares the parameters of the proposed filter with those of existing filters from various studies. The comparison highlights the efficiency of the proposed filter by considering fractional bandwidth (%), S_{21} (dB), S_{11} (dB), upper stopband rejection, and circuit size in guided wavelength. The insertion loss (S_{21}) is reduced to as low as 1.4 dB, and harmonic suppression with an attenuation of 20 dB is extended from 2.8 GHz to 12.8 GHz, achieving a stopband rejection of 4.85 f_0. S_{11} reaches as high as 22.15 dB, and a better fractional bandwidth of 20.4% is achieved. The center frequency is fixed at 2.45 GHz, and the circuit area is reduced to $0.3\lambda_g \times 0.18\lambda_g$. Therefore, the complete design of ASSIR bandpass filter with stubs offers low insertion loss, compact size, and good harmonic suppression with better attenuation. The simple architecture makes the design attractive and affordable. Performance can be further enhanced by minimizing insertion loss by employing superior substrate materials.

Table 2: Comparison of measured responses with other proposed filters

Ref.	f_0 (GHz)	FBW (%)	S_{21} (dB)	S_{11} (dB)	Upper Stopband Rejection (dB)	Size ($\lambda_g \times \lambda_g$)
[9]	2.4	12.1	1.2	15	-	$0.037\lambda_g^2$
[10]	2.9	24	0.7	12	15 (1.89f_0)	0.2×0.2
[11]	2.45	10	>0.79	22.7	-	0.92×0.345
[12]	2.1	19	<1.8	12	18 (3f_0)	0.39×0.28
[13]	1.72	16.3	0.7	-	-	0.05×0.07
[14]	2.1	39	0.8	20.6	29.5 (2.3f_0)	0.39×0.36
[15]	2.5	36	0.6	15	42 (2.44f_0)	0.21×0.18
[16]	3.24	58.3	0.6	14.2	-	0.34×0.34
[17]	3	60	0.8	13	40 (2.36f_0)	0.67×0.17
[18]	12.5	47	1.1	10	34	1.96×1.12
[19]	5.4	11.4	1.2	20	30 (3f_0)	0.5×0.35
[20]	3.4	4.06	1.2	-	30 (3f_0)	0.42×0.157
[21]	5	6.6	0.9	-	30 (4.2f_0)	-
[23]	2.1	17.1	0.93	15	20 (3.19f_0)	$0.05\lambda_g^2$
This Work	2.45	20.4	1.4	22.15	20 (4.56f_0)	0.3×0.18

VII. CONCLUSION

A bandpass filter is presented using a novel asymmetric-short applied to the stepped impedance resonator. Transmission zeros and resonance frequency of the bandpass filter with end coupling are analyzed mathematically and verified by simulation as an initial step. Further, bandpass filters with symmetric-short and asymmetric-short configurations applied to the stepped impedance resonator are developed and validated. The added open stubs at the feedlines of the filter extend the stopband to a greater extent. Thus, the filter has the potential to be used in a number of applications where out-of-band rejection in the stopband, excellent signal strength in the passband, compact size, and affordability are essential requirements.

REFERENCES

[1] M. Makimoto and S. Yamashita, "Bandpass filters using parallel coupled stripline stepped impedance resonators," *IEEE Transactions on Microwave Theory and Techniques*, vol. MIT-28, no. 12, pp. 1413-1417, Dec. 1980.

[2] M. Sagawa, M. Makimoto, and S. Yamashita, "Geometrical structures and fundamental characteristics of microwave stepped-impedance resonators," *IEEE Transactions on Microwave Theory and Techniques*, vol. 45, no. 7, pp. 1078-1085, July 1997.

[3] J. S. Hong and M. J. Lancaster, *Microstrip Filters for RF/Microwave Applications*. New York: Wiley, 2001.

[4] L.-H. Hsieh and K. Chang, "Tunable microstrip bandpass filters with two transmission zeros," *IEEE Transactions on Microwave Theory and Techniques*, vol. 51, no. 2, pp. 520-525, Feb. 2003.

[5] J.-T. Kuo and E. Shih, "Microstrip stepped impedance resonator bandpass filter with an extended optimal rejection bandwidth," *IEEE Transactions on Microwave Theory and Techniques*, vol. 51, no. 5, pp. 1554-1559, May 2003.

[6] C.-F. Chen, T.-Y. Huang, and R.-B. Wu, "Design of microstrip bandpass filters with multiorder spurious-mode suppression," *IEEE Transactions on Microwave Theory and Techniques*, vol. 53, no. 12, pp. 3788-3793, Dec. 2005.

[7] J.-X. Chen and Q. Xue, "Compact microstrip lowpass filter with suppression of spurious response," *IEE Proceedings-Microwave Antennas Propagation*, vol. 153, no. 5, pp. 432-434, Oct. 2006.

[8] C.-X. Sun, L.-Y. Feng, X.-Y. Liu, and H.-X. Zheng, "Compact dual-mode filter using meander shorted stub loaded resonators," *Progress in Electromagnetics Research Letters*, vol. 30, pp. 195-203, 2012.

[9] B. Afzali, H. Abbasi, F. Shama, and R. Dehdasht-Heydari, "A microstrip bandpass filter with deep rejection and low insertion loss for application at 2.4 GHz useful wireless frequency," *International Journal of Electronics and Communications (AEU),* vol. 138, p. 153811, 2021.

[10] D.-S. La, X. Guan, M.-Y. Wang, and R.-Q. Mi, "Compact wideband bandpass filter based on coupled line stub with high selectivity," *International Journal of Electronics and Communications (AEU),* vol. 138, p. 153872, 2021.

[11] S. Chen, L.-F. Shi, G.-X. Liu, and J.-H. Xun, "An alternate circuit for narrow-bandpass elliptic microstrip filter design," *IEEE Microwave and Wireless Components Letters*, vol. 27, no. 7, pp. 624-626, July 2017.

[12] K. D. Xu, F. Zhang, Y. Liu, and Q. H. Liu, "Bandpass filter using three pairs of coupled lines with multiple transmission zeros," *IEEE Microwave and Wireless Components Letters*, vol. 28, no. 7, pp. 576-578, July 2018.

[13] Q. Xue and J. Y. Jin, "Bandpass filters designed by transmission zero resonator pairs with proximity coupling," *IEEE Transactions on Microwave Theory and Techniques*, vol. 65, no. 11, pp. 4103-4110, Nov. 2017.

[14] S. Lu, K.-D. Xu, Y. Guo, Y. Ren, and Q. Chen, "Bandpass filter using coupled line-stub cascaded structure with high stopband rejection," *Microwave Optical Technology Letter*, pp. 1-6, Feb. 2020.

[15] J. Xu, F. Xiao, Y. Cao, Y. Zhang, and X. Tang, "Compact microstrip filter with third-order quasi-elliptic bandpass response," *IEEE Access*, vol. 6, pp. 63375-63381, Nov. 2018.

[16] Q. Yang, M. Shu, C. Guo, J. Li, and A. Zhang, "High selectivity wideband bandpass filter based on stepped impedance open stubs loaded ring resonator," *International Journal of Electronics and Communications (AEU),* vol. 126, p. 153408, 2020.

[17] P. Vryonides, S. Arain, A. Quddious, D. Psychogiou, and S. Nikolaou. "A new class of high-selectivity bandpass filters with constant bandwidth and 5:1 bandwidth tuning ratio," *IEEE Access*, vol. 12, pp. 16489-16497, Feb. 2024.

[18] T. Khorand and M. S. Bayati, "Novel half-mode substrate integrated waveguide bandpass filters using semi-hexagonal resonators," *International Journal of Electronics and Communications (AEU),* vol. 95, pp. 52-58, 2018.

[19] S. Ramkumar and R. B. Rani, "Compact high-selective wide-stopband coupled bandpass filter using middle-shorted hairpin-resonators,"

International Journal of Electronics and Communications (AEU), vol. 162, p. 154580, 2023.

[20] B. Ren, C. Le, X. Guan, and Z. Ma, "Short-circuited stub-embedded ring resonator and its application in diplexer," *IEEE Access*, vol. 7, pp. 179266-179272, 2019.

[21] B. Lee, S. Nam, S.-W. Jeong, and J. Lee, "Post-loaded substrate-integrated waveguide bandpass filter with wide upper stopband and reduced electric field intensity," *IEEE Microwave and Wireless Components Letters*, vol. 30, no. 4, pp. 371-374, Apr. 2020.

[22] Z. L. Su, B. W. Xu, S. Y. Zheng, H. W. Liu, and Y. L. Long, "High-isolation and wide-stopband SIW diplexer using mixed electric and magnetic coupling," *IEEE Transactions On Circuits and Systems—II: Express Briefs*, vol. 67, no. 1, pp. 32-36, Jan. 2020.

[23] A. Iqbal, J. J. Tiang, S. K. Wong, S. W. Wong, and N. K. Mallat, "QMSIW-based single and triple band bandpass filters," *IEEE Transactions on Circuits and Systems—II: Express Briefs*, vol. 68, no. 7, pp. 2443-2447, July 2021.

Pritha Narayanan received the M.E. degree in Applied Electronics from Sathyabama Institute of Science and Technology, Chennai, India, in 2013. She received the B.E. degree in ECE from Adhiparasakthi College of Engineering, Anna University. She is working as an Assistant Professor in the Department of Electronics and Communication Engineering at Panimalar Engineering College, specializing in RF and microwave engineering. Her research focuses on developing novel bandpass filter design for microwave and mm wave applications. She has published over 15 peer-reviewed articles in the field of ECE.

Maheswari Shanmugam received the Ph.D. degree in Microwave Engineering and M.E. degree in Applied Electronics from Sathyabama Institute of Science and Technology, Chennai, India, in 2016 and 2009, respectively. She received the B.E. degree in ECE from the University of Madras. Her area of research includes microwave and millimeter wave circuits. She has more than two decades of teaching experience. Currently she is working as a Professor in Panimalar Engineering College, Chennai. She is a recognized supervisor for doing research in Anna University. She has published more than 30 papers in Web of science, Scopus indexed journals and IEEE conferences. She is a Fellow of IETE.

Analysis of an Oil-Spray Cooling System for an Induction Switched Reluctance Machine Using Computational Fluid Dynamics

Narges Ghandi, Hadi Saghafi*, and Mohammadali Abbasian

Department of Electrical Engineering
Institute of Artificial Intelligence and Social and
Advanced Technologies, Isf.C., Islamic Azad University, Isfahan, Iran
narges.ghandi@iau.ac.ir, h.saghafi@iau.ac.ir, m.a.abbasian@iau.ac.ir
*Corresponding Author

Abstract – The growing interest in electric vehicles has spurred the development of high-performance electric machines. The effective cooling of windings in electric machines is essential as they are the primary site of energy loss. Oil-spray cooling systems have gained popularity due to their ability to reduce temperatures and protect winding insulation. This paper proposes a Computational Fluid Dynamics (CFD) model for the Spray-Cooling Induction Switched Reluctance Machine (ISRM) to enhance the thermal management of electric machines using Ansys Fluent software. The proposed machine demonstrates efficient heat dissipation during transient simulation tests. Oil is applied to both the stator and the rotor during a transient two-phase simulation, enabling effective thermal exchange despite uneven temperature distributions across the components. We first modeled the machine using the finite element method and extracted the losses from ANSYS. This analysis focuses on the energy losses related to the selective oil spray at the end of the rotor. By performing a detailed thermal analysis, we found that increasing the flow rate enhances the Nusselt number, improves heat transfer, and increases the machine losses.

Index Terms – Electric vehicle, Induction Switched Reluctance Machine (ISRM), oil-spray cooling, two-phase thermal management systems.

I. INTRODUCTION

Permanent Magnet Synchronous Motors (PMSMs) and Switched Reluctance Motors (SRMs) are high torque density motors. PMSMs are recognized for their high torque density. In contrast, SRMs are valued for their simple structure, high efficiency, reliability, cost-effectiveness, high fault tolerance, excellent thermal abilities, and suitable torque-speed characteristics [1].

This study builds upon recent advancements in SRM technology, addressing limitations in existing designs. While significant progress has been made in noise reduction techniques using Torque Sharing Function (TSF)-based control [2] and sophisticated modeling approaches [3], there remains a need for robust design optimization methods considering realistic driving cycles. Early work focused on enhancing SRM performance by introducing designs like the Double Stator SRM (DSSRM) in 2010 [4], aimed at mitigating torque ripple and acoustic noise often associated with conventional SRMs. However, the DSSRM design might still face challenges in high-power applications.

Recently, the Induction Switched Reluctance Machine (ISRM) has emerged as a promising alternative, particularly well-suited for demanding industrial and transportation applications [5]. The ISRM utilizes a non-segmented design, with coils placed on both the stator and rotor cores. This configuration, although it introduces rotor copper losses, offers superior efficiency compared to conventional SRMs [6]. The unique design of the ISRM allows for various stator/rotor pole combinations and provides flexibility in optimizing machine performance for specific applications.

The 12/10 ISRM configuration for electric powertrains represents an approach in the Electric Vehicles (EVs) powertrains field [7]. This machine combines the SRM with rotor inductive conductors to improve EV powertrain performance. The rotor conductors act as a magnetic shield, enhancing efficiency by creating short magnetic flux paths. Mohammadi et al. [8] examined an oil-cooled, three-phase ISRM with six stator poles and four rotor poles. A two-dimensional finite element model was used to analyze the machine's magnetic properties, flux path, torque, and efficiency, followed by an analysis of thermal performance with ANSYS Motor-CAD [8].

However, these rotor conductors also lead to significant copper loss and heat generation. While direct liquid cooling systems, like oil-spray cooling used in the Toyota Prius, can cool the internal parts of the machine, designing an ISRM with reduced rotor copper loss can

Submitted On: May 18, 2025
Accepted On: July 7, 2025

https://doi.org/10.13052/2025.ACES.J.400707

eliminate the need for cooling systems and enhance the machine's efficiency. Consequently, it is essential to perform a detailed thermal analysis and optimize the design of the spray cooling system. This subject has not been considered in the literature until now, and it is the main innovation of this paper.

Oil cooling is increasingly recognized as an effective method for thermal management in electric machines, but several aspects require further investigation. Compared to oil-jet cooling, spray cooling offers superior cooling efficiency and more uniform temperature distribution [9, 10]. Research in two-phase thermal management systems has focused on leveraging both liquid and vapor phases to enhance heat transfer. The average velocity of droplets in a spray is used to characterize their speed. Wang et al. [11] used an artificial neural network to analyze the Nusselt number in an EW (End Winding) spray cooling system, addressing uneven spray cooling and its impact on cooling efficiency.

Several studies have investigated specific aspects of oil cooling systems. Zhang et al. [12] details the development of a 3D Lumped Parameter Thermal Network (LPTN) for oil-spray-cooled EWs, while others have explored the effectiveness of spray evaporative cooling in electric motors [21, 22]. These studies often utilize electric traction motor stators with hairpin winding technology and specialized spray nozzles [13]. Depending on the specific application, some cooling systems are better suited for effective thermal management, and Computational Fluid Dynamics (CFD) modeling becomes an essential research tool for guiding and enhancing the design process. For example, Chiu et al. [14] carried out a CFD simulation of a 30 kW SRM to make a comparison between liquid and air-cooling systems.

In the scope of this study, a thermal model dedicated to spray-cooling ISRM has been formulated, evaluated, and adapted for a different ISRM configuration based on the CFD approach. The work begins by illustrating the structure of the ISRM, with a particular focus on the internal arrangement of components and the areas most prone to overheating, such as the stator and rotor. The proposed cooling system relies on the direct application of oil jets, designed to target the most thermally critical surfaces specifically. The three-dimensional model used for simulation is described in detail, including the geometry of the motor, the distribution and orientation of the nozzles, the oil flow rate, pressure, and the fluid's physical properties.

A spray-cooling three-phase ISRM with 12 stator poles and 10 rotor poles was analyzed, and a 2D finite element model was developed to determine its magnetic properties. In this paper, 24 two-phase spray nozzles were specifically designed, and thermal simulations were performed and utilized for cooling purposes. Six nozzles were allocated for the stator and six for the rotor, arranged radially at the front and rear of the ISRM. Radial rotor spray cooling seems to be the better solution, using Ansys Fluent software. Through simulations conducted under various operating scenarios, the study shows that oil-spray cooling can significantly reduce the internal temperatures of the motor. In particular, a substantial temperature drop is observed in areas with higher loss densities, contributing to more continuous operation and a reduced risk of material degradation. Initially, the 12/10 ISRM setup involving oil-spray cooling was employed to establish and confirm a correlation for the Nusselt number. This article, validated with the Nusselt number equation in [15], fully aligns with the findings of this research and reports similar results.

II. INDUCTION SWITCHED RELUCTANCE MACHINE

ISRM refers to an electric machine with a single stator and rotor, featuring several short-circuited coils mounted on the rotor. These coils are energized by additional coils located within the slots of the stator. The rotor's coils, which are not powered by any external source, have currents induced within them due to the machine's operation. The rotor's windings are arranged to create a short magnetic flux path encircling the coil in the stator that is being excited [7, 16]. This type of electric machine, which combines the advantages of reluctance and induction machines, has specific operating characteristics that make the study of its cooling system an original contribution, especially when compared to the existing literature, which is more focused on permanent magnet or conventional induction machines.

The electric machine uses spray cooling for the stator and rotor in this research. Twenty-four spray nozzles are utilized, with six nozzles dedicated to cooling the stator and another six for the rotor. These nozzles are strategically placed at radial positions on the front and rear sections of the ISRM. The research presented involves developing and simulating a thermal model specifically for the spray-cooled 12/10 ISRM. Empirical formulas, derived and simulated within the ISRM framework [15] are central to this effort.

The study validates the thermal model by comparing it with measurement results from electric motors featuring various cooling system designs, also discussed in [15]. Additionally, the formulated Nusselt number equation aligns with the ISRM parameters. The three-dimensional model used for simulation is described in detail, including the geometry of the motor, the distribution and orientation of the nozzles, the oil flow rate, pressure, and the fluid's physical properties. Two- and three-dimensional representation of the 12/10 ISRM is illustrated in Fig. 1, depicting the key structural features

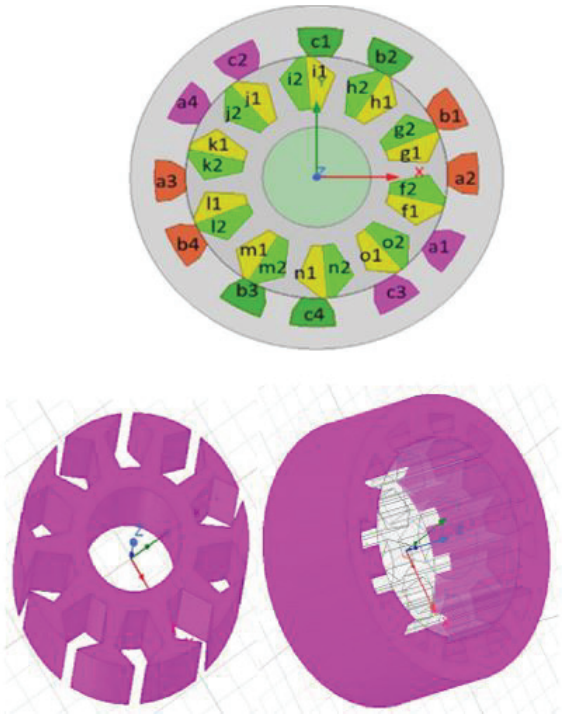

Fig. 1. Cross-section of a 12/10 ISRM 2D, 3D.

necessary for electromagnetic analysis. Visual representations, including a three-dimensional schematic of its stator and rotor and meshed with finite elements, are depicted in Fig. 2. Further details about the 12/10

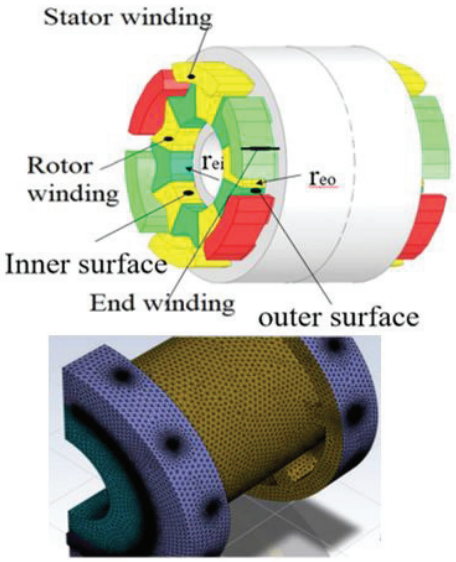

Fig. 2. Proposed prototype three-dimensional schematic of 12/10 ISRM simulated with ANSYS and meshed with finite elements.

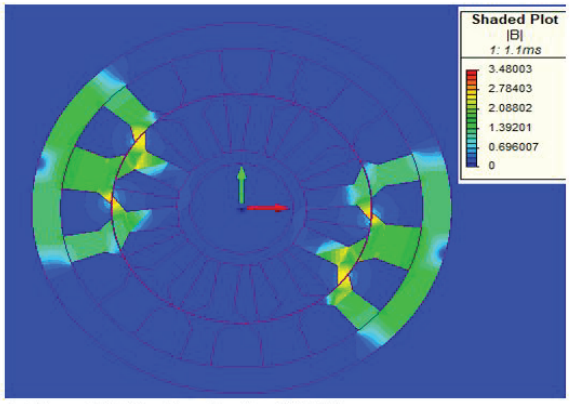

Fig. 3. Flux distribution in the ISRM.

ISRM's specifications can be found in Table 1. Figure 3 shows the magnetic flux distribution in the ISRM, while Fig. 4 illustrates the current density in the ISRM.

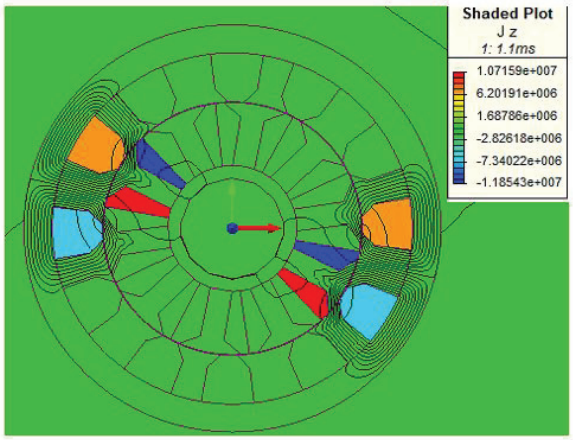

Fig. 4. Current density in the ISRM.

III. SPRAY COOLING SYSTEM

The nozzles are placed in a specific radial position from the stator and the rotors. The housing design of the ISRM device minimizes the contact area between the ISRM suspension and the stator cover, reducing heat transfer through the housing of the simulated device.

A. Simulated spray cooling induction switched reluctance machine

The coolant used in the ISRM is Automatic Transmission Fluid (ATF). Table 2 outlines the liquid's properties, which are essential for comprehending its behavior in fluid dynamics and thermal processes. The key parameters in Table 2 include fluid density (ρ), kinematic viscosity (v), specific heat capacity (C_p), and thermal con-

Table 1: Specifications of the ISRM

Parameter	Value
Number of stator poles	12
Number of rotor poles	10
Phase numbers	3
Rated power, KW	150
Stack length, mm	10
Rated speed, rpm	6000, 3000
The outer radius of the stator, mm	125.4
The inner radius of the stator, mm	88.5
Outer radius of rotor, mm	88
The inner radius of the stator, mm	36.4
Air gap	0.5
Lamination material	M19
Stator winding material	copper
Number of turns per phase	35
Rated current, A	270
Rated voltage, V	600
Torque, N/m	270
Cooling method	oil spray

Table 2: Automatic transmission fluid coolant properties

ATF Properties	Value	Unit
Density ρ @40°C	830.3	kg/m³
Kinematic viscosity ν @40°C	0.0299	kg/m s
Specific Heat capacity C_p @40°C	1984	J/kg-K
Thermal conductivity λ @40°C	0.145	W/m-K

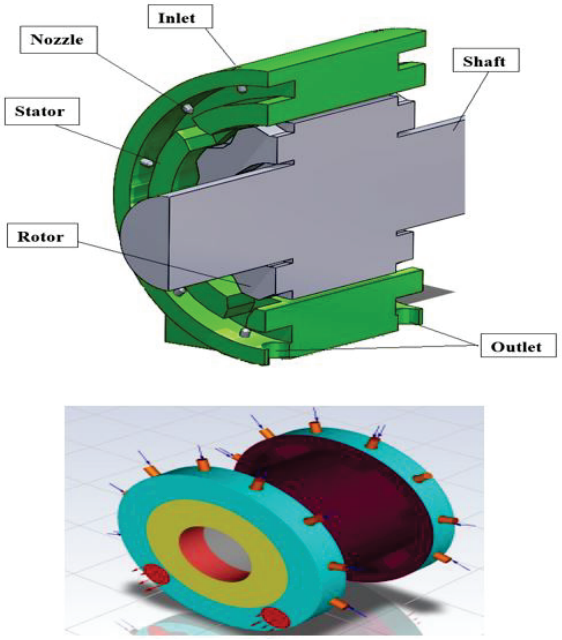

Fig. 5. Schematic of the proposed 12/10 ISRM machine with the spray cooling system.

ductivity (λ). These properties are crucial for analyzing fluid movement and heat transfer in systems, such as those using spray nozzles for cooling. The literature documents various nozzle designs explored for numerous spray applications [17]. Flat jet nozzles are used in the ANSYS simulation shown in Fig. 5. The geometry and arrangement of the nozzles are given in Table 3. Table 3 typically includes critical parameters such as the nozzle diameter, angle of spray, and spacing between nozzles, which are essential for ensuring optimal performance in their respective applications. The critical parameters in Table 3 for effective nozzle performance include the spray nozzle type, dimensions (D_{stator}, D_{rotor}, D_{nozzle}), and distances from the nozzle to the stator (H_{stator}) and rotor (H_{rotor}) surfaces. These factors are essential for precise spray coverage and cooling efficiency.

Table 3: Spray nozzle properties and positioning

Spray Nozzle Properties and Positioning	Value	Unit
Nozzle	Flat jet nozzle	-
$D_{stator,rotor,nozzle}$	0.358	mm
H_{stator}	12.52	mm
H_{rotor}	35.75	mm
Nozzle spray angle γ	130	°

B. Fluid circuits

The machine cooling settings of ISRM are in the form of two circuits. The first fluid circuit regulates the cooling water that lowers the temperature of the ATF. The ATF used for cooling the end windings is circulated through a second fluid circuit, which also serves the liquid cooling system for the ISRM.is carried in the liquid circuit for ISRM cooling. A pump transfers the ATF fluid to the injection nozzles to create the fluid pressure required for injection. Two manual valves are proposed to adjust the radial spray of the nozzles. After the ATF fluid is sprayed on the coils, it is collected in the stator coil tank and then transferred to the storage tank from the designed outlet position. Finally, the fluid is directed to the radiator for cooling and enters the injection cycle again. This process is instrumental in lowering the temperature of the windings, thereby enhancing the overall performance of the device, as depicted in Fig. 6.

C. Parameter range of the study area

In this study, multiple parameters listed in Table 4 are systematically modified and simulated to assess their impact on the system's performance.

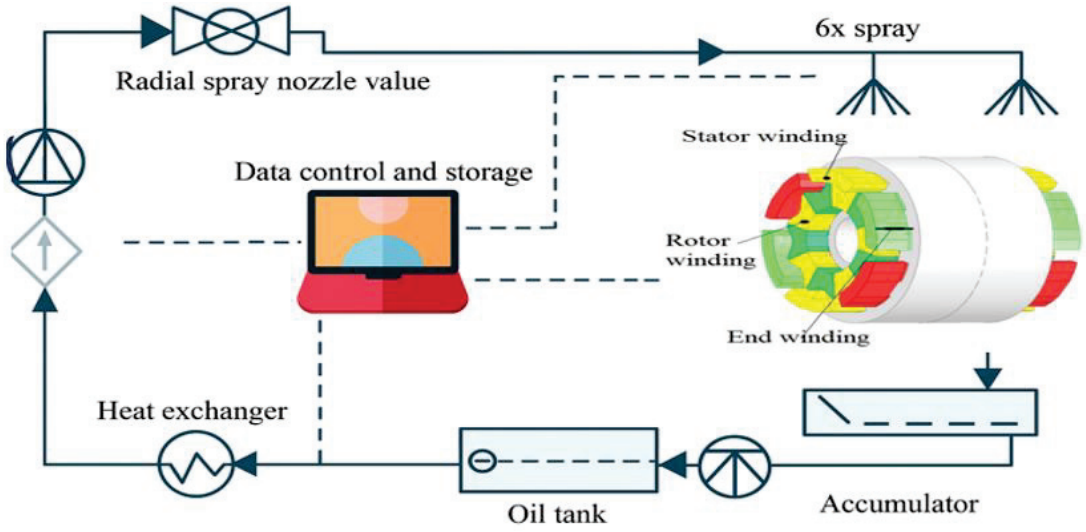

Fig. 6. Setting up the proposed cooling fluid system.

Table 4: Range of parameters altered in the series of measurements

Parameter	Tested Parameter Range	Unit
Heat flux rotor	1241	Watt
Heat flux stator	2708	Watt
Mass flow rate $\dot{V}$	2.4, 3.6, 6, 8.43, 10.83, 14.45, 18	l/min
Number of nozzles on both sides	Radial (24)	-

IV. HYDRODYNAMIC PARAMETERS OF SPRAYS

In the ISRM, a cooling fluid spray system is utilized. This section investigates two approaches to the simulated heat transfer model. In this study, the average temperatures from each side of the ISRM are employed to calculate the heat transfer coefficients for both model approaches. Local heat transfer behavior and temperature heterogeneities are not investigated further. In this research, a heat transfer model approach should be developed that can be transferred to different dimensions of the machine, and therefore, the complexity of the model needs to be reduced. The heat transfer coefficient is calculated as follows:

$$T_b = \frac{T_{in} + T_{out}}{2}, \tag{1}$$

$$h = \frac{Q}{A_{EA} * (T_w - T_b)}. \tag{2}$$

Stator iron losses can be neglected. At this low frequency, the air gap of the rotor was chosen to be relatively large, and its maximum speed was set to n=6000 rpm, so the losses due to air friction can be neglected. Table 2 contains all additional properties of the fluid.

A. Approach 1: Based on Liu et al.

The first model approach simulated test is based on an idea for a model with reduced parameters from Liu et al. [10, 13]:

$$h_{HTC} = C_1.\ddot{V}^{C_2}.L_{char}^{C_3}, \tag{3}$$

$$h_{HTC} = 99300.\dot{V}^{0.432}.L_{char}^{0.31}, \tag{4}$$

where $\ddot{V}$ is the effective volumetric flow rate (see Tables 5 and 7) and $L_{chr}^{c_3}$ is the characteristic length:

$$\ddot{V} = \frac{\dot{V}}{A}.\frac{\omega_1}{\omega_2}, \tag{5}$$

$$L_{chr} = \sqrt{L_{rad}.w_{spray}} = \sqrt{A}. \tag{6}$$

Due to the different axial distances between the spray nozzle and the EW in DE (Drive End) and NDE (Non-Drive End), two different characteristic lengths in the axial direction are studied, while one characteristic length in the radial direction is investigated.

B. Approach 2: Nusselt number

The alternate method utilizes a single-phase heat transfer paradigm for spray nozzles, defining the Nusselt number with Suter's mean diameter, the d32. The specified diameter refers to that of a droplet whose ratio of volume to surface area matches the collective ratio for all droplets within the spray sample. Employing the spray's Reynolds number (see Table 7 for details) [18]:

$$Nu_{d32} = c_4.Ru_{Spray}^{c_5}.Pr_{ATF}^{c_6}, \tag{7}$$

$$Nu_{d32} = 87.633.Ru_{Spray}^{0.969}.Pr_{ATF}^{0.25}, \tag{8}$$

Nusselt number:

$$Nu_{d32} = \frac{h.\,d_{32}}{\lambda_{ATF}}, \tag{9}$$

Reynolds number:

$$Ru_{Spray} = \frac{\rho_{ATF}.V^{\cdot\cdot}.d_{32}}{\eta_{ATF}}, \tag{10}$$

Prandtl number:

$$Pr_{ATF} = \frac{C_{P,ATF}.\eta_{ATF}}{\lambda_{ATF}}, \tag{11}$$

$$\frac{d_{32}}{d_0} = 3,67.\left[We_{d0}^{0,5}.Ru_{d0}\right]^{-0,259}, \tag{12}$$

$$We_{d0} = \frac{\rho_{Air}.\left(\frac{2\Delta P}{\rho ATF}\right).d0}{\sigma_{ATF}}, \tag{13}$$

$$Ru_{d0} = \frac{\rho_{ATF}.\left(\frac{2\Delta P}{\rho ATF}\right)^{0,5}.d0}{\eta_{ATF}}, \tag{14}$$

The surface tension of the ATF is denoted as σ_{ATF}, is sourced from the research conducted by Kemp and Linden [19].

C. Heat transfer surface model

In this study, three end-winding surface area (A_{EW}) models will be used to calculate the effective volumetric flow rate. Both heat transfer models utilize the same three surface modeling methods. Mainly, models of EW are applicable in evaluating cooling system operations and in assessing the efficacy of heat transfer within electric engines and various devices. Utilizing empirical evidence and mathematical formulations, these models determine the effective volumetric flow rate, taking into account the ambient conditions and the specific properties of the substance. For example, EW models can aid in identifying the optimal strategy for dispersing heat and lowering temperatures in oil-cooled electric machines.

The length of EW is $l_{EW} = 2H\ tan\ \frac{\gamma}{2}$ where L_{rad} is based on the ideas of trigonometric manipulations for the modeling approach by Liu and colleagues [13] (see Fig. 7):

$$A_{EW,1} = L_{rad}.w_{spray}(\text{radial}), \tag{15}$$

$$A_{EW,2} = 2\pi.r_{EW,o}.l_{EW}(\text{radial}), \tag{16}$$

$$A_{EW,3} = \pi.\left(r_{EW,o}^2 - r_{EW,i}^2\right) + 2\pi.l_{EW}.\left(r_{EW,0} + r_{Ew,i}\right), \tag{17}$$

where $r_{EW,i}$ is the inner surface radius of the end-winding and $r_{EW,o}$ is the outer surface radius of the end-winding.

Table 5: Experimental Nusselt correlation coefficients for different nozzle arrangements [15]

Nozzle Arrangement	$c_4[-]$	$c_5[-]$	$c_6[-]$
Axial	63.796	0.684	
Radial	87.633	0.969	0.25
Combined	99.136	1.046	

Consistent with previous heat-transfer research in electrical machinery, the fundamental shape of an end-winding is often reduced to a model resembling half of a circular band [13]. An interesting part of the work concerns the comparison between two distinct approaches

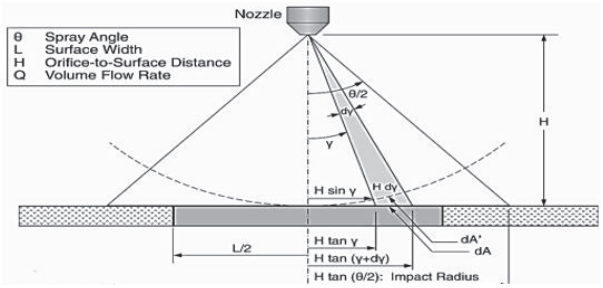

Fig. 7. Radial spray arrangement [20].

to modeling heat transfer. The first is based on empirical correlations derived from previous studies, while the second uses dimensionless parameters such as Nusselt, Reynolds, and Prandtl numbers to describe the forced convection produced by the spray. This comparison helps identify the conditions under which each method is more reliable and representative of the real behavior of the system. Another merit of this paper is the clear connection it establishes between improved cooling and machine performance.

D. Model development

For the analysis of heat transfer behavior, the average chain temperatures from all measured points on each side of the EW are utilized. All empirical and model-based heat transfer coefficients are determined using the same surface model, which varies according to the spray nozzle configuration. The thermal model incorporates all relevant governing equations, including conservation of mass, momentum, and energy, which are explicitly stated in the paper. Boundary conditions were applied using a finite element framework, with Dirichlet and Neumann conditions set according to physical constraints of each domain.

In this paper, the geometry of the model was meshed using the Fluent meshing method in the Fluent software. The type of mesh selected for this simulation is a polyhedral mesh, which is highly suitable for complex models and particularly for simulating fluid flows and physical fields. This type of mesh was chosen due to its specific features, such as high accuracy in simulation and better performance in complex geometries. The number of meshed elements in this model is 256,000, which effectively improves the simulation accuracy in sensitive areas.

The selected solution type is pressure-based and was used in transient mode for precise analysis of fluid dynamics. This simulation was conducted in a two-phase model using the Volume of Fluid (VOF) method, which is suitable for simulating two-phase flows such as liquid-gas. The k-epsilon model was used as the turbulence model to simulate turbulent flows and account

for complex flow behaviors. For a more accurate simulation, Cell Zone Conditions were defined separately for the rotor and stator. Additionally, to correctly model the interactions between the rotor and stator, a Mesh Interface was defined between these two sections. This Mesh Interface enables proper communication and data transfer between the moving part (rotor) and the stationary part (stator). Due to the geometric symmetry in the model, the Symmetry feature was used, which helps reduce computational time and increase simulation efficiency.

At the system inlet, the mass flow inlet was used to specify the mass flow rate, accurately defining the inlet flow conditions. The specific simulation settings include a pressure-based solution type, transient simulation mode, a two-phase model using VOF with surface tension, and a k-epsilon turbulence model. Cell zone conditions were defined separately for the rotor and stator, with a mesh interface established between them, and the use of a symmetry feature for geometric symmetry. The mass-flow inlet was employed for the mass flow rate. This combination of models and simulation conditions enables accurate simulation of flows, interactions between the rotor and stator, and analysis of two-phase systems in a dynamic and complex environment.

Regression models were utilized to calibrate the heat transfer coefficients, pinpointing the coefficients and exponents for both methodologies in equations (3) and (7). Identical coefficients (c_1-c_6) are employed on each side, with the model's design aimed at pioneering the development of additional ATF spray-cooled traction electric machines. The empirical model treats winding configurations in DE and NDE uniformly, without differentiation. The variance between EW's two facets is attributed to the disparate lengths of the hairpin wires and their consequent surface dimensions. The data are validated across varying flow rates at 3000 and 6000 rpm, alongside a stator heat transfer measurement of 2708 W, focusing solely on radial spray analysis. The comparison between the heat transfer observed in the experiments in [15] and the simulation using the displacement Nusselt correlation coefficients is depicted in Fig. 8.

The measurements taken at different flow rates, specifically at 3000 and 6000 rpm, have verified that the rotor's heat transfer is 1241 watts. It's important to note that this study focuses solely on radial spray patterns. Figure 9 clearly shows a noticeable difference in heat transfer between the empirical data and the simulation results, which are calculated using the

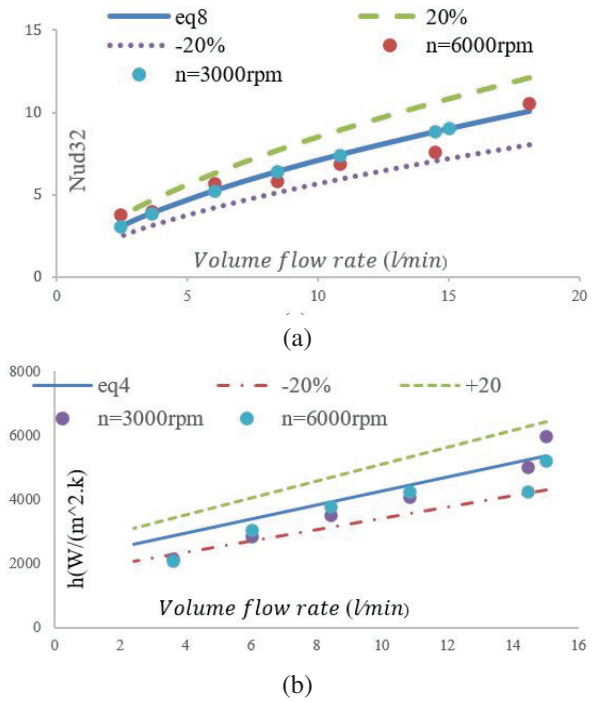

Fig. 8. Comparison of (a) Nusselt number and (b) heat transfer rate as a function of coolant flow rate (l/min) of the ISRM stator. Simulated data are plotted against calculated values derived from equations (4) and (8).

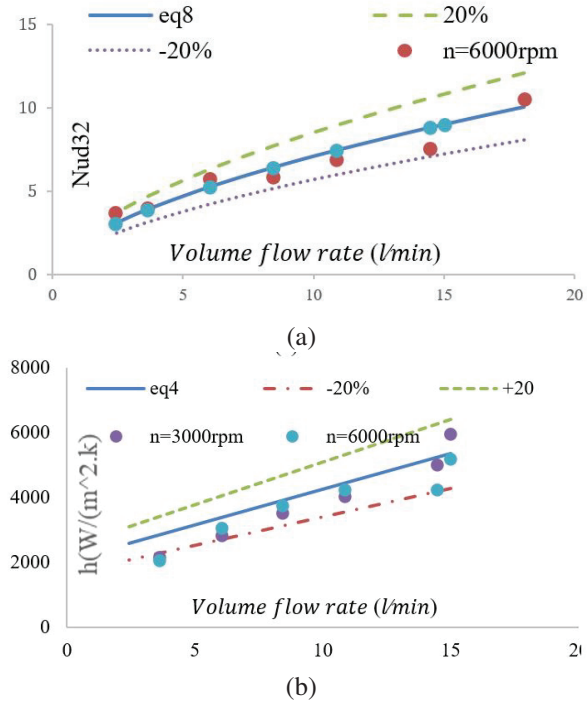

Fig. 9. Comparison of (a) Nusselt number and (b) heat transfer rate as a function of coolant flow rate (l/min) of the ISRM rotor. Simulated data are plotted, derived from equation (4), and against calculated values derived from equations (4) and (8).

Nusselt displacement correlation coefficients. This comparison highlights the potential discrepancies and provides a framework for understanding the effectiveness of the radial spray cooling method under different operational conditions. The flow rate is 2-18 liters per minute. The temperature of the ATF fluid ranges from 40 to 150 degrees Celsius. In radial nozzles, the higher the flow rate, the better the cooling performance. The smaller the mean droplet diameter (*d32*), the more significant the increase in the heat transfer coefficient, and the more extensive the surface area (A_{EW}).

V. MODELING AND SIMULATION RESULTS OF TRANSIENT HEAT TRANSFER

In this section, we will analyze the temperature at three distinct points during the transient state for different flow rates, given that the empirical Nusselt formula closely aligns with the simulation results. This analysis will be conducted using ANSYS software, as shown in Fig. 10. This study investigates the temperature changes at several specific points within a thermal system over time. These points are strategically located inside the rotor, where they are continuously influenced by a heat source with a heat flux of 2708 W/m^2, which is applied over both the stator and rotor surfaces. In addition to various cooling conditions, the temperature spikes suddenly in localized areas, then, within a fraction of a second, it decreases and stabilizes. Temperature decrease time for different flow rates is shown in Figs. 11 and 12. Temperature reaches its maximum value in 0.2 seconds and then reaches a steady state 0.2 seconds later with the injection of ATF fluid. At different flow rates, the stable temperature is different. Upon motor start-up, a brief initial temperature increase occurs before the cooling system becomes fully effective, which contributes to the sharp thermal response observed in the early stage. This behavior has been validated by comparing our results with experimental data reported in the referenced literature, confirming the accuracy of the thermal model under extreme loading conditions.

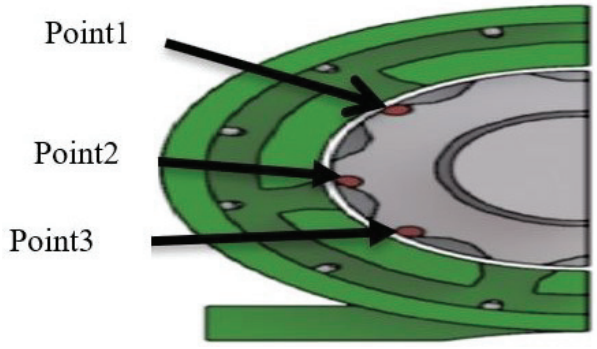

Fig. 10. Three-point placement in transient heat transfer.

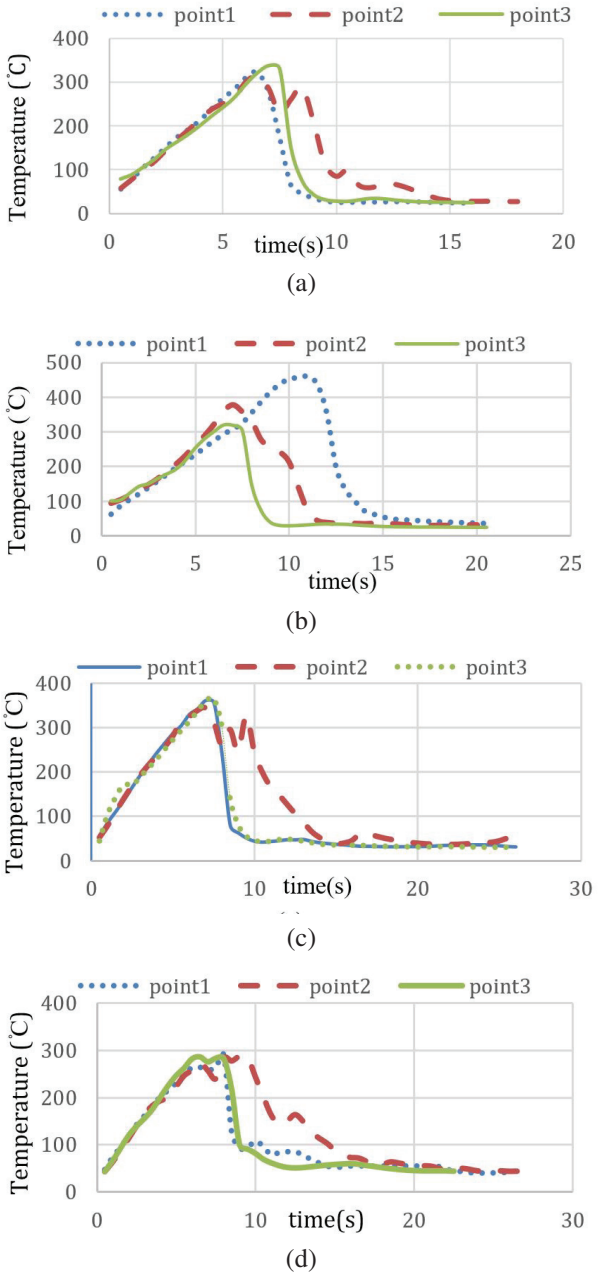

Fig. 11. Temperature changes (Celsius) in terms of time (seconds) for different flow rates. (a) Temperature variations at three selected points for a flow rate of 15 liters per minute, (b) temperature variations at three selected points for a flow rate of 12 liters per minute, (c) temperature variations at three selected points for a flow rate of 5 liters per minute, and (d) temperature variations at three selected points for a flow rate of 3 liters per minute.

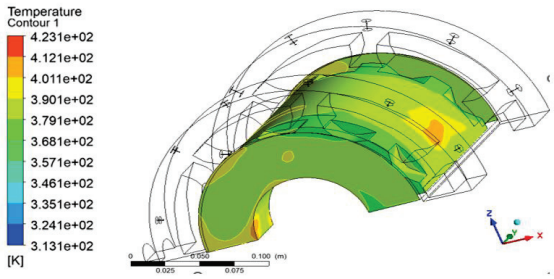

Fig. 12. Temperature contour for a flow rate of 3 liters per minute at 3000 rpm.

VI. ENERGY LOSSES FOR ROTORS

The thermal model was developed based on power losses computed using finite element electromagnetic (FEM) simulations in ANSYS Maxwell. These include core losses (hysteresis and eddy currents) and copper losses, which were calculated with spatial resolution and mapped onto the thermal domain in ANSYS. Relevant electromagnetic field maps, such as magnetic flux density and current density distributions, were extracted to visualize regions of high loss concentration.

In addition, mechanical losses arising from fluid resistance and friction along the cooling path have been taken into account. The circulation of the fluid near the stator coils and within the cooling channels results in a pressure drop and increased energy consumption, especially in the rotor region. As the rotor speed increases, these mechanical losses rise accordingly, as shown in Fig. 13. The machine was initially modeled using the finite element method, and all associated losses were extracted through ANSYS simulations.

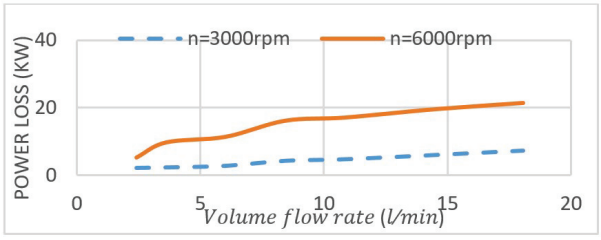

Fig. 13. Power loss (KW) relative to flow rate (l/min).

VII. DISCUSSION

Given the operational requirements and engineering considerations, evaluating the feasibility of implementing the proposed system in industrial applications is of particular interest. In the field of electric machine cooling, and particularly in EVs, the oil-spray system presents a promising alternative to conventional liquid- or air-based approaches. It offers not only high thermal efficiency but also a compact structure and reduced maintenance demands. Intelligent pump control strategies can further enhance energy efficiency, while preliminary estimates suggest that the installation and maintenance costs of this system could fall within a competitive range compared to traditional solutions, especially in designs where simplicity and spatial constraints are critical. To estimate the cost of implementing the proposed oil-spray cooling system for electric machines, a simplified analysis was conducted based on a 150-kW motor equipped with 24 nozzles. Key components include a high-capacity pump with intelligent control, a distribution manifold, a reservoir, extended piping, and installation services. Preliminary estimates suggest a total system cost ranging from USD2300-3420, depending on equipment specifications and integration complexity (Table 6).

Cost estimation can be approached using various methods depending on the design phase and required accuracy. *Empirical methods* leverage data from similar installations; parametric models apply mathematical correlations between system parameters and cost; activity-based costing (ABC) allocates expenses based on actual operational tasks; and bottom-up estimation aggregates costs from individual components. Each method offers distinct advantages across feasibility, detail, and scalability.

Table 6: Summarizing the updated cost estimation for the oil-spray cooling system based on a 150-kW electric machine with 24 nozzles (prices are based on the date the article was submitted)

Component	Estimated Cost (USD)	Remarks
High-capacity pump + smart controller	900-1300	Includes pressure regulation and automation
24 spray nozzles + distribution system	400-720	Depends on the nozzle type and spray pattern
Oil reservoir + extended piping	350-500	Includes thermal insulation if needed
Installation and commissioning	650-900	Labor and calibration services
Total Estimated Cost	2300-3420	Varies by vendor, location, and system scale

VIII. FUTURE WORK

Due to the complexity and uncertainties in spray cooling behavior, fuzzy logic, particularly fuzzy similarity analysis, offers a promising direction for future optimization, enabling effective comparison of thermal configurations under nonlinear or uncertain conditions [23].

In this paper, mechanical vibrations and their interaction with thermal performance are of growing

Table 7: Symbols and nomenclature

Symbol	Nomenclature
A	Area defined along heated surface (m^2)
c_p	Specific heat capacity (J/kgK)
$c_1 \ldots .6$	Coefficients and exponents
d	Distance (m)
D	Diameter (m)
d_{32}	Sauter mean diameter (m)
I	Current (A)
K_V	Housing losses factor (W/K)
L	Length (m)
n	Machine speed (min^{-1})
Nu	Nusselt number
Pr	Prandtl number
P	Power losses (W)
Q	Volume flow rate
$\dot{Q}$	Heat flow rate (W)
Re	Reynolds number
T_{in}	Inlet temperature (°C)
T_{out}	Outlet temperature (°C)
T_w	Surface temperature (°C)
$\dot{V}$	Volume flow rate (1/min)
$\ddot{V}$	Volumetric flux rate (m^3/m^2 s)
w	Width (m)
H_{stator}	Nozzle-to-stator surface distance
H_{rotor}	Nozzle-to-rotor surface distance
H_e	Height of the end-winding
Greek	
h	Heat transfer coefficient ($W/m^2 \cdot K$)
θ	Spray angle
ΔT	Temperature difference (K)
ρ	Density (kg/m^3)
v	Kinematic viscosity (m^2/s)
γ	Nozzle spray angle (°)
Ω	Angle (rad)
Subscripts	
0,1...	Counters
ax	axial
comb	Combined
i	inner
hydra	Hydraulic
0	outer
R_{ad}	Radial

importance, particularly in spray-based cooling systems where moving components and nozzles are exposed to dynamic excitation from the motor or installation environment. Modal analysis serves as a fundamental tool for identifying the natural frequencies, mode shapes, and damping ratios of the system, enabling engineers to predict vibrational behavior and avoid destructive phenomena such as resonance.

Modal analysis can be conducted numerically (e.g., via finite element methods) or experimentally (e.g., using impact hammer or shaker tests), and its results form the basis for further dynamic studies such as harmonic response or random vibration analysis. Aligning the system's natural frequencies away from operational excitation ranges helps prevent fatigue and extends component lifespan.

Moreover, multiphysics modeling, which simultaneously considers thermal, fluidic, and mechanical behavior, offers a more comprehensive understanding of system performance under real-world conditions. For instance, vibrations may influence spray distribution, temperature uniformity, or sensor accuracy. Integrating modal analysis with thermal-fluid simulations thus supports the design of robust, efficient, and vibration-resilient cooling systems.

IX. CONCLUSION

This study introduced an innovative oil-spray cooling system for a 12/10 induction switched reluctance machine (ISRM), showcasing significant advancements in thermal management for Electric Vehicles (EVs). The paper begins by illustrating the structure of the motor, with a particular focus on the internal arrangement of components and the area's most prone to overheating, such as the stator and rotor. The simulation results indicated that increasing flow rates elevate the Nusselt number, thereby enhancing heat transfer and increasing machine losses. An optimal flow rate of 6 l/min was identified, effectively reducing losses at higher speeds while maintaining coil temperatures below 90°C. The study also examines the transient thermal response of the motor, simulating the evolution of heat over time and assessing energy losses in the rotor. These data are used to calibrate and validate the proposed models and to identify potential optimization areas. The rotor winding generates heat, which necessitated the design of the spray cooling system.

Our findings indicate that with the current number of nozzles for this machine, there is a heat problem that needs addressing. In comparison to multiphase spray cooling, oil-spray cooling demonstrates a more consistent temperature distribution and superior thermal management capabilities. To facilitate the successful implementation of oil-spray cooling, several practical guidelines are proposed. The configuration of nozzles, including their quantity (24), spray angles (130°), and placement, significantly influences the uniformity of temperature distribution. While higher flow rates enhance cooling performance, they necessitate greater total flow rates. Additionally, full-cone nozzles have outperformed hollow-cone nozzles regarding heat transfer coefficient (HTC) and overall cooling efficiency. Configurations

featuring a larger number of low-flow-rate nozzles yield better cooling efficiency compared to setups with fewer high-flow-rate nozzles.

REFERENCES

[1] O. E. Özçiflikçi, M. Koç, S. Bahçeci, and S. Emiroğlu, "Overview of PMSM control strategies in electric vehicles: A review," *International Journal of Dynamics and Control*, vol. 12, pp. 2093-2107, 2024.

[2] A. Chithrabhanu and K. Vasudevan, "Quantification of noise benefits in torque control strategies of SRM drives," *IEEE Transactions on Energy Conversion*, vol. 38, no. 1, pp. 585-598, Mar. 2023.

[3] K. Diao, X. Sun, G. Lei, G. Bramerdorfer, Y. Guo, and J. Zhu, "System-level robust design optimization of a switched reluctance motor drive system considering multiple driving cycles," *IEEE Transactions on Energy Conversion*, vol. 36, no. 1, pp. 348-357, Mar. 2021.

[4] M. Abbasian, M. Moallem, and B. Fahimi, "Double stator switched reluctance motors: Fundamentals and magnetic force analysis," *IEEE Trans. Energy Convers*, vol. 25, no. 3, pp. 589- 597, Dec. 2010.

[5] M. Abbasian, "Induction switched reluctance motor," U.S. Patent, US20170370296A1, June 30, 2020.

[6] M. Azamian Jazi and M. A. Abbasian, "Preliminary evaluation of induction switched reluctance machine (ISRM) for electric vehicle application," *IEEE Trans. Transport. Electrific*., vol. 10, pp. 26693-26701, Dec. 2021.

[7] M. Joodi, M. Abbasian, and M. Delshad, "Introducing a 12/10 Induction Switched Reluctance Machine (ISRM) for electric powertrains," *Applied Computational Electromagnetics Society (ACES) Journal*, vol. 39, no. 05, pp. 452-460, May 2024.

[8] A. M. Mohammadi, M. Abbasian, M. Delshad, and H. Saghafi, "Electromagnetic and thermal analysis of a 6/4 induction switched reluctance machine for electric vehicle application," *Applied Computational Electromagnetics Society (ACES) Journal*, vol. 38, no. 5, pp. 361-370, Sep. 2023.

[9] P. Shams Ghahfarokhi, A. Podgornovs, A. Kallaste, A. J. Marques Cardoso, A. Belahcen, and T. Vaimann, "The oil spray cooling system of automotive traction motors: The state of the art," *IEEE Transactions on Transportation Electrification*, vol. 9, no. 1, pp. 428-451, Mar. 2023.

[10] C. Liu, Z. Xu, D. Gerada, F. Zhang, Y. C. Chong, M. Michon, J. Goss, C. Gerada, and H. Zhang, "Experimental investigation of oil jet cooling in electrical machines with hairpin windings," *IEEE Trans. Transport. Electrific.,* vol. 9, no. 1, pp. 598-608, Mar. 2023.

[11] X. Wang, B. Li, K. Huang, Y. Yan, I. Stone, and S. Worrall, "Experimental investigation on end winding thermal management with oil spray in electric vehicles," *Case Stud. Thermal Eng*., vol. 35, p. 102082, July 2022.

[12] F. Zhang, D. Gerada, Z. Xu, C. Liu, H. Zhang, T. Zou, Y. C. Chong, and C. Gerada, "A thermal modeling approach and experimental validation for an oil spray-cooled hairpin winding machine," *IEEE Transactions on Transportation Electrification*, vol. 7, no. 4, pp. 2914-2926, Dec. 2021.

[13] C. Liu, Z. Xu, D. Gerada, J. Li, C. Gerada, Y. C. Chong, M. Popescu, J. Goss, D. Staton, and H. Zhang, "Experimental investigation on oil spray cooling with hairpin windings," *IEEE Transactions on Industrial Electronics*, vol. 67, no. 9, pp. 7343–7353, Sep. 2020.

[14] C. Chiu, Y. Wang, H. Zhang, and J. Lee, "CFD simulation of a 30-kW switched reluctance motor: Comparison of liquid and air cooling systems," *Case Stud. Therm. Eng*., vol. 49, p. 103349, 2023.

[15] P.-O. Gronwald, N. Wiese, M. Henke, and T. A. Kern, "Electric traction motor spray cooling—Empirical model development and experimental validation," *IEEE Transactions on Transportation Electrification*, vol. 9, no. 2, pp. 2185-2194, June 2023.

[16] M. Daneshi, M. Abbasian, and M. Delshad, "Comparison of an induction switched reluctance machine with an interior permanent magnet machine using finite element method," *Applied Computational Electromagnetics Society (ACES) Journal*, vol. 40, no. 1, pp. 1-7, Jan. 2025.

[17] N. Ashgriz, *Handbook of Atomization and Sprays: Theory and Applications*. New York, NY: Springer, 2011.

[18] G. Liang and I. Mudawar, "Review of spray cooling—Part 1: Single-phase and nucleate boiling regimes, and critical heat flux," *Int. J. Heat Mass Transf*., vol. 115, pp. 1174-1205, Dec. 2017.

[19] S. P. Kemp and J. L. Linden, "Physical and chemical properties of a typical automatic transmission fluid," *Proc. SAE Tech. Paper Ser*., pp. 1-14, Oct. 1990.

[20] I. Mudawar and K. A. Estes, "Optimizing and predicting CHF in spray cooling of a square surface," *Journal of Heat Transfer-Transactions of the ASME*, vol. 118, pp. 672-679, 1996.

[21] P. H. Mellor, D. Roberts, and D. R. Turner, "Lumped parameter thermal model for electrical

machines of TEFC design," *IEE Proceedings B - Electric Power Applications*, vol. 138, no. 5, pp. 205-218, 1991.

[22] A. Boglietti and A. Cavagnino, "Analysis of the endwinding cooling effects in TEFC induction motors," *IEEE Transactions on Industry Applications*, vol. 43, no. 5, pp. 1214-1222, 2007.

[23] M. Versaci, F. Laganà, L. Manin, and G. Angiulli, "Soft computing and eddy currents to estimate and classify delaminations in biomedical device CFRP plates," *J. Electr. Eng.*, vol. 76, no. 1, pp. 72-79, Feb. 2025.

Narges Ghandi was born in Isfahan, in 1986. She received her B.Sc. degree in Electrical Engineering from Islamic Azad University, Najaf Abad Branch, in 2007, and her M.Sc. degree in the same field from Islamic Azad University, Khomeini Shahr Branch, in 2015. Since 2018, she has been pursuing her Ph.D. in Electrical Engineering at Islamic Azad University, Khorasgan Branch, Isfahan, Iran.

Hadi Saghafi was born in Isfahan, in 1982. He earned his B.Sc. in 2004, M.Sc. in 2007, and Ph.D. in 2014 in power engineering from Isfahan University of Technology. Since 2015, he has been an assistant professor in the Department of Technical Engineering at the Isfahan (Khorasgan) Branch of Islamic Azad University. His research focuses on microgrids, distributed generation, power electronics control, and their applications in power systems.

Mohammadali Abbasian received a bachelor's degree, M.Sc. degree, and a Ph.D. degree in Electrical Engineering from the Isfahan University of Technology. From 2017 to 2018, he was with the Bundeswehr University, Munich, Germany, as a research scientist. He was an assistant professor at the IAU University, Khorasgan, Isfahan, Iran. His research area is Electrical Machines and Drives.

Wideband Circularly Polarized Metasurface Antenna with Embedded Parasitic Patch and Air-layer for Multi-curvature Stability

Qiang Chen, Jun Yang, Changhui He, Liang Hong, Fangli Yu, Di Zhang, Li Zhang, and Min Huang

Air Force Early Warning Academy
Wuhan, Hubei 430019, China
1062620145@qq.com, yangjem@126.com, 513442678@qq.com, 77054315@qq.com, yufangli_aewa@163.com, deeafeu@163.com, 619246354@qq.com, huangmin_hm@163.com

***Abstract* –** To address the critical limitations of traditional planar antennas, such as susceptibility to carrier platform curvature and narrow bandwidth which hinder integration on complex surfaces, this paper presents a metasurface (MS) based wideband circularly polarized conformal antenna specifically designed for multi-curvature platforms. The design incorporates a systematic three-stage approach. Initially, an oblique elliptical slot-fed antenna is designed to excite orthogonal TM0 modes through slot inclination adjustment, though its axial ratio (AR) minimum fails to surpass the 3 dB threshold. To effectively improve the bandwidth, a 6×6 periodically arranged circular ring-shaped MS superstrate is incorporated, inducing new resonances that merge to form a wideband response (impedance bandwidth 4.1-7.5 GHz, 3 dB AR bandwidth 4.97-7.44 GHz, peak gain 7.45 dBic at 7.1 GHz). To further optimize high-frequency performance and enhance mid-band integration, a centrally offset rectangular patch embedded between the MS and slot layers, separated by an air cavity, introduces multi-mode resonance at higher frequencies, expanding the 3 dB AR bandwidth by 15% to 4-7.5 GHz. Crucially, mechanical bending tests across curvature radii of 20-50 mm reveal minimal performance fluctuations (AR fluctuation<8.3%, gain drop≤1.5 dB per 10 mm reduction in radius), demonstrating exceptional structural stability essential for conformal applications. Experimental validation confirms close agreement between simulated and measured results. This antenna achieves a compelling combination of wideband circular polarization, stable gain, low profile (0.05λ0), and robust multi-curvature conformal capability, holding significant potential for seamless integration with complex-shaped carrier platforms like curved satellite panels, UAVs, or conformal radars.

***Index Terms* –** Bandwidth, circular polarization, metasurface (MS), multi-curvature.

I. INTRODUCTION

Circularly polarized (CP) antennas are pivotal in modern wireless systems, offering robustness against polarization mismatch, multipath interference, and orientation-dependent signal degradation [1–3]. These advantages are critical for applications spanning satellite communications [4], unmanned aerial vehicles (UAVs) [5], biomedical telemetry [6], and conformal radar systems [7], where dynamic environments demand stable signal integrity. Traditional CP designs, such as corner-truncated patches [8], helical structures [9], and sequential-rotation arrays [10], have achieved moderate success but face inherent trade-offs between bandwidth, profile, and adaptability to non-planar platforms [11]. For instance, conventional microstrip-based CP antennas often exhibit narrow axial ratio (AR) bandwidths (<15%) or require complex feeding networks, limiting their utility in emerging multi-curvature systems [12].

Recent advancements in metasurface (MS) technology have revolutionized CP antenna design by enabling unprecedented control over electromagnetic wavefronts [13–15]. MSs, composed of subwavelength unit cells, can manipulate polarization states, enhance gain, and broaden bandwidth without significant structural overhead. For example, Gao et al. [16] demonstrated a bilayer polarization conversion MS achieving a 32.9% 3-dB AR bandwidth. Kedze et al. [12] utilized a 4×4 MS array to realize a 65% impedance bandwidth with 12.17 dBic peak gain. Such designs highlight ability of MS to decouple performance limitations inherent to traditional geometries. Further innovations include AI-optimized MS arrays for dual-band CP operation [17].

Conformal CP antennas, tailored for curved surfaces, represent a critical frontier in antenna engineering. Applications like conformal radar arrays [7] and curved satellite panels [4] demand antennas that maintain electrical performance under mechanical deformation. Recent progress includes Liu et al.'s [18] transparent conformal MS antenna with an 18.6% AR

Submitted On: April 17, 2025
Accepted On: July 23, 2025

https://doi.org/10.13052/2025.ACES.J.400708

bandwidth and Le et al.'s [19] all-textile polarization-conversion MS antenna. However, these solutions struggle with multi-curvature adaptability, often exhibiting impedance detuning or gain degradation when bent across compound radii. Additionally, existing conformal MS designs rarely address the dual challenges of ultra-wideband CP operation and high radiation efficiency (>80%), leaving a gap in practical implementations.

This paper presents an ellipse-shaped slot MS-based conformal antenna that excites orthogonal modes through adjusting the ellipse-shaped slot tilt angle. To extend the bandwidth, a circular ring-shaped MS superstrate is utilized to realize multimodal resonance and collaborative operation with surface waves. Through the ability of wavefront modulation and phase compensation, the proposed antenna's bandwidth and gain are significantly enhanced. To improve high-frequency band performance and achieve mid-band integration, an off-center rectangular patch is embedded between the slot layer and MS layer with an additional air-layer, effectively realizing multimodal collaborative operation in mid-high-frequency bands and further improving the designed antenna's CP performance. Finally, antenna performances under different curvatures are then simulated. The results demonstrate that the further proposed antenna exhibits stable performance with minimal fluctuations across various curvatures, making it highly suitable for integration on complex-shaped platforms and broadening its application scenarios.

II. ANTENNA DESIGN PROCESS AND ANALYSIS

A. Antenna configuration

In this design, as illustrated in Fig. 1, the initial antenna employs a microstrip-line-fed oblique elliptical slot configuration. The feed layer and slot layer are separated by an F4BM flexible dielectric substrate (ε_r = 2.2, tanδ = 0.0014) with dimensions of 50×50 mm and thickness of 0.8 mm. To achieve broadband impedance matching, a stepped-impedance transformer is implemented at the termination of the rectangular microstrip line. Multi-mode resonance is induced by adjusting the elliptical slot's tilt angle, with parametric optimization performed using HFSS 15 to maximize performance. The simulated characteristics of the oblique elliptical slot are presented in Fig. 2, and the optimized geometric parameters are listed in Table 1.

As shown in Fig. 2 (a), the initial antenna exhibits single mode resonance at 5.33 GHz with a -10 dB impedance bandwidth of 4.8∼7.0 GHz, failing to achieve multi-mode excitation. However, a reduction in the reflection coefficient slope near 6 GHz suggests incipient mode coupling, which motivates subsequent design enhancements. Figure 2 (b) reveals that the AR remains

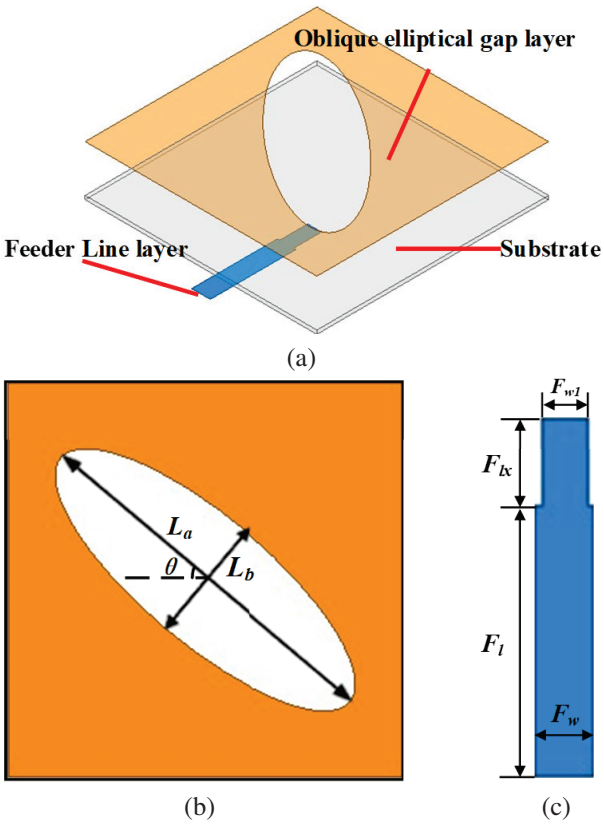

Fig. 1. Geometry of the initial antenna: (a) 3D view, (b) oblique elliptical-shaped layer, and (c) feeder.

above the 3 dB threshold across the impedance bandwidth, indicating insufficient excitation of orthogonal TM10 and TE10 modes for CP generation. The peak realized gain of 6.7 dB (occurred at 7.7 GHz) occurs outside the -10 dB impedance bandwidth.

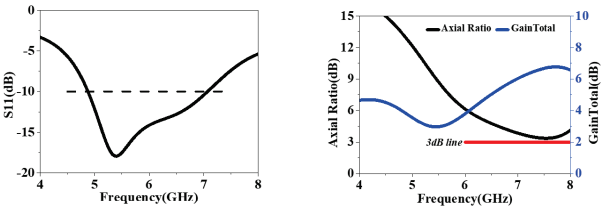

Fig. 2. Simulated results of the source antenna: (a) S11 and (b) Axial Ratio and GainTotal.

To address this limitation, a 6×6 periodically arranged circular patch MS is integrated onto the initial antenna, with its sketch as shown in Fig. 3. The MS is fabricated on an F4BM substrate (ε_r = 2.2, tanδ = 0.0014) and directly loaded onto the oblique elliptical slot without an intervening air gap as shown in Fig. 4 (a). Parametric sweeps in HFSS 15 optimize the MS unit cell

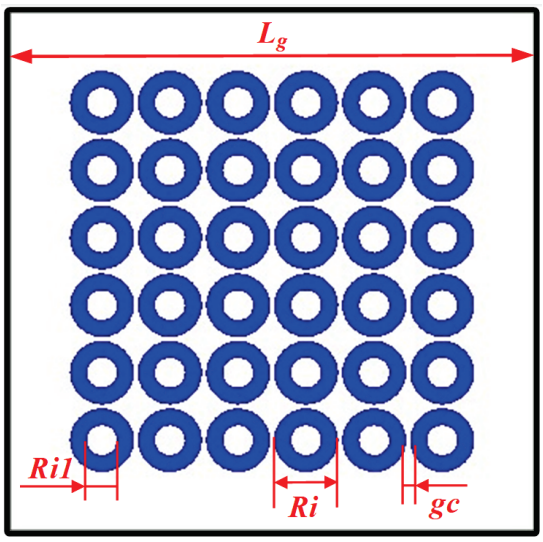

Fig. 3. Sketch of the circular ring-shaped MS superstrate.

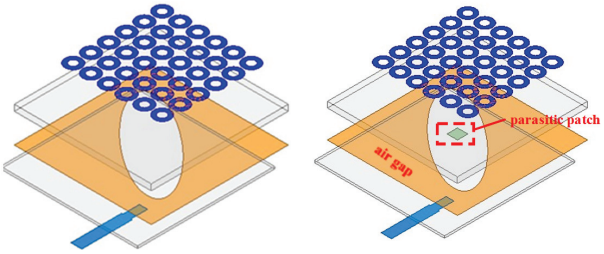

Fig. 4. Geometric evolution process in the proposed antenna design: (a) Antenna 2 and (b) the proposed.

dimensions and inter-element spacing to achieve broadband CP. The final geometric parameters are detailed in Table 1.

Table 1: Optimized dimensions of the proposed antenna

Dimension	Size (mm)	Dimension	Size (mm)
L_a	24	F_w	4
L_b	8	F_{w1}	3
θ	40deg	L_g	50
F_l	18.5	L_1	13.75
F_{lx}	6	R_{i1}	3
R_i	6		

As depicted in Fig. 5 (a), the circular ring-shaped MS wavefront modulation capability introduces new resonance points at both high and low frequencies while shifting the original antenna's resonance to lower frequencies. The merging of these multi-resonance modes achieves a broadband impedance bandwidth of 4.1-7.5 GHz, fully covering the C-band. Post-integration of

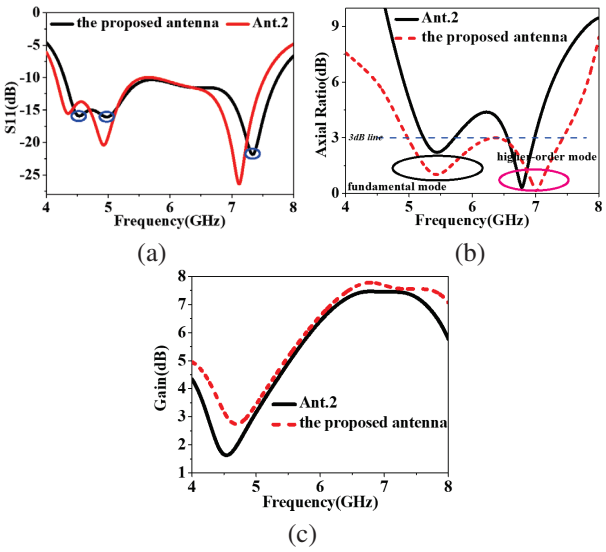

Fig. 5. Comparison of the simulated results of (a) S11, (b) Axial Ratio, and (c) GainTotal in the main lobe for Ant.2 and the proposed antenna.

the MS superstrate results in a global reduction of the AR within the -10 dB impedance bandwidth, with a new AR minimum of 2.2 dB emerging at 5.45 GHz. However, a mid-band AR discontinuity (4.8-5.3 GHz) hinders the formation of a continuous CP response. The gain profile demonstrates attenuation at band edges, peaking at 7.45 dBic at 7.1 GHz (a 1.45 dB improvement over the baseline design) with an average gain of 5.3 dBic across the operational bandwidth. To address the mid-band discontinuity and enhance coupling synergy between the oblique elliptical slot antenna and MS hybrid radiator, an asymmetric parasitic patch is embedded between the MS superstrate and slot layer as shown in Fig. 4 (b). This patch, offset by 1 mm along the +x-axis and separated from the lower dielectric by a 0.5 mm air cavity, disrupts structural symmetry to excite additional resonant modes. HFSS-optimized results (see Fig. 5) reveal three key outcomes. First, the third resonance shifts to higher frequencies, extending the -10 dB impedance bandwidth to 7.74 GHz (10% enhancement), while the first two resonances remain spectrally stable. Second, the AR values exhibit a maximum reduction of 6.9 dB at critical frequencies, effectively bridging the mid-band gap. The low-frequency AR minimum (2.2 dB at 5.45 GHz) remains unchanged, whereas the high-frequency minimum shifts to 7.01 GHz with an ultra-low AR of 0.1 dB, achieving a 3 dB AR bandwidth of 4.97-7.44 GHz (39.8% fractional bandwidth). Third, the air cavity reduces dielectric loss, increasing the average gain by 0.43 dB with a maximum single-frequency improvement of 1.65 dB, while maintaining stable high-frequency performance despite minor low-gain fluctuations.

To further optimize the MS layer layout configuration, the 5×5 and 7×7 periodic layouts were also simulated and analyzed. It should be noted that to evaluate performance under the same radiation aperture, the overall dimensions of all MS layers remain identical at 38.5×38.8 mm^2, with their structures shown in Fig. 6. The simulated radiation performance for all three layouts is presented in Fig. 6.

As observed in Fig. 7 (a), the 5×5 and 7×7 periodic layout configurations produce only one resonance at 5.7 GHz, whereas the proposed layout generates resonances at both low and high frequencies (5 GHz and 7.39 GHz, respectively), effectively extending the -10 dB impedance bandwidth. From Fig. 7 (b), it can be seen that the 5×5 and 7×7 periodic layouts exhibit 3 dB AR notches within the 6.2-7.2 GHz band. Although the 7×7 layout shows an improvement (with AR values around 4 dB within the notch frequency range), the 3 dB AR bandwidth remains discontinuous. Conversely, the 6×6 layout bridges the intermediate band, effectively extending the bandwidth. Regarding gain performance, as shown in Fig. 7 (c), the 5×5 and 7×7 layouts achieve peak gains higher by 1 dB and 0.5 dB, respectively, compared to the adopted layout. However, the 6×6 periodic layout demonstrates optimal overall performance. Therefore, this design adopts the 6×6 periodic layout configuration.

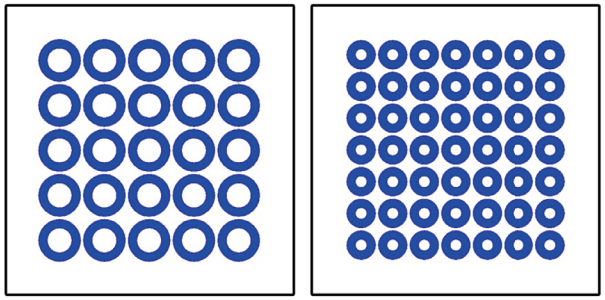

(a) (b)

Fig. 6. Two different MS layout configurations: (a) 5×5 and (b) 7×7.

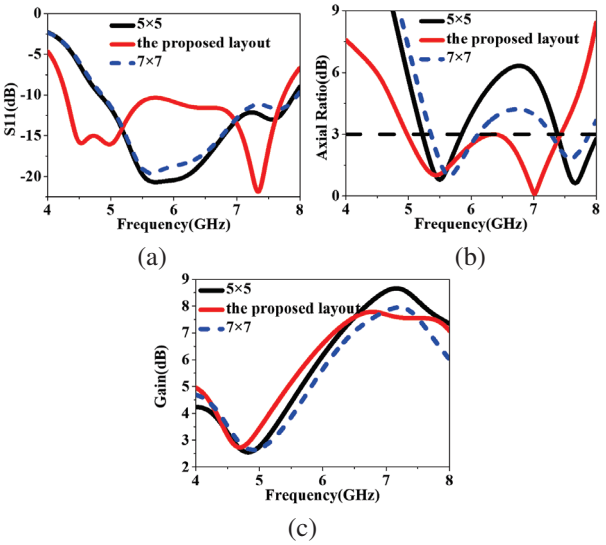

(a) (b) (c)

Fig. 7. Radiation performance of the three MS layout configuration antenna: (a) S11, (b) Axial Ratio, and (c) GainTotal in the main lobe.

B. Design principles of the parasitic patch

The microstrip patch, acting as a parasitic element, is dimensionally coupled to the resonant frequency of the primary radiator, namely the oblique elliptical microstrip patch. Near-field coupling principles and geometric matching criteria are employed to optimize the parasitic patch size. Calculations based on equation (1) reveal that the standalone resonant frequency of this patch is 19.76 GHz, significantly exceeding the target operational band (4-8 GHz). This design ensures that the parasitic patch operates through cooperative near-field coupling with the primary radiator rather than relying on independent resonance.

$$f_r \approx \frac{c}{2L_p\sqrt{\varepsilon_{eff}}}. \tag{1}$$

The design achieves three synergistic performance improvements. First, within the 6-8 GHz band, the 6 mm patch corresponds to an electrical size of 0.16λ-0.21λ, satisfying the magnetic dipole resonance condition to enhance high-frequency radiation efficiency via inductive coupling. Second, the compact parasitic patch induces strong electric field gradients along the slot edges, refining the high-frequency phase distribution and suppressing AR degradation by balancing orthogonal field components critical for CP generation. Third, occupying only 1.44% of the primary radiator area, the patch introduces negligible obstruction to the slot's radiation pattern, preserving radiation efficiency while enabling broadband operation.

To further validate these mechanisms, current distributions on the circular ring-shaped MS superstrate of Ant.2 and the proposed antenna were simulated at 7.0 GHz (see Fig. 8). In the proposed design (see Fig. 8 (a)), a closed-loop current distribution is observed along the major axis of the oblique elliptical slot, satisfying the necessary condition for CP radiation. Conversely, Ant.2 (see Fig. 8 (b)) exhibits dispersed peak currents along the slot's major axis with mutually canceling vector components, failing to establish coherent current circulation for CP operation. These results demonstrate that the parasitic patch perturbs high-frequency currents and synergistically interacts with the MS to achieve phase compensation. This interaction extends the CP bandwidth while enhancing radiation efficiency, advancing confor-

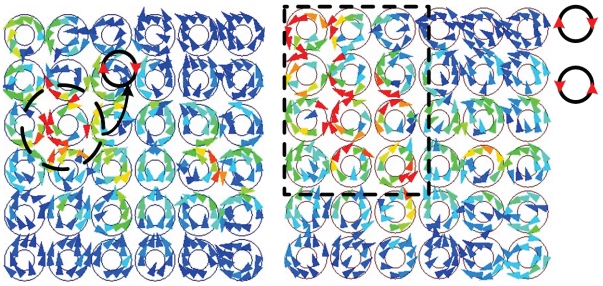

(a) (b)

Fig. 8. Current distributions on the ring-shaped MS for Ant.2 and the proposed antenna.

mal antenna design through a synergistic integration of near-field coupling and geometric optimization.

The parasitic patch (see Fig. 8 (a)) perturbs surface currents to form closed-loop circulation at 7 GHz, enabling coherent CP radiation. This contrasts with [18]'s metasurface-only approach, which exhibited canceling currents (see Fig. 8 (b)). Our time-domain analysis (see Fig. 9) further confirms LHCP via counterclockwise vector rotation-a physical insight absents in [18] or [19].

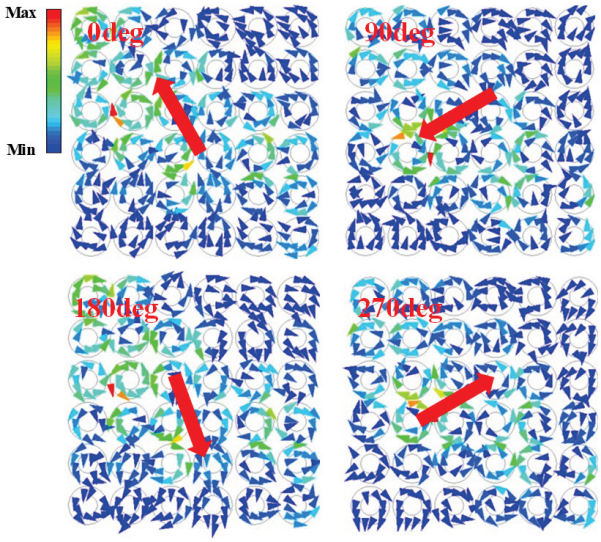

Fig. 9. Surface current vectors on the MS layer at 7 GHz in one period.

To further validate the CP characteristics of the designed antenna in the high-frequency regime, a time-domain analysis of surface current vector evolution on the MS layer was conducted at 7 GHz over one full temporal cycle. As depicted in Fig. 9, at $t = 0$, the current vector tip points to the upper-left direction. After a quarter-period interval (T/4), the vector orientation shifts to the lower-left direction. At t = T/2, the vector points to the lower-right direction. At t = 3T/4, it rotates to the upper-right direction. This sequential 90° directional change at each T/4 interval results in a counterclockwise circular trajectory of the vector tip. This rotational behavior confirms the realization of left-hand circular polarization (LHCP) radiation by the antenna, thereby experimentally verifying the effectiveness of the proposed design.

III. ANALYSIS OF CIRCULAR POLARIZATION PRINCIPLE

To validate CP performance, full-wave simulations were conducted to characterize the amplitude and phase of the far-field electric field in the circular ring-shaped MS-based oblique slot antenna. In the Cartesian coordinate system, the electric field is decomposed into two orthogonal components, E_x and E_y. Ideal CP radiation requires $|E_x| = |E_y|$ with a 90° phase difference ($\Delta\varphi = E_y - E_x = \pm 90°$). For practical engineering applications, CP is considered acceptable if $||E_x| - |E_y|| \leq 3\ dB$ and $|\Delta\varphi - 90°| \leq 15°$

As depicted in Fig. 10, these criteria were applied to analyze Ant.2 and the proposed antenna. For Ant.2, CP operation is limited to two isolated frequency bands, namely 5.2-5.7 GHz and 6.6-6.9 GHz, with a mid-band discontinuity (4.8-5.3GHz) caused by destructive interference between E_x and E_y. In contrast, the proposed design achieves a continuous 3 dB AR bandwidth of 5.1-7.4 GHz through MS-enabled mode merging and parasitic patch coupling. This result aligns with the earlier 3 dB AR bandwidth analysis (see Fig. 5), confirming the design's wideband CP performance.

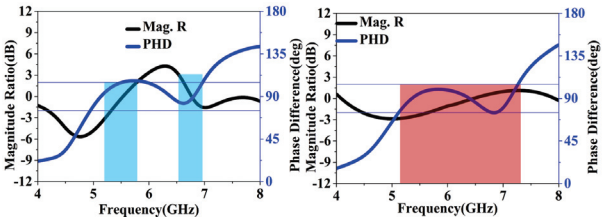

(a) (b)

Fig. 10. Simulated magnitude ratio and phase difference in the orthogonal x- and y-components of the far electric field for (a) Ant.2 and (b) the proposed antenna.

IV. RADIATING MECHANISM OF THE MS-BASED ANTENNA

To investigate the radiation characteristics of the circular ring-shaped MS (Ant.2), Figs. 11 (a,b) present simulated electric field distributions on the central vertical plane at 4.94 GHz and 7.12 GHz. Transmission-line model in Ansys Electronics Desktop is shown in Fig. 12 (a) and the dispersion characteristics of the ring-shaped unit cell, obtained through full-wave simulations,

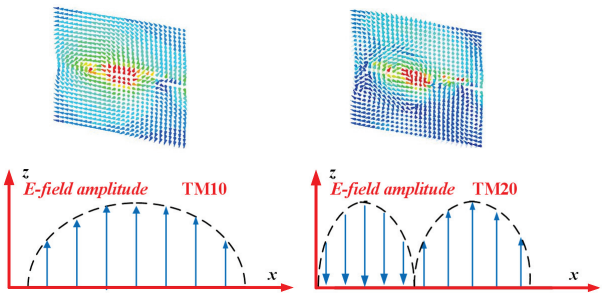

(a) (b)

Fig. 11. Simulated electric field intensity profiles along the central axis of Ant.2 corresponding to different resonant modes are presented: (a) TM10 mode at 4.94 GHz and (b) TM20 mode at 7.12 GHz, accompanied by a schematic diagram illustrating the fundamental operating principle.

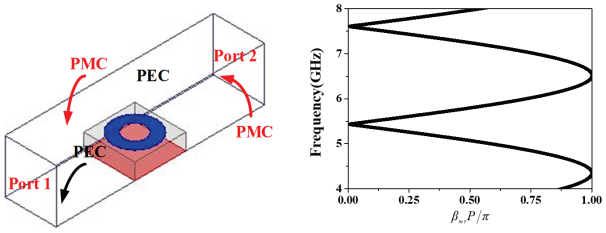

(a) (b)

Fig. 12. (a) Transmission-line model in Ansys Electronics Desktop and (b) dispersion diagrams of the circular ring-shaped MS unit cell.

are shown in Fig. 12 (b), where the dispersion curves exhibit remarkable consistency with conventional circular microstrip units. These frequencies align with the primary and secondary resonant peaks of Ant.2 in Fig. 11 (a). Although a secondary resonance occurs at 4.4 GHz, the 4.94 GHz frequency is selected as the fundamental resonance for analytical coherence due to insufficient amplitude distinction between adjacent spectral components. For comparative analysis, theoretical predictions of TM10 and anti-phase TM20 mode distributions from rectangular patch cavity models are superimposed. The observed field patterns demonstrate topological similarity to standard patch antenna modes, with structural distinctions primarily arising from radiation gaps between IHMS cell arrays. These inter-element apertures effectively reduce the quality factor (Q) compared to conventional rectangular patches, consequently improving impedance bandwidth performance.

Notably, surface wave propagation along Ant.2's upper layer induces supplementary resonance mechanisms, which contribute to bandwidth enhancement. When the substrate thickness h_s satisfies $h_s << \lambda_0$ (free-space wavelength) and MS array dimensions meet specific constraints, the resonance behavior can be analyzed using an equivalent transmission-line model. The spatial periodicity parameters p_x and p_y govern the x- and y-direction configurations, respectively. Mathematical expressions for TM10 and TM20 mode resonance frequencies follow the formulation detailed in reference [20], ensuring theoretical consistency with established microwave engineering principles.

An additional resonance mechanism is induced by surface wave propagation along the top layer of the Ant.2 structure, which contributes to impedance bandwidth expansion. When the substrate height (h_s) is much smaller than both the vacuum wavelength and the MS array width, the resonant characteristics can be analyzed using a simplified transmission-line model. Parameters p_x and p_y denote the unit cell periodicity in orthogonal directions. The mathematical expressions for TM10 and TM20 resonant frequencies are provided in [20].

$$\beta_{mr} p N_x + 2\beta_{eff}\Delta L = p, \tag{2}$$

$$\frac{\beta_{mr} p N_x}{2} + 2\beta_{eff}\Delta L = p, \tag{3}$$

The propagation constant β, in conjunction with parameters N_x and N_y denoting the number of unit cells in orthogonal dimensions (both configured as 6 in this study), serves as key determinants of the proposed antenna's behavior. Peripheral fringing fields at the unit cell array edges introduce additional length extensions ΔL_x and ΔL_y in both propagation axes. The mathematical expressions for these extended lengths are detailed in equations (4)-(7).

$$\frac{\triangle L}{h} = 0.412 \times \frac{\left(\varepsilon_{reff} + 0.3\right)\left(\frac{L_p}{h} + 0.262\right)}{\left(\varepsilon_{reff} - 0.258\right)\left(\frac{L_p}{h} + 0.813\right)}, \tag{4}$$

$$e_{reff} = \frac{e_r + 1}{2} + \frac{e_r - 1}{2}\left(1 + 12\frac{h}{W_p}\right)^{-\frac{1}{2}}, \tag{5}$$

$$W_p = N_y p - g, \tag{6}$$

Three critical parameters govern the proposed antenna's characteristics: substrate height (h_s), relative permittivity (ε_r), and unit cell array effective width (L_p) in transverse dimensions. The propagation constants for edge-extended regions are mathematically defined in equation (6).

$$\beta_{reff} = k_0\sqrt{e_{reff}} = \frac{2pf}{c}\sqrt{e_{reff}}. \tag{7}$$

Figure 12 (b) depicts the dispersion characteristics extracted from full-wave simulation S-parameters. Antenna design employs TM modes in RH region, with theoretical TM10 and counter-phase TM20 resonant frequencies calculated as 4.9 GHz and 7.05 GHz via equations (2)-(3). Modal resonance points are identified at $\beta/\beta 0 = 0.055$ and 0.72 on the dispersion curves. Significantly, predicted TM10 (4.94 GHz) and TM20 (7.12

GHz) resonances align closely with Ant.2's measured 4.9 GHz and 7.12 GHz resonant peaks, demonstrating <0.8% deviation. This dispersion analysis validates the transmission-line model's ability to explain the proposed antenna's radiation mechanism.

V. SIMULATION ANALYSIS AND EXPERIMENTAL VALIDATION

To further validate the proposed design, the antenna prototype was fabricated and experimentally characterized. It should be noted that, during the fabrication process, a 0.5-mm air-layer was created by embedding 2×2 mm^2 dielectric substrates (with identical electromagnetic parameters and 0.5-mm thickness) in the four corner regions of the oblique elliptical slot layer surrounding the nylon supporting pillars. This configuration forms the air cavity while maintaining structural support for the MS layer.

The near-field parameters were measured using a vector network analyzer, while far-field radiation characteristics were evaluated in an anechoic chamber. The experimental results are presented in Figs. 13–14. Figure 13 (a) demonstrates that the measured -10 dB impedance bandwidth extends from 4.28 GHz to 7.92 GHz, exceeding simulation predictions. The measured resonant depths show an average reduction of 1.55 dB compared with simulated results, with a maximum deviation of 2 dB, indicating excellent impedance matching performance. Figure 11 (b) reveals a 3-dB AR bandwidth

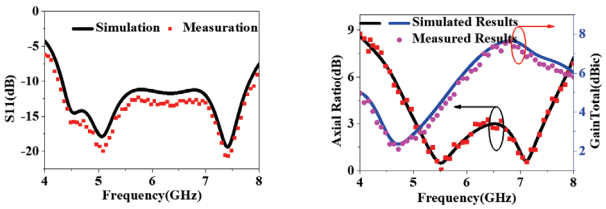

(a) (b)

Fig. 13. Simulated and measured results of the proposed circular ring-shaped MS-based antenna (a) S11 and (b) Axial Ratio and GainTotal.

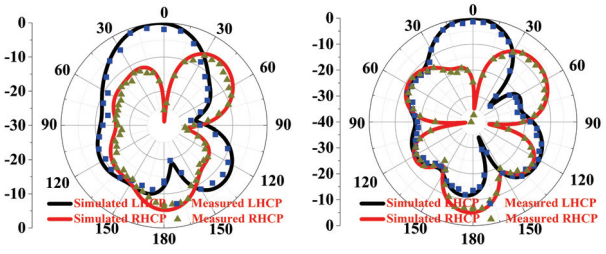

(a) (b)

Fig. 14. Normalization radiation pattern at 7 GHz in the (a) *xoz* plane and (b) *yoz* plane.

from 5.06 GHz to 7.44 GHz. Although partial frequency points within 6.4-6.7 GHz approach 3 dB, the overall agreement with simulation results is favorable. The measured fractional bandwidth reaches 38%, fully contained within the -10 dB impedance bandwidth, indicating superior circular polarization radiation performance.

The measured peak gain reaches 7.61 dBic at 6.81 GHz, showing an average 0.25 dB reduction compared with simulations across the operational bandwidth, while maintaining an average gain of 5.2 dBic. Figure 14 presents the normalized radiation patterns at 7 GHz in both *xoz*- and *yoz*-planes. The measured results exhibit cross-polarization levels below -30 dB in the main beam direction, with a 3-dB beamwidth of 49° (-31° to 18°). The radiation patterns maintain left-hand circular polarization characteristics, showing good consistency with simulated results.

As shown in Fig. 15, the normalized radiation pattern at low-frequency 5.3 GHz was also analyzed. Figure 15 shows that the cross-polarization levels are consistently below -30 dB. The half-power beamwidths (HPBWs) in the E-plane and H-plane are (-52.3°∼52.3°) and (-37.7°∼25.1°), respectively, with absolute widths reaching 104.6° and 62.8°. Thus, it can be observed that the proposed MS-based antenna exhibits a broader broadside radiation characteristic at low frequencies compared to high frequencies. This result consequently validates the design of the proposed MS-based antenna.

As shown in Fig. 16, the radiation efficiency of the antenna was also analyzed in depth. It can be seen from Fig. 16 that the radiation efficiency within the operational bandwidth remains above 87.5%, with a maximum radiation efficiency of 93.9% occurring at 6 GHz. This demonstrates the favorable performance of the proposed MS-based antenna.

These comprehensive measurements confirm that the proposed antenna successfully achieves broadband operation, high gain, and excellent circular polarization performance, fulfilling the design objectives for advanced wireless communication systems.

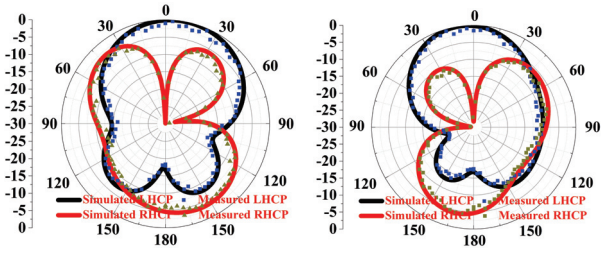

(a) (b)

Fig. 15. Normalization radiation pattern at 5.3 GHz in the (a) *xoz* plane and (b) *yoz* plane.

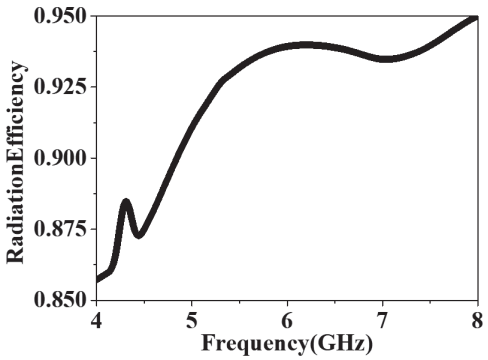

Fig. 16. Simulated radiation efficiency.

VI. ANALYSIS OF THE CONFORMAL ANTENNA WITH THE DIFFERENT BENDING RADII

A. Radiation performance of conformal antenna with different bending radii

When the proposed antenna is subjected to bending deformation, as illustrated in Fig. 17, both the dielectric substrate and the deposited metallic patch undergo corresponding geometric transformation. This mechanical deformation induces spatial reconfiguration of the EM field distribution, thereby perturbing the radiation characteristics along the principal beam direction.

To evaluate the conformal adaptability of the proposed antenna design, radiated performance stability analysis under different radii of curvature was performed as presented in Fig. 10. The simulation results in Fig. 18 (a) demonstrate that across curvature radii of 20 mm, 30 mm, and 40 mm, the reflection coefficient maintains its resonant profile with minimal deviation in the -10 dB impedance bandwidth. Although slight variations are

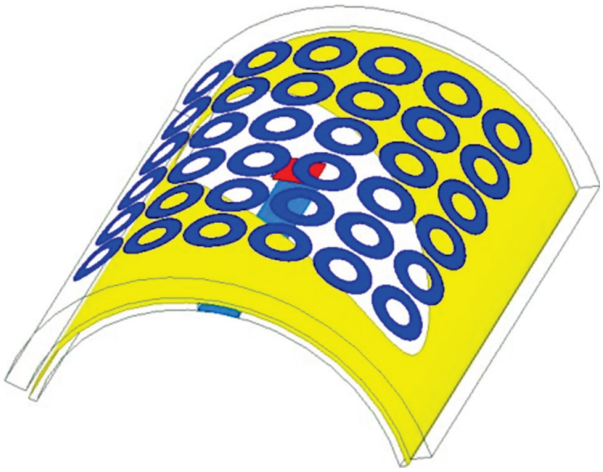

Fig. 17. 3D view of the proposed MS-based conformal antenna with bending radii of 20 mm.

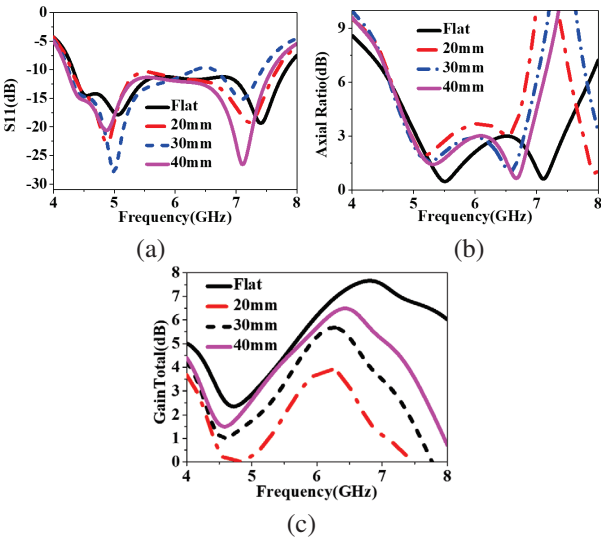

Fig. 18. Antenna performance with the different bending radii: (a) S11, (b) Axial Ratio, and (c) GainTotal in the main lobe.

observed in the resonance dip depth, the integrated operational bandwidth exhibits robust stability with negligible impedance bandwidth fluctuations.

As shown in Fig. 18 (b), with increasing bending degree (curvature radius decreasing from 40 mm to 20 mm), the minimum AR value in the high-frequency band becomes larger, and the frequency corresponding to this minimum AR shifts toward lower frequencies after bending, with an approximate offset of 200 MHz. Meanwhile, the minimum AR values in the low-frequency band exhibit smaller fluctuations but show a slight increase compared to the flat state, with an elevation of about 0.3 dB. It can therefore be concluded that when the curvature radius ranges from 20 mm to 40 mm, the 3 dB AR bandwidth fluctuates within approximately 8.3%, indicating good stability in radiation performance after bending. Figure 18 (c) demonstrates that as the curvature radius decreases (i.e., bending intensifies), the peak gain of the main beam gradually reduces. For every 10 mm decrease in curvature radius, the peak gain decreases by approximately 1.5 dB. This occurs because the energy concentration along the main beam direction decreases when the antenna is bent, resulting in reduced peak gain. Through this analysis, it is evident that the designed antenna maintains favorable performance stability across multiple curvature radii, demonstrating good conformal capability suitable for multi-curvature platforms.

B. Analysis of the conformal antenna

To further illustrate the continuous decrease in main beam gain with reducing bending radius, it is recognized that as the bending radius gradually decreases, the

Table 2: Performance comparisons with the related reported works

Related Reported Antenna	Size ($\lambda_0{}^3$)	S11 (GHz)	3 dB AR Bandwidth (GHz)	Peak Gain (dBic)	Radiating Structure	Efficiency	Performance Stability in Curvature Radius Range	Technique Utilized
Proposed Antenna	**0.05 (height)**	**4.28-7.92**	**5.06-7.44**	**7.61**	**Elliptical slot + Circular ring MS + Parasitic patch**	**>87.5% (Peak 93.9%)**	**Stable (AR fluctuation<8.3%, Gain drop≤1.5 dB/10 mm) for 20-50 mm radii**	**Air-layer embedded parasitic patch + Multi-curvature optimized MS**
[18]	4.1 × 1.14 × 0.05	3.95-4.8	3.9-4.7 (18.6%)	5.5	Transparent PET metasurface	>60%	Not studied	Transparent conformal metasurface
[19]	0.9 × 0.9 × 0.07	5.02-9.12 (Free space)	5.34-8.10 (41.07%)	4.37 (Free space)	Hexagonal slot + Nonuniform MS	74-81%	Stable for bending (30-50 mm radii)	All-textile nonuniform MS
[21]	1 × 1 × 0.1	4.39-7.15	5.43-6.76 (24.4%)	9.35	Slot antenna + INMS	Not provided	Not studied (Planar)	Improved nonuniform metasurface (INMS)
[22]	Not specified	4.3-4.6	4.25-4.58 (7.3%)	11.39	Capacitive-loaded metasurface	Not provided	Not studied	Miniaturized capacitive loading
[23]	0.34 × 0.33 × 0.046	1.58-1.665	1.58-1.67 (5.5%)	5.05 (Measured)	Triangular patches + Shorting pins	Not provided	Not studied	CMA-based coupled resonators
[24]	Not specified	11.2 (Resonant)	1.6% Fractional bandwidth	14.335 (Conformal)	Microstrip array	Not provided	Stable for vehicle roof curvature	Amplitude tapering feed

antenna's physical structure becomes more curved, causing the radiating surface to bend accordingly. Consequently, the field distribution in space changes. To clarify this phenomenon, a plane parallel to the antenna's radiating surface at 10 mm distance was established for the flat state. The electric field distributions under different states were analyzed through simulation to visually reflect the electromagnetic energy distribution, with results shown in Fig. 19. Figure 19 (a) shows that when the antenna is flat, radiated energy concentrates in the main beam direction. However, when bent with a 30 mm radius, the energy distribution shifts and spreads outward. Thus, simulation results demonstrate that antenna bending causes electromagnetic energy to redistribute in space, reducing energy in the main beam direction. This results in continuously decreasing main beam energy with smaller bending radii, consistent with the gain radiation performance observed in HFSS simulations (see Fig. 18), thereby validating the design. It should be noted that, although main beam gain decreases, the circular polarization radiation characteristics and impedance bandwidth performance remain essentially unchanged.

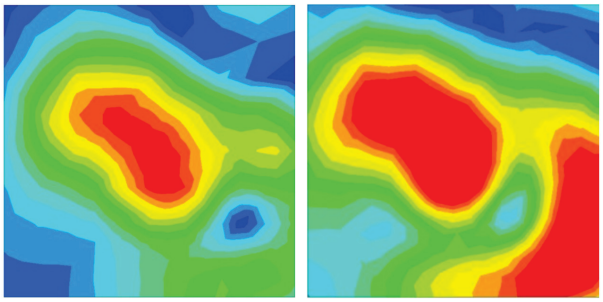

(a) (b)

Fig. 19. E-field magnitude distribution in the plane parallel to the MS at 10 mm distance: (a) flat configuration and (b) bent configuration with 30 mm radius.

VII. CONCLUSION

This paper presents a metasurface (MS) enhanced conformal circularly polarized (CP) antenna achieving broadband operation and curvature stability through three synergistic innovations. By integrating a tilted elliptical slot radiator with an annular MS superstructure, the design attains 38.7% axial ratio (AR) bandwidth via optimized modal phase compensation. A strategically embedded eccentric patch-air cavity combination extends impedance bandwidth to 42.1% (5.2-7.9 GHz) through controlled excitation of higher-order modes, while maintaining curvature-adaptive performance with $<$5% AR variation (ΔAR$<$0.25 dB) across bending radii from 10 mm to 50 mm (0.17λ-0.83λ at 5.2 GHz). Experimental verification demonstrates 8.2 dBi peak gain and 2.4 GHz CP bandwidth, representing a 63% improvement over conventional curved CP antennas. The methodology combines characteristic mode analysis with multi-physics optimization, establishing a framework for curvature-resilient antenna design. Measured results validate the simulation-predicted performance metrics, confirming the architecture's suitability for satellite communications and 5G systems requiring polarization-stable conformal integration. This work advances conformal CP antenna technology through its systematic fusion of MS engineering, multi-mode bandwidth enhancement, and quantified curvature compensation strategies. Future work may focus on multi-physics coupling optimization for complex curved surfaces, extension to terahertz bands, integration with reconfigurable intelligent surface for 6G, multifunctional design for biomedical applications, and fabrication process improvement via 3D printing to enhance engineering applicability.

ACKNOWLEDGMENT

This work was supported in part by the Natural Science Foundation of Hubei Province under Grant 2023AFB452.

REFERENCES

[1] K. Li, Y. Liu, Y. Jia, and Y. J. Guo, "A circularly polarized high gain antenna with low RCS over a wideband using chessboard polarization conversion metasurfaces," *IEEE Trans. Antennas Propag.*, vol. 65, pp. 4288-4292, 2017.

[2] H. X. Xu, Y. Shao, H. Luo, Y. Wang, and C. Wang, "Janus reflective polarization-division metadevices with versatile functions," *IEEE Trans. Microw. Theory Tech.*, vol. 71, pp. 3273-3283, 2023.

[3] H. Tran-Huy, H.-H. Nguyen, and T. H. T. Phuong, "A compact metasurface-based circularly polarized antenna with high gain and high front-to-back ratio for RFID readers," *PLoS One*, vol. 18, no. 8, p. e0288334, 2023.

[4] S. Yang, Z. Yan, M. Cai, and X. Li, "Low-profile dual-band circularly polarized antenna combining transmitarray and reflectarray for satellite communications," *IEEE Trans. Antennas Propag.*, vol. 70, no. 7, pp. 5983-5992, July 2022.

[5] Z. Chen, W. Feng, Y. Yang, Y. Yu, D. Guan, and L. Sun, "Low-profile all-metal dual-band dual-polarized shared-aperture phased arrays for UAV applications," *IEEE Internet Things J.*, vol. 12, no. 15, pp. 31466-31476, Aug. 2025.

[6] S. Bhattacharjee, S. Maity, S. R. B. Chaudhuri, and M. Mitra, "A compact dual-band dual-polarized omnidirectional antenna for on-body applications," *IEEE Trans. Antennas Propag.,* vol. 67, no. 8, pp. 5044-5053, Aug. 2019.

[7] C. E. Santosa and J. T. S. Sumantyo, "Conformal subarray antenna for circularly polarized synthetic aperture radar onboard UAV," in *2020 International Symposium on Antennas and Propagation*, pp. 5-6, July 2021.

[8] D. Wu, J. Liang, and L. Ge, "A wideband dual-circularly polarized series-fed corner-truncated patch array using coplanar proximity coupling," *IEEE Trans. Antennas Propag.,* vol. 72, no. 4, pp. 3292-3301, Apr. 2024.

[9] Z. Hu, Q. Lin, J. Pan, and L.-H. Liang, "Slow-wave dielectric helical structure and its applications in compact omnidirectional circularly polarized antennas," *IEEE Antennas Wireless Propag. Lett.*, vol. 24, no. 7, pp. 1655-1659, July 2025.

[10] Z.-H. Mu, C.-X. Chen, J.-N. Ma, Y.-H. Zhao, and Q. Chen, "Wideband circularly polarized array antenna based on weakly coupled sequential phase feed network," *Microw. Opt. Technol. Lett.*, vol. 64, no. 1, pp. 168-173, Jan. 2022.

[11] X. Gao, L. Y. He, S. J. Yin, C. H. Wang, G. F. Wang, X. M. Xie, H. Xiong, Q. Cheng, and T. J. Cui, "Ultra-wideband low-RCS circularly polarized antennas realized by bilayer polarization conversion metasurfaces and novel feeding networks," *IEEE Trans. Antennas Propag.*, vol. 72, no. 2, pp. 1959-1964, Feb. 2024.

[12] T. H. Lee, J. Jung, and S. Pyo, "Circularly polarized 4×4 array antenna with a wide axial ratio bandwidth," *Electronics*, vol. 13, no. 11, p. 2076, June 2024.

[13] X. Wang, X. Xing, Z. Zhao, J. Li, and Q. Yu, "Dual-band polarization conversion metasurface-assisted compact high-efficiency RFID reader antenna design," *IEEE Trans. Antennas Propag.*, vol. 72, no. 11, pp. 8810-8815, Nov. 2024.

[14] D. Ding, W. Ren, Z. Xue, and W. Li, "A low-profile spin-decoupled folded reflect array antenna with dual-circularly polarized beams," *IEEE Antennas*

Wireless Propag. Lett., vol. 24, no. 5, pp. 1040-1044, May 2025.

[15] S. Xu, Y. Shen, Z. Wei, and S. Hu, "Low-profile circularly polarized hybrid antenna for beam switching and OAM mode switching," *IEEE Trans. Antennas Propag.*, vol. 73, no. 1, pp. 33-43, Jan. 2025.

[16] X. Gao, S. Yin, G. Wang, C. Xue, and X. Xie, "Broadband low-RCS circularly polarized antenna realized by nonuniform metasurface," *IEEE Antennas Wireless Propag. Lett.*, vol. 21, no. 12, pp. 2417-2421, Dec. 2022.

[17] Q. Zheng, C. Guo, J. Ding, M. O. Akinsolu, B. Liu, and G. A. E. Vandenbosch, "A wideband low-RCS metasurface-inspired circularly polarized slot array based on AI-driven antenna design optimization algorithm," *IEEE Trans. Antennas Propag.*, vol. 70, no. 9, pp. 8584-8589, Sep. 2022.

[18] T. Liu, L. Liu, H. Sun, Z. Jin, and L. F. Chernogor, "A broadband circularly polarized antenna based on transparent conformal metasurface," *IEEE Antennas Wireless Propag. Lett.*, vol. 22, no. 12, pp. 3197-3201, Dec. 2023.

[19] T. T. Le, Y. D. Kim, and T. Y. Yun, "All-textile enhanced-bandwidth polarization-conversion antenna using a nonuniform metasurface," *IEEE Antennas Wireless Propag. Lett.*, vol. 22, no. 10, pp. 2432-2436, Oct. 2023.

[20] Q. Chen, H. Zhang, Y.-J. Shao, and T. Zhong, "Bandwidth and gain improvement of an L-shaped slot antenna with metamaterial loading," *IEEE Antennas Wireless Propag. Lett.*, vol. 17, no. 8, pp. 1411-1415, Aug. 2018.

[21] Q. Chen, J. Yang, C. He, L. Hong, T. Yan, F. Yu, D. Zhang, and M. Huang, "Bandwidth and gain improvement of a circularly polarized slot antenna using nonuniform metasurface," *Applied Computational Electromagnetics Society (ACES) Journal*, vol. 39, no. 9, pp. 786-793, Sep. 2024.

[22] J. Yue, W. C. Yang, and W. Q. Che, "Miniaturized low-profile circularly polarized metasurface antenna using capacitive loading," *IEEE Trans. Antennas Propag.*, vol. 67, no. 5, pp. 3527-3532, May 2019.

[23] T. L. Yang, X. Zhang, Q. S. Wu, and T. Yuan, "Miniaturized wideband circularly polarized triangular patch antennas based on characteristic mode analysis," *Applied Computational Electromagnetics Society (ACES) Journal*, vol. 38, no. 10, pp. 783-791, Oct. 2023.

[24] E. Abishek, R. Subramaniam, P. Ramanujam, and M. Esakkimuthu, "Low-profile circularly polarized conformal antenna array with side lobe suppression for vehicular SATCOM applications," *Applied Computational Electromagnetics Society (ACES) Journal*, vol. 38, no. 6, pp. 439-447, June 2023.

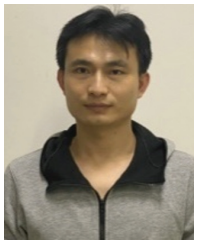

Qiang Chen was born in Jiangxi, China. He received the master and Ph.D. degree from Air Force Engineering University (AFEU), Xi'an, in 2015 and 2019, respectively. He is currently a lecturer with Air Force Early Warning Academy, Wuhan, Hubei. His research interests include microwave circuits, antennas, and arrays.

Jun Yang was born in 1973. He received his Ph.D. degree from Air Force Engineering University, Xian, China, in 2003. Now, he is an associate professor at the Air Force Early Warning Academy, Wuhan, Hubei. His research interest covers radar system, radar imaging, and compressed sensing.

Changhui He was born in 1973. She received the master's degree from Central China Normal University, Hubei, China. She is currently an associate professor at Air Force Early Warning Institute. She is interested in electromagnetic field, microwave technology, and antenna design. She has published over 20 technical papers and authored one book. She holds four national invention patents.

Liang Hong was born in Wuhan, China. He received the B.S. and M.S. degrees from Huazhong University of Science and Technology, Wuhan, China, in 2005 and 2011, respectively. His research interests include microwave devices and microwave technology.

Di Zhang received the B.S., M.S., and Ph.D. degrees from Air Force Engineering University (AFEU), Xi'an, China, in 2013, 2015, and 2019, respectively. He is currently a lecturer with Air Force Early Warning Academy, Wuhan, Hubei. His research interests include RF orbital angular momentum antennas, reflect array antennas, and metasurface.

Li Zhang , Department of Early Warning Technology, Air Force Early Warning Academy Wuhan, Hubei, China, received his master's degree in Radio Physics Major from Lanzhou University in 2016. His research interests mainly focus on Metamaterials and Computational Electromagnetics. He has been actively involved in several research projects related to manipulation of electromagnetic wave characteristics.

Min Huang graduated from Taiyuan University of Technology, Shanxi, China, with a master's degree in physical electronics. She is now an instructor at the Air Force Early Warning Academy, Wuhan, Hubei. Her research interests are electromagnetic field and microwave technology.

FEM Simulation of Severe Stator Winding Inter-turn Short Circuit Faults of Outer Rotor DFIG

H. Mellah[1,2], A. Maafa[1], H. Sahraoui[3], A. Yahiou[1,2], S. Mouassa[1,2], and K. E. Hemsas[2]

[1]Electrical Engineering Department
Faculty of Applied Sciences, University of Bouira, Bouira 10000, Algeria
h.mellah@univ-bouira.dz, omaafa@univ-bouira.dz, abdelghani.yahiou@univ-bouira.dz
souhil.mouassa@univ-bouira.dz

[2]Electrical Engineering Department
LAS Laboratory, Sétif 1 University, Sétif, Algeria
hemsas_ke_dz@univ-setif.dz

[3]Electrical Engineering Department
University of Chlef, Chlef, Algeria
h.sahraoui@univ-chlef.dz

Abstract – Recently, in wind power generation, doubly-fed induction generators (DFIG) have been commonly employed, and their capacity is also increasing, making DFIG's security and reliability more significant. Stator winding inter-turn short-circuit faults (SWITSCF) are a prevalent flaw of theirs. In this paper, a DFIG has been modeled by the finite element method (FEM) in the healthy state and in the faulty state. Several simulations have been carried out for different number of inter turn short-circuit faults (NSWITSCF) to see their effects on the DFIG performance. SWITSCF modifies the impedance, which affects the current amplitudes and phases. As a consequence, the current is asymmetric where a negative sequence component is observed. SWITSCF gives the cause of the existence of the short-circuit current that generates an additional magnetic field. This will make the magnetic circuit largely saturated. Furthermore, with the NSWITSCF increasing, these negative effects appear stronger and move away from a healthy state.

Index Terms – Doubly fed induction generator (DFIG), finite element method (FEM), number of inter turn short-circuit faults (NSWITSCF), outer rotor, wind turbine.

I. INTRODUCTION

Early in the development of human civilization, wind power was exploited, initially for the propulsion of sailing vessels and subsequently for the powering of windmills [1]. Nevertheless, a foundation for wind energy research was not created and explicitly applied to power generation until the early twentieth century, due to the work of numerous scientists in the field of aerodynamics [1, 2]. Modern wind energy conversion technology has developed since the 1970s, with rapid progress observed in the 1990s. References [1–3] show that worldwide markets are interested in renewable energy and have expanded their investments, their worldwide revenue exceeding US$285 billion, which was more than double their investment in conventional energy sources by the end of 2015. According to [3], China is the leader both for wind installations and for capacity added in 2017, followed by the USA and Germany. Different wind turbine concepts have been developed and improved, as well as various wind generators [2, 4]. Many researchers are interested in how to detect and localize the stator winding inter-turn short-circuit faults (SWITSCF) for the stator and for the rotor [5–10].

We can summarize the methods to model SWITSCF in doubly-fed induction generators (DFIG) by two approaches: analytic and numeric [5–11]. Authors [12–16] examined some of the consequences of the stator's ITSCF on DFIG performance with an internal rotor.

Wind energy is produced using DFIG, which can have either an inner [4] or an external [2] rotor. Their capacity is increasing, and the safety, reliability, and continuity of their work have become indispensable in light of the frequent energy crises. Through power electronics, grid-connection and variable wind speed operation are possible. DFIG grid connectivity problems have been addressed by numerous researchers [5–9]. These converters provide a bidirectional power flow between the machine and the network to support both modes of operation, either operating at sub-synchronous speeds or at

Submitted On: January 11, 2024
Accepted On: June 26, 2025

https://doi.org/10.13052/2025.ACES.J.400709

super-synchronous speeds [22]. The algorithm used in the power electronics converter controls the frequency, phase, and terminal voltage of the DFIG [23]. Among the most well-known DFIG faults are the inter-turn short-circuit faults (ITSCF), whether they are in the stator or rotor windings.

Over the past 10 years, research on how SWITSCF affects DFIG performances has drawn a lot of attention [24]. In addition, many scholars have studied ways to identify and locate these kinds of failure [7, 25–28]. However, before electrical faults can be detected and localized, it is necessary to first have an understanding of the differences in behavior that exist between normal and fault conditions in electrical machines.

According to the literature [13–32], there are two approaches for examining the SWITSCF through numerical simulation in all electrical machines which are analytical or numerical approaches. The analytic method is founded on multi-circuit theory [33–35]. The numerical method is usually based on finite element method (FEM) [31, 36]. In order to analyze failure detection mechanisms, having a solid understanding of the DFIG fault through simulation models and features is absolutely necessary. Several studies have looked into a FEM-based model under ITSCF conditions for the stator or rotor winding [7, 12, 14, 16, 17, 26, 37, 38].

Han et al. [39] combines the unified spiral vector model with FEM for the purpose of performance evaluation of brushless doubly-fed induction machines with different rotor winding short circuits. An analytical and numerical model is proposed in order to study the scaling effect on SWITSCF in a permanent magnet generator [40]. Afshari et al. [42] looked at SWITSCF with different numbers of inter turn short-circuit faults (NSWITSCF). However, they only looked at the current behavior of the stator, and they only took slots 4 and 19 into account.

Chen et al. [26] present work with SWITSCF verified by experimentation as well as FEM modelling. Nevertheless, this study solely looks at how SWITSCF affects current and only for specific turns. Some researchers are limited to studying how a SWITSCF affects the magnetic flux density of the DFIG [37]. Three cases of ITSCF for phase A of the rotor winding, namely 2, 5, and 12, were studied by Li and Wang in [12]. Their effects were shown on the rotor current through their time-domain and frequency-domain representations for each case, as well as on the air gap magnetic flux density and the magnetic flux density distribution over the entire machine in each case. Afshari et al. [42], studied through the stator and rotor's current spectrum formulation two closely related phenomena. They discuss SWITSCF and high-resistance connections, as well as the influence such connections have on the amount of energy that is pumped into the electrical grid during sub- and super-synchronous modes. Additionally, they covered how to differentiate between the two.

He et al. [16] provide a quantitative study of vibration, current, and loss characterization of air gap flux density distortion in the healthy case and in the short circuit case of a one-third turn of DFIG based on FEM. Chen et al. investigate how ITSCF affects stator branch currents in Phase A, expressing their findings in terms of total harmonic distortions (THD) and Park's vector trajectory under various numbers of shorted turns from 1 turn to 9 turns [38]. Fu et al. [43] compute the bilateral flux linkage between stator winding and rotor winding based on the DFIG analytical model and use it as a means of SWITSCF detection. Rehman et al. are interested in the influence of SWITSCF rotor winding at different cases on the rotor current but limited their study on 2 slots [7]. The effect of a rotor ITSCF on the radial magnetic flux density of a large hydro generator based on FEM is investigated in [44], then is offered to detect these defects.

In this study, we modelled and simulated the healthy and unhealthy behavior of DFIGs in SWITSCF situations using FEM. We are interested in seeing the effect of SWITSCF on a DFIG with an outer rotor when we simulate the same DFIG but with different numbers of SWITSCF appointed by NSWITSCF for stator phase "A". As a result, a comparison of the current time-domain representation for the three phases of a healthy and unhealthy stator has been presented, Frequency-domain representation for each case has also been investigated, and the distributions of magnetic flux density are presented for a constant speed operation.

The main objective of this research is to deal with the effect of major SITSCF on the DFIG current and magnetic distribution using the FEM and application of the FEM for the outer rotor DFIG under faults.

This paper introduces a time-domain representation of the three-phase stator currents under several NITSCFs to address the effect of this later on their wave forms. We also address the fast Fourier transform (FFT) of the stator current under different NITSCFs to clearly see their effects on the magnitude and harmonics and exploit them for future diagnostic work.

This paper is structured as follows. Section II presents a brief description of the DFIG wind turbine system. Section III presents some rating values and design specifications for the DFIG necessary to build the FEM model. Section IV deals with the simulation setup and steps and the obtained outcomes. Finally, section V concludes the paper by summarizing the findings and discussing future research directions.

II. DFIG WIND TURBINE SYSTEM

Danish scientist Poul la Cour (1846-1908) was the first to connect a windmill to a generator [45]. Three types of wind turbine are deployed in the market:

Fixed-speed wind turbine (FSWT) founded on the use of squirrel-cage induction generator (SCIG), which is connected to the grid directly via a transformer.

Variable-speed wind turbine (VSWT) based on DFIG associated with pitch control. The stator is directly connected to the grid, but the rotor is connected to the grid via a power electronics converter.

Variable-speed wind turbine based on a permanent magnet synchronous generator (PMSG), connected to the grid via an appropriate frequency converter [45].

The energy produced by a VSWT can typically be 2-6% greater than a FSWT, with one study claiming this may be as high as 39% [46]. Petersson [46] indicates that the actual value will depend on site conditions such as the speed and direction of the wind and would include all aspects of the design of the wind turbine. Moreover, a DFIG can increase significantly the energy produced by the wind turbine, with reported increases of 20% for a DFIG compared to a SCIG-based VSWT, and 60% compared to a FSWT [46].

As can be seen in Fig. 1, DFIG is frequently utilized as a primary component in wind turbine systems. In this configuration, the electrical grid is connected to both the stator winding and the rotor winding. The wind turbine converts the wind power (Pw) towards mechanical energy and the role of the DFIG is to convert this mechanical energy to electrical energy [4].

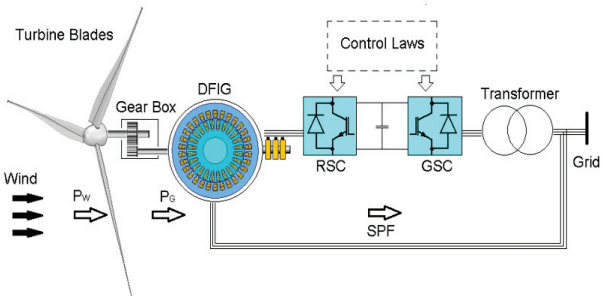

Fig. 1. Typical configuration of a DFIG wind turbine.

The relationship between the frequency of the stator voltage and the frequency of the excitation currents in the rotor is exploited to keep the generation frequency constant and matched to the grid frequency. The algorithms for this are implemented in the power electronics converter [2]. The speed of the rotating magnetic field (n_0) and the rotor shaft velocity (n) are coupled by the following equation:

$$s = 1 - (n/n_0)\,. \tag{1}$$

In the case when n is less than n_0, the stator and rotor currents are in phase and the rotor absorbs energy from the converter. In contrast, when n is greater than n_0, the stator and rotor currents are not in phase and the rotor supplies electrical energy to the converter [2, 4].The input mechanical power P_{mech} needed to reach the maximum power point (MPPT) of the wind turbine depends on the wind turbine power for the MPPT (P_{m_ref}) at the reference speed (ω_{ref}) and the mechanical rotor speed ω_m. Equation (2) should be met for MPPT [2]:

$$P_{\text{mech}} = P_{\text{m\_ref}}\left(\omega_m/\omega_{ref}\right)^3. \tag{2}$$

The mechanical loss of the rotor P_f is found in equation (3):

$$P_f = P_{f\_ref}\left(\omega_m/\omega_{ref}\right)^3, \tag{3}$$

where P_{f_ref} is mechanical loss measured at ω_{ref}, giving the electromagnetic power for the DFIG as:

$$P_{em} = \left(P_{mech} - P_f\right)/(1-S)\,. \tag{4}$$

The DFIG output electrical power in the stator at rated operation is given by equation (5):

$$P_1 = P_{em} - m_1 {I_1}^2 R_1 = m_1 V_1 I_1 \cos\varphi\ , \tag{5}$$

where m_1 is the number of stator phases (in this case 3), R_1 is the stator winding resistance of one phase and is assumed equal in all DFIG phases, V_1, I_1 and $\cos\varphi$ are the nominal values of the voltage, the current and the power factor of a stator phase. I_1 is:

$$I_1 = \frac{2\,P_{em}/m_1}{V_1\cos\varphi\ + \sqrt{(V_1\cos\varphi\ )^2 + 4R_1 P_{em}/m_1}}. \tag{6}$$

III. DFIG GEOMETRY AND FEM MODEL

In finite element modeling, the first step involves constructing and sketching the geometric contours of the DFIG model depending on the specifications of a particular device that has been chosen. Tables 1–3 contain descriptions of some of their parameters. The next stage is to distribute specific materials and their qualities among the different zones. As an illustration, copper will be utilized for the conductors. Air will be used for the spaces between the conductors. In the following stage, phenomena and parameters will be incorporated. Voltage sources and mechanical loads, shaft speed, different boundary conditions, eddy currents, and the non-

Table 1: Rating values and design specifications for the DFIG

Design Specifications	Rating Value
Rated output power	550 (W)
Rated voltage	220 (V)
Rated speed	157 (rad/s)
Poles	4
Stator slots	24
Rotor slots	30

linear behavior of the magnetic circuit are a few examples of these. Others include magnetic circuit saturation.

In order to attain the best possible outcomes, a finite element mesh is generated for each DFIG member, with an exceptionally tiny mesh being utilized for the air gap. The last step is to set the simulation parameters, which include the relative and absolute error levels, the simulation step, and the stop time.

Table 2: Dimensions of the stators and rotors periphery

Parameter	Value (mm)
Stator external diameter	120
Inside stator diameter	50
Rotor external diameter	180
Inside rotor diameter	121
Length of stator and rotor core	65

Table 3: Dimensions of the slots on both the stator and the rotor

Dimension of the Stator Slot	Value (mm)	Dimension of the Stator Slot	Value (mm)
h_{s0}	2	h_{r0}	2
h_{s1}	2	H_{r1}	2
h_{s2}	15	h_{r2}	10
b_{s0}	2.5	b_{r0}	2.5
b_{s1}	9.19419	b_{r1}	8.5281
b_{s2}	5.24462	b_{r2}	10.6303
r_s	2	r_r	2

IV. SIMULATION OUTCOMES

This section presents the results of the simulations carried out in DFIG for a healthy case and various defective cases in Phase A of the stator winding which are 4, 11, 22, 33, and 39 NSWITSCF. Figure 2 provides a perspective in three dimensions of the DFIG that was designed. Although periodic boundary conditions are commonly used in FEM simulations for their computational efficiency, the occurrence of an ITSCF in Phase A introduces asymmetry into the model. Consequently, periodicity conditions cannot be applied, and a full model must be used to accurately represent the faulted behavior.

The basic idea behind FEM is to divide the study domain into small pieces. In the ANSYS environment, the partial differential equation (PDE) is defined for each part of the DFIG. A 3D view of the DFIG outer rotor is depicted in Fig. 2. Figure 3 illustrates the mesh applied to the model. In this section, we also simulate DFIG with a different case of a NSWITSCF to show how the NSWITSCF affects the performance of DFIG.

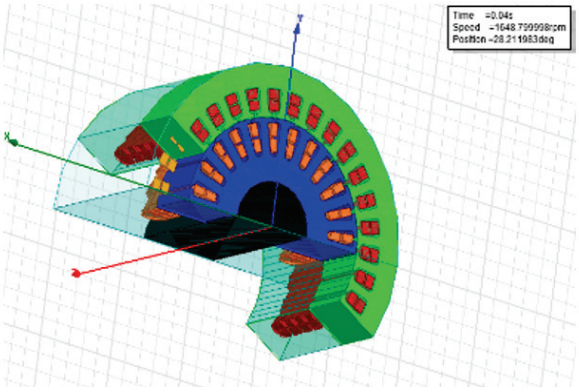

Fig. 2. Three-dimensional view of a section of the designed DFIG.

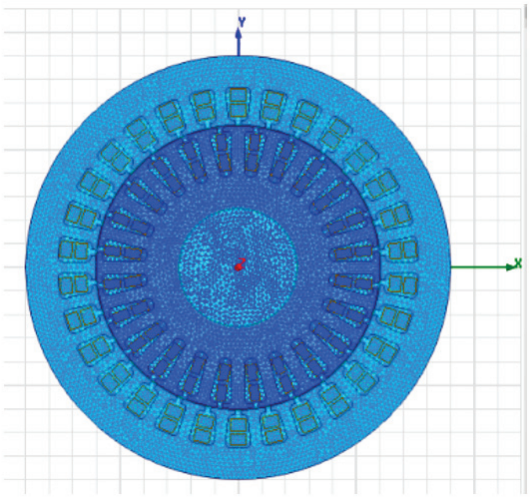

Fig. 3. 2D DFIG outer rotor mesh.

A. Stator currents of Phase A

The stator current in Phase A for a typical case and various NSWITSCF conditions is shown in Fig. 4. Figure 4 compares the stator current waveforms under healthy conditions and different ITSCF scenarios. The black solid line represents the stator current in the healthy state, exhibiting a perfect sinusoidal waveform with a peak value of 2 A. In contrast, the colored dashed and dotted lines depict the stator current behavior as ITSC severity increases, with peak values reaching up to 24 A in the most severe case. The severity of the fault is quantified by the number of inter-turn faults (NITF). A short circuit will raise the stator current and result in overheating of the winding. This is harmful and unhealthy for the machine and can shorten its life. In addition, if the current goes above the maximum supported by the winding and their insulation, it can destroy the machine and is irreversible.

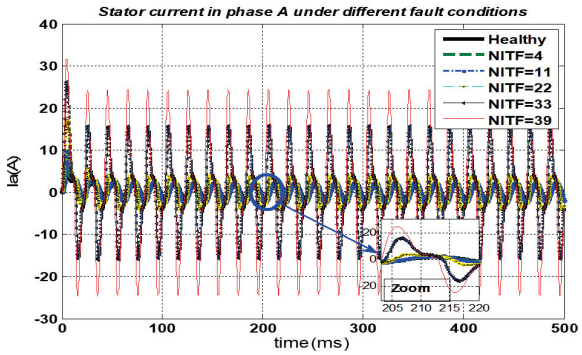

Fig. 4. Stator currents of Phase A in healthy and unhealthy NITF conditions.

To further illustrate the impact of ITSCF on DFIG performances, four parameters, namely THD, THD%, RMS (root mean square) value, and peak value, are computed and analyzed. A comparative assessment is conducted between healthy and unhealthy operating conditions for each parameter. THD% is quantified for each fault condition as the ratio of the total harmonic content in the voltage waveform to its fundamental component. The computed results are presented in Table 4. The distortion level is computed using:

$$\mathrm{THD}(\%) = \frac{\sqrt{\left(V_2^2 + V_3^2 + V_4^2 + V_5^2 + \cdots + V_m^2\right)}}{V_1} * 100. \tag{7}$$

Peak value represents the absolute maximum magnitude of the current waveform during both the transient and steady-state operation.

Table 4 presents the computed parameters cited previously for Phase A under both healthy and unhealthy conditions with varying degrees of ITSCF, identified by the NITF.

Table 4: Analysis of stator current in Phase A under healthy and unhealthy conditions

NITF	THD	THD%	RMS	Peak
Healthy	0.043	4.37%	1.54	4.97
4	0.050	5.08%.	1.66	6.45
11	0.072	7.20%	1.98	9.81
22	0.141	14.10%	2.93	15.63
33	0.357	35.78%	9.18	26.31
39	0.328	32.88%	14.34	31.64

As observed in Table 4, the results indicate that THD increases substantially with fault severity, rising from 4.37% in the healthy condition to a peak of 35.78% at NITF = 33, before slightly decreasing to 32.88% at NITF = 39. This highlights a significant degradation in power quality as the fault becomes more severe. Similarly, the RMS current initially increases with the fault, reaching a critical value of 14.35 A at NITF = 39, compared to just 1.54 A in healthy conditions. Peak current values follow a similar trend, escalating from 4.97 A to 31.64 A, which can impose extreme stress on the winding insulation. This indicates severe waveform distortion and a significant rise in harmonic content, as illustrated in Fig. 4.

These results demonstrate clearly that increasing ITSCF severity leads to elevated current magnitudes, distorted waveforms, and significantly higher harmonic content, which can compromise the operational reliability and safety of the WECS if not promptly detected and mitigated.

B. FFT of stator currents of Phase A

Figure 5 shows the FFT comparison between a healthy case and various cases of NSWITSCF. We can see from Fig. 5 that the number of turns or short circuits directly influences the amplitude of the current. We can exploit this amplitude to make a diagnosis of the state of health of the machine.

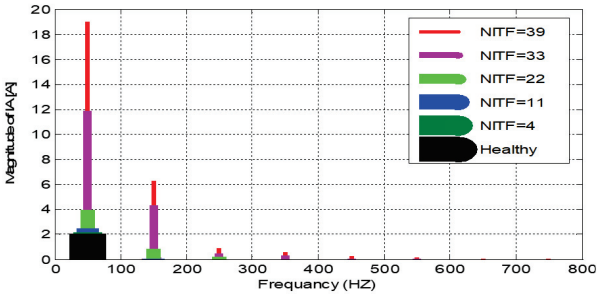

Fig. 5. FFT of Phase A current in healthy and unhealthy NITF conditions.

C. Stator currents of Phases B and C

The impact of inter-turn faults in Phase A on the current in Phases B and C is depicted in Figs. 6 and 7. From these results, we can observe that their effects on

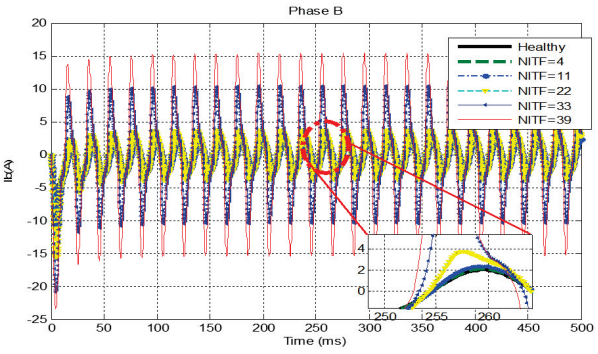

Fig. 6. Stator currents of Phase B in healthy and unhealthy NITF conditions.

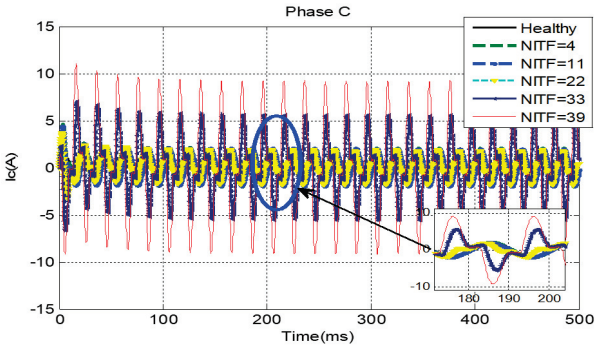

Fig. 7. Stator currents of Phase C in healthy and unhealthy NITF conditions.

the B and C phases are significant. We can see that in short-circuit situations where the current amplitude becomes more important, the system will become imbalanced with each increase in NITSCF.

Tables 5 and 6 illustrate the impact of ITSCF on the current characteristics of Phases B and C in terms of THD, THD%, RMS, and Peak. For Phase B, THD increases from 5.42% in the healthy condition to 30.24% at the most severe fault condition. This is accompanied by a sharp rise in RMS current from 1.7 A to 9.18 A and peak current from 7.94 A to 23.52 A. Notably, Phase C is also affected by the ITSCF occurring in Phase A, exhibiting a similar response to that of Phase B, as shown in Table 6 and Fig. 7. THD escalates from 3.89%

Table 5: Analysis of stator current in Phase B under healthy and unhealthy conditions in Phase A

NITF	THD	THD%	RMS	Peak
Healthy	0.054	5.42%	1.70	7.94
4	0.054	5.43%	1.80	8.92
11	0.058	5.84%	2.04	11.11
22	0.141	14.10%	2.93	15.63
33	0.298	29.85%	6.31	20.88
39	0.302	30.24%	9.18	23.52

Table 6: Analysis of stator current in Phase C under healthy and unhealthy conditions in Phase A

NITF	THD	THD%	RMS	Peak
Healthy	0.038	3.89%	1.50	4.60
4	0.041	4.17%	1.47	4.57
11	0.058	5.83%	1.39	4.40
22	0.345	34.51%	1.13	3.68
33	0.534	53.43%	3.02	7.00
39	0.402	40.21%	5.25	11.01

under normal operation to a maximum of 53.43% at NITF = 33, which is the highest among all three phases. RMS value rises from 1.50 A in the healthy case to 5.25 A for NITSF = 39, and peak current rises from 4.60 A to 11.01 A.

D. 2D distribution of magnetic flux density

Distribution of magnetic flux density is shown in Fig. 8 for both the normal case and various stator

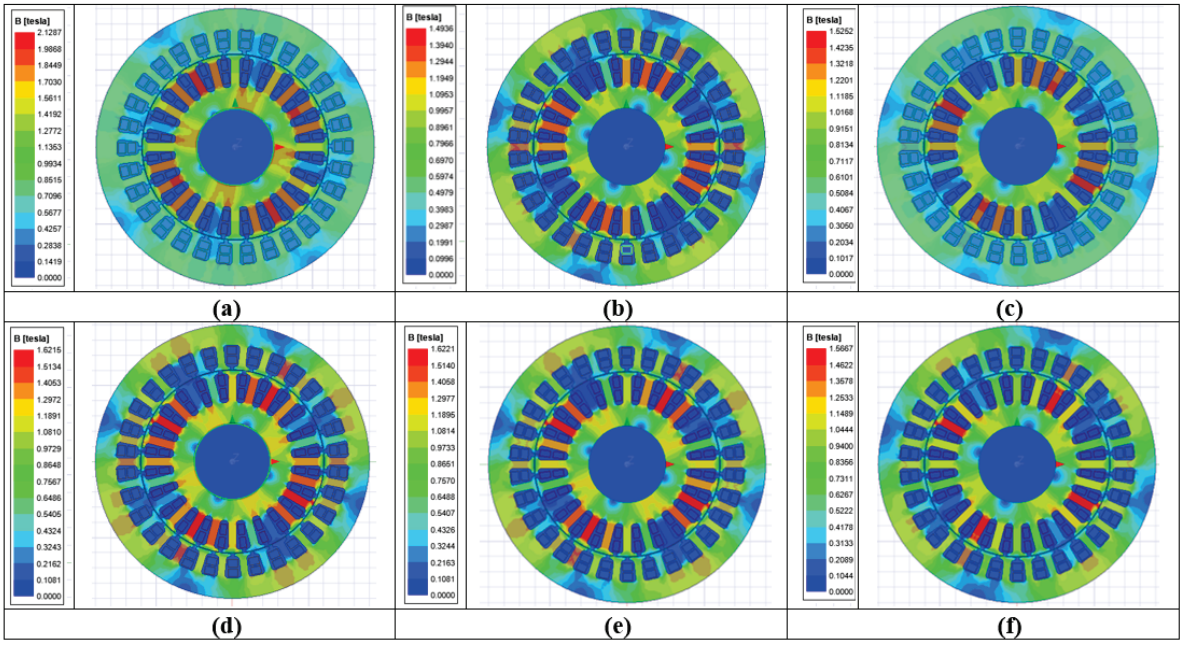

Fig. 8. Magnetic field distribution for healthy and unhealthy DFIG in different cases of NSWITSCF: (a) Healthy, (b) 4 ITSCF, (c) 11 ITSCF, (d) 22 ITSCF, (e) 33 ITSCF, and (f) 39 ITSCF.

winding fault circumstances. It can be seen that both the stator and rotor areas have a strong magnetic field. Both rotor and stator leakage reactance will rise as a result. In certain areas, magnetic saturation will likewise rise. Due to the shift in current flowing through the rotor bars in the defective state, the generator's torque will behave asymmetrically.

V. CONCLUSION

The finite element method (FEM), often used for modeling and simulating electrical equipment, is a numerical method that enables the analysis of complicated and non-linear systems. Time-domain and frequency-domain representations of the stator currents as well as the magnetic flux density distribution under healthy and unhealthy conditions are compared for constant-speed operation. In this paper, we exploited the numeric computing power of FEM to simulate the healthy operation and several faulty operations in order to obtain a comparative analysis between the normal case and numerous cases of ITSCF for a single stator phase of DFIG. With a lesser increase in current in the B and C stator phases, ITSCF in the stator winding significantly increases branch current. The flux is reduced in Phase A of the stator winding as a result of SWITSCF, and the other two phases see less of a reduction. Moreover, when SWITSCF increases, the torque oscillates more and more. DFIG characteristics differ further from typical characteristics as there are more inter-turn short-circuits. This work can shed light on the consequences of SWITSCF, enabling the development of trustworthy fault detection and enhancing the quality of the electrical power that the DFIG wind turbines inject into the grid. To conclude, a bigger NSWITSCF generates a significant increase in faulty branch current, a current increase in all stator phases, and torque oscillation. As a research direction, it is important to extend the effects of the short circuit to the other quantities of the machine. It is important to do studies for a polyphase short circuit. It is important to take into account the effect of the rotation speed. It is important to use its results for diagnostics and fault location.

ACKNOWLEDGMENT

The authors would like to acknowledge the financial support received from the University of Setif-1 in Algeria the Research Project PRFU, under Grant (A01 L07 UN1901 2019 0002).

REFERENCES

[1] P. Veers, K. Dykes, E. Lantz, S. Barth, C. L. Bottasso, O. Carlson, A. Clifton, J. Green, P. Green, H. Holttinen, D. Laird, V. Lehtomäki, J. K. Lundquist, J. Manwell, M. Marquis, C. Meneveau, P. Moriarty, X. Munduate, M. Muskulus, J. Naughton, L. Pao, J. Paquette, J. Peinke, A. Robertson, J. S. Rodrigo, A. M. Sempreviva, J. C. Smith, A. Tuohy, and R. Wise, "Grand challenges in the science of wind energy," *Science*, vol. 366, no. 6464, Oct. 2019.

[2] H. Mellah and K. E. Hemsas, "Design and analysis of an external-rotor internal-stator doubly fed induction generator for small wind turbine application by FEM," *Int. J. Sustain. Green. Energy*, vol. 2, no. 1, p. 1, 2013.

[3] S. Dawn, P. K. Tiwari, A. K. Goswami, A. K. Singh, and R. Panda, "Wind power: Existing status, achievements and government's initiative towards renewable power dominating India," *Energy Strateg. Rev.*, vol. 23, pp. 178-199, 2019.

[4] H. Mellah and E. K. Hemsas, "Design and simulation analysis of outer stator inner rotor DFIG by 2D and 3D finite element methods," *International Journal of Electrical Engineering Technology*, vol. 3, no. 2, pp. 457-470, 2012.

[5] M. Fitouri, Y. Bensalem, and M. N. Abdelkrim, "Modeling and detection of the short-circuit fault in PMSM using finite element analysis," *IFAC-PapersOnLine*, vol. 49, no. 12, pp. 1418-1423, 2016.

[6] J. Cheng, H. Z. Ma, S. Song, and Z. Xie, "Stator inter-turn fault analysis in doubly-fed induction generators using rotor current based on finite element analysis," in *Proceedings of the 2018 IEEE International Conference on Progress in Informatics and Computing (PIC 2018)*, pp. 414-419, Dec. 2018.

[7] A. U. Rehman, Y. Chen, Y. Zhao, Y. Cheng, Y. Zhao, and T. Tanaka, "Detection of rotor inter-turn short circuit fault in doubly-fed induction generator using FEM simulation," in *2018 IEEE 2nd International Conference on Dielectrics (ICD),* pp. 1-4, July 2018.

[8] H. Sabir, M. Ouassaid, and N. Ngote, "Diagnosis of rotor winding inter-turn short circuit fault in wind turbine based on DFIG using hybrid TSA/DWT approach," in *Proceedings of 2018 6th International Renewable and Sustainable Energy Conference, (IRSEC 2018)*, pp. 1-6, Dec. 2018.

[9] S. M. M. Moosavi, J. Faiz, M. B. Abadi, and S. M. A. Cruz, "Comparison of rotor electrical fault indices owing to inter-turn short circuit and unbalanced resistance in doubly-fed induction generator," *IET Electr. Power Appl.*, vol. 13, no. 2, pp. 243-250, 2019.

[10] H. Huangfu, Y. Zhou, J. Zhang, S. Ma, Q. Fang, and Y. Wang, "Research on inter-turn short circuit fault diagnosis of electromechanical actuator based on transfer learning and VGG16," *Electronics (Basel),* vol. 11, no. 8, p. 1232, Apr. 2022.

[11] M. D. Xu, H. Li, and K. Shi, *Microgrid for High-Surety Power: Architectures, Controls, Protection, and Demonstration*. Boca Raton, FL: Taylor & Francis, 2017.

[12] J.-Q. Li and W. X.-M. Wang, "FEM analysis on interturn fault of rotor winding in DFIG," in *2013 International Conference on Electrical Machines and Systems (ICEMS),* pp. 797-802, Oct. 2013.

[13] E. Hamatwi, P. Barendse, and A. Khan, "Development of a test rig for fault studies on a scaled-down DFIG," in *2021 IEEE Energy Conversion Congress and Exposition (ECCE),* pp. 3805-3812, Oct. 2021.

[14] Q. F. Meng, Y. L. He, M. X. Xu, Y. Y. Zhang, and H. C. Jiang, "Effect of field winding interturn short-circuit positions on rotor ump of turbogenerator," in *ACM International Conference Proceeding Series*, New York, NY, pp. 104-109, 2018.

[15] H. Bilal, N. Heraud, and E. J. R. Sambatra, "An experimental approach for detection and quantification of short-circuit on a Doubly Fed Induction Machine (DFIM) windings," *J. Control Autom. Elec*., vol. 32, no. 4, pp. 1123-1130, Aug. 2021.

[16] S. He, X. Shen, Y. Wang, and W. Zheng, "Characteristic factor analysis on stator winding inter-turn fault in DFIG Based on FEM simulation," in *Proceedings - 2017 International Conference on Computer Technology, Electronics and Communication (ICCTEC 2017)*, pp. 209-213, Dec. 2017.

[17] H. Benbouhenni, A. Driss, and S. Lemdani, "Indirect active and reactive powers control of doubly fed induction generator fed by three-level adaptive-network-based fuzzy inference system: Pulse width modulation converter with a robust method based on super twisting algorithms," *Electr. Eng. Electromechanics*, no. 4, pp. 31-38, July 2021.

[18] S. V. Bozhko, R. V. Blasco-Giménez, R. Li, J. C. Clare, and G. M. Asher, "Control of offshore DFIG-based wind farm grid with line-commutated HVDC connection," *IEEE Trans. Energy Convers*., vol. 22, no. 1, pp. 71-78, 2007.

[19] H. Benbouhenni and S. Lemdani, "Combining synergetic control and super twisting algorithm to reduce the active power undulations of doubly fed induction generator for dual-rotor wind turbine system," *Electr. Eng. Electromechanics*, no. 3, pp. 8-17, 2021.

[20] X. Tian, H. Tang, Y. Li, Y. Chi, and Y. Su, "Dynamic stability of weak grid connection of large-scale DFIG based on wind turbines," *J. Eng.*, vol. 2017, no. 13, pp. 1092-1097, Jan. 2017.

[21] A. G. Abo-Khalil, W. Alharbi, A. R. Al-Qawasmi, M. Alobaid, and I. Alarifi, "Modeling and control of unbalanced and distorted grid voltage of grid-connected DFIG wind turbine," *Int. T. Electr. Energy*, vol. 31, no. 5, May 2021.

[22] H. Ahmad, H. Khalid, A. A. Amin, N. Masroor, H. Mahmood, and M. Abubakar, "Improved current controlled doubly fed induction generator model with grid integration under sub and super synchronous conditions," *J. Electr. Eng. Technol*., vol. 16, no. 1, pp. 141-153, Jan. 2021.

[23] S. R. Kabat and C. K. Panigrahi, "Fuzzy logic and synchronous reference frame controlled LVRT capability enhancement in wind energy system using DVR," *Turk. J. Comput. Math. Educ*., vol. 12, no. 6, pp. 4899-4907, June 2021.

[24] H. Mellah, S. Arslan, H. Sahraoui, K. E. Hemsas, and S. Kamel, "The effect of stator inter-turn short-circuit fault on DFIG performance using FEM," *Eng. Technol. Appl. Sci. Res*., vol. 12, no. 3, pp. 8688-8693, June 2022.

[25] O. Imoru, F. V. Nelwamondo, A. Jimoh, and T. R. Ayodele, "A neural network approach to detect winding faults in electrical machine," *Int. J. Emerg. Electr. P*., vol. 22, no. 1, pp. 31-41, Feb. 2021.

[26] Y. Chen, A. U. Rehman, Y. Zhao, L. Wang, S. Wang, M. Zhang, Y. Zhao, Y. Cheng, and T. Tanaka, "Numerical modeling, electrical characteristics analysis and experimental validation of severe inter-turn short circuit fault conditions on stator winding in DFIG of wind turbines," *IEEE Access*, vol. 9, pp. 13149-13158, 2021.

[27] J. Cheng, H. Z. Ma, S. Song, and Z. Xie, "Stator inter-turn fault analysis in doubly-fed induction generators using rotor current based on finite element analysis," in *Proceedings of the 2018 IEEE International Conference on Progress in Informatics and Computing (PIC 2018)*, pp. 414-419, Dec. 2018.

[28] S. He, X. Shen, and Z. Jiang, "Detection and location of stator winding interturn fault at different slots of DFIG," *IEEE Access*, vol. 7, pp. 89342-89353, 2019.

[29] K. Ma, J. Zhu, M. Soltani, A. Hajizadeh, and Z. Chen, "Inter-turn short-circuit fault ride-through for DFIG wind turbines," *IFAC-PapersOnLine*, vol. 53, no. 2, pp. 12757-12762, 2020.

[30] F. Bouaziz, O. Awedni, and L. Krichen, "Modelling and fault diagnosis of rotor inter turn short circuit fault in a doubly fed induction generator-based wind turbine," in *Proceedings 20th International Conference on Sciences and Techniques of Automatic Control and Computer Engineering*, pp. 189-194, Dec. 2020.

[31] Z. Tan, X. Song, W. Cao, Z. Liu, and Y. Tong, "DFIG machine design for maximizing power output based on surrogate optimization algorithm,"

IEEE Trans. Energy Convers., vol. 30, no. 3, pp. 1154-1162, 2015.

[32] V. K. Sharma and L. Gidwani, "Steady-state analysis of permanent magnet synchronous generator with uncertain wind speed," *Adv. Intel. Syst. Comput*., vol. 697, pp. 253-261, 2019.

[33] I. Gómez, G. García, A. McCloskey, and G. Almandoz, "Analytical model to calculate radial forces in permanent-magnet synchronous machines," *Appl. Sci*., vol. 11, no. 22, p. 10865, Nov. 2021.

[34] Z. Xing, Y. Gao, M. Chen, and J. Xu, "Fault diagnosis of inter-turn short circuit of permanent magnet synchronous wind turbine under the random wind," in *2021 IEEE 2nd China International Youth Conference on Electrical Engineering (CIYCEE),* pp. 1-6, Dec. 2021.

[35] Z. T. Mei, G. J. Li, Z. Q. Zhu, R. Clark, A. Thomas, and Z. Azar, "Scaling effect on inter-turn short-circuit of PM machines for wind power application," in *2021 IEEE International Electric Machines & Drives Conference (IEMDC),* pp. 1-8, May 2021.

[36] R. Palka and M. Wardach, "Design and application of electrical machines," *Energies (Basel),* vol. 15, no. 2, p. 523, Jan. 2022.

[37] L. Jun-Qing, M. A. Li, and W. De-Yan, "Influence of stator turn-to-turn short-circuit on magnetic field of DFIG," in *2011 International Conference on Electrical Machines and Systems (ICEMS 2011)*, pp. 1-5, Aug. 2011.

[38] Y. Chen, L. Wang, Z. Wang, A. U. Rehman, Y. Cheng, Y. Zhao, and T. Tanaka, "FEM simulation and analysis on stator winding inter-turn fault in DFIG," in *2015 IEEE 11th International Conference on the Properties and Applications of Dielectric Materials (ICPADM),* pp. 244-247, July 2015.

[39] P. Han, M. Cheng, Z. Zhang, and P. Peng, "Spiral vector modeling of brushless doubly-fed induction machines with short-circuited rotor windings," *Chinese J. Electr. Eng*., vol. 7, no. 3, pp. 29-41, Sep. 2021.

[40] Z. T. Mei, G. J. Li, Z. Q. Zhu, R. Clark, A. Thomas, and Z. Azar, "Scaling effect on inter-turn short-circuit of PM machines for wind power application," in *2021 IEEE International Electric Machines & Drives Conference (IEMDC),* pp. 1-8, May 2021.

[41] S. He, X. Shen, and Z. Jiang, "Detection and location of stator winding interturn fault at different slots of DFIG," *IEEE Access*, vol. 7, pp. 89342-89353, 2019.

[42] M. Afshari, S. M. M. Moosavi, M. B. Abadi, and S. M. A. Cruz, "Study on inter-turn short circuit fault and high resistance connection in the stator of doubly-fed induction generators," in *7th Iran Wind Energy Conference (IWEC2021),* pp. 1-6, May 2021.

[43] Y. Fu, Z. Ren, S. Wei, Y. Xu, and F. Li, "Using flux linkage difference vector in early inter-turn short circuit detection for the windings of offshore wind DFIGs," *IEEE Trans. Energy Convers*., vol. 36, no. 4, pp. 3007-3015, Dec. 2021.

[44] H. C. Dirani, A. Merkhouf, B. Kedjar, A. M. Giroux, and K. Al-Haddad, "Finite element simulation of hydro generators with rotor inter turn short circuit," in *2017 IEEE International Electric Machines and Drives Conference (IEMDC 2017)*, pp. 1-6, May 2017.

[45] H. Mellah and K. E. Hemsas, "Simulations analysis with comparative study of a PMSG performances for small WT application by FEM," *International Journal of Energy Engineering*, vol. 3, no. 2, pp. 55-64, 2013.

[46] A. Petersson, "Analysis, modeling and control of doubly-fed induction generators for wind turbines," Thesis for the Degree of Doctor of Philosophy, Department of Energy and Environment, Chalmers University of Technology, Goteborg, Sweden, 2005.

Hacene Mellah received the B.S. (2006), Magister (2009), and Ph.D. (2020) degrees from Sétif 1 University, Algeria. Since 2020, he has been an Associate Professor at the University of Bouira. His research interests include control and diagnostics of electrical machines, intelligent techniques, and renewable energy.

Amar Maafa received the B.S. (2008) and Ph.D. (2017) degrees in Electrical Engineering from the University of Bejaia, Algeria, and a Magister degree from Batna University in 2011. His research focuses on control, modelling, and diagnostics of wind energy conversion systems.

Hamza Sahraoui has a Ph.D. in Industrial Systems Control and Renewable Energy (2016, Batna 2 University, Algeria). Currently he is an Associate Professor. His research focuses on control systems, nonlinear and adaptive control, and renewable energy.

Abdelghani Yahiou received the B.Eng. (2009), M.Sc. (2012), and Ph.D. (2021) degrees in Electrical Engineering from the University of Setif-1, Algeria. Currently he is an Associate Professor. His research interests include transformer transients, inrush current, ferroresonance, modelling, and measurement systems.

Souhil Mouassa received the Ph.D. from Universidad de Jaén, Spain, and Sétif 1 University, Algeria, in 2021. His research interests include optimal power system planning and operation, power system optimization, microgrids planning and operation, renewable energy sources, demand-side management, and smart homes.

K. E. Hemsas received his Engineering (1991), Magister (1995), and Doctorate (2005) degrees from the University of Sétif 1, Algeria. He is a Full Professor in the Department of Electrical Engineering. His research interests include power quality, modelling, control and diagnosis of electrical machines, renewable energy, and artificial intelligence.

A Novel Compact and Lightweight Harmonic Tag for Insect Tracking

Zhan-Fei Su, Xian-Rong Wan*, Jian-Xin Yi, Zi-Ping Gong, and Zi-Yao Wang

College of Electronic Information
Wuhan University, Wuhan, 430072, China
zfsu333@whu.edu.cn, xrwan@whu.edu.cn, jxyi@whu.edu.cn,
zpgong@whu.edu.cn, qlzywzy@whu.edu.cn
*Corresponding Author

***Abstract* –** Harmonic radar sensor systems is a special wireless sensor system that has been used in insect tracking in recent years due to its excellent anti-clutter capability. Generally, a harmonic radar sensor systems consists of a radar transceiver and a specially designed harmonic tag. However, tags tend to become entangled with vegetation in insect tracking experiments. This paper proposes a strong echo signal and miniaturized low-mass passive tag design method, which targets Internet-of-Things insect tracking applications. We introduce foldable structures in antenna designing with advanced non-linear selection criterion under the unified frequency operation environment. The conversion loss (CL) of the tag is not impacted by the measures taken to minimize its mass and size. The results using both simulated and real data demonstrate remarkable improvements in size of tags, weight of tags, and echo signal strength of tags within our proposed method on the passive tags. The effectiveness of the method is verified by the results of harmonic radar illuminate tag. This work possesses the advantages of a low profile, lightweight design, strong echo signal, and compact dimensions.

***Index Terms* –** Compact size, frequency doubler, harmonic radar, harmonic tag, harmonic transponder, radio frequency identification (RFID), tag antenna.

I. INTRODUCTION

With the widespread adoption of the Internet of Things (IoT) and wireless sensor networks in everyday life, Radio Frequency Identification (RFID) has become an increasingly important technology for tagging, tracking, sensing, and locating objects [1-5]. Traditional RFID systems rely on a single frequency for both querying and responding, which can result in unwanted self-interference or clutter noise caused by environmental reflections. In contrast, sensor systems based on harmonic radar and transponders provide an attractive solution to these challenges. In this approach, the radar queries the tag at the fundamental frequency, and the tag attached to the target reflects higher-order harmonics, which the radar system can detect. In most cases, these transponders operate at the second harmonic frequency.

Harmonic radar sensor systems were first explored over 50 years ago and have since undergone rapid development [6]. Due to its high robustness against radar clutter interference, harmonic radar-based sensor systems have found applications in a variety of scenarios, such as search and rescue operations [7], temperature and humidity measurements [8], vital signs detection [9], wireless liquid sensing [10], indoor equipment detection [11], and object detection [12], among others. In the late 20th century, harmonic radar and transponder systems attracted the attention of entomologists due to their exceptional anti-interference capabilities, leading to their use in insect tracking [13]. In the application of harmonic radar for insect tracking, the design of insect harmonic tags is one of the key technologies. The system's working principle is illustrated in Fig. 1.

In insect tracking applications, the harmonic tag attached to the insect receives the fundamental frequency signal transmitted by the harmonic radar and generates a second harmonic signal, which is propagated back to the harmonic radar's receiver, allowing the insect's position to be determined. Mascanzoni and Wallin used tags consisting of a monopole antenna and a diode to track beetles [13]. The shape of the tag is like a whip and is placed on the beetle's body. The harmonic radar successfully detected the insect. Brazee et al.'s tracking of weevils using similar tag [14] also succeeded. In [15], the dipole ring tag designed by Colpitts and Boiteau, has improved the detection range compared to the monopole tag [16]. Its structure is composed of dipole antenna(copper wire), inductance coil and Schottky diode. Similar tags are also mentioned in literature [17], with a "J" shape design. However, experiments tracking bees found tag height makes it difficult for insects to enter or leave the rearing box. Riley and Smith addressed this problem by installing tags on insects when they leave the rearing box [18] and removing them when the insects return to the

Submitted On: February 22, 2025
Accepted On: June 28, 2025

https://doi.org/10.13052/2025.ACES.J.400710

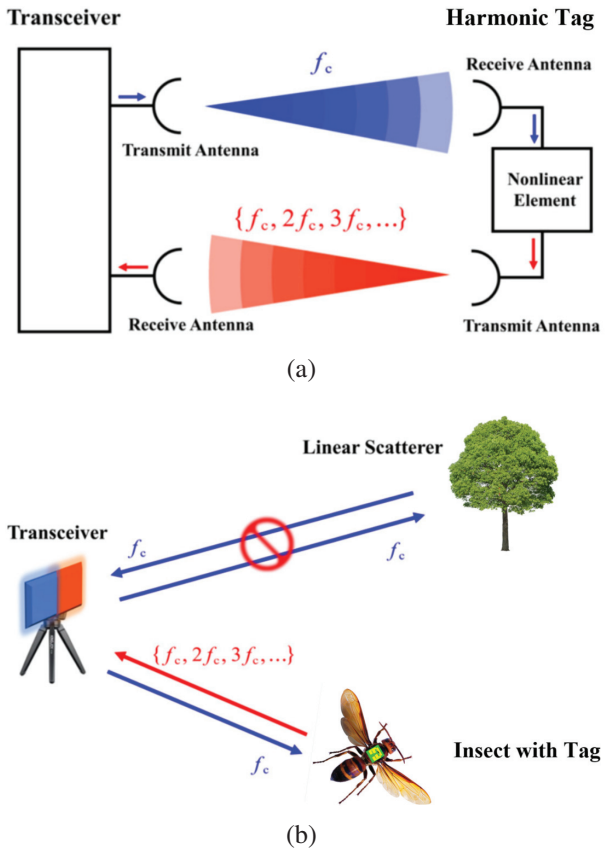

Fig. 1. Schematic of the harmonic radar system. (a) The composition of a harmonic radar. f_c represents the fundamental carrier frequency. (b) Working principle of harmonic radar. Blue lines represent the signals with the fundamental carrier frequency. Red lines represent the signals with the harmonic carrier frequency. Linear scatterer echo usually does not contain nonlinear frequency components, so it will not be detected by harmonic radar.

box. On the other hand, Capaldi found that the insect body caused electromagnetic field distortion [19], resulting in a decrease in antenna efficiency [18]. Milanesio et al. introduced a disc for installing tags [20], alleviating this problem. These tag designs were successfully tested in experiments. However, the disadvantages include low conformity to insect body, difficulties in attaching the tag, and making it mechanically robust. Meanwhile, in insect tracking experiments, the tags may get entangled in vegetation or become difficult to move in and out of nests, which can lead to tag deformation and reduce their performance.

Therefore, to reduce the impact of the tags on insect activity and improve their reliability, it is necessary to design low-profile tags. With the tag processing technology mature, printed tags are increasingly used in harmonic radar experiments to track insects. The harmonic tag in literature[21] utilizes a Minkowski fractal structure, which effectively enhances the tag's gain. Lavrenko improved the matching method of traditional dipole tags [22] by combining the printed matching inductor circuit with a linear antenna, reducing the flying resistance of insects. Kiriazi designed the tags with a butterfly knot topology [23] to facilitate the movement of snails. Tsai introduced composite left and right transmission line tags [24], which use a short-circuit pillar structure, improving performance. Although existing printed tags have achieved a low-profile structure, their size and weight still require further improvement. The tag described in literature [25] reduced its size, however, to achieve the desired weight and dimensions, the operating frequency of the tag needs to be raised to higher frequencies. This means lower detection range and increased price of radar modules. Therefore, designing an ideal miniaturized tag that does not compromise conversion gain remains a challenge.

To address this challenge, this paper proposes a compact and lightweight passive tag design methodology. The approach employs a folded antenna topology to reduce the tag's size, while utilizing polyimide (PI) as the substrate material. This reduces the tag's mass and enables a low-profile structure. The effectiveness of the proposed method is validated through simulations and experimental data, with comparisons made to existing designs.

The main contributions of this article are summarized as follows.

1) The mechanism of harmonic generation in nonlinear devices is theoretically analyzed. Simulations are performed to assess the impact of different nonlinear devices on conversion loss (CL), and theoretical calculations confirm the consistency of the simulation results.
2) The conventional formula for calculating the reflection coefficient (S_{11}) of harmonic tags is revised to address physical inconsistencies observed under certain conditions, such as values exceeding unity. The proposed formula eliminates these limitations and provides a more accurate metric for assessing impedance matching between the tag antenna and the nonlinear load.
3) A folded antenna topology is designed, where the radiating element is folded into a square pattern. This reduces the physical size of the tag antenna while maintaining its effective electrical length. Compared to traditional linear or other folded geometries, this design improves spatial efficiency, enabling tag miniaturization. Additionally, the effect of increasing the patch width on the tag's radiation performance is analyzed. A wider

patch enhances the current distribution area on the radiating surface, which is directly correlated with improved antenna gain.

The structure of this paper is organized as follows. Section II discusses the analysis and simulation of the tag model, including the mechanism of harmonic generation by diodes, methods for selecting nonlinear components, and the correction of the complex power wave reflection coefficient formula for tag antennas. Section III delves into the analysis and design of the tag, presenting simulation comparisons between the square topology and other structures for reducing tag size, the effect of patch width on current distribution across the radiation surface, and the impact of different matching techniques on tag antenna performance. Section IV focuses on the experimental testing of the tags. Finally, section V concludes with the main findings.

II. TAG MODEL ANALYSIS AND SIMULATION

The tag consists of nonlinear components, a tag antenna, and a matching circuit. Tags suitable for insect tracking should possess characteristics such as low CL, small size, low air resistance, and strong echo signal. Selecting appropriate nonlinear components, such as multiplier devices, to generate harmonic carrier signals for the tag is essential for minimizing tag CL. Additionally, this paper designs a passive tag antenna with a folding structure, achieving tag miniaturization and size reduction. Moreover, the intensity of the echo signal received by the harmonic radar determines its detection range. To ensure efficient energy transmission between the nonlinear components and the tag antenna, a matching circuit must be designed to ensure optimal energy transfer.

A. Theoretical analysis of nonlinear components

Various active or passive nonlinear components can generate harmonic signals for tags, including diodes [26,27], nonlinear transmission lines [28,29], transistors [30,31], and phase-locked loops [32]. When comparing factors such as operating frequency, harmonic factor, size, and power requirements, diodes emerge as the optimal choice as multipliers for passive tags [33].

The tag antenna intercepts signals from the harmonic radar, inducing a voltage that drives the diode by generating current. Owing to the inherent properties of the diode, it can alter the state of the initial current, resulting in the production of current containing harmonic signals. The precise alterations in the operational state are depicted in Fig. 2. The left panel of Fig. 2 illustrates the relationship between induced voltage and time before passing through the diode. Upon reaching the threshold voltage required to activate the diode, the

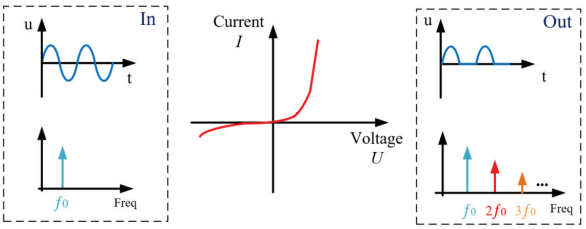

Fig. 2. Diode frequency doubling phenomenon.

operational state of the tag antenna corresponds to the representation in the right panel of Fig. 2. Subsequently, the voltage amplitude is halved, and the tag antenna produces various harmonic frequencies, including the 2nd and 3rd harmonics. This phenomenon arises from the exponential relationship between the diode's voltage-current (V-I) characteristic, illustrated in the central diagram of Fig. 2. Passage of the signal through the diode induces nonlinear distortion of the input signal, leading to a frequency-doubling phenomenon.

The theoretical analysis is as follows, the Schottky equation for the diode in small signal operation is given by [34]:

$$I = I_s \times \left(e^{\frac{V_d}{n \times V_t}} - 1 \right). \tag{1}$$

Where I is the current through the diode, I_s is the reverse saturation current of the diode, n is the ideality factor, V_t is the thermal voltage, and V_d is the voltage across the diode.

In equation (1), when V_d = 0, the equation can be expanded using Taylor series as:

$$I = I_s \times \left[\left(\frac{V_d}{n \times V_t} \right) + \left(\frac{(V_d)^2}{2!(n \times V_t)^2} \right) + \left(\frac{(V_d)^3}{3!(n \times V_t)^3} \right) + \ldots \right]. \tag{2}$$

The voltage source provided to the diode in the tag is the induced voltage on the tag antenna, which can be equivalent to a sine signal:

$$V_d(t) = A sin(\omega_0 t). \tag{3}$$

In equation (3), A represents the amplitude of the junction voltage, $\omega_0 = 2\pi f_0$, f_0 denotes the frequency of the fundamental signal.

Periodic signals that satisfy the Dirichlet conditions can be represented by the Fourier series as a combination of such signals. Substituting equation (4) into equation (2) yields:

$$I = I_s \times \left[\left(\frac{A \sin(2\pi f_0 t)}{n \times V_t} \right) + 0.5A^2 \left(\frac{1 - \cos(2\pi \times 2 f_0 t)}{2!(n \times V_t)^2} \right) + \ldots \right]. \tag{4}$$

From equation (5), it can be observed that the current through the Schottky diode contains signals with frequencies that are multiples of the fundamental frequency

$2f_0$, and expanding further will yield harmonic signals of the 3rd order and above.

Classical p–n junction diodes have high junction capacitance, rendering them unsuitable for high-frequency applications. Conversely, Schottky diodes, formed by metal-semiconductor contacts, exhibit lower junction capacitance, rendering them suitable for high-frequency operation [34]. However, Schottky diodes, being hot carrier diodes, typically exhibit a reverse saturation current on the order of 10^{-6} A, whereas for other diode types, the reverse saturation current is typically on the order of 10^{-14} A. Consequently, Schottky diodes are more suitable than other diode types as nonlinear components in RF harmonic tags.

B. Analysis of the dynamic equivalent model of nonlinear components

Figure 3 illustrates the circuit schematic of a traditional dual-port passive harmonic transponder, along with the energy flow paths for the fundamental wave and the second harmonic. The red arrows represent the energy flow path of the fundamental wave, while the green arrows indicate the energy flow path of the second harmonic. To enhance the nonlinear conversion process in the diode, quarter-wavelength short-circuited and open-circuited stubs (denoted as TL1 and TL2, respectively) are placed around the diode [35]. The quarter-wavelength short-circuited stub TL1 at the input acts as an open circuit at the fundamental frequency f_0, allowing the injected fundamental signal to reach the diode. However, at the second harmonic frequency $2f_0$, TL1 behaves as a short circuit, grounding the second harmonic at point a. On the output side, the quarter-wavelength open-circuited stub TL2 acts as a short circuit at the fundamental frequency f_0, thereby shorting the fundamental signal while minimally affecting the second harmonic. This is because, at f_0, the open-circuited stub is a quarter-wavelength long, but at $2f_0$, it becomes a half-wavelength long, maintaining an open-circuit condition at $2f_0$. Consequently, the fundamental signal is short-circuited and reflected at point b.

The injected RF signal at the fundamental frequency f_0 passes through the input matching network and reaches the diode's input terminal. Meanwhile, the quarter-wavelength open-circuited stub on the output side shorts the fundamental signal at f_0. Nonlinear transformation schematic model at f_0 is depicted in Fig. 4 (a). At the second harmonic frequency $2f_0$, the short-circuited and open-circuited stubs function as a short circuit and an open circuit, respectively. At this point, the diode acts as a generator for second harmonic energy. Due to the stubs and the output matching network designed for $2f_0$, maximum second harmonic power is delivered to the output port. Nonlinear transformation schematic model at $2f_0$ is shown in Fig. 4 (b).

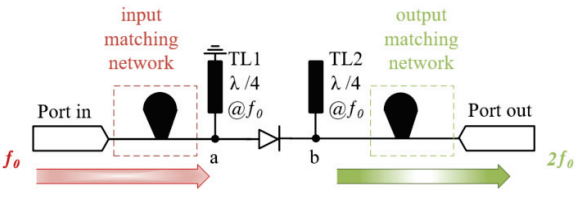

Fig. 3. The schematic diagram of the harmonic tag.

To simplify the analysis, the input and output matching networks are omitted in Fig. 4. The diode is represented using the Shockley model, which includes the junction resistance R_j, junction capacitance C_j, and series resistance R_s, the latter comprising the epitaxial layer resistance R_{epi} and substrate resistance R_{sub} [18]. Parasitic capacitance C_p and parasitic inductance L_p are used to model the packaging effects. The fundamental RF signal source in Fig. 4 (a) is represented by a Thévenin equivalent circuit, while the diode, acting as the second harmonic signal source in Fig. 4 (b), is modeled using a Norton equivalent circuit. Additionally, V_1 represents the node voltage. The SPICE parameters of the diode, sourced from SKYWORKS, Central Semi and AVAGO Technologies, are listed in Table 1.

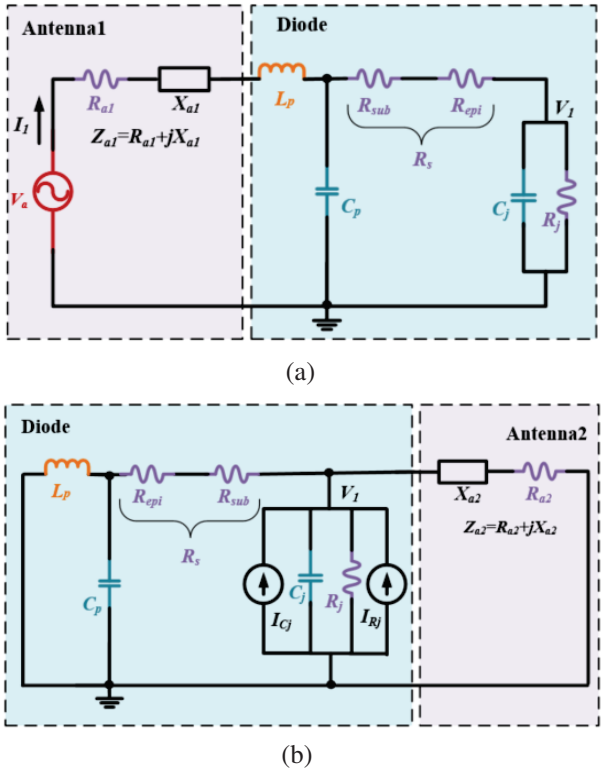

Fig. 4. Nonlinear transformation schematic model. (a) Fundamental frequency. (b) Harmonic frequency.

Table 1: The main SPICE parameters of the diode

Parameter	SMS 7630	CDC 7630	HMPS 2820	HSMS 2850
C_j(pF)	0.14	0.40	0.50	0.50
M	0.40	0.40	0.50	0.50
V_j(V)	0.34	0.34	0.65	0.35
R_s(Ω)	20.00	51.00	8.00	25.00
I_s(A)	5e-6	3.8e-6	2.2e-8	3e-6
n	1.05	1.05	1.08	1.06
I_{Bv}(A)	1e-4	1e-4	1e-4	3e-4
B_v(V)	2.00	2.00	15.00	3.80
E_G(eV)	0.69	0.69	0.60	0.69
C_g(pF)	0.16	0.16	0.08	0.08
L_s(nH)	0.07	0.07	2.00	2.00

The working principle of the tag is illustrated in Fig. 4. In Fig. 4 (a), the radiation resistance and reactance of the tag's fundamental frequency antenna are denoted as R_{a1} and X_{a1}, respectively. The antenna receives the fundamental signal transmitted by the harmonic radar's transmit antenna, generating current I_1 and voltage V_a, which deliver energy to the diode. In Fig. 4 (b), the radiation resistance and reactance of the harmonic antenna are represented as R_{a2} and X_{a2}, respectively. The diode's junction resistance (R_j) and capacitance (C_j) produce currents I_{Cj} and I_{Rj}, which contain harmonic components. These currents radiate electromagnetic waves through the tag's harmonic antenna, reflecting back to the harmonic radar's receive antenna.

As described in [36], the theoretical model's validity and accuracy can be verified by comparing theoretical calculations with simulation results, enabling the optimization of diode selection and circuit design. To comprehensively evaluate the diode's CL characteristics, this study employs a combined approach of theoretical formula calculations and software simulations.

The fundamental current can be written as:

$$I_{f0} = I_s \times \left[2 \times i \times J_1\left(-i\frac{V_1}{n \times V_t}\right)\right] \times \cos(\omega_0 t), \quad (5)$$

where $J_{v(x)}$ is the Bessel function of first kind of order v. The injecting current can be obtained by applying the Kirchhoff Circuit Laws considering the effect of the packaging components

$$I_{in} = I_{f0} + V_1 \times i\omega_0 C_j + \left(\left(I_{f0} + V_1 \times i\omega_0 C_j\right) \times R_s + V_1\right) \times i\omega_0 C_p. \quad (6)$$

The injecting voltage can be expressed by

$$V_{in} = V_1 + \left(I_{f0} + V_1 \times i\omega_0 C_j\right) \times R_s + I_{in} \times i\omega_0 L_p. \quad (7)$$

The injecting power can be calculated by

$$P_{f0} = real\left(\frac{V_{in} \times I_{in}^*}{2}\right). \quad (8)$$

The second-harmonic current due to the junction resistance can be calculated by

$$I_{Rj} = I_s \times \left[-2 \times J_2\left(-i\frac{V_1}{n \times V_t}\right)\right] \times \cos(2\omega_0 t). \quad (9)$$

The generated second-harmonic current can be expressed by

$$I_t = I_s \times \left[-2 \times J_2\left(-i\frac{V_1}{n \times V_t}\right)\right] - i \times \frac{C_{j0} \times M \times V_1^2 \times \omega_0}{2V_j}. \quad (10)$$

The current coming out of the diode I_{out} can be written by

$$I_{out} = I_t \times \frac{Z_p}{Z_p + R_s + \frac{(Z_{out} + i2\omega_0 L_p) \times (i2\omega_0 C_p)^{-1}}{Z_{out} + i2\omega_0 L_p + (i2\omega_0 C_p)^{-1}}} \cdot \frac{(i2\omega_0 C_p)^{-1}}{Z_{out} + i2\omega_0 L_p + (i2\omega_0 C_p)^{-1}}, \quad (11)$$

where Z_{out} is the output impedance equal to the complex conjugate of the packaged diode's impedance in order to maximize the power transfer to the output port. Then, the generated second harmonic power reaching the output can be expressed by

$$P_{2f0} = real\left(\frac{I_{out}^* \times I_{out} \times Z_{out}}{2}\right). \quad (12)$$

The CL can be expressed by

$$CL = P_{f0}(dBm) - P_{2f0}(dBm). \quad (13)$$

Using the SPICE parameters of the diodes, several commonly used diodes were selected for validation. During the validation process, the input power was swept from -50 dBm to -30 dBm. The harmonic balance simulation results for each diode-based transponder, along with the calculated CL values as a function of input power, are shown in Fig. 5 (a). Additionally, a frequency sweep was performed over the range of 4–12 GHz, and the relationship between frequency and CL is depicted in Fig. 5 (b).

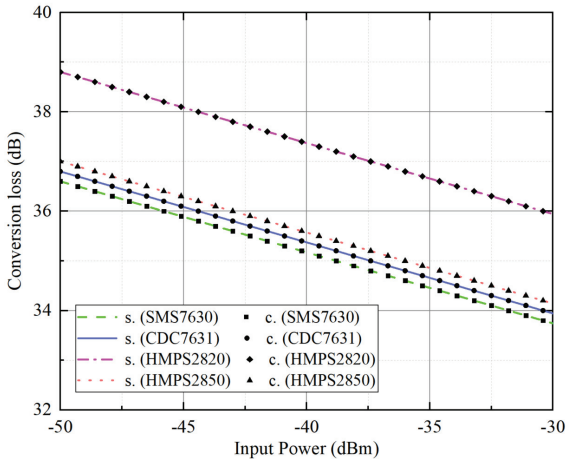

(a)

Fig. 5. *Continued.*

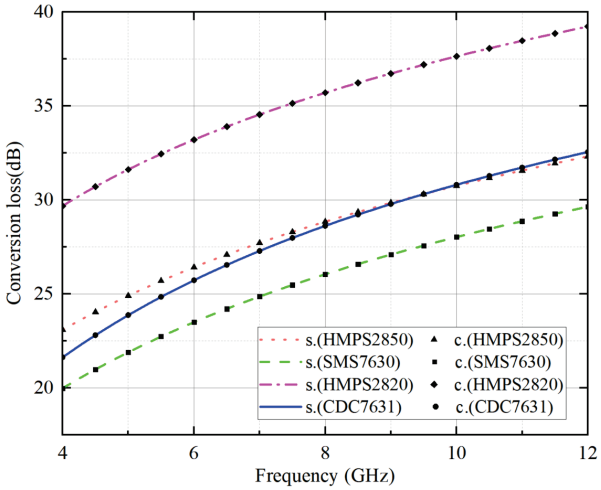

(b)

Fig. 5. Comparison of calculated and simulated CL performance of four typical selected diode-based tag. (a) The injecting power is in a range of -50 to -30 dBm. (b) Operating frequency in the range of 4 to 12 GHz.

It is evident from both figures that the simulation results from the harmonic balance simulator are consistent with the calculated *CL* values. Based on these results, it can be concluded that within the power and frequency range of interest, the diode SMS-7630 exhibits superior *CL* performance compared to the other diodes.

C. Improved calculation method for tag antenna reflection coefficient

In tag optimization, impedance matching has long been recognized as one of the key factors for achieving optimal tag performance. To maximize power transfer, the input impedance of the diode connected to the antenna must be conjugate-matched to the antenna's impedance. The reflection coefficient (S_{11}), as observed in tag antenna simulations and reflects the matching relationship between the tag antenna and the diode. Lower values of S_{11} generally indicate higher radiation efficiency.

Although a loop diameter of 1 mm is a common choice for linear dipole tags [22], no simulation analysis currently substantiates this choice. However, with a reference impedance of 50 ohms, the reflection coefficient (S_{11}) obtained from finite element simulation software often exceed 0 dB. This discrepancy can be attributed to the following reasons.

The reflection coefficient (S_{11}) can be expressed as [37]:

$$S_{11} = 20\log|\Gamma| = 20\log\left|\frac{Z_a - Z_s}{Z_a + Z_s}\right|. \tag{14}$$

$$|Z_a - Z_s| > |Z_a + Z_s|. \tag{15}$$

The diode impedance can be expressed as $Z_s = R_s + jX_s$, the tag antenna impedance can be expressed as $Z_a = R_a + jX_a$, substituting the values into the equation, we obtain:

$$\left|\sqrt{(R_a - R_s)^2 + (X_a - X_s)^2}\right| > \left|\sqrt{(R_a - R_s)^2 + (X_a + X_s)^2}\right|. \tag{16}$$

After expanding the equation:

$$R_a^2 - 2R_sR_a + R_s^2 + X_a^2 - 2X_sX_a + X_s^2 > R_a^2 + 2R_sR_a + R_s^2 + X_a^2 + 2X_sX_a + X_s^2. \tag{17}$$

After simplification:

$$-2R_sR_a - 2X_sX_a > 2R_sR_a + 2X_sX_a. \tag{18}$$

The final expression can be written as:

$$-\frac{R_s}{X_s}R_a > X_a. \tag{19}$$

When the reactance is smaller than $-\frac{R_s}{X_s}$ of the input resistance, the simulated reflection coefficient (S_{11}) can take values exceeding the physically possible range, resulting in unrealistic results. The result is shown in Fig. 6, where the pink dashed line represents this phenomenon (while the curve derived using the improved formula is shown by the red dashed line in Fig. 6, which exhibits an offset compared to the pink dashed line from the Original Simulation). Therefore, the method for calculating the reflection coefficient needs to be improved.

It needs to be corrected to the complex power wave reflection coefficient as:

$$\Gamma = \frac{Z_a - Z_s^*}{Z_a + Z_s}. \tag{20}$$

This allows the traditional reflection coefficient curve to be used to describe the impedance matching between the tag antenna and the diode. The simulated reflection coefficient using the improves formula is shown by the solid blue line in Fig. 6. To verify the

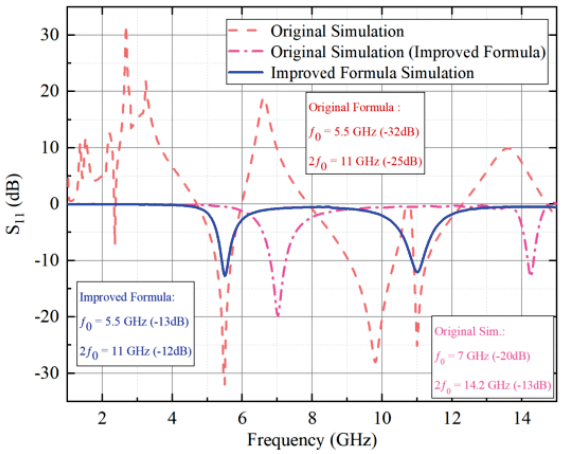

Fig. 6. Comparison of the reflection coefficient (S_{11}) before and after formula correction.

effectiveness of the proposed method, a tag was fabricated based on the unmodified reflection coefficient (S_{11}) calculation method, as shown in Fig. 20 (a).

III. TAG ANALYSIS AND DESIGN

A. Analysis of folding topology structure

The common antenna topology used in insect tags is the dipole antenna, primarily due to its simple structure, ease of fabrication, moderate size, and high radiation efficiency. However, its relatively large size can impact the mobility of the insect [38]. The goal of this paper is to design a square meander-line antenna, clearly demonstrating the small-size design concept of a folded antenna, and compare its performance with two other meander-line designs: sinusoidal and triangular. To maintain structural consistency, these three meander-line designs are based on the traditional baseline dipole antenna design as a template. All three designs were simulated using electromagnetic field simulation software based on the finite element method (FEM), and their performance was compared in terms of size reduction, actual gain, reflection coefficient, and bandwidth.

For ease of comparison, all antennas (Antenna1-Antenna4) use the same dielectric substrate (PI), width W, and driver patch width as shown in Fig. 7. Antenna 1 is the baseline dipole model, maintaining the original topology of the dipole antenna, with a patch length *Patch_l1* and a dielectric substrate length L_1; Antenna 2 is the Sinusoidal Model, with a patch length *Patch_l2* and dielectric substrate length L_2; Antenna 3 is the Triangular Model, with a patch length *Patch_l3* and dielectric substrate length L_3; and Antenna 4 is the Square Model, with a patch length *Patch_l4* and dielectric substrate length L_4. Their size comparisons are shown in Table 2. The simulation results optimized using the software are shown in Fig. 8, with a center operating frequency of 5.5 GHz. Any further changes to their dimensions would result in a frequency shift.

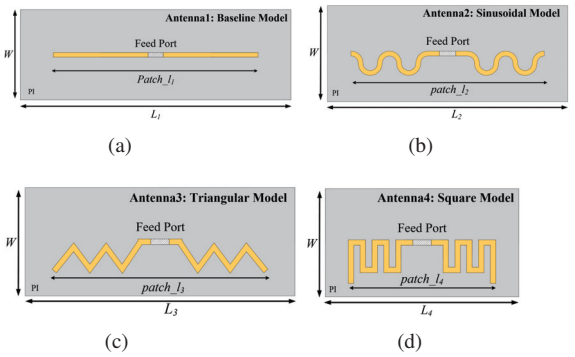

Fig. 7. Four different topology dipole antennas. (a) Baseline. (b) Sinusoidal. (c) Triangular. (d) Square.

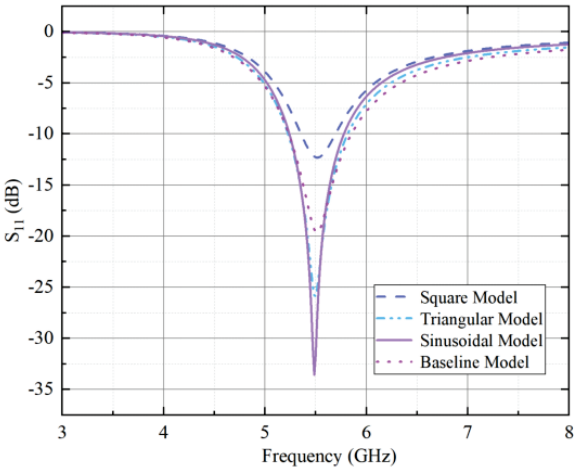

Fig. 8. Comparison of the reflection coefficient (S_{11}) for four different topology dipole antennas.

The comparison of the four antenna models' return loss was performed in the frequency range of 3-8 GHz, with a focus on performance around the center frequency of 5.5 GHz. The four models are: Square Model (dark blue dashed line), Triangular Model (light blue dash-dot line), Sinusoidal Model (purple solid line), and Baseline Model (pink dotted line), as shown in Fig. 8. Overall, the Triangular Model and Sinusoidal Model achieve a better balance between return loss depth and bandwidth. Specifically, the Triangular Model reaches a minimum return loss of -22 dB, with a -10 dB bandwidth of 580 MHz. The Sinusoidal Model further improves the minimum return loss to -31 dB, with a bandwidth of 500 MHz. The Baseline Model, while having the widest bandwidth of 600 MHz, achieves a minimum return loss of only -18.5 dB. The Square Model, with a shallower minimum return loss of -11 dB and the narrowest bandwidth of 350 MHz, shows better suitability for compact designs. The detailed performance parameters for all four antennas are listed in Table 2.

The comparison of the four antenna models' reflection coefficients (S_{11}) was performed in the frequency range of 3-8 GHz, with a focus on performance around the center frequency of 5.5 GHz. The four models are: Square Model (dark blue dashed line), Triangular Model (light blue dash-dot line), Sinusoidal Model (purple solid line), and Baseline Model (pink dotted line), as shown in Fig. 8. Overall, the Triangular Model and Sinusoidal Model achieve a better balance between the reflection coefficient and bandwidth. Specifically, the Triangular Model reaches a minimum reflection coefficient (S_{11}) of -22 dB, with a -10 dB bandwidth of 580 MHz. The Sinusoidal Model further improves the minimum reflection coefficient (S_{11}) to -31 dB, with a bandwidth of 500 MHz. The Baseline Model, while having the widest

Table 2: Comparison of different antenna structures

Type	Ant.1	Ant.2	Ant.3	Ant.4
L_n (mm)	30	25	25	18
Patch_ln (mm)	22.7	20.1	20	14.7
Size Reduction	N/A	17.2%	17.2%	40%
Reflection Coefficient (dB)	-18.5	-31	-22	-12.7
Band Width (MHz)	600	500	580	350
Gain (dBi)	1.98	2.02	1.94	1.9

bandwidth of 600 MHz, achieves a minimum reflection coefficient (S_{11}) of only -18.5 dB. The Square Model, with a shallower minimum reflection coefficient (S_{11}) of -11 dB and the narrowest bandwidth of 350 MHz, shows better suitability for compact designs. The detailed performance parameters for all four antennas are listed in Table 2.

To further analyze and compare the performance of the four antennas, their gain radiation patterns are shown in Fig. 9. The gain patterns display the antennas' radiation performance at a frequency of 5.5 GHz, with the vertical axis representing gain (in dBi). The radiation patterns show symmetry and stability, with the red dashed line representing the E-plane ($\phi = 90°$) and the black solid line representing the H-plane ($\phi = 0°$). From the peak gain readings, it is evident that the Square Model antenna does not experience a significant reduction in gain despite its compact size.

The comparison of the four antenna topologies is shown in Table 2. From Table 2, it is clear that, compared to the other models, the Square Model has the smallest size at the 5.5 GHz operating frequency, with its reflection coefficient, bandwidth, and gain all within the normal operating range.

To investigate the effect of patch width on antenna gain, the surface current distribution characteristics of three different line-width antennas were compared. Simulation results show that as the line width increases, the surface current distribution becomes more uniform, and the current density in the radiation region increases significantly. This uniform current distribution reduces the ineffective power loss within the antenna, thereby improving radiation efficiency. Furthermore, the increase

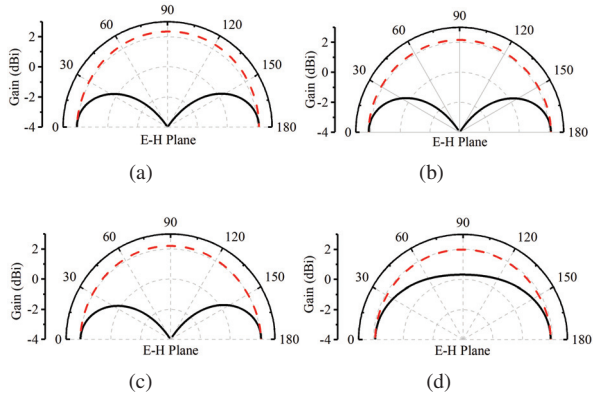

Fig. 9. Comparison of gain radiation pattern for four different topology dipole antennas. The red dashed line represents the E-plane, and the black solid line represents the H-plane. (a) Baseline. (b) Sinusoidal. (c) Triangular. (d) Square.

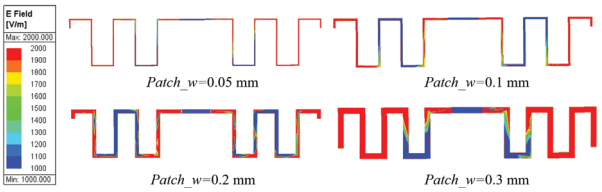

Fig. 10. Electric field distribution with different line widths.

in line width expands the current radiation area, enhancing the antenna's equivalent radiation area, and further improving its directivity and gain. A detailed comparison of the electric field distributions is shown in Fig. 10.

B. Tag design and simulation

The tag design process typically involves the following steps: determining the operating frequency of the tag, selecting the diode model to be used, establishing the diode port impedance, designing the antenna topology, selecting the dielectric substrate material, and designing the matching circuit between the diode and the tag antenna. Since tag operations often work near the X-band frequency range [35], this study uses 5.5 GHz as the fundamental frequency of the tag. In section II, harmonic simulations and calculations show that the SMS-7630 diode exhibits low CL, making it the chosen nonlinear component for this work. In section III.A, with the objectives of minimizing size while maintaining high antenna radiation gain, the performance of different folded antenna topologies is analyzed through simulations, leading to the selection of the Square Model as the tag antenna topology. Additionally, simulations of

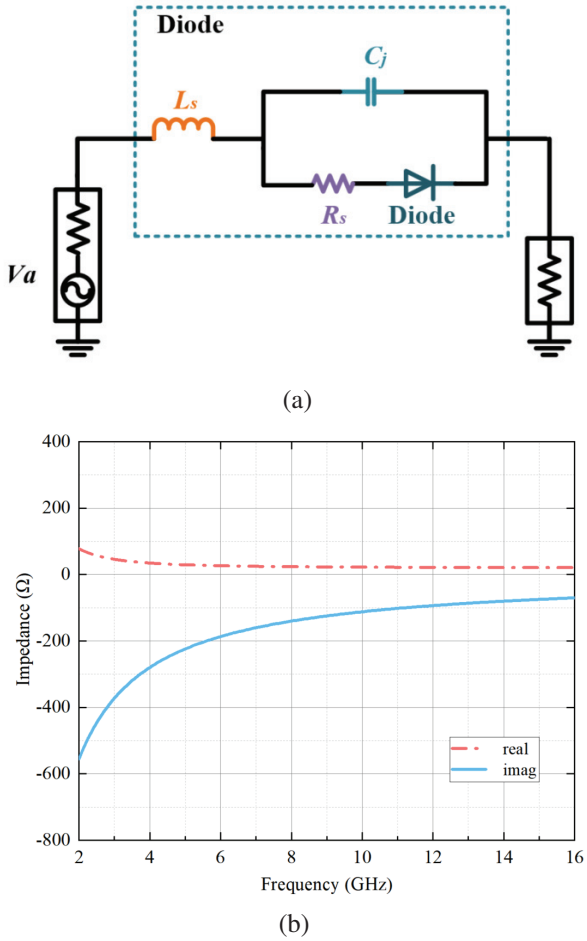

Fig. 11. Diode impedance simulation: (a) Diode model simulation. (b) The impedance values of the SMS-7630 Schottky diode.

current distribution reveal that increasing the width of the antenna's radiation patch enhances the gain.

The determination of the diode impedance is critical, as it directly affects harmonic conversion efficiency and the design of the matching circuit. Figure 11 shows the simulated impedance variations of the SMS-7630 diode at different frequencies. At the fundamental frequency of 5.5 GHz, the diode impedance is $27 - i203\ \Omega$; at the harmonic frequency of 11 GHz, the impedance is $22 - i102\ \Omega$. By adjusting the antenna structure and introducing a matching circuit, conjugate matching between the tag antenna and the diode can be achieved. Furthermore, as shown in Table 3, PI stands out as the ideal material for lightweight tag design among common dielectric substrates.

Common dielectric substrate materials are listed in Table 3. For example, PI has a density of 1.37 g/cm^3, FR4 has a density of 2.23 g/cm^3, Teflon ZYF300CA has a density of 2.27 g/cm^3, and Rogers RO4350B has a

Table 3: Comparison of different materials

Material	FR4	PI	Rogers RO4350B	Teflon ZYF300CA
ε_r	2.2	3.3	3.48	3.0
Density (g/cm^3)	1.8	1.37	1.86	2.27
Mass (g)	1.8	1.37	1.86	2.27

density of 1.86 g/cm^3. Based on the mass-density formula $m = \rho \cdot V$, the mass of PI is the lightest at 1.37 g. Furthermore, the PI substrate is flexible, making it ideal for lightweight tag designs. Therefore, PI material (dielectric constant $\varepsilon_r = 3.3$) is selected to support the low-mass design of the tag.

Matching circuits are crucial components in the tag design. Figure 12 illustrates three types of matching circuits. In the diagram, the gray regions represent the dielectric substrate, the yellow areas denote the radiation patches, and the blue sections correspond to the diode's parallel inductive matching circuits.

Matching circuits are critical components in tag design. To ensure stable tag operation, it is essential to choose a matching circuit with impedance stability near the operating frequency range. Figure 12 compares three types of parallel inductive matching circuits. In the illustration, gray regions represent the dielectric substrate, yellow areas denote the radiation patches, and blue sections correspond to the parallel inductive matching circuits of the diode.

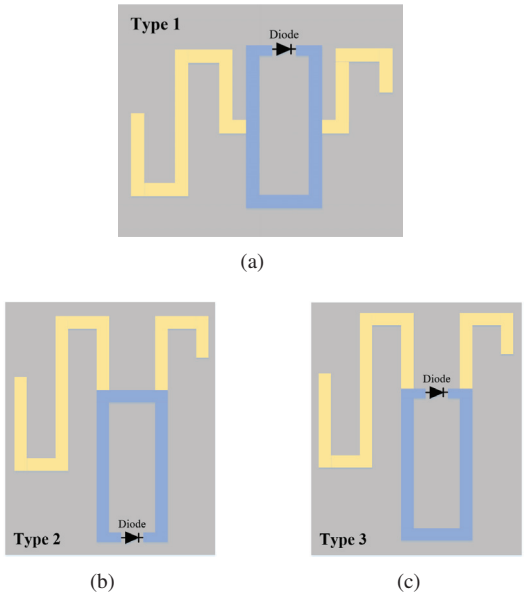

Fig. 12. Three parallel inductive matching circuit methods. (a) Center. (b) Down. (c) Top.

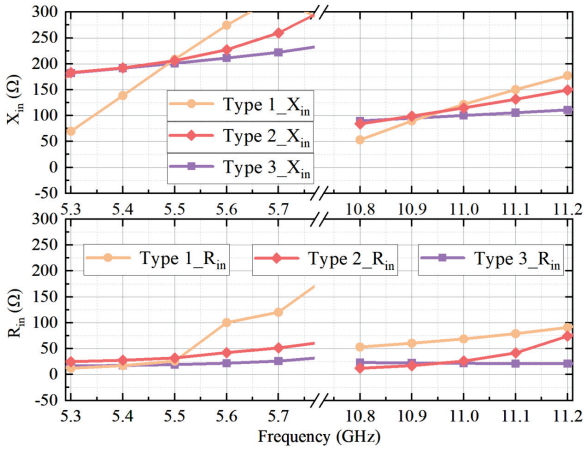

Fig. 13. The impedance plots of three parallel inductance configurations.

Figure 13 illustrates the impedance simulation results for three types of matching circuits, offering a comparative analysis of their performance. The diagram is divided into two segments: the lower segment shows the real part of the impedance (R_{in}), while the upper segment represents the imaginary part (X_{in}). The frequency ranges under consideration are 5.3–5.7 GHz for the fundamental frequency and 10.8–11.2 GHz for the harmonic frequency, with a discontinuity separating these ranges. The orange, red, and purple lines correspond to Type 1, Type 2, and Type 3 matching circuits, respectively.

The impedance simulation reveals that the Type 1 matching circuit experiences the largest variation in impedance, indicating potential instability across the operating frequencies. While the impedance variations for Type 2 and Type 3 are relatively close, the impedance of Type 3 demonstrates greater stability, particularly at the harmonic frequencies, with a smaller rate of change compared to Type 2. This stability is critical for ensuring efficient signal processing and minimizing mismatch losses, especially in nonlinear circuits like those involving harmonic tags.

Given these observations, Type 3 is deemed the most appropriate choice for the tag's matching circuit, as it offers a superior balance of impedance stability and performance over the required frequency ranges.

The previous analysis concluded that increasing the line width of the microstrip dipole helps improve the current distribution of the tag antenna. To further enhance the performance of the square antenna, the impact of widening the line width was examined. A wider line width increases the current distribution, which boosts the gain and, in turn, improves the radiation efficiency. Additionally, a wider line width optimizes the current distribution on the antenna surface, thereby minimizing losses caused by current concentration. Therefore, increasing

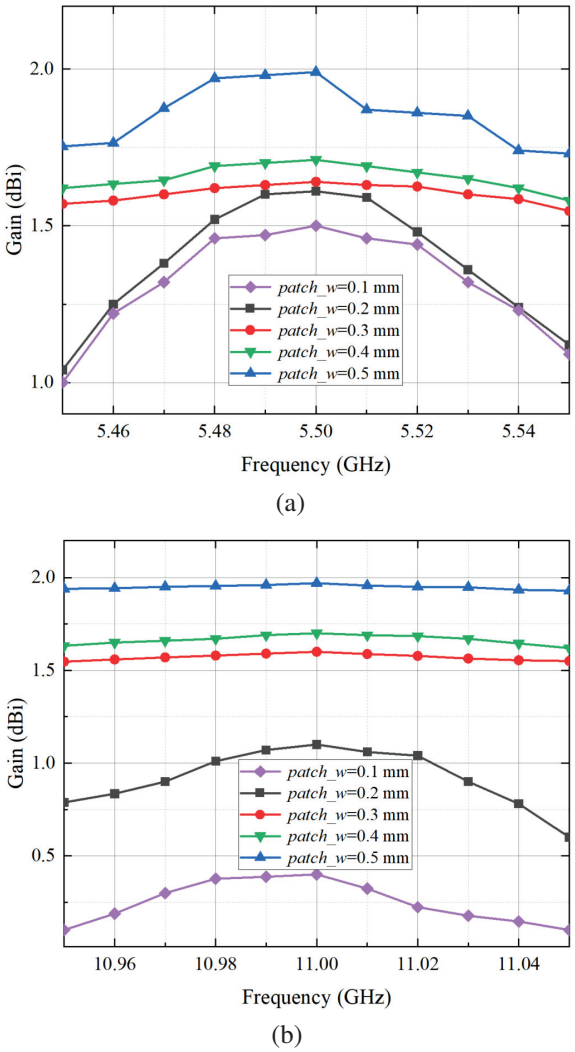

Fig. 14. Comparison of gain for different line widths. (a) Fundamental frequency (b) Harmonic frequency.

the line width not only improves the antenna gain but also optimizes its overall radiation performance. The relationship between tag gain and radiation patch width is shown in Fig. 14.

The impedance matching between the tag antenna and the diode was analyzed using simulation software, and the results are shown in the Smith chart in Fig. 15. The solid red curve represents the impedance variation of the diode, while the dashed green and black curves represent the impedance variations of the tag antenna before and after matching, respectively. The square markers correspond to the fundamental frequency of 5.5 GHz, and the circular markers correspond to the harmonic frequency of 11 GHz. By introducing a series inductor into the tag antenna and a parallel capacitor into the diode, conjugate matching between the tag antenna and the

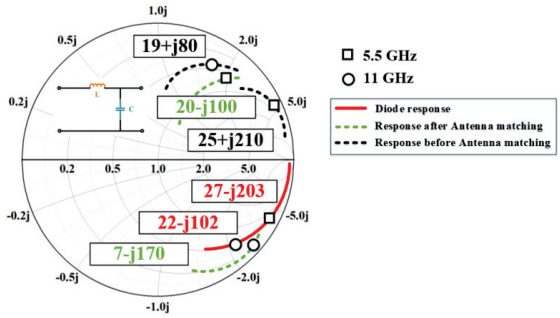

Fig. 15. Smith chart matching.

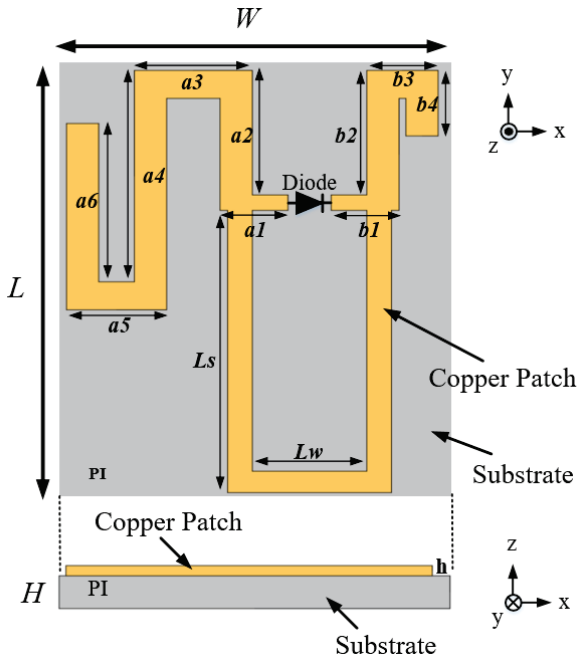

Fig. 16. Schematic diagram of the topology structure of the tag in this work.

diode was achieved at both the fundamental and harmonic frequencies.

The final tag structure is shown in Fig. 16, which illustrates the geometric configuration of the tag, including the radiation patches and the dielectric substrate. The diode is soldered between the radiation patches. The yellow regions represent copper radiation patches, labeled $a1$ to $a6$ and $b1$ to $b4$. The patches labeled with lengths Ls and Lw act as inductive loops, facilitating impedance matching between the antenna and the diode. The gray region indicates the dielectric substrate(PI, dielectric constant $\varepsilon_r = 3.3$). Detailed parameters of the tag antenna are listed in Table 4.

FEM simulations are commonly used in antenna design to analyze electromagnetic field distribution, radiation characteristics, and impedance matching. These simulations are crucial for understanding the physical characteristics of the antenna and optimizing its design. However, in tag design, it is also necessary to analyze the equivalent circuit model of the antenna because the tag antenna is typically a component of the tag system. In harmonic radar detection experiments, evaluating the overall performance of the tag—including the diode and the antenna—is more important than solely focusing on the antenna's electromagnetic properties. By representing the tag antenna and diode as an equivalent circuit model, the tag's performance can be assessed more intuitively. Therefore, equivalent circuit model simulations were conducted alongside FEM simulations, as shown in Fig. 17.

Table 4: Tag structure parameters

Parameter	Values	Parameter	Values
Frequency	5.5/11 GHz	H	0.11 mm
L	14 mm	h	0.035 mm
W	7.4 mm	$a1$ to $a6$	14.8 mm
Lw	2.8 mm	$b1$ to $b6$	6.3 mm
Ls	8 mm	Substrate	PI
Diode Length	1.2 mm	Diode Type	SMS-7630

The simulation results indicate the presence of resonant frequencies at both the fundamental and harmonic frequencies, as shown in Fig. 18, confirming the tag's effective operation. The FEM simulation results show that the reflection coefficient (S_{11}) is less than -10 dB near 5.5 GHz and 11 GHz, indicating high radiation efficiency, maximizing energy transmission, and improving the tag's overall efficiency.

To directly compare the performance of the designed tag, existing tags [15] are reproduced through simulation and fabrication at the same operating frequency for testing. Figure 19 shows the radiation patterns of two tags at the fundamental frequency of 5.5 GHz and the harmonic frequency of 11 GHz. The results indicate that both tags exhibit omnidirectional radiation in the XZ and

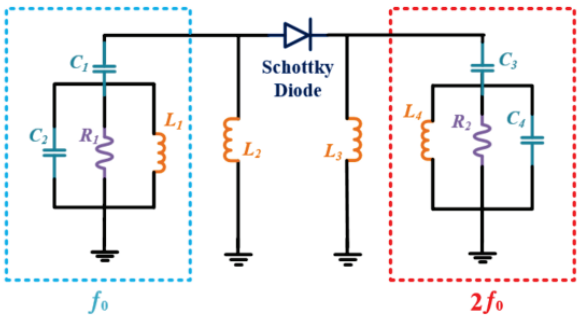

Fig. 17. Equivalent circuit model of this work.

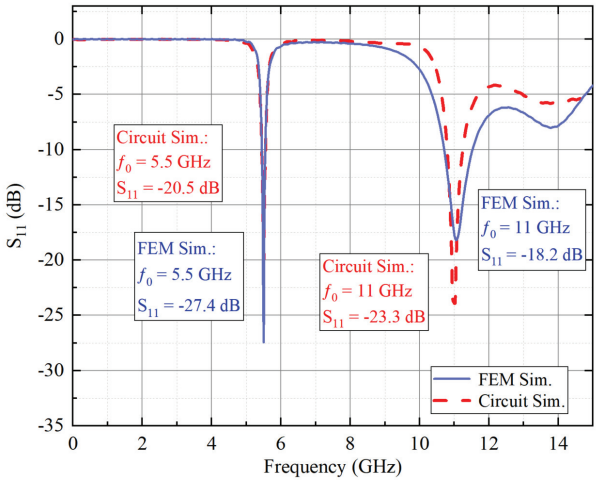

Fig. 18. Simulated S-parameters of this work.

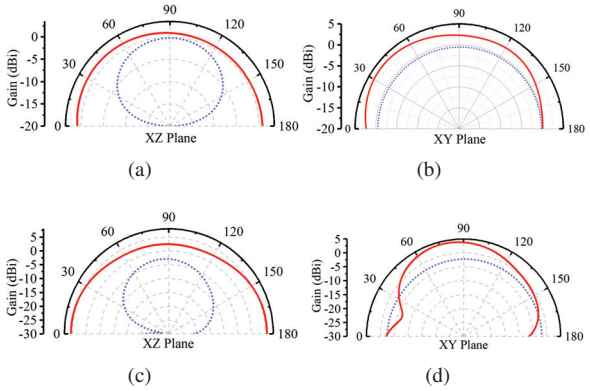

Fig. 19. The normalized radiation patterns of the tag at (a), (b) 5.5 GHz and (c), (d) 11 GHz frequencies are shown for the XZ and XY planes.The blue dashed line represents the wire tag, while the red solid line represents this work.

XY planes. However, the linear tag shows directional deviations in the XZ plane at both frequencies, leading to uneven radiation and limiting the coverage area of the harmonic radar. In contrast, the tag designed in this study demonstrates stronger and more uniform radiation characteristics in its radiation patterns, outperforming the linear tag.

IV. PERFORMANCE MEASUREMENT AND DISCUSSION

Figure 20 presents images of the fabricated tags. The schematic diagram of the indoor testing platform is shown in Fig. 21 (a). During indoor experiments, a signal source emitted the base frequency signal, and a signal analyzer received the harmonic signals generated by the tags. The performance of each tag was assessed based

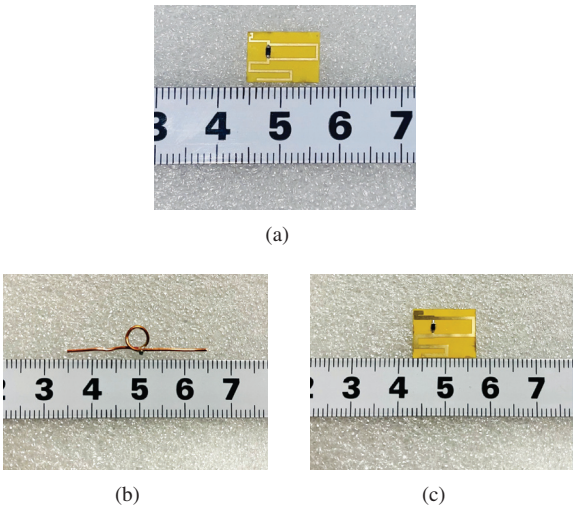

Fig. 20. Fabricated tags. (a) Unmodified tag. (b) Wire tag. (c) This work.

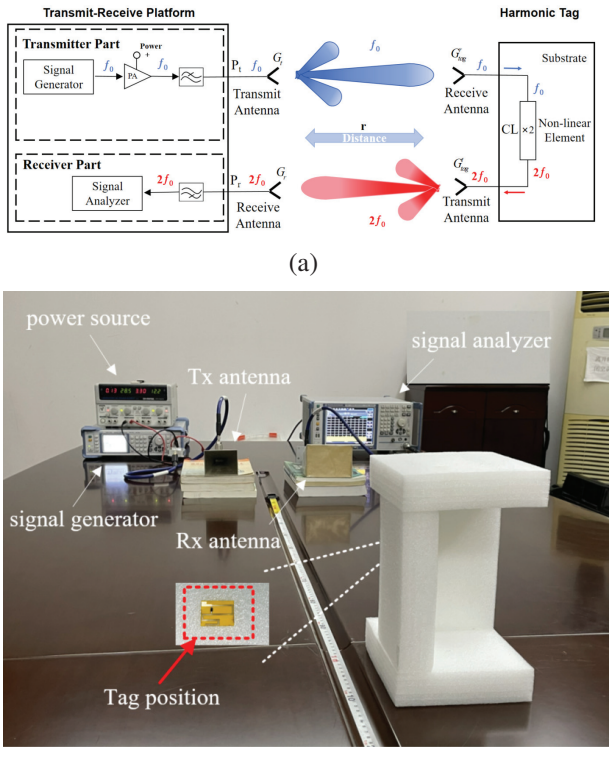

Fig. 21. The harmonic experimental testing system for the two types of tags. (a) Indoor harmonic platform test schematic. (b) The measurement setup indoors.

on the displayed received signal power. Stronger signal power indicated superior performance, while weaker signals indicated poorer performance. To assess this work's

performance in simulated real-world conditions, outdoor tests were conducted with harmonic radar in a realistic radio propagation environment. The schematic diagram of the outdoor testing platform is provided in Fig. 23 (a). The harmonic radar receives the echo (harmonic) signals and measures the radar range Doppler. Specific procedures for indoor and outdoor experiments are detailed in sections IV.A and IV.B, respectively.

A. Indoor harmonic system platform testing

Figure 21 (b) illustrates the measurement setup of the indoor testing platform. The tag is affixed to a movable foam material, and the experimental distance is calibrated using a measuring tape. At the transmitting end, the platform consists primarily of a signal generator and a transmitting antenna, while the receiving end includes a signal analyzer and a receiving antenna. To mitigate harmonic interference from the transmitting end, a low-pass filter is placed between the transmitting antenna and the signal generator. Additionally, a power amplifier (PA) is inserted between the signal generator and the low-pass filter to boost transmission power. Table 5 provides the parameters of the harmonic system platform depicted in Fig. 21.

Based on the Friis transmission equation [39], theoretical link budget analysis is conducted to obtain the received power of the signal analyzer:

$$P_r = P_t + G_t + G_r + G^t_{tag} + G^r_{tag} - TL_{f_0} - TL_{2f_0} - CL_d - L^t_s - L^r_s - L^{f_0}_{pol} - L^{2f_0}_{pol}. \quad (21)$$

$$C^g_{tag} = G^t_{tag} + G^r_{tag} - CL_d. \quad (22)$$

According to equation (22), C^g_{tag} represents the tag's conversion gain, which indicates the tag's influence on the system's received power. It is evident that as the tag gain increases and CL decreases, the tag's conversion gain increases, leading to stronger tag performance. Definitions of other parameters are provided in Table 6.

Considering the effect of the Fresnel zone on antenna and tag radiation in propagation experiments, the measurement distance needs to be greater than $2*L^2/\lambda$, where L is the maximum linear dimension of the antenna. Therefore, a test distance starting from 0.5 m and totaling 3 m is planned, with measurements taken every 0.5 m. From Fig. 22, it can be seen that the simulation and measurement results of this work are generally consistent, with the difference between them caused by fabrication and soldering tolerances. The unmodified tag's signal could not be detected at any distance. At a 3-meter range, the wire tag's reflected signal power measured -123.8 dBm, while our proposed tag achieved -118.3 dBm. Under identical test conditions, our tag demonstrates superior performance compared to both the wire tag and unmodified tag.

Additionally, under the same operating frequency of 5.5 GHz, the wire tag has dimensions of 30 × 5 mm^2, with a gain of 0.7 dBi at the fundamental frequency and -1.6 dBi at the harmonic frequency. Its tag conversion gain (C^g_{tag}) is -31.3 dB; this work has more compact dimensions of 12 × 8.4 mm^2, with a gain of 1.9 dBi at the fundamental frequency and 1.5 dBi at the harmonic frequency, and a tag conversion gain (C^g_{tag}) of -30.4 dB. This study achieves a reduction in tag size, an increase in

Table 5: Transceiver link parameters

Parameter	Value
Transmitter power	11 dBm
Tx antenna gain (f_0)	19 dBi
Transponder gain (f_0)	1.9 dBi
Harmonic CL	33.8 dB(@-30dBm)
Transponder gain ($2f_0$)	1.5 dBi
Rx antenna gain ($2f_0$)	17 dBi

Table 6: Definition of formula parameters

Parameter	Definition
P_r	Receiving power of the instrument
P_t	Transmitting power of the instrument
G_t	Transmitting antenna gain
G_r	Receiving antenna gain
G^t_{tag}	Transmitting antenna gain of the tag
G^r_{tag}	Receiving antenna gain of the tag
TL	Transmission loss
CL_d	Frequency doubling circuit CL
L_s	System circuit loss
C^g_{tag}	Tag conversion gain
L_{pol}	Polarization loss

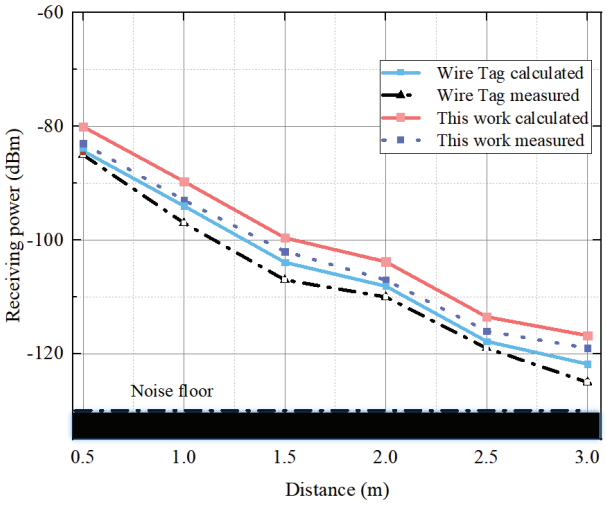

Fig. 22. The relationship between tag measurement distance and received power.

gain, and consequently, an enhancement in echo power under the same operating frequency as existing tags. The experimental results conclusively demonstrate that the proposed tag design exhibits superior performance and enhanced functionality compared to conventional counterparts. Furthermore, these findings validate the effectiveness of the modified reflection coefficients (S_{11}) calculation methodology.

To gain a deeper understanding of the transponder's performance under varying incident power densities, we employed a frequency-sweeping method to plot the relationship between received power and transmitted power, as illustrated in Fig. 23. In this figure, we represent the simulated and measured harmonic conversion losses with purple and red curves, respectively, corresponding to the right y-axis. Additionally, we depict the simulated and measured received power with pink and black curves, which align with the left y-axis, facilitating a straightforward comparison between the theoretical model and experimental data.

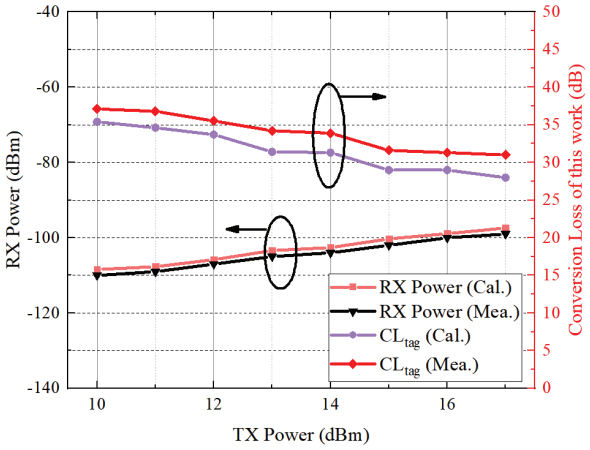

Fig. 23. Measured and simulated received power and CL versus the transmitted power.

During the measurement, the signal generator output power was set from +10 to +17 dBm, while the noise floor of the spectrum analyzer was –125 dBm. To ensure data reliability, the transmit power was reduced in 1 dB steps. The measured results closely follow the trend of the simulated curve, with any deviations mainly caused by fabrication and soldering tolerances.

B. Outdoor harmonic radar testing

The results of the indoor experiments demonstrate the superiority of this approach. To evaluate its performance in real-world conditions, harmonic radar was employed in an outdoor setting to detect moving tags. The radar system transmits a fundamental frequency signal at 5.5 GHz and receives a harmonic frequency signal

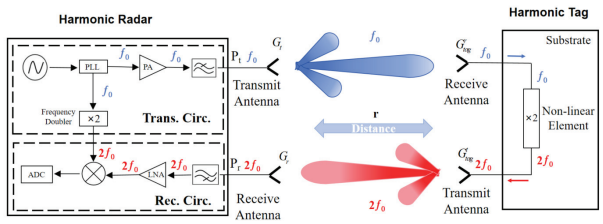

Fig. 24. Harmonic radar schematic diagram.

at 11 GHz. The precise system parameters are detailed in Table 7.

Outdoor field experiments were conducted using a harmonic radar system in an open area to validate the performance of the proposed harmonic tag.The harmonic radar consists of a transmit path and a receive path, as illustrated in Fig. 24.

In the transmit path, a high-precision oscillator and a phase-locked loop (PLL) are employed to generate a stable 5.5 GHz fundamental signal with low phase noise. The signal is amplified by a PA, filtered to suppress out-of-band noise, and transmitted through a directional antenna to ensure efficient radiation toward the target.The receive path is designed to capture the second harmonic response generated by the nonlinear behavior of the tag. The received 11 GHz signal is filtered, amplified by a low-noise amplifier (LNA), and mixed with a locally generated 11 GHz signal produced by a frequency doubler driven by the same PLL source. After mixing, an intermediate frequency (IF) signal is obtained, which is subsequently digitized by an analog-to-digital converter (ADC) for further processing, including target detection and localization analysis.The experimental setup is shown in Fig. 25 (a), where two squares indicate the positions of the harmonic radar and the moving tag. The harmonic radar is located at the origin, with the y-axis aligned with the radar's main lobe direction and the x-axis perpendicular to it, as illustrated in Fig. 25 (b).

Figure 25 (b) depicts the positional information: the blue area denotes the location of the harmonic radar, the

Table 7: Harmonic radar system parameters

Parameter	Value
Frequency	5.5/11.0 GHz
Waveform	Sawtooth FMCW
Transmitting Power	10 W(40 dBm)
Valid Bandwidth	50/100 MHz
Chirp Period	500 μs
Gain of TX Antenna	19.13 dBi@5.5 GHz
Gain of Rx Antenna	21.27dBi@11.0 GHz

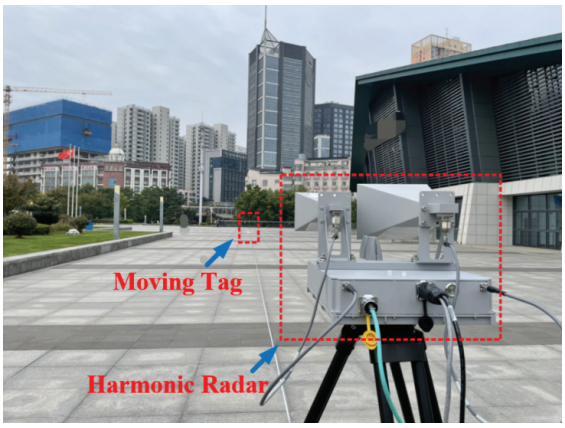

(a)

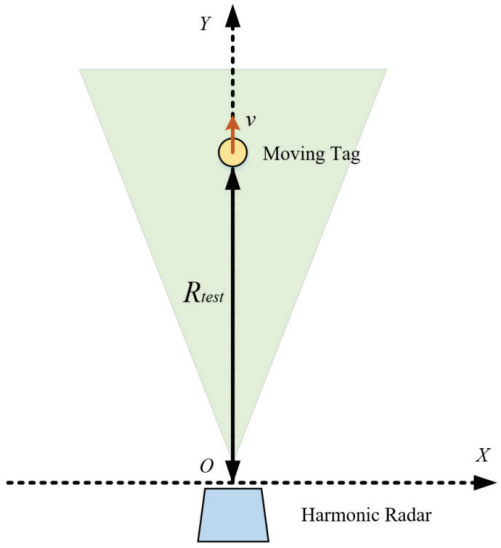

(b)

Fig. 25. Harmonic radar detection experiment. (a) Harmonic radar test experimental scene. (b) Experimental scene diagram.

green area delineates its radiation zone, and the yellow area signifies the mobile tag. Throughout the experiment, the tag travels along the positive y-axis direction, where R_{test} denotes the distance between the tag and the harmonic radar. We can evaluate the performance of the tag in the experiment through the distance Doppler of the harmonic radar.

Figure 26 depicts the distance Doppler information of the tag during its motion. The figure reveals that in the collaborative experiments between the tag and the harmonic radar in this study, there exists robust signal return strength characterized by stable and noise-free signals. Notably, even at a distance of 35 m, the harmonic radar can still capture strong echo signals, thus showcasing the tag's high performance and its applicability to

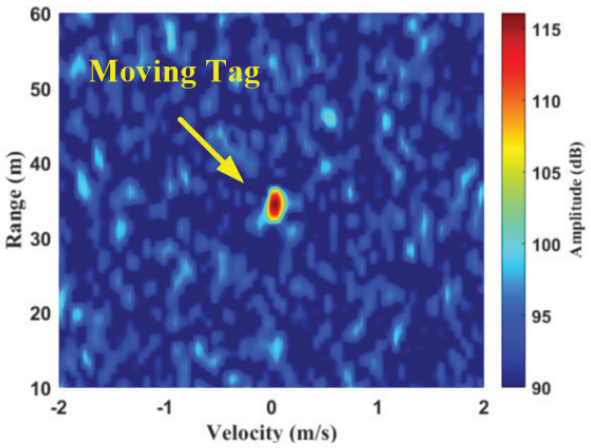

Fig. 26. Harmonic radar receiving tag echo power.

Table 8: Comparison between this paper and previous related works

Ref.	**[20]**	**[21]**	**[40]**	**Wire tag**	**This work**
Applica-tion	Track Insect	Track Insect	Monitor Wall	Track Insect	Track Insect
Type	Passive	Passive	Passive	Passive	Passive
Polariza-tion	LP	LP	LP	LP	LP
Op. freq. (GHz)	9.41 &18.8	5.88 &11.76	1.2 &2.4	5.5 &11	5.5 &11
Substr.	Copper	Rogers	Paper	Copper	PI
Area/λ^2	0.53 ×0.53	0.53 ×0.53	0.3 ×0.26	0.53 ×0.53	0.25 ×0.15
Gain(dBi) @f_0;@$2f_0$	\	\	3.3 ;3	-0.7 ;-1.6	1.9 ;1.5
CL_d(dBm) @-30dBm	\	\	-37	-33.8	-33.8
C^g_{tag}(dBm) @-30dBm	\	\	-30.7	-36.1	-30.4
Mass	12mg	6mg	3g	10mg	5mg

insect exploration experiments in intricate environments. A comparison between this paper and other state-of-the art works is listed in Table 8. They are all fully passive harmonic transponders. Our proposed harmonic tag not only achieves the smallest size and lightest weight, but also maintains strong signal strength. This makes it particularly advantageous in size- and weight-sensitive applications, such as tracking small organisms (e.g., insects) and environmental monitoring, where the tag's dimensions, weight, and signal strength are all critical to system performance. By employing an innovative antenna structure and highly efficient nonlinear

component matching techniques, we have significantly reduced the overall size and weight of the tag while preserving excellent radiation characteristics and signal conversion efficiency. This optimized design ensures the tag's adaptability in real-world applications, minimizes interference with the movement of tracked subjects, and greatly enhances its reliability and stability.

V. CONCLUSION

The main contribution of this paper lies in the theoretical analysis of the harmonic generation mechanism and device selection for nonlinear components, the correction of the harmonic tag echo loss calculation formula, and the design of a miniaturized, low-mass insect tag without compromising signal strength. In this study, the fundamental and harmonic frequencies achieved gains of 1.9 dBi and 1.5 dBi, respectively, both of which surpass those reported in previous research. Furthermore, the performance of the tag has been thoroughly validated through established experimental platforms. In an indoor test environment, we used a signal generator emitting 11dBm of power, with echo power measured at -118.3 dBm at a distance of 3 meters and a conversion gain of -30.4 dB, confirming the superiority of our method. Additionally, outdoor tests using harmonic radar also showed strong echo signals. This innovative method contributes to solving the harmonic radar detection and tracking problem by reducing losses, minimizing size and weight, and enhancing the echo signal strength, all of which demonstrate higher performance compared to previous studies. Future work will focus on investigating the adaptability of the tag for insects.

REFERENCES

[1] M. M. Sheikh, "Analysis of reader orientation on detection performance of Hilbert curve-based fractal chipless RFID tags," *Applied Computational Electromagnetics Society (ACES) Journal*, vol. 39, no. 6, pp. 490-504, 2024.

[2] L. Zhang, A. Poddar, U. Rohde, and M. Tong, "A novel reconfigurable chipless RFID tag based on notch filter," *Applied Computational Electromagnetics Society (ACES) Journal*, vol. 39, no. 9, pp. 801-813, 2024.

[3] C. Chen and Q. Feng, "A compact broadband circularly polarized slot antenna for universal UHF RFID reader and GPS," *Applied Computational Electromagnetics Society (ACES) Journal*, vol. 36, no. 5, pp. 589-595, 2021.

[4] R. Ma and Q. Feng, "Broadband CPW-fed circularly polarized square slot antenna for universal UHF RFID handheld reader," *Applied Computational Electromagnetics Society (ACES) Journal*, vol. 36, no. 6, pp. 747-754, 2021.

[5] M. N. Zaqumi, J. Yousaf, M. Zarouan, M. A. Hussaini, and H. Rmili, "Passive fractal chipless RFID tags based on cellular automata for security applications," *Applied Computational Electromagnetics Society (ACES) Journal*, vol. 36, no. 5, pp. 559-567, 2021.

[6] J. Shefer and R. J. Klensch, "Harmonic radar helps autos avoid collisions," *IEEE Spectr.*, vol. 10, no. 5, pp. 38-45, 1973.

[7] K. Grasegger, G. Strapazzon, E. Procter, H. Brugger, and I. Soteras, "Avalanche survival after rescue with the RECCO rescue system: A case report," *Wilderness Environ. Med.*, vol. 27, no. 2, pp. 282-286, 2016.

[8] B. Kubina, J. Romeu, C. Mandel, M. Schüßler, and R. Jakoby, "Design of a quasi-chipless harmonic radar sensor for ambient temperature sensing," *in SENSORS,* Valencia, Spain, pp. 1567-1570, 2014.

[9] A. Singh and V. M. Lubecke, "Respiratory monitoring and clutter rejection using a CW doppler radar with passive RF tags," *IEEE Sens. J.*, vol. 12, no. 3, pp. 558-565, 2012.

[10] L. Zhu, H. Huang, M. M.-C. Cheng, and P.-Y. Chen, "Compact, flexible harmonic transponder sensor with multiplexed sensing capabilities for rapid, contactless microfluidic diagnosis," *IEEE Trans. Microw. Theory Techn.*, vol. 68, no. 11, pp. 4846-4854, 2020.

[11] G. J. Mazzaro, A. F. Martone, and D. M. McNamara, "Detection of RF electronics by multitone harmonic radar," *IEEE Trans. Aerosp. Electron. Syst.*, vol. 50, no. 1, pp. 477-490, 2014.

[12] V. G. Yadav, L. Zeng, and C. Li, "Circular polarized antennas with harmonic radar: Passive nonlinear tag localization," *IEEE Journal of Selected Areas in Sensors*, vol. 1, pp. 9-19, 2024.

[13] D. Mascanzoni and H. Wallin, "The harmonic radar: A new method of tracing insects in the field," *Ecol. Entomol.*, vol. 11, no. 4, pp. 387-390, 1986.

[14] R. Brazee, E. Miller, M. Reding, M. Klein, B. Nudd, and H. Zhu, "A transponder for harmonic radar tracking of the black vine weevil in behavioral research," *Trans. ASAE*, vol. 48, no. 2, pp. 831-838, 2005.

[15] B. Colpitts and G. Boiteau, "Harmonic radar transceiver design: Miniature tags for insect tracking," *IEEE Trans. Antennas Propag.*, vol. 52, no. 11, pp. 2825-2832, 2004.

[16] N. Tahir and G. Brooker, "Recent developments and recommendations for improving harmonic radar tracking systems," in *Proceedings of the 5th European Conference on Antennas and Propagation (EUCAP)*, pp. 1531-1535, 2011.

[17] R. Maggiora, M. Saccani, D. Milanesio, and M. Porporato, "An innovative harmonic radar to track flying insects: The case of Vespa velutina," *Sci. Rep.*, vol. 9, no. 1, p. 11964, 2019.

[18] J. Riley and A. Smith, "Design considerations for an harmonic radar to investigate the flight of insects at low altitude," *Comput. Electron. Agric.*, vol. 35, no. 2-3, pp. 151-169, 2002.

[19] E. A. Capaldi, A. D. Smith, J. L. Osborne, S. E. Fahrbach, S. M. Farris, D. R. Reynolds, and J. R. Riley, "Ontogeny of orientation flight in the honeybee revealed by harmonic radar," *Nature*, vol. 403, no. 6769, pp. 537-540, 2000.

[20] D. Milanesio, M. Saccani, R. Maggiora, D. Laurino, and M. Porporato, "Design of an harmonic radar for the tracking of the A sian yellow-legged hornet," *Ecol. Evol.*, vol. 6, no. 7, pp. 2170-2178, 2016.

[21] H. Zhu, D. Psychoudakis, R. Brazee, H. Thistle, and J. Volakis, "Capability of patch antennas in a portable harmonic radar system to track insects," *Transactions of the ASABE*, vol. 54, no. 1, pp. 355-362, 2011.

[22] A. Lavrenko, B. Litchfield, G. Woodward, and S. Pawson, "Design and evaluation of a compact harmonic transponder for insect tracking," *IEEE Microw. Wirel. Compon. Lett.*, vol. 30, no. 4, pp. 445-448, 2020.

[23] J. Kiriazi, J. Nakakura, K. Hall, N. Hafner, and V. Lubecke, "Low profile harmonic radar transponder for tracking small endangered species," in *2007 29th Annual International Conference of the IEEE Engineering in Medicine and Biology Society*, pp. 2338-2341, 2007.

[24] Z.-M. Tsai, P.-H. Jau, N.-C. Kuo, J.-C. Kao, K.-Y. Lin, F.-R. Chang, E.-C. Yang, and H. Wang, "A high-range-accuracy and high-sensitivity harmonic radar using pulse pseudorandom code for bee searching," *IEEE Trans. Microw. Theory Techn.*, vol. 61, no. 1, pp. 666-675, 2012.

[25] N. Tahir and G. Brooker, "Toward the development of millimeter wave harmonic sensors for tracking small insects," *IEEE Sens. J.*, vol. 15, no. 10, pp. 5669-5676, 2015.

[26] V. Palazzi, F. Alimenti, M. Virili, C. Mariotti, G. Orecchini, P. Mezzanotte, and L. Roselli, "A novel compact harmonic RFID sensor in paper substrate based on a variable attenuator and nested antennas," in *2016 IEEE MTT-S International Microwave Symposium (IMS)*, pp. 1-4, 2016.

[27] M. I. M. Ghazali, S. Karuppuswami, and P. Chahal, "Embedded passive RF tags towards intrinsically locatable buried plastic materials," in *2016 IEEE 66th Electronic Components and Technology Conference (ECTC)*, pp. 2575-2580, 2016.

[28] S. Mondal and P. Chahal, "A passive harmonic RFID tag and interrogator development," *IEEE J. Radio Freq. Identif.*, vol. 3, no. 2, pp. 98-107, 2019.

[29] F. Yu, K. G. Lyon, and E. C. Kan, "A novel passive RFID transponder using harmonic generation of nonlinear transmission lines," *IEEE Trans. Microw. Theory Techn.*, vol. 58, no. 12, pp. 4121-4127, 2010.

[30] H. Wang, A. Hsu, K. K. Kim, J. Kong, and T. Palacios, "Gigahertz ambipolar frequency multiplier based on CVD graphene," in *2010 International Electron Devices Meeting*, pp. 23.6.1-23.6.4, 2010.

[31] T. Song, H.-S. Oh, J. Yang, E. Yoon, and S. Hong, "A 2.4-GHz sub-mW frequency source with current-reused frequency multiplier," in *IEEE Radio Frequency Integrated Circuits (RFIC) Symposium, 2006,* San Francisco, CA, USA, p. 4, 2006.

[32] C.-C. Wang, Y.-L. Tseng, H.-C. She, and R. Hu, "A 1.2 GHz programmable DLL-based frequency multiplier for wireless applications," *IEEE Trans. Very Large Scale Integr. (VLSI) Syst.*, vol. 12, no. 12, pp. 1377-1381, 2004.

[33] S. Mondal, D. Kumar, and P. Chahal, "Recent advances and applications of passive harmonic RFID systems: A review," *Micromachines*, vol. 12, no. 4, p. 420, 2021.

[34] R. Ludwig and G. Bogdanov, *RF Circuit Design: Theory and Applications*, 2nd ed. Noida: Pearson Education India, 2008.

[35] J. Zhang, S. D. Joseph, Y. Huang, and J. Zhou, "Compact single-port harmonic transponder for backscattering communications and energy harvesting applications," *IEEE Transactions on Microwave Theory and Techniques*, vol. 71, no. 7, pp. 3136-3143, 2023.

[36] X. Gu, N. N. Srinaga, L. Guo, S. Hemour, and K. Wu, "Diplexer-based fully passive harmonic transponder for sub-6-GHz 5G-compatible IoT applications," *IEEE Transactions on Microwave Theory and Techniques*, vol. 67, no. 5, pp. 1675-1687, 2019.

[37] W. L. Stutzman and G. A. Thiele, *Antenna Theory and Design*. Hoboken, NJ: John Wiley & Sons, 2012.

[38] A. Kumar and A. Lavrenko, "Compact folded meander-line harmonic tag antenna for insect tracking," in *2023 17th Eur. Conf. Antennas Propag. (EuCAP)*, pp. 1-5, 2023.

[39] H. T. Friis, "A note on a simple transmission formula," *Proceedings of the IRE*, vol. 34, no. 5, pp. 254-256, 1946.

[40] V. Palazzi, F. Alimenti, P. Mezzanotte, G. Orecchini, and L. Roselli, "Zero-power, long-range, ultra low-cost harmonic wireless sensors for massively distributed monitoring of cracked walls," in *2017 IEEE MTT-S International Microwave Symposium (IMS),* Honolulu, HI, USA, pp. 1335-1338, 2017.

Zhan-Fei Su was born in Shandong, China. He received the M.S. degree in electronics and communication engineering from the Xi'an University of Posts and Telecommunications, Xian, China in 2021. He is currently working toward the Ph.D. Degree at the School of Electronic Information, Wuhan University, Wuhan, China. His research interests include antennas designs, nonlinear circuit designs, microwave circuit designs, harmonic transponders and their applications.

Xian-Rong Wan was born in Hubei, China. He received the B.E. degree from the former Wuhan Technical University of Surveying and Mapping, Wuhan, China, in 1997, and the Ph.D. degree from Wuhan University, Wuhan, in 2005. He is currently a Professor and the Ph.D. Candidate Supervisor with the School of Electronic Information, Wuhan University. In recent years, he has hosted and participated in more than ten national research projects and authored or coauthored more than 80 academic articles. His main research interests include design of new radar system such as passive radar, over-the-horizon radar, and array signal processing.

Jian-Xin Yi received the B.E. degree in electrical and electronic engineering and the Ph.D. degree in radio physics from Wuhan University, Wuhan, China, in 2011 and 2016, respectively. From August 2014 to August 2015, he was a Visiting Ph.D. Student with the University of Calgary, Calgary, AB, Canada. He is currently an Associate Professor with the School of Electronic Information, Wuhan University. His main research interests include radar signal processing, target tracking, and information fusion. Dr. Yi was a recipient of the 2017 Excellent Doctoral Dissertation Award of the Chinese Institute of Electronics. He has been supported by the Post-Doctoral Innovation Talent Support Program of China.

Zi-Ping Gong was born in Hubei, China. He received the B.E. and Ph.D. degrees from Wuhan University, Wuhan, China, in 1999 and 2007, respectively. His main research interests include high frequency (HF) radio wave propagation, antenna theory analysis, and antenna design.

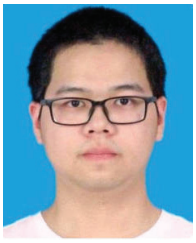

Zi-Yao Wang was born in Hubei, China. He received the B.E. degree in measurement and control technology and instrument in 2020 from Wuhan University, Wuhan, China, where he is currently working toward the Ph.D. degree in electronic science and technology. His research interests include design of harmonic radar system and radar signal processing.